A contribution to gamma-ray astronomy of GeV-TeV Active Galaxies with Fermi and H.E.S.S.

Berrie Giebels

A contribution to γ-ray astronomy of GeV-TeV Active Galaxies with *Fermi* and H.E.S.S.

Berrie Giebels

Laboratoire Leprince-Ringuet
Ecole polytechnique, CNRS/IN2P3

Mémoire présenté en vue de l'obtention de

l'Habilitation à Diriger les Recherches de
l'Université Paris Sud 11

Soutenue à Orsay, le 20 avril 2011, devant le jury composé de

Réza Ansari, Examinateur
John Carr, Rapporteur
Gilles Henri, Rapporteur
Rene Ong, Rapporteur
Reynald Pain, Président

Contents

Chapter 1

Ultra High Energy Cosmic Rays, Gamma Rays and Active Galactic Nuclei

The question is not what you look at, but what you see.

Henry David Thoreau

Abstract

More than a century after their discovery, the origin of the most energetic cosmic rays and the nature of the accelerator producing them, remain a largely open question. The quest of their origin through a wide variety of observations has not only provided a wealth of clues, but also some fascinating new insights on ways the Universe has found to outperform with regard to more than one aspect what our terrestrial laboratories are capable of. The direct detection of the most energetic events exceeding $\geq 10^{20}$ eV is however complicated because of the extremely low fluxes, the deflective effects of cosmic magnetic fields, and the short distance they can travel without interacting with the CMBR. Good detection rates are achievable at lower energies but then neutral messengers, generated in interactions in the vicinity of where particle acceleration occurs, have to be searched for. The promising neutrino astronomy (with the sun and SN1987A as only cosmic sources so far) and gravitational radiation astronomy being still in their infancy, one has to resort to the more copious γ-rays. These have the inconvenience of mostly washing out information about the primary particle which generated it and having a limited horizon at the highest energies, but come with the bonus that high-energy γ-ray detectors can achieve an order of magnitude better spatial resolution than the other forms of cosmic rays, making them very effective to perform astronomical measurements, i.e. associating a specific position in the sky with the observed emission and performing an association with a class of known objects. In the case of Active Galaxies, an obvious class of cosmic accelerators, the γ-ray spectra and variability probe the acceleration mechanism closer than any direct observation currently available. Photons are also prone to propagation effects over cosmological distances - which is a blessed nuisance since it hinders the knowledge of the emitted radiation but also probes the intergalactic fields well enough despite the lack of knowledge on the intrinsic source. A better understanding of particle acceleration occuring in active galaxies in particular, and of the origin of the most energetic cosmic rays in general, requires thorough research of multi-wavelength observations and their relationships with the most energetic gamma-rays.

1.1 Ultra High Energy Cosmic Rays (UHECR)

1.1.1 Introduction

At the time this manuscipt is written, the Large Hadron Collider (LHC) has started operating its accelerator which, in its nominal configuration, accelerates bunches of 10^{11} protons up to energies reaching $12\,\mathrm{TeV}$, with the two beams carrying an energy of $724\,\mathrm{MJ}$ (or 10^{16} erg) and creating collisions reaching energies of $10^{17}\,\mathrm{eV}$ in the lab frame. The LHC is the most recent achievement of the high energy branch of experimental physics, which grew in searching for new particles and understanding the nature of their interactions at the subatomic scale through intensive studies of the interactions of daughter particles from cosmic ray induced cascades in the atmosphere. These were used as an investigation tool, and their actual origin was a completely different matter. It was however established as soon as 1962 that particles with energies of the order of $10^{20}\,\mathrm{eV}(=100\,\mathrm{EeV})$, or approximately 10 joules[1], were present in the cosmic

[1] which is three orders of magnitude higher than what an LHC as large as the Earth could possibly achieve

radiation [Linsley, 1963], despite fluxes of the order of one particle per km^2 and per *century*. The cosmic ray spectrum is now measured over 12 orders of magnitude in energy and more than 30 orders of magnitude in flux: Figure 1.1 shows only the 27 most energetic octaves, over which the spectrum $J(E)$ behaves as a series of successive power laws, $J(E) \propto E^{-\Gamma}$, indicating that some acceleration mechanism is at play in a region where the balance between energy gain and escape probability determines the index Γ of the power law [Blandford & Eichler, 1987]. Hillas [1984] established a criterion stipulating that a cosmic acceleration region impregnated with a magnetic field B (the strength of which would be small enough that energy gain would not be lost too fast by synchrotron radiation), which would accelerate or contain a particle with energy E and charge Z, should have a characteristic size at least as large as the Larmor radius

$$R = \frac{p}{ZeB} \simeq \frac{(E/10^{20}\,\mathrm{eV})}{11Z(B/1\,\mathrm{G})}\,\mathrm{pc},$$

which readily excludes our own Galaxy as the container or the location of the accelerator of cosmic ray protons[2] with energies larger than $10^{16}\,$eV since the disk has a thickness of $\sim 300\,$pc and the magnetic field is on average $10^{-6}\,$G (but varies from $10^{-4}\,$G in the vicinity of the Earth to $10^{-10}\,$G in the intergalactic medium). Cosmic rays cannot come from that far away either: Kuzmin and Zatsepin, and then independently Greisen, established in 1966 that the $2.7\,$K cosmic background radiation would look like $\sim 100\,$MeV photons in the rest frame of protons with $E \geq 10^{20}\,$eV, producing pions within one interaction length through $\mathrm{p} + \gamma_{2.7\mathrm{K}} \rightarrow \pi^0 + X$ and hence not be able to come unaffected from distances to the Earth much larger than $50\,$Mpc, called a "GZK radius". (Similarly, nuclei with $E \geq 5 \times 10^{18}\,\mathrm{eV/n}$ would be limited to about $100\,$Mpc through $\mathrm{A} + \gamma_{2.7\mathrm{K}} \rightarrow \Delta^{++} + \mathrm{X}$). So while the Universe might be filled with even more extreme accelerators, only those within that distance are directly accessible to us.

Another hurdle to the direct study of UHECRs comes from our lack of knowledge of the intergalactic magnetic fields in which they propagate, which in turn induces a systematic uncertainty in the estimation of the magnitude of the angular deflexion on their momentum - and hence on the angular resolution with which an instrument can make astronomical associations. While Dolag et al. [2005] estimates that the r.m.s. deflexion of the proton component in UHECRs within one GZK radius is of the order of a degree, it might actually exceed 10° according to Sigl et al. [2003] and Ryu et al. [2010]. Although better characterized, Galactic magnetic fields (GMF) could also have measurable deflective effects on high-Z charged nuclei UHECRs [Kachelrieß et al., 2007] and hence bias the estimation of the instrumental acceptance. Authors of large deflective angle claims hence recommend rather drastic exclusion zones, of the order of half of the observable sky in one case, in order to avoid bias effects in the search for anisotropy, spatial correlations, or associations with known sources.

1.1.2 Indirect detection of UHECRs

Above energies of the order of $10^{15}\,$eV fluxes become too weak to yield statistically significant detections on balloon-based or space-based detectors, so ground-based techniques have to be used instead. The atmosphere, of $\sim 27 X_0$ radiation lengths (of $X_0 = 40\,\mathrm{g\,cm^{-2}}$), and 2.5 times less interaction lengths, is then used as part of the detector. The primary energy, the nature of the primary particle, and its direction, are determined through the study of the light emitted by fluorescence of nitrogen caused by the longitudinal development of secondaries in the extended air shower (EAS), or by the lateral spread directly detected on the ground. In the absence of any calibrator, the understanding of the complete detection chain can only be assessed through Monte Carlo simulations, themselves largely tuned to accelerator-based cross-section measurements, particle distributions, and verification of interactions. The maximal energy at which, for instance, the pion distribution is known forward of the proton-proton interactions, is currently $10^{14}\,$eV (as measured by the UA7 experiment at the SPS; Paré et al. [1990]), but will be increased up to $10^{17}\,$eV by the LHCf experiment [Bongi et al., 2010].

[2] While this criterion is widely accepted in the community, Vukcevic & Schlickeiser [2007] claim that conditions in the magnetic fields can be found for which would relax the above mentioned Hillas criterion by as much as 4 orders of magnitude, and hence allow protons with energies several hundreds of EeV to still be confined to the Galaxy.

The transverse momentum in nuclear reactions of $\sim 0.3\,\mathrm{GeV}/c$ induces a lateral extension in nuclear EAS which has a very profitable consequence of the drawback of having to deal with secondary particles at different levels of the cascade development, since effective areas[3] up to $7000\,\mathrm{km}^2\,\mathrm{sr}$ are achieved by the current generation of instruments devoted to their detection such as the Pierre Auger Observatory (PAO; Pierre AUGER Collaboration et al. [2010], Abraham et al. [2008]) and the High Resolution Fly's Eye (HiRes; Abbasi et al. [2008]), while the KASCADE experiment [Antoni et al., 2003] has a much smaller effective area. The PAO and HiRes are sensitive to the highest energies, and have now clearly shown evidence of a turnover in the cosmic ray spectrum at energies $> 10^{20}\,\mathrm{eV}$ (Figure 1.1), where fluxes are as low as one particle per square kilometer per century. This is now widely considered as evidence of the GZK suppression in the end of the observable cosmic ray spectrum, which was predicted if the UHECRs sources are located at distances $\gg 50\,\mathrm{Mpc}$. It also ended a decade long debate on the compatibility between different measured spectra in this energy range, plagued by the uncertainties in calibrations.

Some basic questions such as the composition of cosmic rays at ultra-high energies are even more difficult to address in this way, since the primary particle is broken up at its first interaction in the atmosphere and the subsequent showers fluctuate strongly enough that the primary composition is erased. The GeV-energy composition is relatively well known and compatible with accelerated ordinary interstellar matter, with protons and nuclei accounting for the bulk of the flux, and electrons about $1-2\%$ (but much less above - see e.g. Ave et al. 2008 and Ahn et al. 2009 for a review of heavy nuclei balloon measurements up to $\sim 10^{14}\,\mathrm{eV/n}$ by the TRACER and CREAM experiments). Therefore finding where *ions* are accelerated up to those energies is the key to understanding the bulk of the energy input in cosmic rays, while *electron* accelerators might seem of lesser importance for this specific quest. Cosmic ray ion acceleration and electron acceleration can occur in the same sites [Melrose, 2009], but even for Galactic cosmic ray sources, there is still no standard picture on how both are related [Butt, 2009]. There seems however to be no major difficulty in explaining the local cosmic ray electron/positron component through nearby pulsar activity [Yüksel et al., 2009] or supernova remnants [Blasi, 2009] . A direct composition measurement with unprecedented statistics is now expected from the Alpha Magnetic Spectrometer (AMS) recently docked on the ISS for a 5-year mission (compared to balloon flights with exposures of a few days) carrying a $0.125T$ magnet spectrometer which should be capable of measuring the composition in the $100\,\mathrm{GeV}$ range (though its main objective is the search for anti-matter and signatures of dark matter annihilation products).

1.1.3 The origin of UHECR

Among the most powerful known sources of non-thermal radiation and most luminous known electromagnetic emitters, following the principle that there is 'no extragalactic smoke without fire' (quoting Porcas 1983), objects from the Active Galactic Nuclei (AGN) class of galaxies are prime candidates in the search for the origin of UHECRs. Their luminosities are in the range $10^{42}-10^{48}\,erg\,s^{-1}$, for which the most common interpretations are linked to infalling gas onto a supermassive black hole, and the wide variety of subclasses inferred from observational properties are often assumed to come from orientation and obscuration effects [Antonucci, 1993]. Other types of extremely energetic phenomena also investigated include gamma-ray bursts (see, e.g., Waxman 1995a or Murase et al. 2008), and neutron stars in the Metagalaxy with petagauss ($10^{15}\,\mathrm{G}$) magnetic fields called magnetars [Arons, 2003; Ghisellini et al., 2008], but these will not be further discussed here.

[3] A_{eff}, the physical area weighted for the probability of a detected or reconstructed interaction, defined as

$$A_{\mathrm{eff}}(E,\theta,\Phi) = \int\int_{\Sigma} R(E,\theta,\Phi,x,y)\,dx\,dy$$

where R is the instrument's efficiency for incoming primaries of energy E with angles (θ,Φ) and position (x,y) over an area Σ. This quantity heavily relies on Monte Carlo simulations for ground-based detectors, where Σ is much larger than the physical area of the detector. When the detection mechanism relies on the detection of light as well, its transmission through the atmosphere becomes model-dependent as well which adds $\mathcal{O}(5\%)$ systematic uncertainties on energy-dependent variables [Tonachini, 2011].

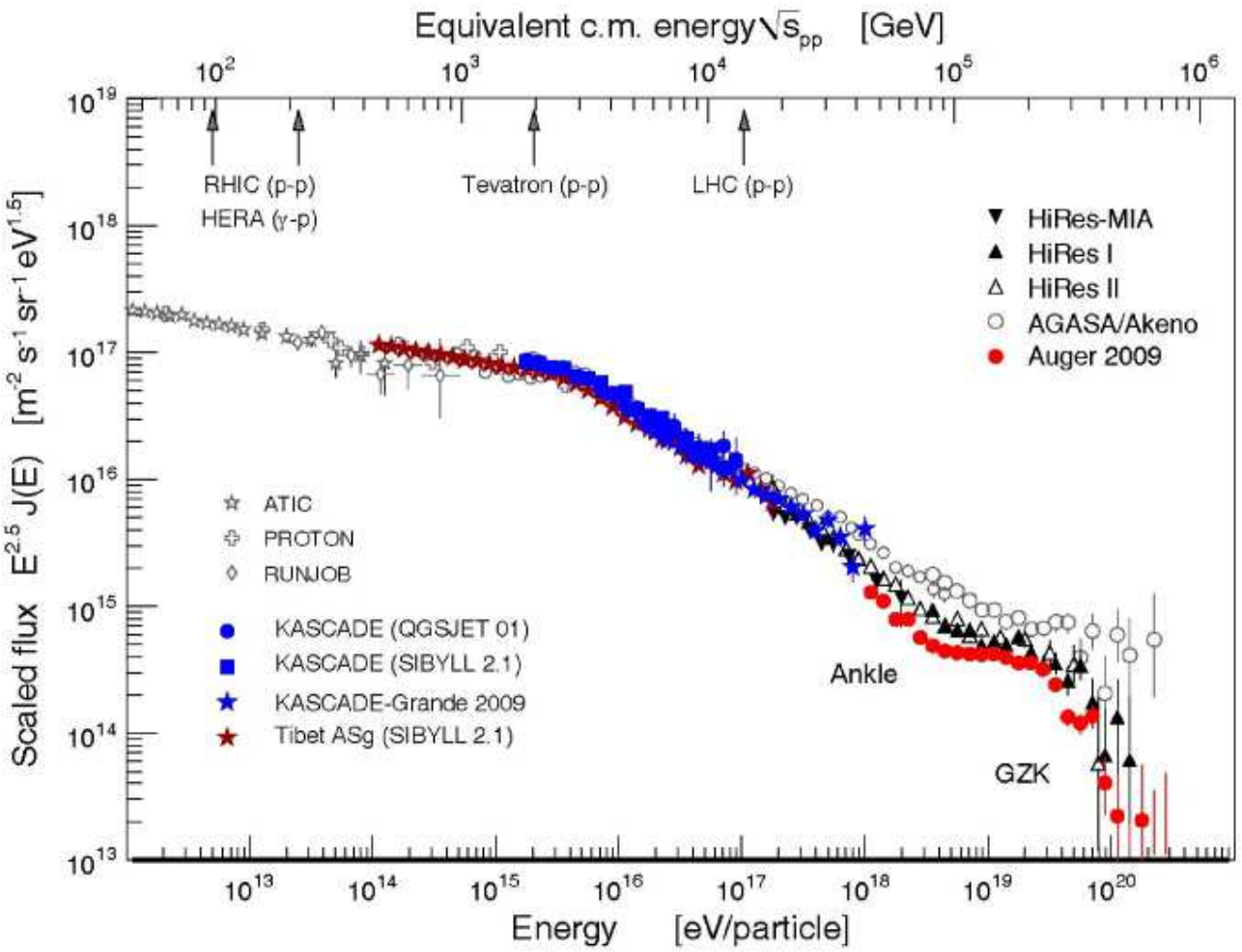

Figure 1.1: *Cosmic ray spectrum as determined with the measurements from many space and ground-based instruments. Also indicated on the graph, the center-of-mass energy for pp collisions at the LHC, well above the so called "knee" in the CR spectrum at* $E \simeq 5 \times 10^{15}$ eV *where the spectrum changes from* $J(E) \propto E^{-2.7}$ *to* $\propto E^{-3}$ *(called a spectral* softening*). At the so called "ankle" at* $E \simeq 10^{18}$ eV *the spectrum changes again to* $\propto E^{-2.7}$ *(called a spectral* hardening*), and the GZK cutoff at* $\sim 6 \times 10^{19}$ eV*. (Reproduced from Matthiae [2010]).*

The most striking evidence for cosmic accelerators at play in AGN come from the observation with radiotelescopes of relativistic outflows and superluminal expansions in quasar systems [Pearson et al., 1981] harbouring a very massive black hole, at apparent transverse speeds up to $\beta_{app} = \mathbf{v}_{app}/c \simeq 50$ [Lister & MOJAVE Collaboration, 2009] (also visible in Galactic binary systems Mirabel & Rodríguez 1994). These outflows are also thought to have dramatic consequences on the star formation of the galaxy which hosts the black hole [Di Matteo et al., 2005]. While the observations of superluminal expansions were, as early as 1966, hypothesized by Martin Rees [Rees, 1966] to occur as a pure geometrical effect of the velocity projection on the sky when the velocity β makes a small angle with the observer's line of sight $\mathbf{n}$, it still requires a solar-mass fraction of radio-emitting plasma moving at highly relativistic speeds with Lorentz factors of $\Gamma \sim 10$ typically. The extreme luminosities observed in some AGN is hence interpreted as a geometrical configuration where the angle θ between β and the line of sight $\mathbf{n}$ is small enough that the jet emission, which relativistic aberration confines within a half-angle of $\sim 1/\Gamma$ radians from β, is seen by the observer with a Doppler factor $\delta = [\Gamma(1 - \beta \cdot \mathbf{n})]^{-1}$ which enhances significantly the observed flux by factors $\sim \delta^4$ compared to what is expected from isotropic $1/r^2$ flux-dependent [Blandford & Konigl, 1979] - conditions under which the observed phenomenon is called a *blazar* and here the angle has a beaming effect leading again to different categories

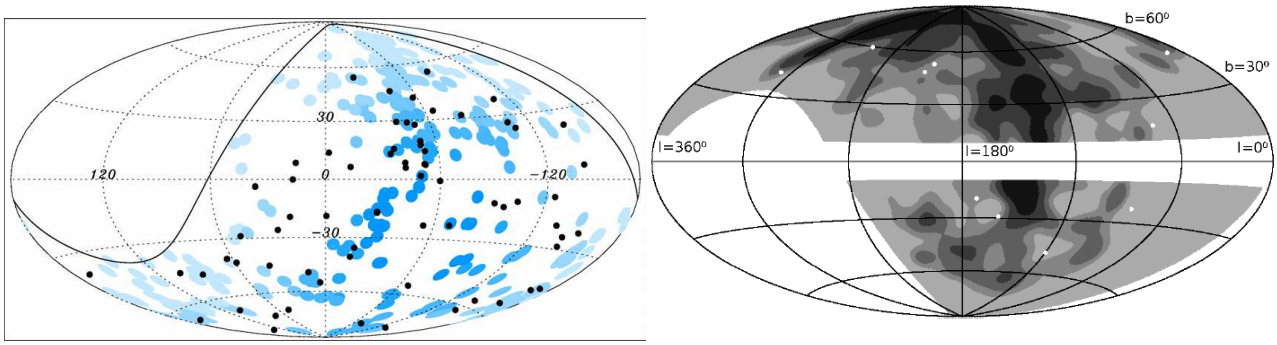

Figure 1.2: *GZK-class cosmic ray positions above 55 EeV in galactic coordinates, as measured in the southern hemisphere by the PAO (left) and the HiRes experiment (right). (Reproduced from The Pierre Auger Collaboration et al. [2010]) and Abbasi et al. [2010]).*

of AGN with relativistic outflows [Urry & Padovani, 1995][4]. The speed β of the emitting region is related to its apparent transverse speed through $\beta_{app} = \frac{\beta \sin\theta}{1-\beta\cos\theta}$ such that in the limit of $\theta \ll 1/\Gamma$, $\beta_{app} \simeq 2\Gamma^2\theta < 2\Gamma$ (e.g. Krolik 1999) which shows that the bulk Lorentz factors are roughly of the same order as the apparent transverse speeds. The energetic requirements for AGN to accelerate a proton up to $\geq 10^{20}$ eV can be roughly calculated: as pointed out by Waxman [2004], the lower limit on the required nonthermal isotropic luminosity L for a relativistic flow with Lorentz factor Γ and speed β, in which a region of size R/Γ with average magnetic field strength B, accelerates protons up to E is

$$L > 10^{45.5} \frac{\Gamma^2}{\beta} \left(\frac{E}{10^{20}\,\mathrm{eV}} \right)^2 \mathrm{erg\,s^{-1}},$$

which the most powerful AGN indeed reach. This condition can be relaxed by a factor Z^2 in the case of heavier ions.

Evidence for positionally coincident UHECR events with some outstanding objects of the AGN class is therefore intensely sought for. If $1/r^2$ flux-dependent effects smear out over time a limited detector acceptance, a significant correlation of their spatial distribution on the sky with comprehensive catalogs of specific extragalactic source types (such as the successive editions of Véron-Cetty & Véron (VCV) catalogs of quasars and AGN; Véron-Cetty & Véron 2006, 2010, or galaxies in the 2MASS Redshift Survey 2MRS from Huchra et al. [2005], used by HiRes) would be an interesting result as well.

The location of the most nearby AGN known as Centaurus A (Cen A) is indeed barely 4° away (Figure 1.2) from the region with the largest excess of arrival directions as measured by the PAO [The Pierre Auger Collaboration et al., 2007; Moskalenko et al., 2009; The Pierre Auger Collaboration et al., 2010]. This source is however not visible for similar northern hemisphere based detectors, so contrary to results based on the whole UHECR sample of this field, it is currently impossible to confirm it. No such spatial coincidence exists for a similar object, M87, but since it is 5 times more distant and has a reduced exposure compared to Cen A, this would not be unexpected even if M 87 had a similar UHECR luminosity. Since the jet emanating from Cen A makes a $50-80$ degree angle with the line of our sight to this object [Tingay et al., 1998], GZK-class events would need to be deflected at angles well above the expected rms deflexion angles if they are related to the jet geometry, making other apparent structures such as the radio lobes more likely acceleration sites. Lemoine & Waxman [2009] propose that, if an association with Cen A is significant, such an excess could be interpreted as an echo of GRB-generated cosmic rays in the galaxy of Cen A rescattered in the radio lobes, and not necessarily to an acceleration mechanism related to the jet. The subject is still hotly debated and has not ended at this point..

When considering the overall directional properties of the most energetic UHECRs, there is a fundemental disagreement between the HiRes and PAO. While the PAO claims that isotropy

[4]Note that $\delta \sim \Gamma$ in the limit of $\theta < 1/\Gamma$, and that the bolometric luminosity drops as θ^{-6} when $\theta \gg 1/\Gamma$

of an amount of 27 events[5] can be excluded at the 99% confidence level [The Pierre Auger Collaboration et al., 2007], there is no significant anisotropy in the cosmic ray arrival directions at any energies in the HiRes experiment based on 13 events with the same energy cut [Abbasi et al., 2010].

An even stronger statement from the PAO is the *astronomical* result that the bulk of the most energetic events could be associated with active galaxies since they have a correlation of $69^{+11}_{-13}\%$ with the AGN from the 12th VCV catalog (compared with 21% expected for isotropic cosmic rays) restricted to $\sim 75\,\mathrm{Mpc}$ (or one GZK length at those energies). The HiRes experiment's isotropic distribution of 13 GZK events contradicts this, and exclude at the 95% confidence level a correlation with galaxies in the 2MRS catalog [Abbasi et al., 2010] as well as (obviously) being incompatible with a 69% correlation despite smaller statistics, since 9 events are expected to match the spatial proximity criterion when just 2 are observed. The more recent results from the PAO [The Pierre Auger Collaboration et al., 2010], now including 69 GZK events, revise however both the degree of correlation with the updated 13th VCV catalog and its significance to $38^{+7}_{-6}\%$. This new correlation factor would now require that only 5 out of the 13 HiRes events should be associated with active galaxies, reducing the level of discrepancy between the two experiments given the smaller difference between 2 observed associated events and the 5 expected ones.

So while the current generation of UHECR detectors have tremendously contributed to the improvement of our knowledge, important questions such as where and how cosmic rays are accelerated clearly remain open. The high energy multi-messenger astronomy potential might be achieved if the space-based JEM-EUSO experiment [Takahashi & the JEM-EUSO Collaboration, 2009] flies on board the ISS around 2015. Observing cosmic ray interactions in the atmosphere at high altitude from above increases the effective area up to $2 \times 10^5\,\mathrm{km}^2$ and the sensitivity compared to PAO by more than two orders of magnitude thereby quickly outperforming the statistics of any existing ground-based experiment at that time (with however a poorer directional and energy reconstruction). The sensitivity of the JEM-EUSO experiment might be sufficient to perform the first charged particle astronomical measurements, without however much capacity to determine the nature of the primary particle.

Besides being widely considered as having an extragalactic origin, there is still no conclusive evidence yet that a source class such as the AGN generates UHECRs. Their origin remains one of the major puzzles to solve, and it carries some of the most fascinating questions addressed by particle astrophysics with increasingly improved means, pushing the detectors and the computing power to the limits of the currently achievable techniques (but unfortunately still orders of magnitude below the limits of funding, scientific or not). Therefore, the study of possible cosmic ray sites must rely on the *neutral* messengers they are bound to create when a fraction of them interact with their surroundings, either within or after having left the acceleration region. The medium around these sites hence act as a calorimeter for those particles. Whether the interactions are electromagnetic - curvature or synchrotron radiation on local magnetic fields, inverse Compton on local photon fields - or hadronic, the mean free paths of these interactions should ideally be short enough that they must occur in the vicinity of the accelerator (provided the interaction medium exists there too). Investigating how AGN work as cosmic accelerators through the study of their emission in γ-rays, the most energetic electromagnetic form of information capable of reaching us directly by definition, is therefore particularly interesting because (i) the mechanisms which generate them arise from well understood radiative mechanisms at play and (ii) they occur in the vicinity of cosmic ray creation sites given the extremely fast cooling times involved. The γ-ray flux characteristics - currently its variability and spectral properties - depend on, and therefore allow to constrain, the environment they are accelerated in and interact with: each of the observed photons can in principle be associated with an interacting charged particle.

[5] using a cut on events with reconstruced energies below $56\,\mathrm{EeV}$

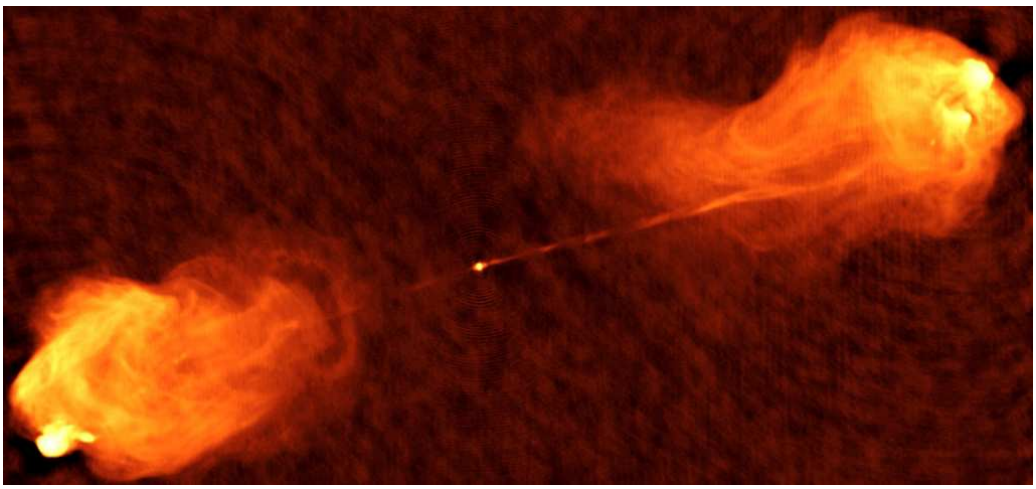

Figure 1.3: *The radio galaxy Cygnus A, as seen by aperture synthesis interferometry with the Very Large Array at 5 GHz. The inclination of the jet with respect to the observer is* $> 75^\circ$*, and has a Lorentz factor* $\Gamma > 10$*. The jet remains collimated until it reaches the radio lobes 50 kpc from the centre. (Reproduced from Carilli & Barthel [1996]. Credit: NRAO).*

1.2 Active Galactic Nuclei and γ-rays

1.2.1 Black hole and jet

Streams of relativistic plasma (called jets) have been found originating from galactic binary systems where the compact object can be a neutron star [Mirabel & Rodríguez, 1999; Fender et al., 2004] or a black hole [Corbel, 2006] (also called micro-quasars), from extragalactic supermassive black holes in a small fraction of AGNs hosted in elliptical galaxies, and are almost certainly present in GRBs. They are probably a collimated outflow of the infalling gas and are found to extend over large distances (Figure 1.3) from their origin. It has thus become natural to associate AGN with particle acceleration, given the very large luminosities and the relativistic outflows, but what exactly the different mechanisms could be which transfer the available energy into UHECRs and how they interact has been approached by Blandford [2001] as an *engineering problem*: the basic physics, from general relativity to radiative mechanisms, are probably understood to a sufficient level and that no fundamentally new physics are required in the investigation of the mechanisms at play, which are at the heart of the system the dynamics of plasma and magnetic fields around a spinning black hole. There, it is widely believed that large scale magnetic fields are twisted up into a toroidal field due to differential rotation, causing the ejection of surrounding plasma due to either a centrifugal acceleration of plasma loaded on the magnetic field lines [Blandford & Payne, 1982] or due to its magnetic tension (see Spruit 2010 also for a discussion of both mechanisms, or Meier et al. 2001 for a review). Such hypothesis are also tested in laboratory experiments but of course at much smaller scales, and with some plasma parameters being similar, see e.g. Suzuki-Vidal et al. 2010.

If these fields are anchored in the black hole magnetosphere then power could be extracted electromagnetically from the rotation of the black hole (the Blandford-Znajek (BZ) mechanism; Blandford & Znajek [1977]) through the generation of an electric field of $\sim 10^7 \frac{M}{M_\odot} \frac{B}{1\,\mathrm{G}}\,\mathrm{V}$ which could optimally dissipate a power of $\sim 10^{45} (\frac{B}{10^4\,\mathrm{G}} \frac{M}{10^9 M_\odot})^2\,\mathrm{erg\,s^{-1}}$ [Krolik, 1999], which is comparable to the energy of the accreting inflow. With the increase of computing power, complex general relativistic magnetohydrodynamic (MHD) calculations of the behaviour of plasma in the vicinity of a spinning black hole spacetime are now possible up to a level where the initial analytic calculations, usually based on simplifications (such as assuming force-free conditions), can be tested. One of the first confirmations of energy extraction almost from first principles was performed by Koide et al. [2002], where an electromagnetic power of $4 \times 10^{52}\,\mathrm{erg\,s^{-1}}$ is extracted from a system with a maximally spinning stellar-mass black hole threaded by a $10^{15}\,\mathrm{G}$ magnetic field, giving further confidence that BH rotation extraction mechanisms could power

the jets, or perhaps even the only mechanism to reach the observed ultra-relativistic speeds (McKinney 2005, with also an interesting discussion on a variety of possible types of magnetic field geometries in a BH accretion disk, or Komissarov 2005 for a numerical comparison of two possible mechanisms). This power has then still to be converted into kinetic energy by MHD mechanisms, so such studies leave still much to be explored about the disk-BH-jet connection [Blandford, 2002]. Given the fast pace at which this field is moving, we might not be too far from a situation where simulated data could be tested in a comparison with real data. A jet launched according to this scenario is furthermore expected to be dominated by electron/positron pairs since the outflow is initially dominated by magnetic fields (hence sometimes called a Poynting flux jet; Sikora et al. [2005], Drenkhahn & Spruit [2002] for a resembling case in the context of gamma-ray bursts).

An ion-electron plasma is expected to dominate the jet mass flux in case it is the fields in the accretion disk which launch the outflow. The bulk of the jet momentum should however be carried by the ions since the radiative drag in strong external radiation fields occuring near the BH should prevent electrons from carrying momentum until the jet expands. How the jet is powered remains largely debated, as it involves the transfer from gravitational energy to kinetic rotational energy, coupled to the outflow through the magnetic field. The release of gravitational binding energy from the accretion of matter onto a compact object is a formidable energy reservoir: the fraction of the gravitational energy which can be released as radiation when hydrogen accretes onto a supermassive black hole lies somewhere between 7% and a staggering 40% [Shakura & Sunyaev, 1973; Frank et al., 1992; Fabian, 2009], the latter case being for maximally rotating black holes (where efficiency is increased passively by the BH spin since the Schwarzschild radius is much smaller than the non-rotating case and hence observable matter can fall even deeper into the gravitational well; Thorne 1974). Not all of the gravitational energy is necessarily radiated away since in some accretion models, called radiatively inefficient accretion flows (RIAF), more than 99.9% of the energy can remain trapped with the gas and pass into the black hole - or eventually used to power an outflow. These models allow to explain why the environment of some SMBHs, such as the one in the centre of our Galaxy, appear extremely underluminous compared to their expected luminosity when accretion rates are very low [Narayan et al., 1995; Blandford & Begelman, 1999], but they could also play an important role in the context of the most energetic γ-ray emitting AGN.

Whether jets are powered by the accretion energy or by tapping of the black hole rotation, what observables can be defined to disentangle them, and what the chemical composition of a jet ultimately is, remain major questions to be addressed.

1.2.2 Acceleration mechanisms and jet scenarios

Once a highly relativistic MHD outflow is obtained, the stage is set for the generation of the radiative particle distribution: something happens which turns a fraction of a thermal distribution in the flow into a much more energetic non-thermal distribution of particles with Lorentz factors $dn(\gamma)/d\gamma$, which subsequently interact with the ambient medium and cause the observed electromagnetic emission. This is however unlikely to be achieved through a local electric field accelerating particles as it happens in laboratory experiments, since cosmic plasmas, when considered under ideal MHD conditions, should short-circuit any local electric field due to the high electron mobility [O'C Drury, 2001] so a way has to be found to create an accelerator in a globally neutral medium.

The theoretical scenarios, elaborated through simulations or analytical methods, provide the first elements which can be effectively compared with the observations once the particle distribution starts radiating. Two scenarios, those most commonly found in the literature and still subject to research, are shortly discussed below.

Shock acceleration

The flow can be locally subjected to a discontinuity, possibly arising from an instability in the jet, velocity gradients, the appearance of a Mach disk [Komissarov & Falle, 1997], or a collision,

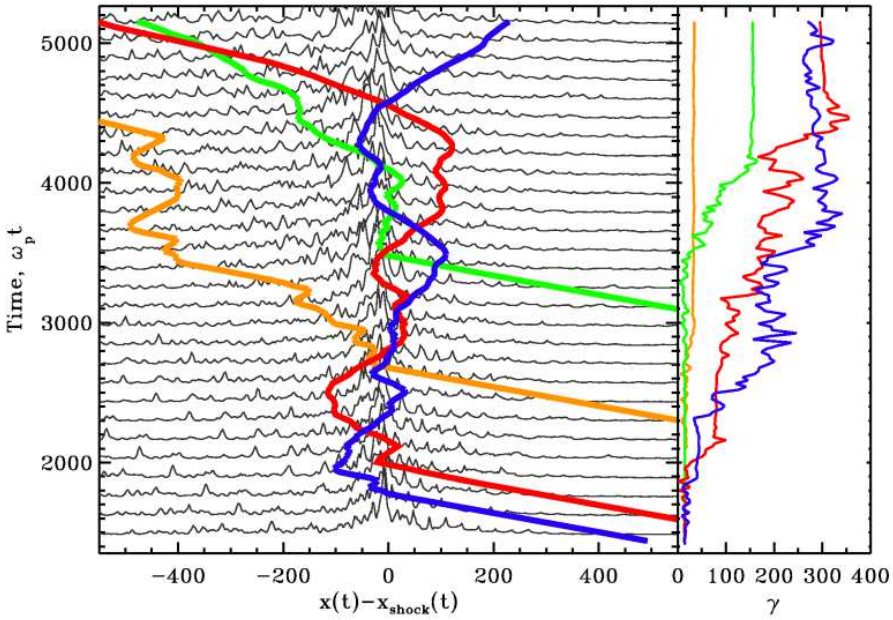

Figure 1.4: *The build-up of energetic particles in a relativistic shock, as evidenced (for the first time probably) in a PIC simulation producing the Fermi acceleration from first principles: the spacetime trajectories of the particles (coloured lines, left) in the averaged magnetic energy profile (black lines, left) build up an acceleration history $\gamma(t)$ (right) of increasingly energetic accelerated particles. (Reproduced from Spitkovsky [2008]).*

which can create turbulence and form a shock (for a review, see Begelman et al. 1984) which is *relativistic* if the upstream flow has a speed $\sim c$ in the frame of the shock. If the shock thickness is shorter than the mean free path λ of the complex MHD interactions the particles undergo within the flow (due to turbulence or to Alfvèn waves rather than Coulomb collisions, which act as a scattering mechanism on their propagation), then the shock is also called *collisionless*. Such shocks have been observed in the solar system, and are thought to be one of the best candidate mechanisms to generate cosmic rays via the Fermi mechanism [Blandford & Eichler, 1987; Henri et al., 1999], where particles can cross the shock multiple times and gain an energy $\Delta\gamma$ from the relative flow motions after each crossing before escaping from the shock (see Figure 1.4; for a review see Kirk & Duffy [1999]). In efficient shocks the gain can be $\Delta\gamma \sim \gamma$. The differential distribution of accelerated electrons generated at such shocks is expected to be of power-law type $n(\gamma) \propto \gamma^{-\sigma}$ with indices of $\sigma \simeq 2.2 - 2.3$ [Achterberg et al., 2001], which do not compare well with the distributions needed to reproduce the most energetic AGN nearing $\sigma \geq 1.5$. However, shock configurations and magnetic field characteristics seem to play an important and complex role in the output spectrum. Using Monte-Carlo simulation techniques, which allow one to explore the influence of parameters directly, Baring & Summerlin [2009] show conditions can exist such that flat distributions ($\sigma \leq 1.5$) are actually obtained in relativistic shocks where turbulence is very small, notably when the ratio η of λ to the Larmor radius r_L is large ($\eta = \frac{\lambda}{r_L} \geq 100$) and accelerated particles lose little energy by synchrotron cooling. The study of colliding plasma shells is also intensively carried out using particle-in-cell (PIC) simulations, which include a high level of MHD microphysics but are extremely computing-intensive and are limited in dynamic range, but the length of the simulations (and hence the particle energies) is steadily increasing [Spitkovsky, 2008; Sironi & Spitkovsky, 2009; Amano & Hoshino, 2009].

Magnetic Reconnection

Extremely powerful releases of energetic plasma are known to happen in the solar corona [Lin et al., 2003] and in the magnetosphere of the Earth [Baker & Stone, 1976]. They are thought to arise when reconnections occur at plasma boundaries where magnetic field lines are oppositely directed (see e.g. Uzdensky [2006] for a review of magnetic reconnections in astrophysical systems, and the original publications of Petschek [1964]) and reconnect, converting the stored magnetic energy into kinetic energy. This phenomenon appears to be an efficient particle accelerator, for which more energetic ($\sigma \sim 1$) power-law type distributions than Fermi mechanisms are predicted based on PIC simulations (with however modest maximal Lorentz factors of ~ 100 and a narrow dynamic range - but that could be simply a computing

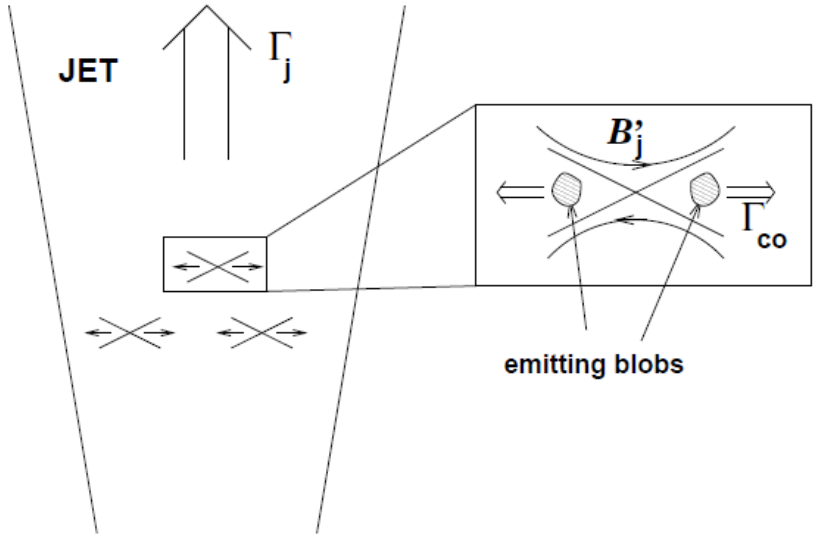

Figure 1.5: *Illustration of a magnetic reconnection event happening within a relativistic outflow of bulk Lorentz factor Γ_j, generating plasma blobs escaping the reconnection region at relativistic speeds with a Lorentz factor Γ_{co}, such that the observed Lorentz factor can be as high as $\Gamma_{obs} = \Gamma_j \Gamma_{co}$. Reasonable values of $\Gamma_j \sim 10$ require hence even lower values of Γ_{co} to match the highest observed requirements on Γ_{obs}. (Reproduced from Giannios et al. [2009]).*

resource limit as in shock-type PIC simulations; Zenitani & Hoshino 2001; Drake et al. 2006), and could also possibly generate the pulsar winds [Lyubarsky & Kirk, 2001], hence the research to establish under which conditions reconnection layers could accelerate particles in a relativistic jet.

For this to happen, it is often assumed that instabilities or other mechanisms exist in the jet to trigger the dissipation. Lyubarsky [2010] propose a way to generate alternating magnetic fields in a jet via a type of instability which would be more efficient than usual dissipation mechanisms only in AGN flows (compared to conditions in pulsar winds). This in turn allows scenarios such as described by e.g. Giannios et al. [2009] where reconnections form small scale wedge-like jets within the macroscopic jet itself (Figure 1.5). While agreeing well with the observed dynamic timescales, the exact radiative properties of the generated particle distribution are still under study.

1.2.3 γ-ray emission processes

There is little doubt that the physical processes at play in AGN generating the observed non-thermal electromagnetic emission are well known: new physical principles are unlikely to be needed either in the acceleration mechanisms or the radiative mechanisms (or in any other class of cosmic accelerator). Given the broad band of wavelengths associated with synchrotron emission and comptonized photons, it is unavoidable that information on an underlying radiative particle distribution roughly distributed as $n(\gamma) \propto \gamma^{-p}$, from the least energetic but more numerous up to the most energetic but rarefied emitters, must rely on measurements from radio to γ-rays, spanning a wide range of detector techniques with their inherent capabilities and constraints. The electromagnetic output of γ-ray emitting AGN, when displayed over broad energy ranges, is the spectral energy distribution (SED) and is usually expressed as $E^2 \frac{dN}{dE} = \nu F_\nu$ (the energy flux per increment of the natural logarithm of the energy/frequency) and in units of $\mathrm{erg\,cm^{-2}\,s^{-1}}$ such that the total energy contained in the spectrum as a function of energy/wavelength is proportional to the area under the curve [Peebles, 1993][6]. Using such representation, γ-ray emitting AGN are usually characterized by two broad structures, each thought to originate directly or indirectly from the *same* underlying accelerated particle distribution radiating through different mechanisms depending on the nature of the interaction (Figure 1.6). Fossati et al. [1998] proposed the so-called *blazar sequence*, where the dominance of the high energy component and its peak emission energy is anticorrelated with the total luminosity. It should be noted that the luminosity per unit frequency $L_\nu(\nu)$ is obtained in

[6] However when addressing a specific analysis from a single instrument at X-ray energies or higher, fluxes are expressed simply as differential fluxes $F(E) = \frac{dN}{dE}$.

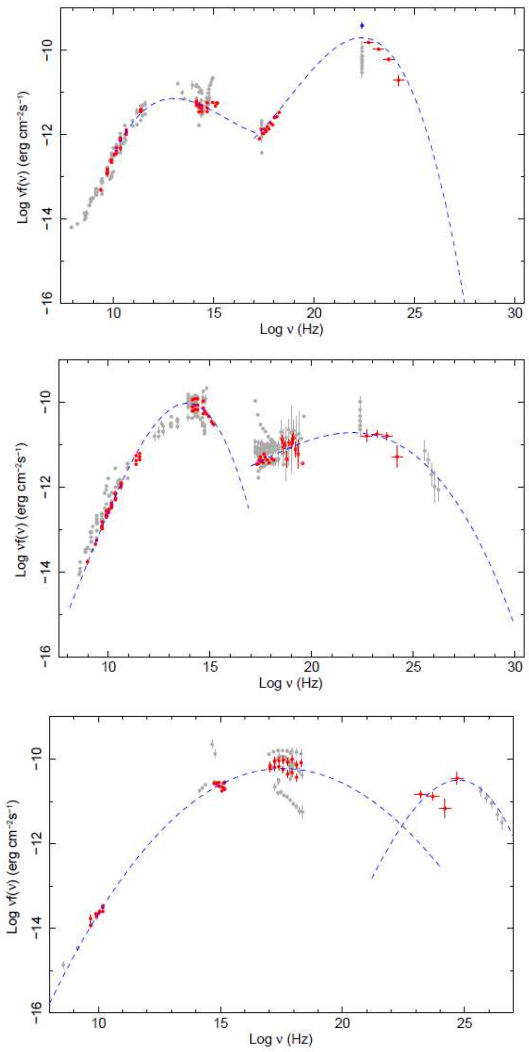

Figure 1.6: *The spectral energy distribution of the FSRQ PKS 1510-089 (top), the low-frequency peaked object BL Lacertae (middle) and the high-frequency peaked BL Lac-type object 1ES 1959+650 (bottom), a sample of the Fermi bright blazars [Abdo et al., 2010e] also detected in the VHE γ-ray regime. Red measurements are quasi simultaneous, while the grey points are archival data. The attention should be drawn to the fact that the X-ray emission is on the high-energy component in the first two objects, but on the low-energy component for 1ES 1959+650, and to the increasing VHE γ-ray flux at the high energy end of the spectrum. The dominant radiative component changes also from the second to the first radiative component, the overall luminosity decreases while the contribution of VHE γ-rays increases. The lines are the result of a third degree polynomial fit in νF_ν to each component and is meant to characterize them (peak, width), not to derive any physical parameter of a model.*

assuming an isotropic emitter, related to the observed energy flux $F(\nu)$ only through the luminosity distance d_L by $(1+z)L_\nu(\nu) = 4\pi d_L^2 F(\frac{\nu}{1+z})$, while it is rather clear that the emission is strongly anisotropic. Blazars are usually divided into flat spectrum radio quasars (FSRQs) and BL Lacertae (BL Lac) type objects [Urry & Padovani, 1995] based on their optical characteristics. The discriminating parameters are usually the bolometric luminosity $P = \int \nu L_\nu$, and the predominance of the nonthermal continuum in BL Lacs while strong emission lines characterize FSRQs. The divide appears however rather artificial in the γ-ray continuum according to recent authors, where the two populations might be separated by their γ-ray luminosity [Ghisellini et al., 2009] at the $L_\gamma = 10^{47}\,\mathrm{erg\,s^{-1}}$ mark.

With a population of relativistic particles at hand and assumptions on physical parameters one can calculate the energy-dependent electromagnetic output using a radiative model. Many exist and are available in the literature, but they come in different flavours of basic models which can described by three varieties, depending on either the nature of the photon field particles interact with, or even more fundamentally, the leptonic or hadronic nature of the interactions. The idea behind this being that the combination of a particle distribution with cooling mechanisms and radiative transfer provides ultimately a test for the acceleration scenarios and the nature of the emitting radiative population.

Leptonic models

In its most simple form, a spherical emission region R threaded by a randomly oriented but constant magnetic field B in which energetic electrons with number density $n(\gamma) = K\gamma^{-\sigma}d\gamma$ ($\gamma_{min} < \gamma < \gamma_{max}$) cool rapidly through two mechanisms [Rybicki & Lightman, 1985]:

- The interaction with the magnetic field generates synchrotron radiation, a well known mechanism providing photons mostly at an energy $E_s \simeq 0.67\,\mathrm{eV}(\frac{\gamma m_e c^2}{1\mathrm{TeV}})^2(\frac{B_\perp}{1\mathrm{nT}})$ (which sets the limit for the most energetic photons), on a cooling timescale $\tau_s = \frac{5\times10^8}{\gamma B_\perp^2}\,\mathrm{s}$, and emitting a power $P(E) \propto E^{-(\sigma-1)/2}$ commonly recognized as being the cause of the low frequency component in blazar SEDs such as those of Fig. 1.6. While synchrotron radiation of energetic electrons can reach arbitrarily high values, the balancing of the mean free path in the most efficient shocks with the associated gyroradius leads to a constraint on the highest possible observed synchrotron energy. If the synchrotron losses dominate in a shock acceleration region, then this leads to a maximal emitter synchrotron radiation energy of $E_s^{max} \simeq 70\,\mathrm{MeV}$, which is independent of the magnetic field [Guilbert et al., 1983; de Jager et al., 1996]. This is typically thought to occur in the Crab Nebula where the synchrotron cutoff occurs around 20-30 MeV, making this one of the most efficient cosmic accelerators. In this context, blazars are more inefficient accelerators by three to four orders of magnitude since the synchrotron cutoff occurs at energies $10-100\,\mathrm{keV}$ with assumptions that $\delta \geq 10$. The most efficient blazars with synchrotron emission up to $\sim 700\,\mathrm{MeV}$, so-called "MeV synchrotron BL Lacertae" [Ghisellini, 1999], have yet to be found. The difficulty of finding them is enhanced if this is the most extreme step in the blazar sequence since their peak luminosity would be in the *Fermi* range at flux levels below the 1-year sensitivity in the $\geq 100\,\mathrm{MeV}$ range, and well below that in all other wavelengths.

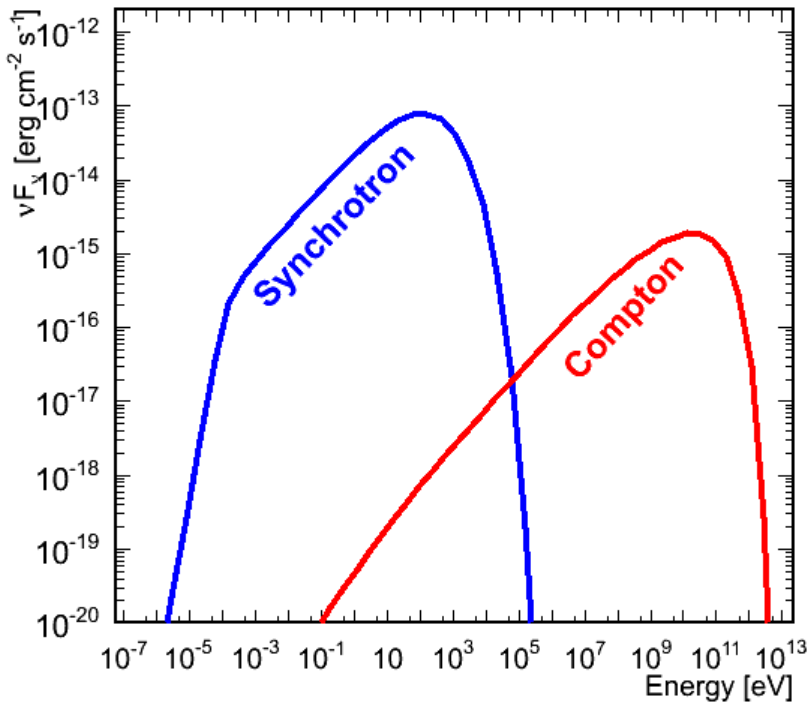

Figure 1.7: *The radiative spectrum in νF_ν using a simple one-zone homogenous SSC model (as in Sanchez 2010) for a $R = 10^{16}\,\mathrm{cm}$ radius blob filled with an electron density of $n_0 = 100\,\mathrm{cm}^{-3}$ distributed as a power law $n(\gamma) = n_0\gamma^{-2}$ restricted to Lorentz factors between $\gamma_{min} = 1$ and $\gamma_{max} = 10^5$, with an average magnetic field of $B = 0.1$ and at a distance of $z = 0.1$.*

- The electrons with initial energy E_e and Lorentz factors γ comptonize off the synchrotron photons themselves, which act as a calorimeter for the accelerated particles. The comptonized photons energy E_C ranges from zero to a maximum value $E_{C,max} = \frac{E_e^2}{E_e + m_e^2 c^4/4E_s}$, but is on average either $E_C \simeq \frac{4}{3}\gamma^2 E_s$ in the case $E_s\gamma/m_e c^2 \ll 1$ (called the Thomson regime of the Compton cross-section $\sigma_C \sim \sigma_T$), or $E_C \simeq \frac{1}{2}\gamma m_e c^2$ if $E_s\gamma/m_e c^2 \gg 1$ (the Klein-Nishina limit). In the latter case the cross section is $\sigma_C = \frac{\pi r_e^2 m_e c^2}{E_C}[\ln(\frac{2E_C}{m_e c^2} + 0.5)]$ showing a drastic $1/E_C$ drop in scattered luminosity for increasing energies.

  Piecing together into a numerical code the emission from a given distribution of electrons in spherical geometry [Jones, 1968; Gould, 1979; Band & Grindlay, 1985] (treating the radiative transfer as in Kataoka et al. 1999), computing the synchrotron emissivity (using e.g. the Chebyshev coefficients expansion described in MacLeod 2000) and the Compton

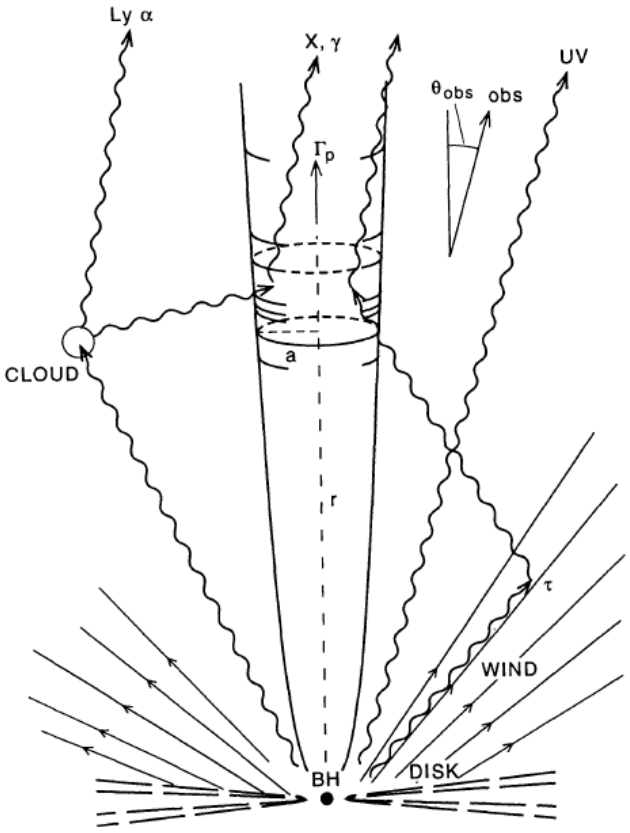

Figure 1.8: *A blazar typical jet and γ-ray emission region configuration, where a supermassive black hole (BH) is fed by an accretion disk the radiation of which can be scattered into the central jet by either the disk wind or gas clouds. (Reproduced from Sikora et al. [1994]).*

emissivity using the Jones [1968] kernel, yields what might be considered a standard model of synchrotron self-Compton (SSC) emission (see Fig.1.7 for an illustration) since there is little room for disagreement between modelers agreeing on these basic properties [Sanchez, 2010]. Despite not addressing dynamical aspects, since injection and cooling timescales are not taken into account at this stage, it is an extremely useful construction to assess time-averaged properties of the blazar emission zone parameters. One-zone homogenous SSC models are still widely used in current publications, especially when litlle or no time-dependent measurements are available to constrain them.

While this scenario seems to rather well describe low luminosity AGN from the BL Lac class, it fails however to match the observations of the more luminous blazars, notably of the FSRQ class. Since this class of AGN shows evidence for a luminous accretion disk or other thermal excess signatures, an alternative hypothesis to the SSC scenario is that some source external radiation to the jet, such as the accretion flow or scattered/reradiated portions of it, provides target photons for the comptonization mechanism [Sikora et al., 1994; Ghisellini & Madau, 1996; Sikora et al., 1997]. In the comoving frame of the radiative region in the jet which moves with a Lorentz factor Γ in the observer's frame, this enhances the energy density of the diffuse radiation field by a factor Γ^2 and their mean energy by Γ, effectively increasing the amount of Compton cooling and the predominance of the second SED component (as in the SED of the FSRQ PKS 1510-089 in Figure 1.6).

A concept which has still to be corroborated but would allow some form of unification of the SSC and EC models through the blazar sequence from Fossati et al. [1998] might find its origin in the higher accretion rates thought to occur in the FSRQ class. More luminous disks provide a higher rate of EC cooling, while self-synchrotron photons dominate the Compton cooling in underluminous flows (where less gas is available and the accretion becomes radiatively inefficient), appearing as a blazar of the BL Lac class [Cavaliere & D'Elia, 2002; Maraschi &

Tavecchio, 2003].

Proton-induced γ-ray emission

There are indications that the relativistic outflows should contain a heavier species than electrons. One indication is that the power which a jet must supply to the lobes of strong radio sources [Rawlings & Saunders, 1991] requires probably more than the observed leptonic/electromagnetic content, for which Celotti & Ghisellini [2008] add ~ 1 proton per relativistic emitting electron/positron. Another indication comes from the observation of spectral breaks in hot spots of Cygnus A occuring at electron Lorentz factors compatible with the mass ratio between protons and electrons [Stawarz et al., 2007]. Radiative models where protons generate the observed SEDs are hence particularly interesting since they provide a more direct connection with proton CR acceleration and UHECRs.

Generally, the leptonic models constitute the preferred concept for TeV blazars, essentially because (i) the capability of the (relatively) well understood shocks to accelerate electrons to TeV energies [Sikora & Madejski, 2001; Pelletier, 2001] and (ii) the effective conversion of the kinetic energy of these relativistic electrons into the X-ray and VHE γ-ray emission components through the synchrotron and inverse Compton radiation channels. The hadronic models generally lack these virtues. They assume that the observed γ-ray emission is initiated by accelerated protons interacting with ambient matter [Bednarek, 1993; Dar & Laor, 1997; Pohl & Schlickeiser, 2000], photon fields (PIC model, Mannheim 1993), magnetic fields [Aharonian, 2000] or both [Mücke et al., 2003].

The attractive feature of hadronic VHE blazar models is that they involve interactions of protons with photon and B-fields which require particle acceleration to the extreme energies exceeding 10^{19}eV of UHECR in order to generate the observed $\sim 10^{12}$eV γ-rays(while electrons need 7 orders of magnitude less energy to achieve similar γ-ray energies), which is possible if the acceleration time is close to $t_{\rm acc} = r_L/c$. This corresponds (independent of a specific acceleration mechanism) to the maximum (theoretically possible) acceleration rates [Aharonian et al., 2002] which can only be achieved by the conventional diffusive shock acceleration in the Bohm diffusion regime. Another attractive feature is the expected neutrino flux which naturally arises from hadronic interactions, setting flux level predictions for existing and future high energy cosmic neutrino detectors [Henri et al., 1999; Neronov & Ribordy, 2009] for which AGN (and GRBs) are the most natural candidates for detecting high-energy neutrinos.

However, the required high efficiency of radiative cooling of accelerated particles imposes extreme parameters characterizing the sub-parsec jets and their environments, in particular very high densities of the thermal plasma, radiation and/or B-fields. This concerns in particular the hadronic models of VHE blazars which are able to reproduce the hard γ-ray spectral indexes through the synchrotron emission of protons (as all other hadronic interactions inherently predict much softer spectral features). These proton-synchrotron models require highly magnetized ($B \gg 10$G) condensations of γ-ray emitting clouds containing protons compatible with UHECR energies, where the magnetic pressure dominates over the pressure of relativistic protons [Aharonian et al., 2002]. More recently, Sikora [2010] reviewed the efficiencies of proton acceleration and cooling in AGN jets, as well as their coupling to the more radiatively efficient electrons and concluded that while protons are likely to be present in AGN, their contribution to the high energy part of the electromagnetic SED is negligible.

1.2.4 γ-ray Variability

One of the most striking features of AGN is their flux variability on all timescales, and at all wavelengths. Variability of non-blazar AGN from the optical to X-rays has been (very nicely) reviewed by Gaskell & Klimek [2003]; some of their points relevant for γ-ray variability are briefly addressed here (and in more detail in the next section for PKS 2155−304). A complete summary of variability in γ-ray emitting AGN is out of the scope of this manuscript, and it is limited to the most recent (at the time this document is written) and (necessarily subjective)

interesting developments brought by the space-based Fermi and AGILE experiments in the high energy (HE; $E > 10\,\mathrm{MeV}$) and very high energy (VHE;$E > 100\,\mathrm{GeV}$) range.

The EGRET experiment clearly established blazars as a largely variable class of objects (when time series with enough significant flux estimates could be determined), with about 80% of the FSRQs and 50% of the BL Lac objects being variable [Mukherjee et al., 1997] (or at least not being statistically compatible with a constant flux). Similar numbers were found within the first 3 months of Fermi observations[Abdo et al., 2009a] with a larger sample, where however 5 of the brightest EGRET blazars are missing, as they returned from a flaring state to indetectable flux levels. Some important questions remained, such as the occurence of flux-dependent spectral variability in the blazar class, which could not be conclusively addressed by EGRET, but the continuously increasing amount of Fermi data will address this. Also, Fermi's much larger effective area enables us to probe short-term variability in the brightest blazars on timescales of $\sim$ hours, an order of magnitude faster than EGRET's capabilities. This will be most important for the FSRQ class where the MeV emission dominates the spectral energy distribution, for which the current generation of ground-based telescopes, despite their tremendous effective area, cannot probe variability better than Fermi (when such sources are detected at all). Now that it has been established that there is a spectral divide between the two blazar subclasses [Abdo et al., 2009a; Ghisellini et al., 2009], and that the sampling resolution has been considerably improved, it would be interesting to find out whether the emission mechanisms responsible for these differences could also have an imprint on the HE timing properties. With a livetime close to 90%, the new generation of space-based experiments is now also providing among the longest light curves ever established at any wavelength.

How rapidly the observed γ-ray flux varies provides a constraint on the γ-ray-emitting region's size. Indeed, a *meaningful* measured variability timescale Δt_{var} can be linked to the characteristic size R of the emitting region through which the changes causing the variability propagate at a speed v, through simply stating that $\Delta t_{var} \sim R/v$. Assuming that changes cannot propagate at speeds greater than the speed of light $c = 3 \times 10^{10}\,\mathrm{cm\,s^{-1}}$, the light-crossing timescale R/c is a usual limit set on an isotropically γ-ray-emitting region size. The physical mechanism at play which causes the observed variability can be due to a fresh injection of particles in the dissipative region, such that the timescales reflect an acceleration timescale or a cooling timescale. But flux variations could also arise from e.g. orientation changes in the velocity of the emitting region, since even small changes in $\beta \cdot \mathbf{n}$ would generate large changes in the observed Doppler boost.

This allows in turn to address the question why HE and VHE γ-rays are seen at all! Provided all the observed electromagnetic emission, such as the distributions in Fig. 1.6, are confined within a region of size R, then the energy density can be computed. The mean free path λ for HE photons of energy E_γ for the interaction $\gamma + \gamma \rightarrow e^- + e^+$ through that density can be smaller than R, making the emission region optically thick for γ-rays, if the density N of target photons at the energy $E_t = (m_e c^2)^2 / E_\gamma (1+z)^2$ is such that $\lambda = 1/N(E_t)\sigma \simeq R$. The ratio λ/R, called the opacity $\tau_{\gamma\gamma}$, can significantly exceed 1 for γ-rays in the $300\,\mathrm{GeV}$–$3\,\mathrm{TeV}$ range, independently of the emission mechanisms. Since the opacity depends on the number density and the photon energy, these can be made significantly smaller in the frame of the jet if these quantities are actually Doppler boosted. This can in turn put one of the tightest constraints on a minimum value of the Doppler factor, by estimating how much Doppler boosting is necessary for photons with observed energy E_γ to escape from a source with radius R and a flux density $F(E_t)$ where now $E_t = (m_e c^2)^2 \delta^2 / E_\gamma (1+z)^2$ (note the introduction of δ). The opacity for photons of *observed* energy E_γ can then be rewritten as

$$\tau_{\gamma\gamma}(E_\gamma) \approx \frac{\sigma_\mathrm{T}}{5} \frac{1}{hc} \frac{d_L^2}{R} \frac{1}{\delta^3 (1+z)} F(E_t). \tag{1.1}$$

where σ_T is the Thomson cross section, and d_L the luminosity distance.

Imposing that $\tau_{\gamma\gamma} < 1$ for photons with observed energy E_γ yields a lower limit on δ for given R that can be derived numerically from the observed SED, and provides stronger constraints on this limit with increasing E_γ. This quite powerful and quite mild model-dependent constraint, given its strong dependence $\propto \delta^{-6}$, was first used in the context of observed EGRET γ-ray

variability by Mattox et al. [1993] where $\Delta t_{var} = 2$d required $\delta = 7.6$ in order to compensate for $\tau_{\gamma\gamma} \simeq 10^4$. In §2 it will be discussed how factors of $\delta = 50 - 100$ are derived to avoid significant TeV γ-rays opacity in the brightest and fastest VHE γ-ray bursts to date. Such values come close to those commonly derived for γ-ray bursts [Piran, 2000]. It will be often used and quoted again in Section 3.

The phenomena which happen in the immediate vicinity of the central engines in AGN occur on angular scales which are not accessible with the current angular resolutions of HE γ-ray instruments. Despite their considerable distance, the angular size on the sky of extragalactic supermassive black holes is however still larger than those in our (relative) neighbourhood[7]. Table 1.1 shows that the gravitational radius $R_S = 2GM/c^2$, a very important size in such systems, of the $3.0 \times 10^9 M_\odot$ central black hole in the radiogalaxy M87, is about two orders of magnitude larger on the sky than the $10 M_\odot$ black hole candidate of Cyg X-1 despite being a million times more distant. At the apparent gravitational radii angular scale, some of the heavier and more distant objects are therefore better resolved than the lighter counterparts in the Milky Way. Galactic black holes also do not exhibit some features which seem to characterize strongly the AGN such as ultrarelativistic jets or broad iron lines, but comparisons between both types of systems often draw interesting theoretical speculation given that only weak differences in the accretion physics are expected despite the $10^5 - 10^8$ mass difference [Done & Gierliński, 2005].

Name	BH mass [$M_\odot$]	Distance [l.y.]	angular size
Cyg X-1	10	3.0×10^3	$\leq 0.1\,\mu$as
Sgr A*	2.0×10^6	2.4×10^4	$13\,\mu$as
M31	3.0×10^7	2.4×10^6	$1\,\mu$as
Cen A	5.5×10^7	1.3×10^7	$0.6\,\mu$as
M87	3.0×10^9	5×10^7	$8\,\mu$as

Table 1.1: *The apparent angular size in microarcseconds of the Schwarzschild radius R_S of some black holes at increasing distances.*

The one-sided outflow of the nearby AGN M87 can be traced down with VLBI observations, which has a resolution of $\sim 100\,\mu$as, down to a scale of $100 R_S$ of the nucleus (and probably an order of magnitude closer with shorter wavelength interferometry; Krichbaum et al. 2007), while the high spatial resolution of the *Chandra X-ray Observatory* trace the jet down to within $10^5 R_S$. Since $\sim 80\%$ of the accretion luminosity of a rapidly spinning black hole originates from within $6 R_S$ we are still far from resolving the largest depths of the potential well. The detection of variable VHE γ-ray emission in M87 [Acciari et al., 2009a], followed by an increase of radio emission measured with the VLBA, can be interpreted as radio wavelength photons produced at larger radii from the core than the γ-ray emission, as was long hypothesized. These measurement showed that γ-rays originate from, and hence are probes of, the immediate vicinity of the black hole.

1.3 High- and Very-high γ-ray observations

1.3.1 Ground-based detectors

The detection of cosmic γ-rays is essentially based on either direct or indirect methods. The former uses space-borne high-energy particle physics type detectors, based on the tracking of the γ-ray pair conversion and the calorimetry of the subsequent electromagnetic cascade. This technique is constrained almost by definition in weight, size and power consumption, which limits respectively the maximal γ-ray energy (since the shower depth of an electromagnetic cascade varies $\propto \ln(\frac{E}{E_c})$ where E_c is the critical energy of the conversion medium, and hence any detector will poorly contain cascades above a given energy[8].), the effective area, and the

[7] There seems however much to be learned about jets as well from young stellar objects (YSO), where no black hole is present but which carry similarities with the manner AGN function [Bally et al., 2000]

[8] however since γ-ray fluxes decrease rapidly with energy, such energies might well never be seen by a detector!

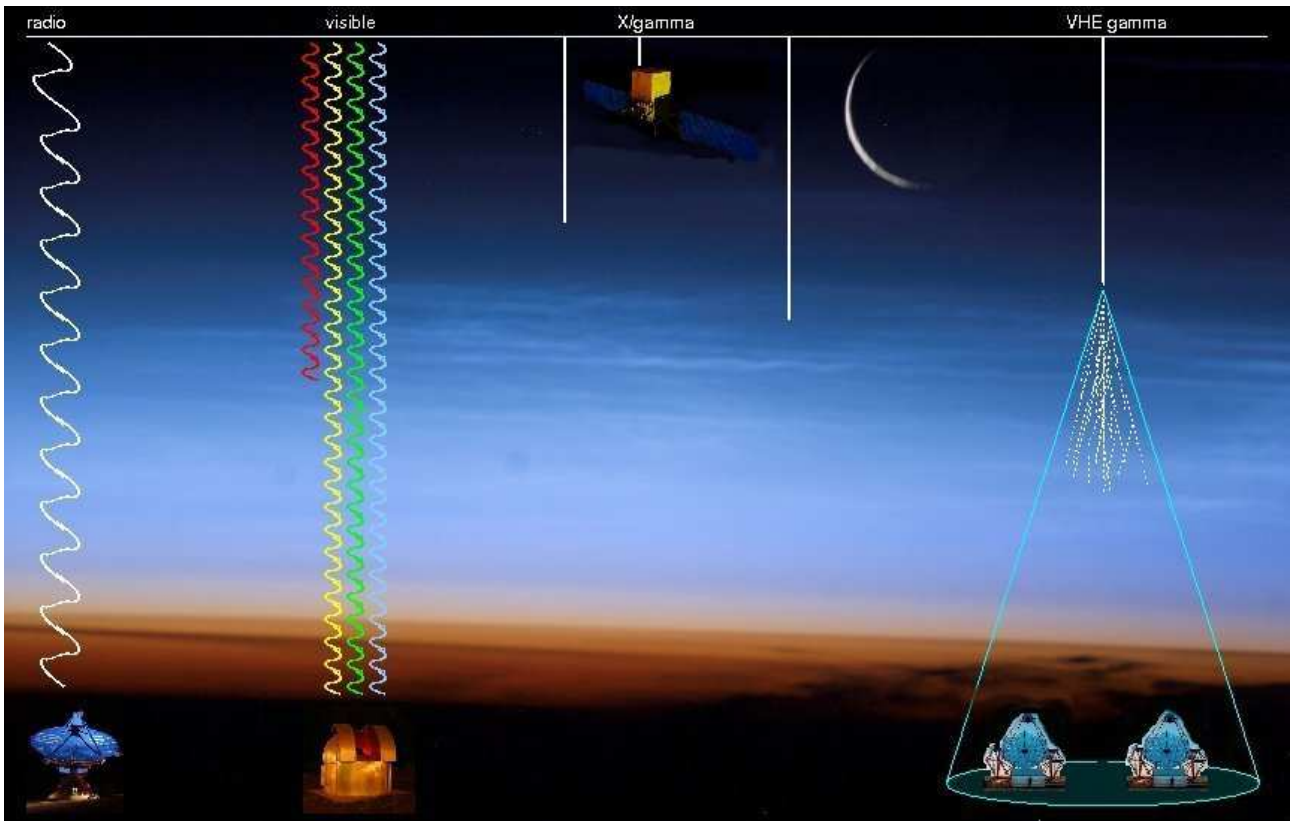

Figure 1.9: *Illustration of the link between radiation frequency and the associated instrument. While radio telescopes are only limited by baseline length, and optical telescopes can still be competitive on the ground, higher energy radiation cannot be accessed from the ground until the interaction of the γ-ray is energetic enough to generate a detectable Čerenkov flash.*

dynamic range. They have however a large field of view (fov), almost avoiding any need for pointed observations since the performance of the instrument (angular and energy resolution) changes slowly within the fov. With livetimes close to 90%, space-based observatories provide some of the best continuous astronomical monitoring of the sky ever realized.

The indirect methods rely on the detection of the secondary particles induced by the γ-ray pair creation in the atmosphere - and rely therefore entirely upon simulations of the interactions and the correct understanding of the atmosphere to convert the observable into characteristics of the primary particle, which constitutes one of the main systematic errors. The detection can be done directly on the ground using scintillators (e.g. the CASA-MIA experiment, Borione et al. 1994), with resistive plate chamber arrays in the ARGO-YBJ Experiment [Aielli et al., 2006], or with large area all-weather water Čerenkov detectors such as Milagro [Atkins et al., 2004; Sinnis, 2009], the most sensitive extensive air shower detector to date, which has provided a 1 to 100 TeV survey of the γ-ray sky in which counterparts to 6 *galactic Fermi* sources were found with significances of 5 standard deviations or more [Abdo et al., 2009d]. While this method has the advantage of a sky-wide field of view and achieve a high duty cycle, it has also the drawbacks of a high energy threshold (of about $10\,\mathrm{TeV}$; the shower maximum for a detector at $\sim 4500\,\mathrm{m}$ a.s.l. corresponds to $E_\gamma \sim 10^{15}\,\mathrm{eV}$), and poor energy resolutions/background rejections resulting in a low sensitivity (Table 1.2).

The atmospheric Čerenkov technique is based on the detection of the air cascade at energies $\geq 10\,\mathrm{GeV}$ through the faint optical $2-3\,\mathrm{ns}$ Čerenkov flash of the shower, which is emitted by relativistic electrons in a conical beam with angle $\approx$ the Čerenkov angle $\theta_C = \cos^{-1}(\beta n)^{-1} \simeq 1^\circ$. This flash illuminates a $\sim 100\,\mathrm{m}$ radius surface on the ground, where the shower has a $\sim 0.5^\circ$ angular size. The detection devices are usually equipped with photomultipliers (PMT), able to detect single photons with a fast response and gains up to $10^5 - 10^7$. So thanks to the large size of the Čerenkov light pool, just like the extensive air shower detectors, the effective area can be much larger than the physical size of the detector itself. The Čerenkov wavefront

sampling method resembles most the EAS technique, since detectors reconstruct the direction through the arrival timing differences. It was for a long time considered a valuable method to perform γ-ray astronomy, with the first attempts using either plain open photomultipliers (PMT) such as the AIROBICC experiment [Padilla et al., 1998], or PMTs with a small reflector as in the THEMISTOCLE experiment [Kovacs et al., 1990; Fontaine et al., 1990], but still at the price of a high energy threshold. Since the energy threshold E_{th} of this technique is $E_{th} \propto \sqrt[-1]{A}$ where A is the collection area, an advance came through the use of huge mirrors from solar farm-type installations focussing the Čerenkov light onto a secondary optics system associated with PMTs such as the CELESTE [Giebels et al., 1998; Paré et al., 2002; de Naurois et al., 2002] and STACEE [Hanna et al., 2002; Covault et al., 2001]. While the threshold was lowered at energies around $100\,\mathrm{GeV}$, the small field of view of this technique along with the poor background rejection of Čerenkov wavefront sampling hampered strongly its contribution to the scientific achievements of the rapidly evolving field of ground-based γ-ray astronomy, led by the imaging ACTs (IACT).

Here, the photons are collected by a large segmented mirror which are usually mounted according to the Davies-Cotton design which, in the context of Čerenkov shower images, is superior to a parabolic mirror for off-axis images [Lewis, 1990]. The image of the shower is then taken by a camera with PMT pixels, which have physical widths smaller than the shower image on the plate scale (expressed in $\mathrm{cm\,deg^{-1}}$). The most common and widespread technique to analyze the image is through the Hillas parametrization derived from an elliptical shape fit, which allow for both a direction/energy estimation and the nucleonic background rejection. The estimation of the significance of an excess in the direction of the aimed source compared to OFF events is usually defined with Eq. 17 in Li & Ma 1983. This permitted the Whipple collaboration, using a 10-m telescope, to find the first galactic (the Crab Nebula, Weekes et al. 1989) and the first extragalactic VHE γ-ray sources (the blazar Mkn 421, Punch et al. 1992). The HEGRA experiment, located in La Palma, Spain, demonstrated later that a stereoscopic view of the same cascade viewed by multiple smaller $8.5\,\mathrm{m^2}$ IACTs improved significantly the hadronic background rejection [Daum et al., 1997] and the angular and energy resolution. The CAT (Cherenkov Array at Thémis) IACT operated on the site of the former solar plant Thémis in the French Pyrénées from 1996 to 2003, using a 17.8 $\mathrm{m^2}$ dish and a high definition camera with a 4.8° field-of-view, comprised of a central region of 546 phototubes [Barrau et al., 1998]. The γ-ray image analysis with such a high-definition camera was be significantly improved, and compared events to an abacus of theoretical average images in order to derive the primary direction and the energy [Le Bohec et al., 1998].

The spectrum extraction for most instruments, both ground- and space-based, commonly involves a fit of the observed spectrum $S(E)$ with a template model expressed as a spectral shape $F(E)$, which is convoluted (or forward-folded) with the detector response functions. The most common shapes used in HE and VHE γ-ray astronomy are the two-parameter power law

$$F(E)dE \propto E^{-\Gamma}dE,$$

the 4-parameter broken power law

$$F(E)dE \propto \begin{cases} E^{-\Gamma_1}dE & \text{for } E < E_b \\ E^{-\Gamma_2}dE & \text{if } E > E_b, \end{cases}$$

where E_b is the energy where the power law index changes from Γ_1 to Γ_2, or the simplest smoothly curving function, a three-parameter parabola in νF_ν space

$$F(E)dE \propto E^{a+b\ln(E)}dE.$$

The signal S is defined for a point-like source as

$$S = \int \frac{dF(E,\theta,\phi)}{dE} \times A_{\mathrm{eff}}(\theta,\phi,E)dE \times T$$

where $F(E,\theta,\phi)$ is the energy and direction-dependent flux, T the exposure time and A_{eff} the effective area[9] which can be calibrated during a beam test for space-based instruments (see

[9] Omitting deliberately instrument response functions discussions here - see the test beam articles, in particular Thompson et al. 1993

	Fermi	ACT	EAS
Effective area [m^2]	$\simeq 1$@1 GeV	$\simeq 10^5$@1 TeV	10^5@10 TeV
Angular resolution	1°@1 GeV	0.1°	0.5°
FOV	90°	5°	2sr
Energy resolution	$\leq 10\%$@ 1 GeV	20(10)% @500(10^3) GeV + syst	60%
Sensitivity [erg cm^{-2} s^{-1}]	10^{-12} (1yr)	10^{-13} (50h)	10^{-12} (1yr)
Duty cycle	$\simeq 90\%$	$\simeq$10%	$\geq 90\%$

Table 1.2: *Comparative characteristics of the three current γ-ray detection methods: a limited volume but space-based such as Fermi , a ground-based ACT, and an extensive air shower (EAS) array as Milagro. Note that the sensitivity for ACTs is based on a 50h exposure, since it is difficult to allocate more observing time that that on a given source per year.*

e.g. AGILE: Barbiellini et al. 2002, EGRET: Thompson et al. 1993, AMS: Falco 2010, Fermi: Couto e Silva et al. 2001). Note that $\theta = \theta(t)$ and $\phi = \phi(t)$ except for fast transient events such as GRB where F and T are intrinsic properties.

The combination of large mirrors, stereoscopic viewing, and high-definition cameras, led to the designs of the currently operating H.E.S.S. , MAGIC and VERITAS instruments. The drawback of this technique is the small field of view of a few degrees, a limited livetime $\sim 10\%$ due to the same constraint as ground-based optical telescopes of clear, dark night skies for carrying out observations limiting light curves to be continuous only over a time up to ~ 6h, and varying sensitivities and energy thresholds due to the specifics of this technique. Also the energy threshold, and hence the effective area, vary with the zenith angle during observations so that producing a light curve at a given energy threshold requires spectrum-dependent corrections (more on this in §3.4). Despite this, the IACT technique is currently the most successful one in the advances of VHE γ-ray astronomy, reaching sensitivities of 10^{-13} erg cm^{-2} s^{-1} with exposures of ~ 50h. Clearly, space- and ground-based instruments are extremely complementary, and are very likely to remain so until much larger γ-ray detectors can be put in space (or on the Moon).

1.3.2 Space-based missions

After a long generation of γ-ray detectors based on moderately precise high-voltage spark-chamber technology running on expandable gas, such as SAS-2 (1972-1973), COS-B (1975-1982) and EGRET (on board of *CGRO*, 1991-2000), the newest and most recent observatories *AGILE* [Tavani et al., 2008, 2009] and *Fermi*-LAT use robust and finely segmented silicon-based trackers, improving the angular resolution by an order of magnitude. but also increasing the fov up to about πsr through a more compact design [Spandre & The GLAST Lat Collaboration, 2007; Atwood et al., 2009]. A summary of the LAT performance is given in Atwood et al. [2009]. The angular resolution (or point spread function, PSF) of the LAT is strongly energy-dependent, as it varies as $E^{-0.7}$ (Table 1.2), which further complicates analyses at low energies where sources are more numerous and have to be disentangled if they are separated by an angular distance $\leq$ PSF and more background events are included. The bulk of the background is rejected by a segmented anti-coincidence shield which covers the tracker array [Moiseev et al., 2007], but unfortunately a fraction of the background contaminates the photon spectra, especially at low energies, and has to be dealt with in the offline analysis [Rochester et al., 2010].

The Large Area Telescope (LAT) onboard *Fermi* detects γ-rays in the range 20 MeV–300 GeV where the lowest energy is limited by the charged particle background and albedo photons and the highest energy mostly by statistics. The whole sky is covered within two orbits, or 3 h, with an integrated flux sensitivity above 100 MeV of $\sim 2\times10^{-6}$ cm^{-2} s^{-1} and $\sim 4\times10^{-7}$ cm^{-2} s^{-1} for respectively Galactic and extragalactic regions, providing among the longest quasi-continuous light curves ever recorded. An extremely important figure is that the LAT detects the Crab Nebula, a standard candle used in TeV astronomy, within a year at ~ 100 GeV[Abdo et al., 2010c], an energy usually defined as the border between high energy (HE, $E > 100$ MeV) and very high energy (VHE, $E > 100$ GeV) where ACTs become sensitive. Of crucial importance for AGN studies evoked here is of course the LAT's uniform all-sky monitoring capabilities along

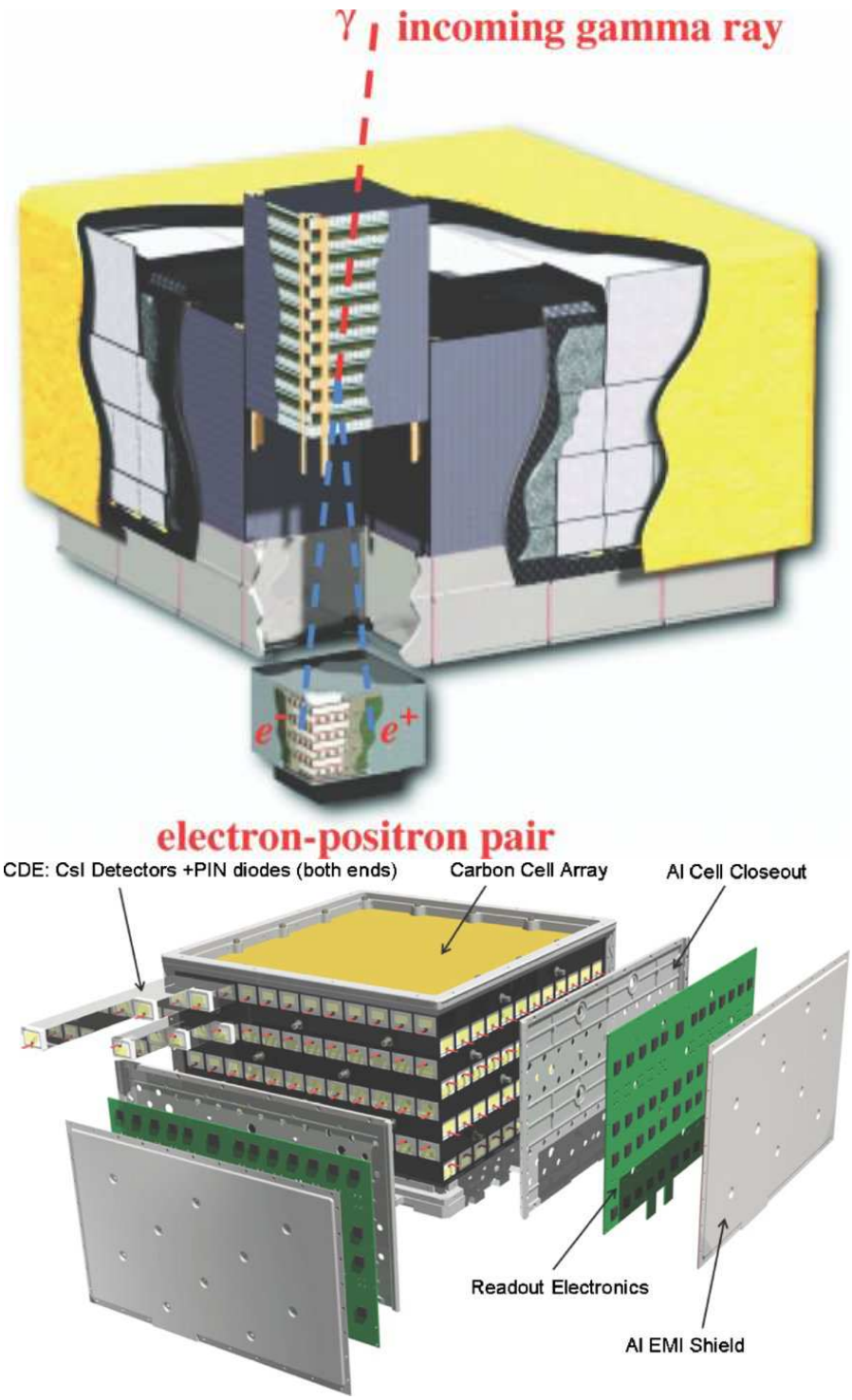

Figure 1.10: *Top: Schematic diagram of the LAT. The telescope's dimensions are 1.8 m × 1.8 m × 0.72 m. The power required and the mass are 650 W and 2789 kg, respectively. Bottom: The LAT calorimeter module is based on Thalium doped Cesium Iodide CsI(Tl) scintillator detector elements (CDE) which account for about 2000 kg, constituting a large part of the mass of the LAT. The total calorimeter depth (at normal incidence) is 8.6 radiation lengths. The depth of the LAT is 10.1 radiation lengths, including the tracker. The logs are arranged in 8 layers, with alternate x/y orientations, allowing the x/y localisation of the shower axis, as well as that of the follow-up of the shower development in depth z which is a considerable improvement over EGRET. To materialise the tower arrangement of the calorimeter, there are 16 molded supporting structures - one per tower - featuring individual cells in which the CsI logs can be inserted. These structures are made of a carbon fiber and epoxy composite, which has a number of advantages over metallic structures as they are lighter, stronger and stiffer [Ferreira et al., 2004]. Figures from Atwood et al. [2009].*

with its efficiency, allowing observers at any other wavelength to have (almost) guaranteed GeV observations of their favourite sources without need to apply for observations. Within a year, the LAT has collected $\sim 200 \times 10^6$ γ-rays, 3 orders of magnitude more than its predecessor. The first *Fermi* catalog [Abdo et al., 2010d] (1FGL), based on 11 months of scientific operations, contains 1451 sources of which 1043 are at Galactic latitudes $b > 10°$. From this latter sample was then derived the first LAT AGN catalog (1LAC), comprising 300 BL Lac objects (compared to 13 for EGRET), 296 flat-spectrum radio quasars (FSRQs, of which EGRET saw 66), and 113 AGN of other (or unknown) type. Given the now significant population of HE sources in the 1FGL catalog, it is worth noting the attempts to correlate UHECR events with 1LAC sources [Nemmen et al., 2010]. This study has provided some interesting correlations on angular scales an order of magnitude larger than those derived from the PAO, but with both populations

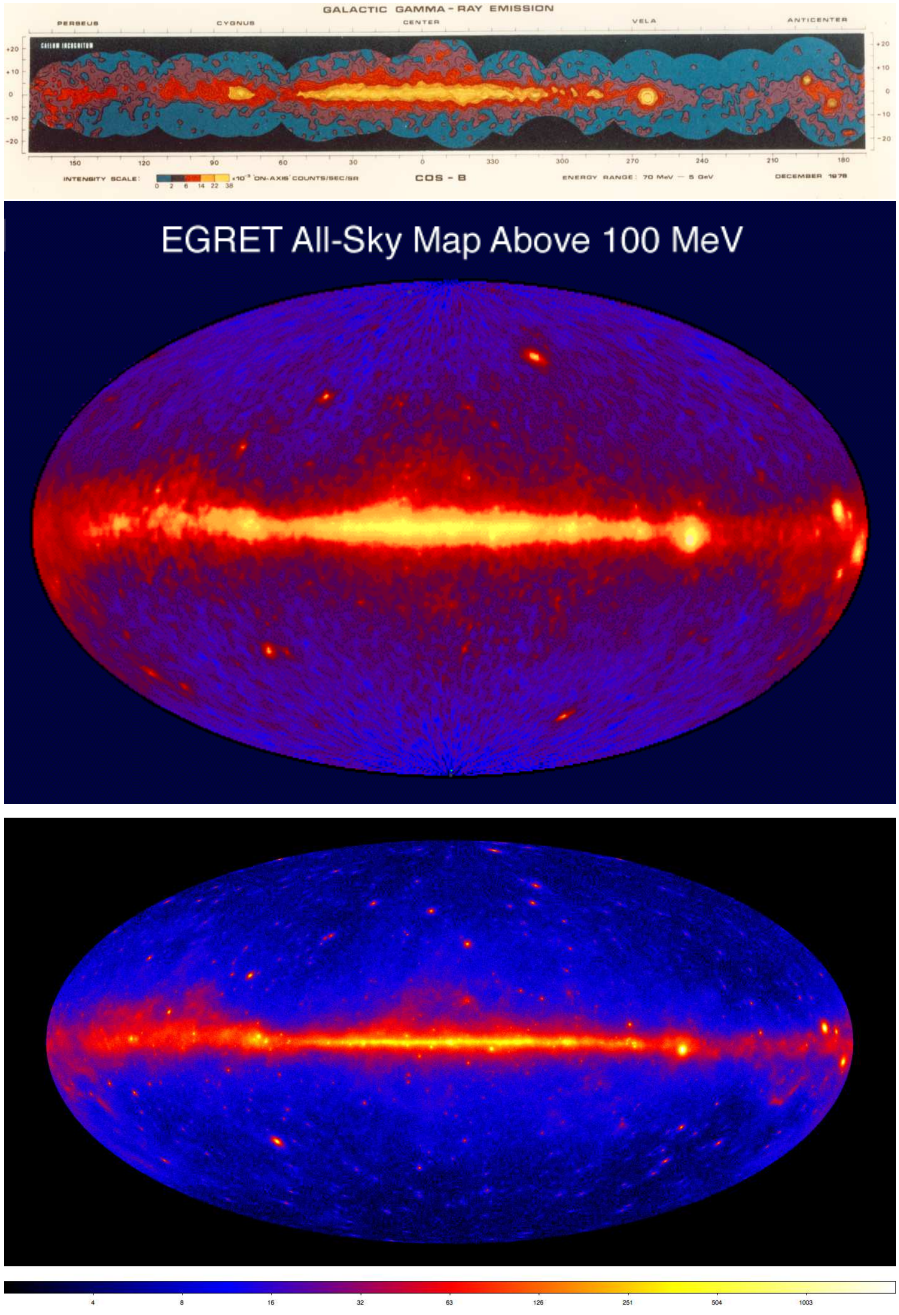

Figure 1.11: *Evolution of the γ-ray sky at energies* $> 100\,\mathrm{MeV}$ *in Galactic coordinates. From Top to Bottom: COS-B (1975-1982) used a spark chamber technology to provide the first γ-ray skymap at these energies, based on* 10^5 *γ-rays, showing the diffuse component of the Galaxy, the Vela and Crab pulsars, and the first extragalactic source 3C 273 [Mayer-Hasselwander et al., 1982]. Upper limits in the extragalactic sky were at the level of* $\sim 5 \times 10^{-7}\,\mathrm{cm}^{-2}\,\mathrm{s}^{-1}$ *The Energetic Gamma Ray Experiment Telescope, (EGRET, 1991-2000) operated a similar expandable spark chamber on board the Compton Gamma Ray Observatory (CGRO) and detected 271 γ-ray sources based on* 1.5×10^6 *γ-rays and provided a sensitivity in the extragalactic sky of* $(6.2 \pm 1.7) \times 10^{-8}\,\mathrm{cm}^{-2}\,\mathrm{s}^{-1}$ *[Hartman et al., 1999]. The Fermi Gamma-ray Space Telescope (2008-), formerly GLAST, uses a compact solid-state silicon technology providing a wide field of view and detected 1451 sources in its first 11 months of operation* 2×10^8 *γ-rays and upper limits at* $3 \times 10^{-9}\,\mathrm{cm}^{-2}\,\mathrm{s}^{-1}$ *after a 1 year sky survey Abdo et al. 2010b.*

bound to grow with time, the statistical significance of such methods can only improve. Note also the interest of links between VHE γ-ray emission and non-electromagnetic messengers (e.g. neutrinos) by Tluczykont et al. [2010].

1.3.3 Status of ground-based VHE γ-ray observatories

Exhaustive reviews of the second generation of ACTs and their achievements can be found in Ong [1998]; Hoffman et al. [1999]; Ong [2003], while the achievements of HESS, MAGIC and VERITAS (usually referred to as the major third generation instruments) are summarized in (a.o.) Aharonian et al. [2008a], Buckley et al. [2008], and/or Hinton & Hofmann [2009]. The new generation of major ACTs reach effective areas of $\sim 10^5\,\mathrm{m}^2$ which, combined with a $> 99.9\%$ efficiency in rejecting the hadronic background thanks to fine grain imaging and stereoscopic reconstruction of the atmospheric showers. The improvement is such that the current status of VHE γ-ray emitters has risen to about 120 sources and is still growing[10].

[10]The TeVCat at `http://tevcat.in2p3.fr` provides an updated list with full references and search tools

Figure 1.12: *The HESS telescope array, located in Namibia, is an array of four imaging atmospheric Čerenkov telescopes separated by a 120 m baseline which allows an optimal triangulation of the . Each of these telescopes is equipped with a tessellated spherical mirror of 107 m^2 area and a camera comprised of 960 photomultiplier tubes, covering a 5° fov. The system works in a coincidence mode [Funk et al., 2004], requiring at least two of the four telescopes to trigger the detection of a cascade. This stereoscopic approach results in a high angular resolution of 5' per event, and an energy resolution of 6% on average.*

The H.E.S.S. telescope array, located in Namibia, is an array of four imaging atmospheric Čerenkov telescopes separated by a 120 m baseline which allows an optimal triangulation of the cascade. Each of these telescopes is equipped with a tessellated spherical mirror of 107 m^2 area and a camera comprised of 960 photomultiplier tubes, covering a 5° fov. The system works in a coincidence mode [Funk et al., 2004], requiring at least two of the four telescopes to trigger the detection of a cascade. This stereoscopic approach results in a high angular resolution of 5' per event and an energy resolution of 6% on average. The HESS array was fully operational since the end of 2003 and has achieved some impressive results, such as the Galactic plane survey has yielded 14 new sources [Aharonian et al., 2006d] among which the Galactic Centre which has still an uncertain association [Aharonian et al., 2004] and the first image of an *extended* VHE source [Aharonian et al., 2006a] RX J1713.7-3946, one of the most iconic discoveries of the field. The telescope array will be refitted with new mirrors by the end of 2011.

The Very Energetic Radiation Imaging Telescope Array System (VERITAS) consists of 4 telescopes, each having a 106 m^2 area, with 499 PMTs per camera and a 3.5° fov. It is located in Arizona at 1268 m a.s.l. [Weekes et al., 2002], and has settled into its final configuration during summer 2009, but with an uneven baseline distance due to local constraints (though the original baseline distance was 80m). VERITAS has discovered in VHE γ-rays the IBL W Comae [Acciari et al., 2008] and one of the two currently known VHE emitting starburst galaxies (M82; VERITAS Collaboration et al. 2009, when HESS discovered NGC 253; Acero et al. 2009, while both were later also detected by *Fermi*; Abdo et al. 2010a). The mirrors of the VERITAS telescopes are continuously maintained.

Finally, the MAGIC observatory consist of a large 17 m diameter dish (or 236 m^2) located on the island of La Palma at 2200 m a.s.l., and is operational since 2003. It was complemented in 2009 by a similar telescope located at 85 m from the first one (performances and details of the setup are so far scarce; Cortina et al. 2009) which allow a stereoscopic view but no triangulation. Among the most notable MAGIC results are the discovery in VHE γ-rays and the modulation in the VHE signal of the γ-ray binary LS I +61 303 [Albert et al., 2006] and the extension down to $\sim$60 GeV of the Crab Nebula spectrum [Albert et al., 2008b].

Thanks to the improved shower image quality and stereoscopy, the reconstruction techniques have also improved beyond the standard Hillas parametrization. New analysis methods include:

- the improvement of the above mentioned method developed for CAT, mainly by improving the night sky background noise treatment through the use of all pixels in the fit, and adding parameters such as the depth at which the cascade started in the atmosphere (called the *Model* analysis [de Naurois & Rolland, 2009];

- the 3-dimensional characterization of the Čerenkov photosphere which takes into account

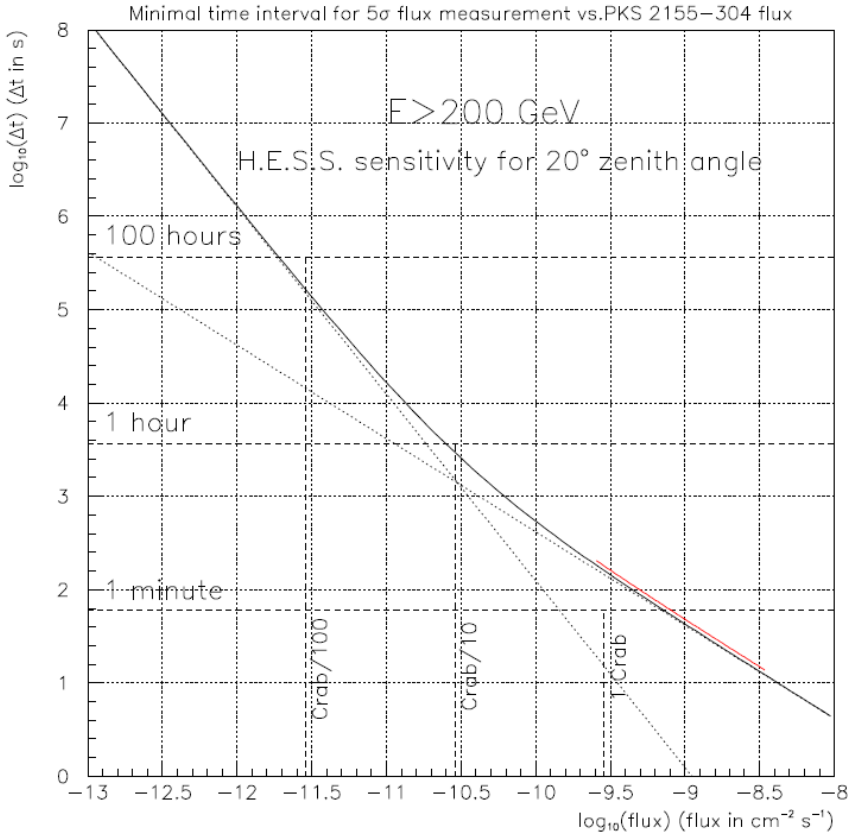

Figure 1.13: *Minimal observation duration for a 5 standard deviation detection of a source by H.E.S.S. at a zenith angle of* 20°*, as a function of the γ-ray flux, for an energy threshold of* $200\,\mathrm{GeV}$*. The red line superimposed to the curve indicates the highest range of fluxes observed with H.E.S.S. during the γ-ray flares of PKS 2155-304 in July 2006, discussed in §2. The dotted lines are the extrapolations of the photon statistics-limited sensitivity at low fluxes, and the background-limited sensitivity at high fluxes.*

the signal correlations among telescopes [Lemoine-Goumard et al., 2006];

- the use of multivariate analyses, such as boosted decision trees (BDT) or random forest trees, trained on e.g. the Hillas parameters, which improve the background rejection considerably [Albert et al., 2008a; Ohm et al., 2009].

Interestingly, the above mentioned 3-D and *Model* methods (plus the Hillas analysis adaped to the HESS array as described in Aharonian et al. 2006c) are sufficiently different that they can also be optimized through BDTs trained with a Monte Carlo simulation to perform a better background rejection and hence improve the sensitivity [Fiasson et al., 2010].

The flux sensitivity of the ACT technique has improved by an order of magnitude within a decade, reaching a significance of 5 standard deviations on Crab Nebula equivalent fluxes within exposures of $\sim 1\,\mathrm{min}$ or less. This is illustrated in Figure 1.13 (from Degrange, Superina, Giebels, & Volpe 2008) which shows the minimal time Δt necessary for H.E.S.S. to measure a significance of 5 standard deviations on a source as a function of the γ-ray flux above $200\,\mathrm{GeV}$ for a 20° zenith angle. For fluxes at the level of 10% that of the Crab Nebula or less, the flux error is dominated by the fluctuations of the hadronic background. For higher fluxes however the sensitivity is only limited by the photon statistics.

1.3.4 VHE AGN Observation strategies, before and after Fermi

With limited observation time and small fields of view, the first question once the instrument is up and running is *where to look?* Not mentioning how telescopes manage conflicts between different source classes in the same observation window (should we observe a supernova or an AGN?), the main question addressed here is how known AGN are targeted for VHE emission searches. While this question is not entirely moot for Fermi, ACTs need a strategy for the few hundreds of effective observation hours available yearly.

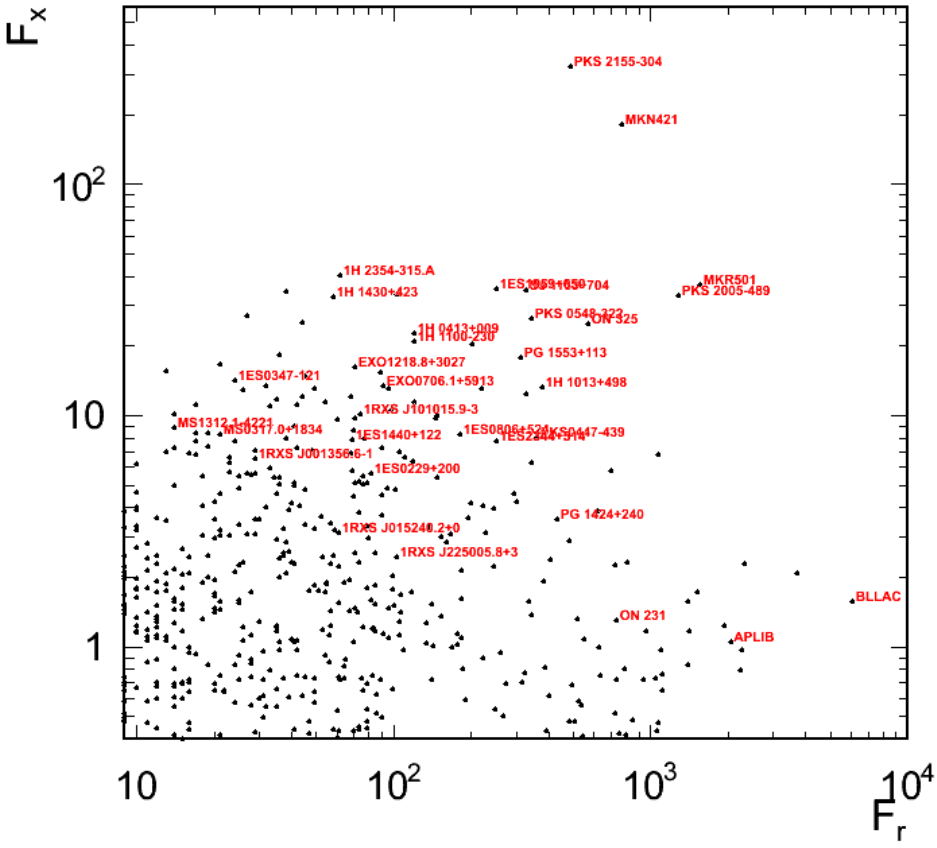

Figure 1.14: *Blazar objects from the Roma-BZCAT catalogue of blazars [Massaro et al., 2009], containing both BL Lac and FSRQ blazars, with the VHE detected objects in red. The y-axis is the 5 GHz radio flux in units of Jy, and the x-axis is the 1 keV flux also in Jy.*

Before Fermi

The most obvious way to look for VHE candidates is to find indicators in other wavelengths which might have promising features. The Fermi predecessor EGRET, active during 1991-2000 in the nearest energy band to the VHE, has a.o. yielded a catalog of sources [Hartman et al., 1999], in which power-law γ-ray spectra showing no signs of cutoff up to the few GeV range would be valid targets. But as was anticipated, after finding instrumental issues, the effective area at high energies was severly impacted by the cosmic ray rejection . The type of *hard* and *faint* emitters were difficult to detect with EGRET's reduced sensitivity at $\geq 10\,\mathrm{GeV}$ energies (as is discussed in 1.3.2), to the point that it was only seeing a small fraction of HBL objects which are potential TeV emitters. The few HBL EGRET did detect (Mkn 421, Mkn 501, PKS 2005-489 and PKS 2155-304) with a rather faint significance were already VHE candidates for other reasons. Therefore, EGRET was not the instrument of choice to find VHE targets.

The energy band following next, at $\sim$ MeV energies, has the huge inconvenience of requiring a space-based Compton effect detector, where the cross-section is at its lowest and backgrounds are very high, reducing the effective areas to their lowest value. The COMPTEL experiment also on board *CGRO*, with $A_{eff} \sim 20-40\,\mathrm{cm}^2$ and 32 detected sources [Schönfelder et al., 2000], was therefore even less suited than EGRET to find VHE-emitting candidates.

The X-ray band proved actually to be of the highest interest for this task. Indeed, the most effective selection mechanism to date relies on the fact that a given VHE threshold E_{th} can be associated a sensitivity to comptonizing electrons with maximal Lorentz factors $\gamma \sim E_{thresh}/m_e c^2$. In the presence of a magnetic B field these electrons would however also have to radiate synchrotron radiation at an average energy $E_s = \gamma B^2$ which, for typical ACT thresholds of $E_{th} \simeq 100\,\mathrm{GeV}$, would correspond to X-ray radiation, so high X-ray fluxes in BL Lacs would signal

the presence of a high number of TeV electrons. Using the time-averaged X-ray properties in all-sky X-ray catalogs, such considerations led Stecker et al. [1996] to make a list of VHE candidates which effectively yielded detections by the Whipple group of e.g. 1ES 2344+514 [Catanese et al., 1998], of PKS 2155-304 by the University of Durham Mark 6 telescope of 2155-304 [Chadwick et al., 1999], and of 1ES 1959+650 by the Utah Seven Telescope Array detector with 3 m diameter at Dugway, Utah [Nishiyama, 1999][11]. This approach was later improved by Costamante & Ghisellini [2002] through the use of multiple BL Lac samples, the requirement that good candidates should also be relatively strong radio emitters, and the application of a SSC model to predict the VHE flux $F_{\rm VHE}$ (though not applying corrections for propagation effects, unlike Stecker et al. 1996), providing one of the most successful target list for the VHE collaboration as it has yielded a good fraction of the currently known extragalactic VHE emitters discovered by the HESS, MAGIC and VERITAS collaborations.

The link between X-rays and VHE γ-rays becomes even more evident when sensitive X-ray instruments are pointed towards AGN simultaneously during a variable flux episode; as for now, when significant VHE flux variability is present in the source, it tends to mostly correlate with the X-ray flux $F_{\rm X}$ fluctuations [Katarzyński et al., 2005] usually tied through the index ζ of a power law relation $F_{\rm VHE} \propto F_{\rm X}^{\zeta}$[Katarzyński & Walczewska, 2010]. Such correlations are the proof that the underlying radiative particle distribution is the same for the two radiative populations [Mastichiadis & Kirk, 1997], and the index ζ is one of the observables which allow to further investigate how the synchrotron/Compton emissions are linked since for simple SSC models $\zeta \sim 2$ is expected while $\zeta \sim 1$ for EC emission models. However the value of ζ depends on the light curve sampling and length since the Fourier power spectra are not necessarily identical between two wavelengths Katarzyński et al. [2005].

With more capable X-ray observatories becoming available over time, X-ray and radio-bright sources have been better studied: using the Roma-BZCAT blazar sample, one of the most complete and up to date and currently used tool for searching new targets, Figure1.14 shows current situation in the radio(5 GHz)/X-ray(1 keV) flux plane. One of the greatest difficulties in using X-ray samples from specific catalogs is their archival nature: since BL Lacs are known to be potentially extremely variable in the X-ray band, one of the weaknesses of this approach is that it does not necessarily reflect the state of an interesting source which might be lower, or the state of an uninteresting source which might be higher. Therefore, all-sky X-ray monitors are invaluable tools to notify an increasing X-ray behaviour which might signal a higher VHE γ-ray flux as well. Some blazars were, and still are, found in a high VHE state during high X-ray flux states. However the sensitivity of the current all-sky X-ray monitors is barely sufficient for a few of the brightest BL Lac objects - transient X-ray states in most of them are unnoticed by such monitors.

Since Fermi

New candidate VHE γ-ray emitters can now be found in the more sensitive Fermi source catalogs, through the search for sources that are susceptible to produce significant emission in the 200 GeV - 1 TeV energy band. A rather successful way to perform this is through the extrapolation of the Fermi spectrum up to 1 TeV using the best-fit parameters of a power-law and rank the sources based on their predicted fluxes. (The attenuation caused by the EBL was taken into account in the extrapolation using the model of Franceschini et al. 2008, which will be described in more detail in 2). This method has been applied and then communicated to ground-based instruments as private communications, once with 1 year of Fermi data, then one year later with 2 years of Fermi data. This method of which a detailed description can be found in Fortin et al. [2009] has yielded many new VHE discoveries (VERITAS: Ong & Fortin 2009, HESS: Hofmann & Fegan 2009, MAGIC: ATel #2923). This method was however limited to sources with latitudes $|b > 10^{\circ}|$, well above the Galactic plane, and hence the discovery of VHE emission from the source VER J0521+211 [Ong, 2009] at $b = -8.7^{\circ}$ was done using the presence of a cluster of $> 30\,$GeV photons at that location, a testimonial to Fermi's power in finding VHE γ-rays!

[11] These last two observatories have ceased their operations.

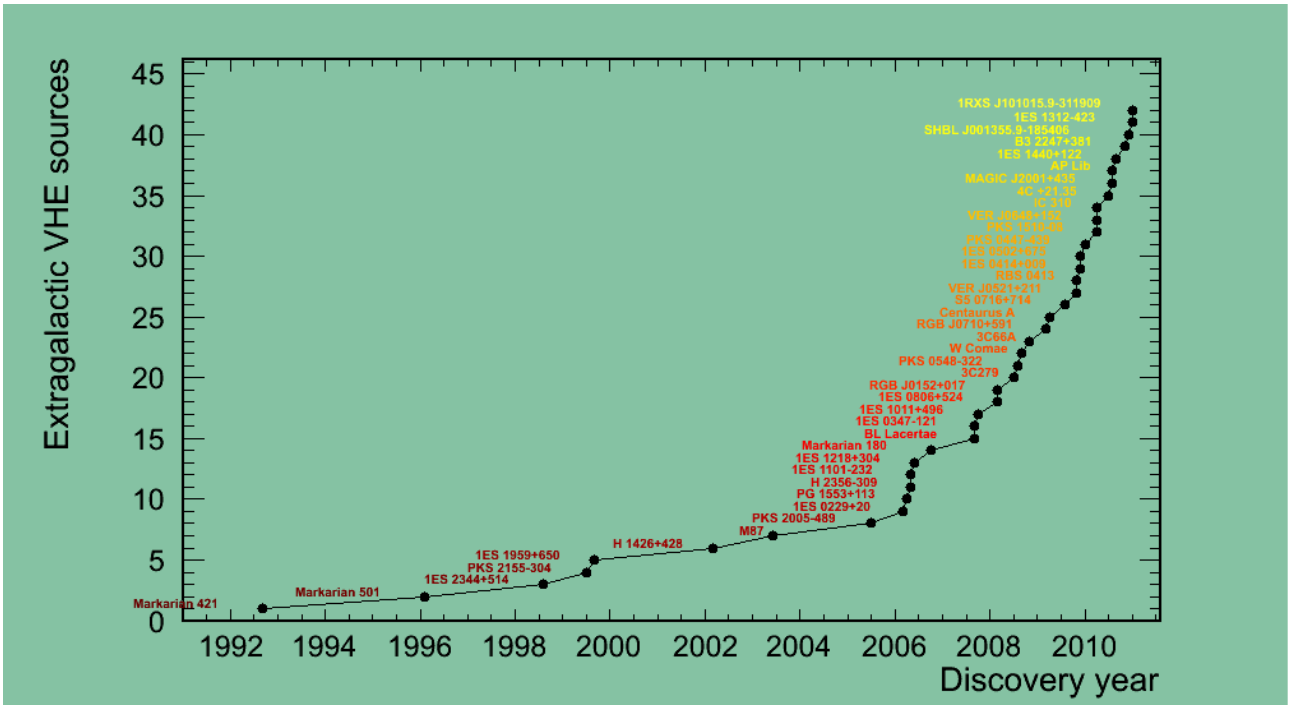

Figure 1.15: *The cumulative amount of VHE γ-ray emitters from Table 1.3 as a function of time. Among some notable dates are: PKS 2005-489, the first extragalactic discovery of H.E.S.S. in 2003, and the inflexion point early 2006 which is a mark of the new generation of ACTs becoming fully operational.*

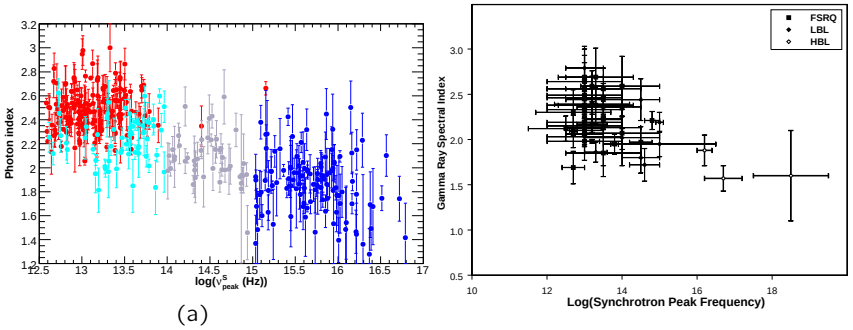

(a) (b)

Figure 1.16: *(a) The Fermi blazar photon index as a function of its derived synchrotron peak frequency ν^s_{peak}, as derived in Nemmen et al. [2010]. (b) A similar study using the EGRET data, as published in Nandikotkur et al. [2007]. Thanks to a much larger population and a better energy resolution, a clear correlation appears where the blazar spectrum becomes increasingly harder when the synchrotron peak ν^s_{peak} moves blueward from the optical to the X-rays, due to Fermi's high energy sensitivity adding the IBL-HBL population to the visible HE sky.*

1.4 A status of AGN γ-ray observations

1.4.1 The extragalactic HE/VHE γ-ray sky in 2011

At the time this review is being written, all but 4 of the grand ensemble of VHE extragalactic γ-ray sky sources are seen by *Fermi*, so the global HE spectral characteristics can be well summarized by the 671 AGN present in the 1LAC sample. Fig. 1.16(a) shows that the HE γ-ray index Γ_{HE} becomes harder when the synchrotron peak shifts globally blueward. This should be compared with Fig. 2 in Nandikotkur et al. [2007], displayed in Fig. 1.16(b), where this trend was first seen using only EGRET blazars, but with 37 FSRQs and 13 BL Lacs. It appears hence that the FSRQ γ-ray spectra are different from the BL Lac population, with the average

Name	R.A.	DEC	Type	Discovery date	Redshift
M87	12 30 49.4	+12 23 28	FRI	05.01.2003	0.0044
Centaurus A	13 25 28	-43 01 06	FRI	03.01.2009	0.0018
IC 310	03 16 43.0	+41 19 29	UNID	03.01.2010	0.0189
Markarian 421	11 04 27.3	+38 12 32	HBL	08.01.1992	0.031
Markarian 501	16 53 52.2	+39 45 36	HBL	01.01.1996	0.034
1ES 2344+514	23 47 04.8	+51 42 18	HBL	07.01.1998	0.044
Markarian 180	11 36 26.4	+70 09 27	HBL	09.01.2006	0.045
1ES 1959+650	19 59 59.9	+65 08 55	HBL	08.01.1999	0.048
AP Lib	15 17 48.96	-24 23 06	LBL	07.01.2010	0.049
BL Lacertae	22 02 43.3	+42 16 40	LBL	08.01.2007	0.069
PKS 0548-322	05 50 42.9	-32 16 34	HBL	07.01.2008	0.069
PKS 2005-489	20 09 29.3	-48 49 19	HBL	06.01.2005	0.071
RGB J0152+017	01 52 33.5	+01 46 40.3	HBL	02.01.2008	0.08
SHBL J001355.9-185406	00 13 56.0	-18 54 07	HBL	11.01.2010	0.095
W Comae	12 21 31.7	+28 13 59	IBL	08.01.2008	0.102
1ES 1312-423	13 15 03.4	-42 36 50	HBL	12.01.2010	0.108
PKS 2155-304	21 58 52.7	-30 13 18	HBL	06.01.1999	0.116
B3 2247+381	22 50 06.6	+38 25 58	HBL	10.01.2010	0.118
RGB J0710+591	07 10 30.1	+59 08 20.5	HBL	02.01.2009	0.125
H 1426+428	14 28 32.6	+42 40 21	HBL	02.01.2002	0.129
1ES 0806+524	08 09 49.2	+52 18 58	HBL	02.01.2008	0.138
1ES 0229+20	02 32 48.4	+20 17 16	HBL	02.01.2006	0.14
1RXS J101015.9-311909	10 10 15.9	-31 19 09	HBL	12.01.2010	0.143
H 2356-309	23 59 09	-30 37 22	HBL	04.01.2006	0.165
1ES 1218+304	12 21 21.9	+30 10 37	HBL	05.01.2006	0.182
RBS 0413	04 13	+18 45	HBL	10.29.2009	0.19
PKS 0447-439	04 47	-43 9	HBL	12.01.2009	0.2
1ES 0414+009	04 14	+00 09	HBL	11.12.2009	0.287
S5 0716+714	07 21 53.4	+71 20 36	LBL	07.01.2009	0.31
1ES 0502+675	05 02	+67 5	HBL	11.17.2009	0.34
PKS 1510-08	15 12 50.5	-09 06 00	FSRQ	03.01.2010	0.36
VER J0648+152	06 48 49.7	+15 16 22	UNID	03.01.2010	?
4C +21.35	12 24 54.4	+21 22 46	FSRQ	06.01.2010	0.432
MAGIC J2001+435	20 01 13.5	+43 53 02.8	HBL	07.01.2010	?
1ES 1440+122	14 42 48.3	+12 00 40	IBL	08.01.2010	?
PG 1553+113	15 55 43.0	+11 11 24	HBL	03.01.2006	?
VER J0521+211	05 21	+21 10	UNID	10.25.2009	?
1ES 1101-232	11/3/1938	-23 29 31	HBL	04.01.2006	0.186
1ES 0347-121	03 49 23.2	-11 59 27.0	HBL	08.01.2007	0.188
1ES 1011+496	10 15 04.1	+49 26 01	HBL	09.01.2007	0.212
3C66A	02 22 39.6	+43 02 08	LBL	10.01.2008	0.444
3C279	12 56 11.1	-05 47 22	FSRQ	06.01.2008	0.5362

Table 1.3: *Extragalactic objects seen by ground-based Čerenkov telescopes, ranked by increasing distance, taken from the TeVCat*[13]*. The selection criterion is not as strict as in the past: unpublished but announced (in Astronomer Telegrams - ATEL - or conferences) sources are also included. The* ***boldface*** *sources correspond to those not (yet?) detected (oficially) by the LAT. The cumulative distribution evolution as a function of time is shown in Fig. 1.15*

photon index of the former being ≥ 2.2, while the average photon index of the latter is < 2. The blazar index versus luminosity characteristics as seen by *Fermi* appear also to largely follow the so-called blazar sequence[Fossati et al., 1998], based on a one zone, homogeneous synchrotron self-Compton and external Compton model, where the peak luminosities of the two radiative components are located at increasingly higher frequencies when the observed γ-ray luminosity decreases, and where the external Compton cooling becomes progressively more inefficient than the self-Compton.

On the other side, the *observed* VHE spectra from all extragalactic objects have photon indexes > 2, so that, for almost all BL Lacs, the combination of *Fermi* and ACTs constrains the peak of the observed SED (in νF_ν representation)[Abdo et al., 2009c]. This should now allow the best characterization ever made of both components of the SED, the monitoring with unprecedented accuracy of how these components evolve, and how they are related.

FSRQ

The FSRQ class of blazars are the most powerful γ-ray emitters as well as the most luminous. This is best illustrated by the gigantic flare exhibited by 3C 454.3 on December 2, 2009 [Escande & Tanaka, 2009] when it reached a flux of $F(E > 100\,\mathrm{MeV}) \simeq 2 \times 10^{-5}\,\mathrm{cm}^{-2}\,s^{-1}$, which is up to date the brightest transient ever detected in the HE range. For comparison, the brightest persistent source in the HE sky is the Vela pulsar, at about half that flux. This population is also extremely variable, and their spectra show significant spectral curvature in the HE range. Since *Fermi* probes these sources mostly at their peak luminosity frequency, and with unprecedented resolution, theorists working on FSRQs are guaranteed to have a field day. The detection of the FSRQ 3C279 [MAGIC Collaboration et al., 2008] at $z = 0.536$ during an optical flare in 2006 by the MAGIC experiment at the 5.8σ level and a dedicated low-energy analysis was the first of this kind with an ACT. The corresponding GeV flux, had *Fermi* been there to see it, would have been a really exceptional state, an order of magnitude higher than the highest GeV flux seen so far on this source, as is pointed out in Abdo et al. [2009c] in order to match the *Fermi* extrapolation to higher energies assuming a conservative EBL attenuation and no further spectral steepening. This detection is clearly paving the way for upcoming ACTs with $< 100\,\mathrm{GeV}$ thresholds, which could probe the FSRQ Compton component variability at timescales not accessible to *Fermi*, and eventually find out whether they can exhibit very fast variability as well.

BL Lacertae

The vast majority of Very High Energy (VHE) gamma-ray emitting Active Galaxies belong to the BL Lac class, itself subdivided into High-Frequency, Intermediate Frequency and Low Frequency peaked BL Lacs (HBL,IBL and LBL respectively) depending on the position of the synchrotron bump in the SED: in UV/X-rays for HBL, in the IR/UV range for IBL and in the IR or lower for LBL. The VHE gamma-ray emitters are mostly HBL, with AP Librae being only the third LBL seen by an Atmospheric Cherenkov Telescope (ACT). LBL objects tend to have higher luminosities, are mostly found in radio surveys (while HBLs are mostly found in X-ray surveys), and might be a distinct class from HBLs though there could be a continuity between the LBL and HBL as proposed by the "blazar sequence".

The most constraining observations on jet kinematics and the γ-ray emitting region probably come from AGN observations with ACTs, mostly the high-frequency peaked class of BL Lac objects (HBLs), which exhibit the most extreme events with large amplitude minute-timescale variability in their VHE γ-ray fluxes. Among the fastest and largest transient events are those reported by the Whipple telescope [Gaidos et al., 1996], by the H.E.S.S. array in PKS 2155-304 (Aharonian et al. 2007, and further described in §2) and the MAGIC telescope on Mkn 501[Albert et al., 2007]. These findings have given raise to considerable theoretical developments in the literature as existing models have to struggle to either remain simple but invoke uncomfortably large bulk Lorentz factors of 100 or higher in order to allow $\sim$ TeV γ-rays to escape from the compact area, or use multiple emitting zones, or allow the emission region to become very small. More details on this are in §3.3.

Intriguingly, the power density spectrum of one of the giant flares of PKS 2155-304 shows no sign of high-frequency cutoff in the red noise power law distribution up to the Poisson noise level, so it cannot be excluded that even faster variability could be detected in the light curves if they were sampled by more sensitive instruments (or if the fluxes were higher). This will be discussed in §2 and §4.

The BL Lac object PKS 2155-304 was also the first source of this type to be targeted during a simultaneous space-ground multi-wavelength campaign in 2009 involving *Fermi*(Aharonian et al. 2009c, further described in §3). Observing the soft spectrum of the archival EGRET measurements on this object would have been quite disconcerting since the this soft spectrum is incompatible with a smooth connection to the lowest known VHE spectrum (Fig. 1.17) and would therefore rule out a single radiative IC population. The *Fermi* observations during this campaign turned out to be actually in good agreement with the simultaneous VHE spectrum, and provided the first simultaneous IC characterization of an HBL. An interesting feature of

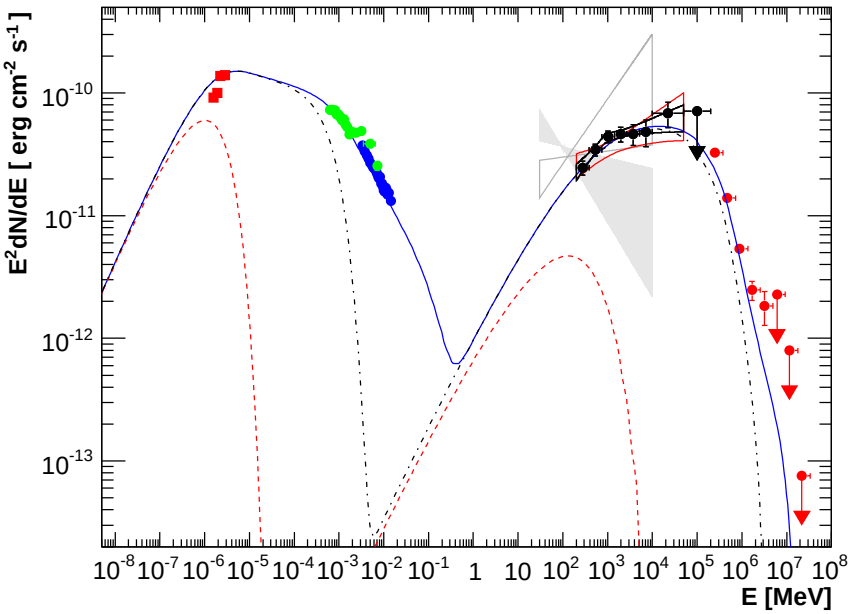

Figure 1.17: *The spectral energy distribution of PKS 2155-304 during the 2009 MWL campaign, involving optical measurements from ATOM, X-ray observations carried out by both Swift and RXTE, HE and VHE γ-ray observations from Fermi and HESS, respectively. The archival EGRET measurements appear in grey. The plain, dotted, and dash-dotted lines are produced by the same synchrotron self-Compton (SSC) model but with different electron cutoff energies, as described in Aharonian et al. [2009c], and they show that low (or quiescent) flux states can accomodate the absence of correlated X-ray/VHE variability (see text).*

this campaign was that the X-ray and VHE light curves, despite significant variability, were not correlated, when the VHE and optical fluxes appeared to be correlated to some degree. While the latter correlations have yet to be confirmed and understood, the observed X-ray/VHE behaviour could actually be reproduced with a simple SSC model since the highest electrons, those radiating the X-rays through the synchrotron mechanism, are barely noticed at VHE energies due to a combination of large Klein-Nishina suppression, a low density of target photons, and EBL attenuation.

With the advent of quasi-continuous, well-sampled observations of flaring BL Lac objects, VHE γ-ray light curves can now be characterized beyond finding the fastest doubling/halving time scales. Tools commonly used in X-ray observations can now usefully be applied to the *whole* data set instead of picking the most interesting part of it (or at least what might look as such). In this way it has now been established that, at least for PKS 2155-304, the 2006 flaring state is compatible with a stationary lognormal process[Degrange et al., 2008] whose power spectum density is red noise, sharing a characteristic of accreting sources shining with thermal radiation such as Cyg X-1 or some Seyfert galaxies for instance. This might be important enough that it should be sought for not only in the other jet-dominated non-thermal emissions from AGN, but also again in the same source to find out whether the Power Spectral Density (PSD) slope or lognormal factor are subject to changes. Its eventual ubiquity would also have to be reproduced by time-dependent emission models.

Not much was known about BL Lac objects in the HE range, so it was not clear until *Fermi* started observing what exactly was happening in that regime, i.e. whether BL Lacs were just very faint, or if they were bright at higher energies where EGRET's sensitivity dropped. It was hence surprising to find many hard BL Lac objects among the bright sources seen by *Fermi*[Aharonian et al., 2009c]. Their spectra are generally power laws over 3 decades in energy, with sometimes small deviations at energies $\geq 1\,\mathrm{GeV}$. The overall SED is rather unsurprising, as the high end of the HE and the low end of the VHE spectra tend to be well within range, and in some cases even slightly overlap, since a few of the hardest sources with HE indexes of ~ 1.5 have a spectral bin as high as $100\,\mathrm{GeV}$. A rather special case is the HBL PG 115+113, of

unknown redshift, which has the largest spectral difference ($\Delta\Gamma \sim 3$) between the HE and the VHE regimes. Since its distance is still unknown, it cannot be ruled out that the observed large spectral break is not related to the source but to the γ-ray propagation[Abdo et al., 2010a]. This source, like many other BL Lacs visible in both the HE and VHE ranges, exhibits surprisingly little variability in either energy band[Abdo et al., 2010a] over long time scales when it is actually known to be largely variable at X-ray and optical wavelengths.

There are high hopes that *Fermi*, given its intra-day overall sky surveillance and the fact that it shares the same radiative population as VHE instruments, will prove to be a more efficient provider of flaring states in blazars of interest for ACTs than all-sky X-ray monitors such as the ASM onboard *Rossi-XTE* or the BAT onboard *Swift*. But looking at the rich Astronomer's Telegram history of *Fermi* the extremely variable extragalactic sky is so far essentially composed of FSRQs and a low-frequency peaked BL Lac.

non-blazars

Unlike most blazars, high frequency VLBI can probe the jets in a few selected VHE sources such as M87 and Centaurus A[Aharonian et al., 2009a] down to size scales 100 gravitational radii as was mentioned in §1.2.4. These sources are widely thought to be members of the unbeamed parent population of blazars [Urry & Padovani, 1995], as their nucleus appears largely underluminous but the overall jet energetics indicate that the accretion energy might emerge in the jet instead [Di Matteo et al., 2003], so even observations at large angles of the jet can provide valuable insights of jet physics. In M87, it was possible to establish that the acceleration and the collimation of the jet occurs within $\sim 100\,R_S$. A joint ACT campaign, along with VLBA observations, has revealed that an increase of the nucleus radio flux might be the lagged counterpart of a similar VHE γ-ray transient, implying that the γ-ray emission, and hence the acceleration of the underlying radiative population, is likely to happen well within the collimation region[Acciari et al., 2009a]. Scenarios to explain how γ-ray variability can be detected in off-axis jet systems include e.g. a multiblob SSC model similar to those used for blazar emission[Lenain et al., 2008], a two-zone spine-sheath layer mechanism[Tavecchio & Ghisellini, 2008], and pulsar-type acceleration due to centrifugally accelerated electrons in a rotating jet magnetosphere[Rieger & Aharonian, 2008]. Unifications of these scenarios with the beamed population is going to be an interesting development to follow in the future, as well as its long-term HE characterization by *Fermi*.

Another possible emerging population of γ-ray emitting AGN unseen before *Fermi* are the narrow-line Seyfert-1 galaxies (NLS1) of which up to now 4 have been detected[Abdo et al., 2009e]. It was not completely unexpected that the rather rare radio-loud sample of NLS1 galaxies could be also high-energy emitters since in some scenarios they are probably have a pole-on orientation[Remillard et al., 1991]. The HE spectra are however extremely steep so, given their distance, nothing is expected to be visible by ACTs by extrapolating the *Fermi* spectra, but suprises can arise given the rather complex SEDs which leave probably more room open to radically different models than there is for BL Lac models.

Prospectives for UHECRs

If the γ-ray luminosity can be used to derive the UHECR power, AGN have the required output to host an accelerator which generates cosmic rays up to $10^{20}\,\mathrm{eV}$. But can the population of blazars account for the required energy production rate of $\sim 10^{44}\,\mathrm{erg\,Mpc^{-3}\,yr^{-1}}$ to match the observed flux CRs at energies $10^{19} - 10^{21}\,\mathrm{eV}$ against GZK losses [Waxman, 1995b]? Using the 1LAC catalog, Dermer & Razzaque [2010] derived the cumulative $100\,\mathrm{MeV} - 100\,\mathrm{GeV}$ γ-ray luminosity density for the above mentioned classes of γ-ray emitters, and found that BL Lac type AGN (and their probable unbeamed parent population FR1 galaxies) are likely to be at the origin of the local UHECRs since their luminosity density is sufficient - at least for Fe ions - while the FSRQ do not have sufficient luminosity to power the UHECR within a GZK radius (Fig. 1.18). Understanding how particle acceleration occurs in BL Lac systems, which are the bulk of the extragalactic VHE γ-ray emitters, might well be an unescapable path to understanding the generation of UHECRs.

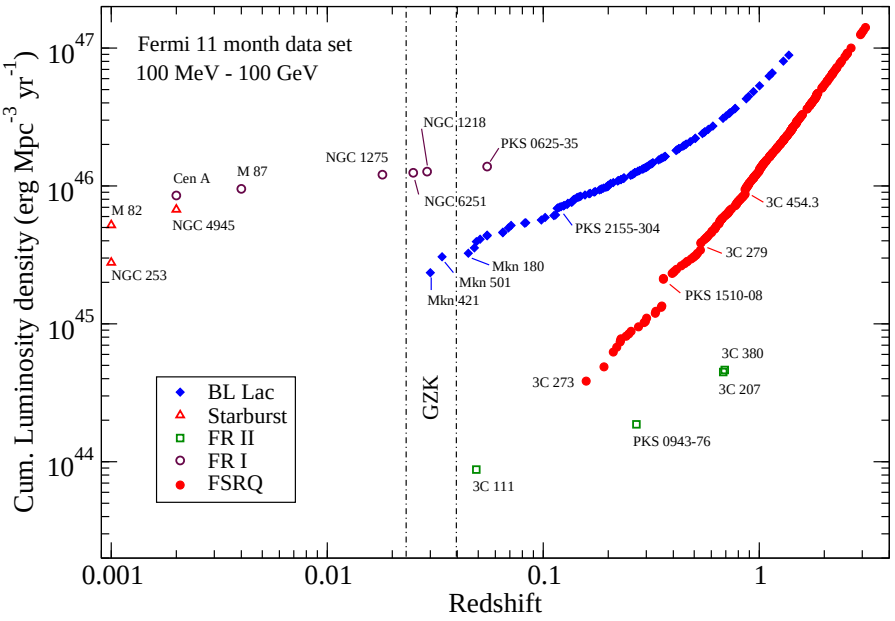

Figure 1.18: *Cumulative γ-ray luminosity for different γ-ray emitting AGN. the BL Lac class (blue), including the "misaligned" ones from the FR1 class, provide the sufficient density as well as outpower the FSRQs (red) within a GZK radius (here the* $100 - 200\,\mathrm{Mpc}$ *range). (Reproduced from Dermer & Razzaque 2010).*

Chapter 2
Propagation: Extragalactic Background Light

2.1 Introduction

Photons of energy E_γ can create an electron/positron through pair production when colliding with target photons of energy E_t provided that $E_\gamma E_t \geq 2m_e^2c^4$, with reaction product distributions according to the Bethe-Heitler cross-section. The observed VHE spectra $F_{\rm VHE}(E)$ of extragalactic sources appears attenuated, by interacting background photon fields, compared to the intrinsic spectrum $F_{\rm VHE,int}$ through $F_{\rm VHE}(E) = \exp(-\tau(E,z))F_{\rm VHE,int}$ where $\tau(E,z)$ is the optical depth for photons with observed energy E at a distance z. At energies $\varepsilon = 100\,$TeV, interactions with CMB photons make the universe opaque beyond a few Mpc [Gould & Schréder, 1966]. Below $10^{12}\,$eV, the target photon field are the optical and the infrared extragalactic background light (EBL), with an undetermined horizon $z \geq 0.3$ due to uncertainties in the EBL density at optical to UV wavelengths. Due to difficulties in subtracting local Galactic foregrounds, this part of the cosmic background is poorly enough constrained that VHE γ-ray attenuation can be a useful tool to probe the EBL despite all the uncertainties in the intrinsic emitted spectrum [Stecker et al., 1992; Biller, 1995]. BL Lac objects can be used for this since the radiative particle distribution is expected to be close to the injection function, for which theoretical constraints exist, because the Lorentz factor $\gamma_{\rm cool}$ at which electrons cool within the dissipative region is expected to be large enough[Ghisellini et al., 2010] that the radiative electron spectrum is not affected within a time $\sim R/c$. The HESS collaboration used its observations of 1ES 1101-232 ($z = 0.186$), together with the assumption that the intrinsic spectrum could not have an index $\Gamma < 1.5$ to estimate a stringent upper limit to the EBL [Aharonian et al., 2006b]. Even though the initial constraint on the photon index is still debated (see, e.g., Katarzyński et al. 2006), it can be noticed that the blazars seen in the LAT do not violate this limit (Figure 1.16), and that the use of such constraints turn out to be so far the most efficient way to constrain the EBL and hence properties of the star formation rate and of the early Population III stars[Raue et al., 2009]. The FSRQ class, despite the advantage of being at larger distances on average than BL Lacs, might be more tricky to use for such purposes, since not only much faster cooling time scales deviate the radiative spectrum faster from the injected one, but also because significant γ-ray absorption is expected inside the source itself which might create artificially hard spectra [Aharonian et al., 2008c].

2.2 EBL induced HE-VHE curvature

The imprint of the EBL on VHE spectra has long been sought for. The modulation of the EBL spectral density around $0.1\,$eV could be visible as a kink in the VHE spectrum around $1\,$TeV directly in the spectrum of VHE sources themselves. This was sought for in e.g. the blazar H 1426+428 by Aharonian et al. [2003b]) but results were rather inconclusive given the large statistical errors. The signature of the EBL can also be searched for in the global population of VHE sources since increasing distances should increase the attenuation and the photon index should become softer if the intrinsic index remains constant!. One of such studies, the most recent before Fermi started operations, is illustrated in Figure 2.1, where the photon index of the VHE sources available in 2009 is checked against the distance by Mori [2009]. Not finding a hoped-for correlation with z either, de Angelis et al. [2009] attribute the scatter of points as coming from different emission state dependent values of Γ.

Anticipating results shown in §3, the effect of the EBL could actually be uncovered using VHE photon indexes with the knowledge of the Fermi spectrum associated to each source.

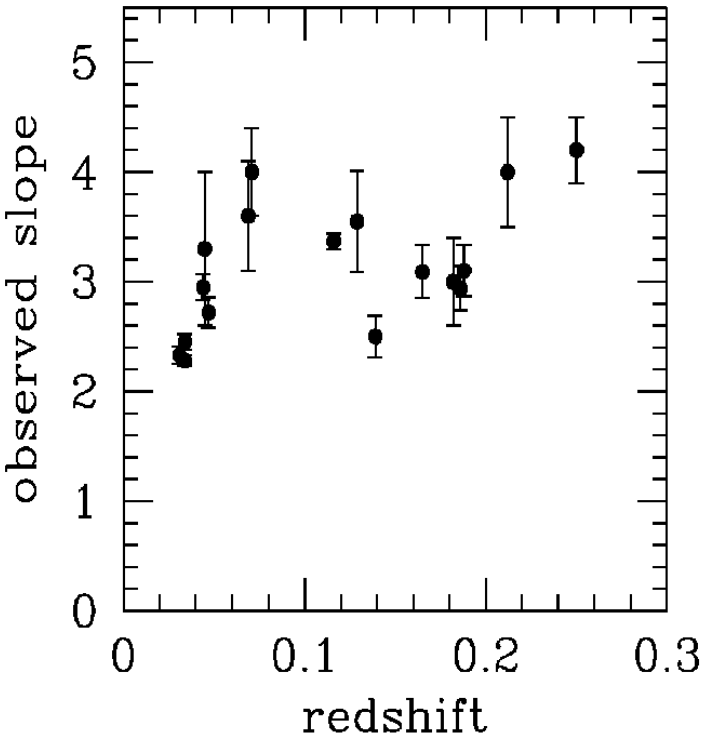

Figure 2.1: *Observed photon indices of all known VHE blazars known in 2009, versus the distance. No obvious pattern is found in the data, while an upward trend would be expected provided all spectra were intrinsically similar. (Reproduced from Mori 2009).*

In Abdo et al. [2009c] we studied a.o. the evolution with z of the high-energy component for those AGN detected in the HE and VHE regimes, in looking for the νF_ν slope steepening $\Delta\Gamma = \Gamma_{TeV} - \Gamma_{GeV}$ of the extrapolated *Fermi* index Γ_{GeV} resulting in the observed index Γ_{TeV}. This resulted in Fig. 2.2, which has here been updated from the 15 original sources to the now 22 joint HE-VHE sources. The largest $\Delta\Gamma$ are evident in the spectra of the more distant sources 1ES 1101+496, H 1426+428and PG 1553+113. By contrast, the spectra of the nearby radio galaxies M 87 and Cen A show no evidence of a spectral change. This distribution has a Pearson correlation factor of $r = 0.76 \pm 0.14$, but since it was not really a correlation that was expected, but an evolution towards higher values of $\Delta\Gamma$, the Kendall rank coefficient was also calculated to this distribution and was found to be $\tau_K = 0.68 \pm 0.15$. A few interesting facts which enforce the validity of this study are that (i) the bulk of these sources showed no time-dependent flux variability in Abdo et al. [2009c] and that (ii) no clear flux-dependent spectral variability for BL Lac sources was found in the dedicated spectral variability study of Abdo et al. [2010b].

It became then interesting to calculate the expected spectral difference $\Delta\Gamma_e$ using the optical depth $\tau(E,z)$ derived from a conservative EBL model - in this case the distribution derived by Franceschini et al. [2008], which also include evolutionary effects. This results in the line of Fig. 2.2 (updated from Sanchez [2010]), showing the minimal $\Delta\Gamma$ expected for that model. Provided this model is correct, **insignificant deviations from the line indicate that the VHE spectrum is compatible with an extrapolated Fermi spectrum absorbed by this EBL model, such that the spectral change is purely extrinsic, and if $\Gamma_{GeV} < 2$ the intrinsic Compton peak is undefined in** νF_ν. Conversely, significant deviations mean that the difference $\Delta\Gamma - \Delta\Gamma_e$ can be attributed to an *intrinsic* spectral feature. The VHE sources without HE counterpart are not represented here, but assuming $\Gamma_{GeV} \geq 1.5$, could provide upper limits. This study is obviously bound to undergo more changes when spectral details will become available from the huge backlog of ATEL-announced VHE sources since little information is usually provided in ATELS.

In the case that the distribution of Figure 2.2 is purely induced by EBL models, and no evolution effect of the HE or VHE spectrum in BL Lacs occurs over this distance range (as the 1LAC blazar γ-ray index evolution in Abdo et al. 2010d suggests), this representation or variants thereof can also be used to test some specific EBL models within redshifts $z \leq 0.3$: Stecker & Scully [2010] subsequently developed a first order polynomial expression with two constants to test two evolution models using a χ^2 fit on the $\Delta\Gamma$ distribution, while Yang & Wang [2010] calculate limits on the EBL density in the specific energy band which dominates

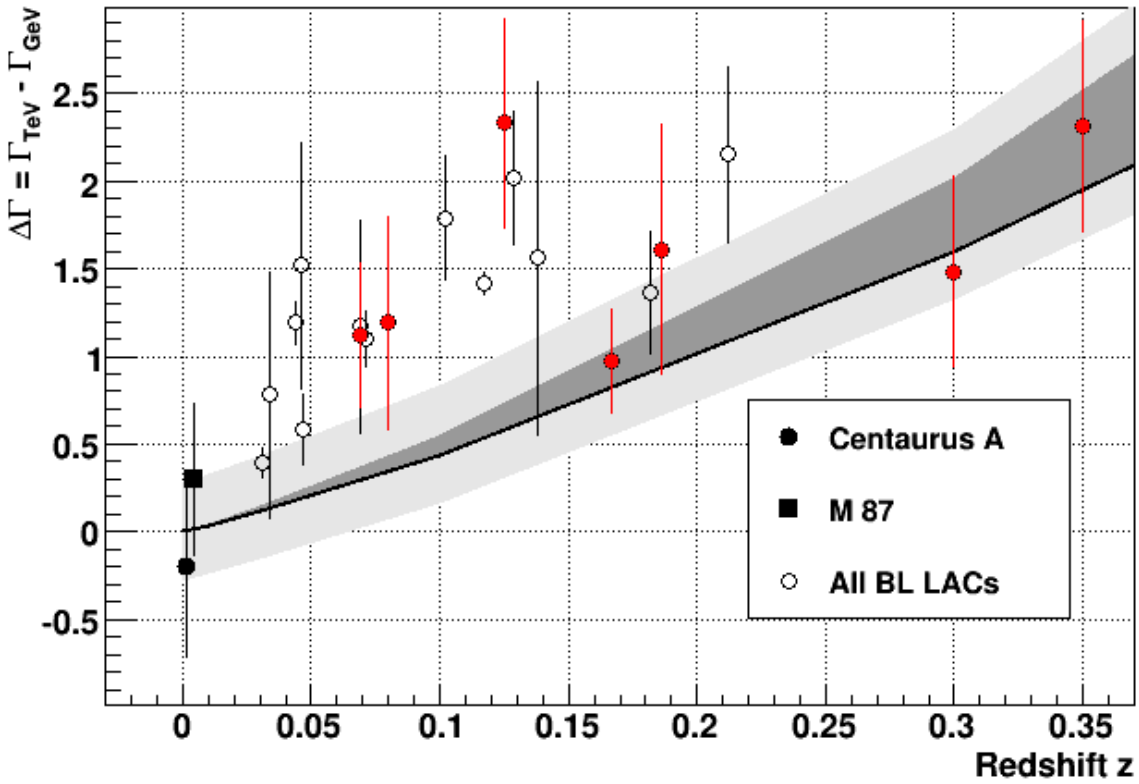

Figure 2.2: *The difference in spectral slope* $\Delta\Gamma$ *as a function of distance, for a fraction of the currently known sample of joint HE-VHE detected sources, since some BL Lac objects have no known redshift (Table 1.3), or are* known *VHE emitters but their details are not known yet. The spectral slope difference clearly increases with distance; while* $\Delta\Gamma \simeq 0$ *for the nearby FR1 radio galaxies M87 and Cen A,* $\Delta\Gamma \geq 1.5$ *when* $z \geq 0.2$*. The most distant emitter 3C279 is omitted since* (i) *it is a highly variable source with spectral variations,* (ii) *it has not been seen in VHE* γ*-rays since Fermi started observations and it would not have been in a flux state to match both spectra, and* (iii) *it belongs to the FSRQ class which* could *have strong intrinsic features. The black line indicates the expected* $\Delta\Gamma$ *from an attenuation induced by a conservative EBL model from Franceschini et al. 2008*

the γ-ray interactions.

This representation can also be used to constrain the distance: indeed about 50% of all BL Lacs have no redshift estimation, such that assuming that the observed VHE spectrum is the result of an attenuated *Fermi* spectrum, instead of assuming that it is the result of an attenuated $\Gamma = 1.5$ intrinsic spectrum (which was done in Aharonian et al. 2006b), provides a new and much more robust estimate. This was first applied to constrain the distance of PG 1553+113 by Abdo et al. [2010a] and afterwards by Prandini et al. [2010] to infer the redshift of the blazar PKS 1424+240. More developments can be expected as the amount of HE-VHE blazars increases.

Particle	Process	energy	mean free path
Protons	$p + h\nu_{2.7K} \rightarrow \pi^0 + X$	$\geq 5\times10^{19}$ eV	50 Mpc
Nuclei	$A + h\nu_{2.7K} \rightarrow \Delta^{++} + X$	$\geq 5\times10^{18}$ eV/n	100 Mpc
Gammas	$\gamma + h\nu_{EBL} \rightarrow e^+ + e^-$	10^{12} eV	500 Mpc
Gammas	$\gamma + h\nu_{2.7K} \rightarrow e^+ + e^-$	10^{15} eV	10 kpc
Neutrinos	$\nu + \nu_{1.95K} \rightarrow W/Z_0 + X$	$\geq 4\times10^{22}$ eV	40 Gpc

Table 2.1: *Cosmological horizons for cosmic rays of different nature. The EBL progressively diminishes the γ-ray horizon down to a minimum of a few pc for $E = 2\times10^{15}$ eV which interact with the peak of the CMBR density, and then increases again (see e.g. Coppi & Aharonian 1997). The horizon for protons progressively drops to $\mathcal{O}(10\,\mathrm{Mpc})$ for $E \geq 10^{23}$ eV, while neutrinos are limited by the hypothetical cosmic neutrino background but have by far the highest energy threshold of all these high-energy messengers.*

2.3 On pair production in the extragalactic magnetic field

The EBL density limit estimation in Aharonian et al. [2006b], and indeed in most other similar studies, did not consider emission from the cascade initiated when the created pairs upscatter CMBR photons back to VHE energies [Protheroe, 1986]. Cascade emission may make the universe appear more transparent than under the assumption of pure absorption. Inversely, including cascade emission when deconvolving for propagation effects on a given EBL leads to intrinsic spectra different from the pure absorption case. The impact of this emission on the EBL upper limit, as derived from the spectrum, is considered here. Electrons may diffuse on the extragalactic magnetic field (EMF), causing their emissions to be lost for the observer, while in the total absence of any EMF, a large fraction of the lost γ-ray flux can be expected back in the direction of the observer and to contribute to the spectrum of the point-like source: a γ-ray with energy E will create a e^+/e^- pair with energies $\gamma_e m_e c^2$, where on average $\gamma_e \simeq \frac{E}{2m_e c^2}$, and these pairs can upscatter CMBR photons at energies $E' \simeq \gamma^2 h\nu_{CMBR}$. For a canonical VHE source, assuming $E = 10^{12}$ eV, this will yield electrons with $\gamma_e \simeq 10^6$ and hence upscattered CMBR photons with $E' \simeq 600$ MeV, which are unlikely to interact again. However $E \geq 10^{13}$ eV photons would generate $E' \geq 60$ GeV photons which can repeat the cycle, and a numerical computation of the following cascade is needed to determine the change in the observed spectrum. The EBL and EMF governing the propagation of the cascade are described in §2 of the work published in [D'Avezac et al., 2007]. The cascade equations and numerical method are described in §3 and applied to the case of the distant VHE γ-ray emitter 1ES 1101-232 in §4.

This study showed that the impact of extragalactic cascade emissions on the HE-VHE spectrum of 1ES 1101-232 is to soften the observed spectrum in the VHE range compared to pure absorption because most of the cascade emissions occurs at 100 GeV and below. As a result, the upper limits on the EBL determined by H.E.S.S. are strengthened in the sense that taking cascades into account leads either to harder intrinsic spectra than judged plausible, or to a reduced EBL upper limit. Inversely, using lower limits on the EBL coming from galaxy counts, the intrinsic spectrum of 1ES 1101-232 is found to have $\Gamma \leq 1.95$ with very hard values if there is an important contribution from cascade emission. This is at odds with current theoretical and observational understanding of blazars. A cutoff at energies ≤ 10 TeV in the intrinsic spectrum would limit the cascade contribution. This contribution was found to be quenched if the EMF intensity is greater than 10^{-6} nG, as expected away from voids. A lower EMF increases the amount of cascade emission reaching the observer in the HE band, with a signature in the *Fermi* band for intensities $\sim 10^{-8}$ nG but at the price of a hard intrinsic spectrum so as to fit the H.E.S.S. observations.

This study paved the way for setting limits to the very poorly constrained EMF, based on the knowledge of the HE and VHE spectrum of distant blazars, and to compare the computed cascade contributions with the measurements. This was carried out using the *Fermi* derived upper limits for a sample of distant BL Lac by Neronov & Vovk [2010] and Tavecchio et al. [2010] who both estimated a lower bound on the EMF of $B \geq 3-5\times10^{-16}$ G (and who both acknowledged this work), and on the specific distant BL Lac object 1ES 0229+200 by [Dolag et al., 2011] who derived $B \geq \mathcal{O}(10^{-16}-10^{-15})$ G for the EMF value (and didn't acknowledge this

work..). Note that all these values are the same as the value of the quenched contribution limit derived in §2.4..

2.4 “Cascading on extragalactic background light”

A&A 469, 857–860 (2007)
DOI: 10.1051/0004-6361:20066712

Astronomy & Astrophysics

Cascading on extragalactic background light *(Research Note)*

P. d'Avezac[1], G. Dubus[1,2,3], and B. Giebels[1]

[1] Laboratoire Leprince-Ringuet, UMR 7638 CNRS, École Polytechnique, 91128 Palaiseau, France
e-mail: Guillaume.Dubus@obs.ujf-grenoble.fr
[2] Institut d'Astrophysique de Paris, UMR 7095 CNRS, Université Pierre & Marie Curie, 98bis Bd. Arago, 75014 Paris, France
[3] Laboratoire d'Astrophysique de Grenoble, UMR 5571 CNRS, Université Joseph Fourier, BP 53, 38041 Grenoble, France

Received 8 November 2006 / Accepted 21 April 2007

ABSTRACT

Context. High-energy γ-rays propagating in the intergalactic medium can interact with background infrared photons to produce e^+e^- pairs, resulting in the absorption of the intrinsic γ-ray spectrum. TeV observations of the distant blazar 1ES 1101-232 were thus recently used to put an upper limit on the infrared extragalactic background light density.
Aims. The created pairs can upscatter background photons to high energies, which in turn may pair produce, thereby initiating a cascade. The pairs diffuse on the extragalactic magnetic field (EMF) and cascade emission has been suggested as a means for measuring its intensity. Limits on the IR background and EMF are reconsidered taking into account cascade emissions.
Methods. The cascade equations are solved numerically. Assuming a power-law intrinsic spectrum, the observed 100 MeV–100 TeV spectrum is found as a function of the intrinsic spectral index and the intensity of the EMF.
Results. Cascades emit mainly at or below 100 GeV. The observed TeV spectrum appears softer than for pure absorption when cascade emission is taken into account. The upper limit on the IR photon background is found to be robust. Inversely, the intrinsic spectra needed to fit the TeV data are uncomfortably hard when cascade emission makes a significant contribution to the observed spectrum. An EMF intensity around 10^{-8} nG leads to a characteristic spectral hump in the GLAST band. Higher EMF intensities divert the pairs away from the line-of-sight and the cascade contribution to the spectrum becomes negligible.

Key words. radiation mechanisms: non-thermal – galaxies: BL Lacertae objects: individual: 1ES 1101-232 – galaxies: intergalactic medium – cosmology: diffuse radiation – gamma rays: observations

1. Introduction

The observed very high energy (VHE) spectra of extragalactic sources are attenuated by pair production (PP) on background photon fields. At energies $\epsilon = 100$ TeV, interactions with CMB photons make the universe opaque beyond a few Mpc (Gould & Schréder 1966). In the 1–10 TeV range, the target photon field is the infrared extragalactic background light (EBL), with an undetermined horizon $z \gtrsim 0.2$ due to uncertainties in the EBL density at optical to UV wavelengths. Conversely, observations of absorbed VHE spectra of blazars can constrain the EBL density at these wavelengths, provided their intrinsic emission is known (Stecker et al. 1992; Biller 1995). Recently, the HESS collaboration used its observations of 1ES 1101-232 ($z = 0.186$), together with a reasonable assumption on the intrinsic spectrum, to estimate a stringent upper limit to the EBL (Aharonian et al. 2006). This estimation did not consider emission from the cascade initiated when the created pairs upscatter EBL photons back to VHE energies (Protheroe 1986; Protheroe & Stanev 1993; Aharonian et al. 1994; Biller 1995; Aharonian et al. 2002). Cascade emission may make the universe appear more transparent than under the assumption of pure absorption. Inversely, including cascade emission when deconvolving for propagation effects on a given EBL leads to intrinsic spectra different from the pure absorption case.

The impact of this emission on the EBL upper limit, as derived from the 1ES 1101-232 spectrum, is considered here. Electrons may diffuse on the extragalactic magnetic field (EMF), causing their emissions to be lost for the observer (Protheroe 1986; Aharonian et al. 1994; Plaga 1995). The EBL and EMF governing the propagation of the cascade are described in Sect. 2. The cascade equations and numerical method are described in Sect. 3 and applied to the case of 1ES 1101-232 in Sect. 4. The implications on the EBL and EMF limits are set out in Sect. 5.

2. Extragalactic backgrounds

In addition to the CMB, the diffuse photon background is constituted of integrated emission from stars (peaking around 2 μm, see Fig. 1) and heated dust (peaking around 200 μm). The EBL spectral energy distribution is difficult to measure directly because of the strong zodiacal and galactic foregrounds. Lower limits have been set using source counts while SED shapes have been derived from simulations of galaxy formation (Primack 2002; Lagache et al. 2003; Xu et al. 2001). The EBL shape *HESS 2006* (Fig. 1) was computed by Primack et al. (1999) and normalised by a factor 0.45 in Aharonian et al. (2006) to account for the TeV observations of 1ES 1101-232. *Primack 2005* refers to an EBL normalised instead to fit the lower limit set by galaxy counts. The *Spitzer* observations suggest higher fluxes in the 10–1000 μm range (Dole et al. 2006). This affects attenuation above 20 TeV but has been verified to have no consequence on the results presented here.

The created pairs can be deflected from the line-of-sight by an extragalactic magnetic field (EMF). Faraday rotation and

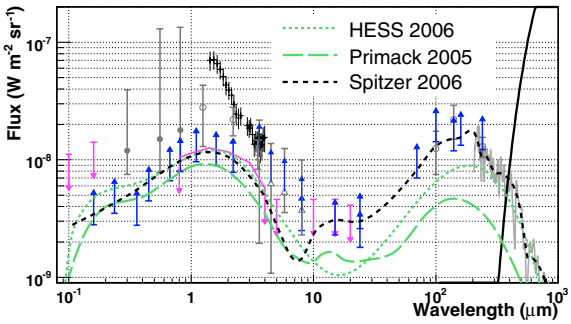

Fig. 1. EBL+CMB photon density (at $z = 0$) used in this work. The *HESS 2006* and *Primack 2005* EBL derive from a simulation of galaxy formation (Primack et al. 1999, 2005, respectively). The *Spitzer 2006* EBL is a best fit to available observations (Dole et al. 2006, from which the measurements shown here were also taken).

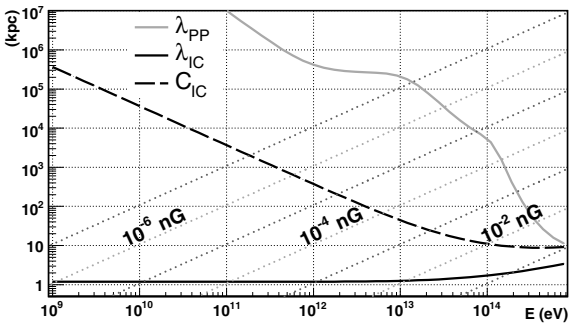

Fig. 2. Mean free path λ_{PP} for PP on the EBL+CMB background as a function of the VHE photon energy. The mean free path λ_{IC} and IC cooling length C_{IC} of the pairs on the CMB is also shown as function of electron energy. C_{IC} flattens (then rises) at high energies as the interaction enters the Klein-Nishina regime. The electron then loses its energy in a single interaction ($\lambda_{IC} \approx C_{IC}$). IC losses of the pairs take place on a small scale compared to the γ-ray attenuation length for photon energies <300 TeV. The electron gyroradius R_L for various EMF intensities is indicated by dashed diagonal lines. The pairs are expected to be isotropised by the EMF for energies and B intensities such that $R_L \leq C_{IC}$.

synchrotron emission in radio yield estimates of magnetic fields in galaxies (roughly >10 nG), or in clusters (≤0.1−1 nG) and even some super- clusters (≤nG) (Kronberg 1994; Widrow 2002; Vallée 2004). The EMF outside these structures is unconstrained and may be as low as 10^{-19} nG (Fan et al. 2003, and references therein). For such very weak EMFs, the deflection of electrons due to IC interactions is negligible and the cascade occurs along the line-of-sight with a short delay of the secondary emission (Plaga 1995; Cheng & Cheng 1996; Dai et al. 2002). Diffusion on a stronger EMF creates a halo around γ-ray sources and isotropizes the cascade emission (Aharonian et al. 1994). This occurs when the gyroradius R_L of the pairs is much lower than their Compton cooling length $C_{IC} = E(\mathrm{d}E/\mathrm{d}l)^{-1}_{IC}$. Since mostly CMB photons are upscattered, the minimum B required to isotropise pairs of energy E is $3 \times 10^{-6} E^2_{TeV}(1+z)^4$ nG. Much of the isotropic re-emission is lost to the observer and the pairs diffuse on a scale $\sim(R_L C_{IC})^{1/2}$. For intermediate EMFs, the TeV electrons in the beamed relativistic jet are deflected by $\sim C_{IC}/R_L$. Halo sizes $\gtrsim 0.1°$ could be resolved by γ-ray detectors and used to estimate the EMF intensity (Neronov & Semikoz 2006). Photons in 0.1° haloes have propagation times varying by $\sim 10^5$ years, averaging out any time variability (Fan et al. 2003). In the following, the cascade emission is assumed to be unresolved from the source and delays are not considered. The TeV emission detected by HESS from 1ES 1101-232 appears to be at a low flux level with no significant variability.

3. Cascade equations

The cascade is described by a set of two coupled equations involving the photon energy density $n_P(\varepsilon)$ and the electron (positron) energy density $n_E(E)$:

$$c\partial_t n_P = -\frac{1}{\lambda_{PP}} n_P + c_B \int_\varepsilon^{+\infty} G_{IC}(e,\varepsilon)\, n_E(e)\mathrm{d}e \quad (1)$$

$$c\partial_t n_E = -\frac{1}{\lambda_{IC}} n_E + 2\int_E^{+\infty} G_{PP}(e,E)\, n_\varepsilon(e)\mathrm{d}e + \int_E^{+\infty} G_{IC}(e, e-E)\, n_E(e)\mathrm{d}e. \quad (2)$$

The first term in both equations is the sink term due to PP (Eq. (1)) or IC losses (Eq. (2)). λ_{PP} and λ_{IC} are the mean free path for each interaction. The second term is the source term corresponding to cascade emission (Eq. (1)) or pair creation (Eq. (2), with a factor 2 for the pair). The cascade emission factor c_B is 1 when the EMF is ignored, and approximated to 0 when the electron population is considered isotropised. The pair production term is written in terms of $G_{PP}(\varepsilon, E) = \int \partial_E \sigma_{PP}(\varepsilon, \varepsilon_B) u(\varepsilon_B)\mathrm{d}\varepsilon_B$, where $\partial_E \sigma_{PP}$ is the differential cross-section and u is the photon background energy density (EBL+CMB). The IC radiation term $G_{IC}(E, \varepsilon)$ is defined similarly. The third term in Eq. (2) reflects IC cooling of electrons from higher energies. All of these terms are functions of z.

The integrated cross-sections for PP and IC on isotropic target photons are taken from Gould & Schréder (1966) and Jones (1967). Analytic expressions of the differential cross- sections derived by Zdziarski (1988) for background densities in the form of blackbodies or power laws are used to calculate G_{PP} and G_{IC}. The cascade equations are solved numerically by combining n_P and n_E into a single vector V defined on a logarithmic scale of energies ($\varepsilon_0 \zeta^i$), from $\varepsilon_0 = 10^7$ eV up to 10^{17} eV in 250 steps (thus $\zeta = (10^{17}/10^7)^{1/250}$). To ensure energy conservation, the integrals on G_{PP} and G_{IC} are calculated as

$$\int G_{IC}(e,\varepsilon)\, n_E(e)\mathrm{d}e = \sum_k V_{k,E} \int_{\zeta^{-1/2}}^{\zeta^{1/2}} \frac{\epsilon_0 \zeta^k u G_{IC}(\epsilon_0 \zeta^k u, \varepsilon)\mathrm{d}u}{\zeta^{1/2} - \zeta^{-1/2}} \quad (3)$$

The cascade equations may then be rewritten as a matrix $\mathbf{P}$ acting on the vector V: $V(t+\delta t) = \exp(\delta t \mathbf{P}) V(t)$ (exp is developed to the 4th order in δt). The terms in $\mathbf{P}$ are of the order of λ^{-1}_{IC} or less, hence it is enough to take steps of size $c\delta t = 0.1$ kpc, updating the matrix $\mathbf{P}(z)$ every $\delta z = 0.001$ with $\mathrm{d}z = H_0(1+z)[\Omega_M(1+z)^3 + \Omega_\Lambda + (1-\Omega_M-\Omega_\Lambda)(1+z)^2]^{1/2}\mathrm{d}t$ and values for H_0, Ω_M and Ω_Λ taken from WMAP (Peiris et al. 2003). Thus, at $z = 0.2$, $\delta z \approx 3 \times 10^4 c\delta t$.

4. Application to 1ES 1101-232

The SED of the attenuating EBL can be deconvolved from γ-ray observations of extragalactic sources (TeV blazars), given a priori knowledge on the intrinsic spectra. Modelling observed spectra as power-laws, the effect of PP is to soften the intrinsic spectral index, increasingly so with EBL intensity. Hence, using observations of the farthest TeV blazar and assuming the hardest possible intrinsic spectrum puts an upper limit on the

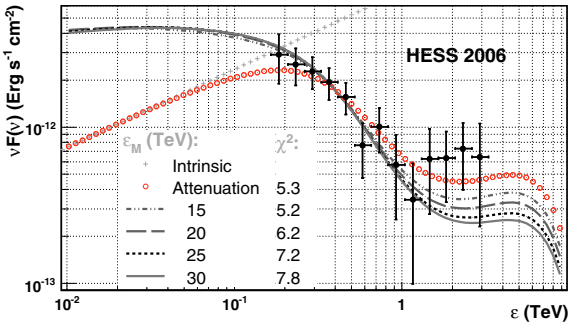

Fig. 3. 1ES 1101-232 observed and modelled spectra with a maximal (*HESS 2006*) EBL and including cascades with no magnetic field. HESS observations points are in black (Aharonian et al. 2006). Markers indicate the attenuation only observed spectrum (circles) and the corresponding intrinsic spectrum (crosses), whereas the lines indicate the observed spectra with cascade emissions. Intrinsic spectra are in the form of $\nu F_\nu \propto E^{0.5}\mathrm{d}\nu$ and adjusted to the data. Cascade emission accumulates at 100 GeV and below, softening the spectra compared to pure absorption. The HESS upper limit on the EBL remains valid after taking the full emission from cascades into account.

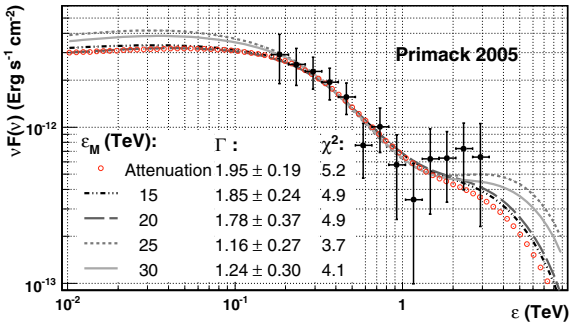

Fig. 4. 1ES 1101-232 observed and modelled spectra with a minimal (*Primack 2005*) EBL and including cascades with no magnetic field. The intrinsic spectrum is now adjusted to the HESS data leaving the spectral index Γ free. For pure absorption, the best index is Γ = 1.95. With cascades, the index hardens as IC emission softens the propagated spectrum. For high ϵ_M, the best index softens again so as to limit the amount of cascading but the fit worsens. Significant cascading on the minimal EBL and in a very weak EMF implies a very hard input spectrum in order to account for the observations.

EBL responsible for attenuation. Current theoretical understanding of shock acceleration limits the intrinsic particle distribution in blazars to a power-law of index no harder than a 1.5 and correspondingly, an intrinsic photon spectrum $\mathrm{d}N \propto E^{-\Gamma}\mathrm{d}E$ with $\Gamma \geq 1.5$ (Aharonian et al. 2006).

1ES 1101-232, at $z = 0.186$, is currently the farthest known TeV source and was used by the HESS collaboration to set an upper limit to the EBL corresponding to the *HESS 2006* SED shown in Fig. 1. The comparison between a $\Gamma = 1.5$ power-law attenuated by the *HESS 2006* EBL (without cascade, $c_B = 0$) and the data is shown in Fig. 3, reproducing the results of Aharonian et al. (2006). Attenuated spectra taking into account the full cascade emission with $c_B = 1$ (i.e. a null EMF) are also shown for various values of the maximum energy ϵ_M to which the intrinsic power-law extends. Since cascades initiated at higher energies increase the photon populations in lower ones, one might expect the final spectra to appear harder than for pure absorption. However, because IC occurs predominantly on the CMB, the cascade emission accumulates below 100 GeV, softening the spectrum between 100 GeV and 1 TeV. High values of ϵ_M lead to more cascading and more softening. The χ^2 values suggest $\epsilon_\mathrm{M} < 15$ TeV, although further observations, particularly above 1 TeV, would be necessary in order to confirm this. For such low ϵ_M values, not many photons initiate cascades. For higher ϵ_M, the softening is such that a lower EBL would be needed to match the data. Thus the *HESS 2006* upper limit found by Aharonian et al. (2006) holds strong, even in this extreme limit where all the cascade emission is received by the observer.

Inversely, the intrinsic γ-ray spectrum at the source can be obtained given some assumption on the intervening EBL. Using the lower limit on the EBL set by galaxy counts (*Primack 2005* in Fig. 1) gives a limit on how soft the intrinsic spectrum can be. For pure absorption, the best fit has $\Gamma = 1.95 \pm 0.19$ (Fig. 4). As expected, this is softer than the $\Gamma = 1.5$ assumed above, yet still suggests that a good fraction of the γ-ray energy in 1ES 1101-232 is output above a TeV. A hard $\Gamma \leq 2$ intrinsic spectrum is needed if cascade emission is to contribute significantly to the low-energy continuum (Aharonian et al. 2002). 1ES 1101-232 is the first blazar where the intrinsic spectrum is constrained to be hard enough for this, even in the minimal EBL limit.

Including cascade emission in the fit (Fig. 4) hardens even more the intrinsic spectrum as the cutoff ϵ_M increases and cascades contribute more and more to the observed spectrum. For higher ϵ_M, the best fit Γ increases again to mitigate the pronounced softening from the strong cascading but the fit worsens. This also holds for (implausibly) high values of $\epsilon_\mathrm{M} > 100$ TeV, for which cascade emission largely dominates at a few TeV. The hard intrinsic spectra found here, assuming the *Primack 2005* is indeed the minimum possible EBL, suggest either that ϵ_M is not greater than a few TeV, so that there is little cascade emission in the TeV range, or that a large part of the cascade emission is lost due to diffusion on the EMF.

As discussed in Sect. 2, the electron diffusion on the EMF depends on the ratio $R_\mathrm{L}/C_\mathrm{IC}$. The effect on the observed spectra is now taken into account by setting $c_B = 0$ when $R_\mathrm{L}/C_\mathrm{IC} < 300$ (corresponding to a maximum deviation on the line-of-sight of 0.1°–0.2° equal to the best GLAST angular resolution) and $c_B = 1$ otherwise. For example, an EMF of 10^{-6} nG means that emission from electrons of energy $E \lesssim 20$ TeV is suppressed. This will lead to low-energy cutoff in the cascade spectrum as only emission from pairs above a certain energy reaches the observer. The overall spectrum appears as a hump between $\gamma^2 h\nu_\mathrm{CMB}$ (with γ the Lorentz factor of the electrons for which $R_\mathrm{L} = 300 C_\mathrm{IC}$) and 100 GeV (above which absorption dominates). Hence, a non-zero EMF leads to a reduction of the overall cascade emission seen by the observer (compared to Figs. 3–4) but can also lead to a well-defined signature above the continuum.

Figure 5 shows the observed spectra for a *Primack 2005* EBL and for EMF intensities between 10^{-9} and 10^{-6} nG. The intrinsic power-law index was left free but its cutoff ϵ_M was fixed at either 10 TeV or 20 TeV. The best fit index Γ is then found for each value of the EMF. In both cases, the spectra for an EMF $\gtrsim 10^{-6}$ nG are not much different from the pure absorption case as most of the cascade emission is isotropised and lost to the observer. With $\epsilon_\mathrm{M} = 10$ TeV, the best-fit intrinsic slopes are flat in νF_ν and the cascade emission is essentially indistinguishable from the GeV continuum for any value of the EMF. The intrinsic emission is assumed here to be a simple power-law over the whole energy range. More realistic modelling would result in a curved intrinsic Compton component. The cascade emission

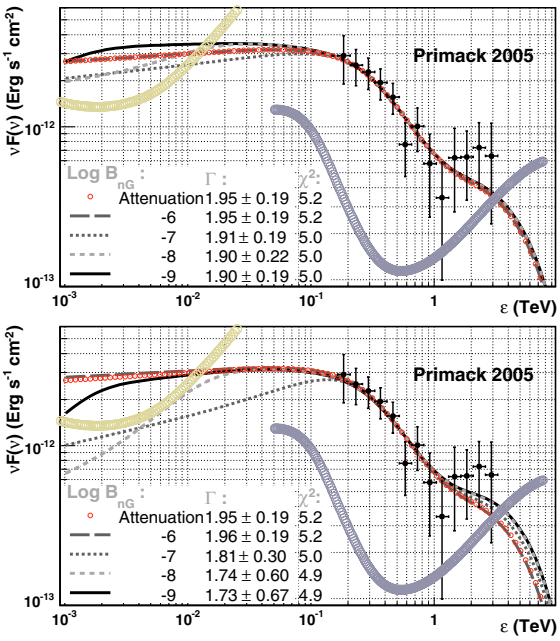

Fig. 5. Observed spectra for the *Primack 2005* EBL and various EMFs between 10^{-9} and 10^{-6} nG. The spectra are adjusted to the HESS points, leaving Γ free but fixing ϵ_M = 10 TeV (*top*) or 20 TeV (*bottom*). For high EMFs the cascade emission does not reach the observer and the spectrum is identical to the pure absorption case. For very low EMFs the results are similar to those shown in Fig. 4. Intermediate values lead to a more or less pronounced bump at 1–100 GeV energies over the intrinsic continuum. Hatches represent projected 5-σ sensibilities for one year of observation with GLAST (≤30 GeV) and 50 h with HESS-2 (≥50 GeV).

might then be more readily identifiable over an intrinsic continuum rising from GeV to TeV energies.

Stronger cascading, as a result of a higher cutoff energy ϵ_M and/or a higher EBL density, makes the hump apparent for the same reason. The intrinsic spectrum is then necessarily much harder, enabling the contribution from the cascade to stand out over the continuum. The bottom panel of Fig. 5 shows that EMF intensities of 10^{-9}–10^{-8} nG can be identified using GLAST and HESS-2 if ϵ_M = 20 TeV. Cascade emission is not diluted for EMF intensities weaker than 10^{-9} nG and there is no spectral feature to measure the EMF. Surprisingly, in most cases 1ES 1101-232 is only slightly above the GLAST one-year detection limit. Unless they become active and flaring, low flux state blazars detected by HESS such as 1ES 1101-232 are likely to be difficult to detect with GLAST, illustrating the advantage provided by the large collecting area of ground-based Cherenkov arrays (but at higher energy thresholds). Similar results are obtained by keeping ϵ_M at 10 TeV but using the stronger *HESS 2006* EBL. However, in this case, the fitted intrinsic slopes are very hard ($\Gamma \approx 1.1$) when the EMF intensities are lower than 10^{-7} nG.

The softest values of Γ, which are the most plausible given the present knowledge on blazars, favour values of the EMF higher than 10^{-6} nG and/or a cutoff energy below 20 TeV. VHE emission from nearby, little-attenuated blazars can be investigated for evidence of cutoffs at energies >20 TeV – although it should be noted that e.g. HESS observations of Mkn 421 (z = 0.03) taken at a high flux actually measure an exponential cutoff at 3 TeV (Aharonian et al. 2005). EMF intensities $\gtrsim 10^{-6}$ nG are consistent with measures inside clusters and superclusters. Such structures may reach 10–50 Mpc in size, which is greater than the attenuation length for γ-rays above 50 TeV. Furthermore, the largest voids, where the EMF is expected to be very small, have a size of 20 h^{-1} Mpc (Patiri et al. 2006), smaller than the distance to 1ES 1101-232. Hence, cascades are likely to be initiated inside walls. As C_{IC} is only of the order of 1 Mpc, such cascades reemit most of their energy within the confines of the clusters, and thus are subject to diffusion. In this case, the cascade emission can only be detected by resolving the faint halo surrounding the γ-ray source.

5. Conclusion

The impact of extragalactic cascade emissions on the GeV–TeV spectrum of 1ES 1101-232 has been investigated and shown to soften the observed spectrum in the TeV range compared to pure absorption. This occurs because most of the cascade emissions occurs at 100 GeV and below. As a result, the upper limits on the EBL determined by HESS are strengthened in the sense that taking cascades into account would lead to harder intrinsic spectra than judged plausible, or to a reduced EBL upper limit. Inversely, using lower limits on the EBL coming from galaxy counts, the intrinsic spectrum of 1ES 1101-232 is found to have $\Gamma \leq 1.95$, with very hard values if there is an important contribution from cascade emission. This is at odds with current theoretical and observational understanding of blazars. A cutoff $\lesssim$10 TeV in the intrinsic spectrum would limit the cascade contribution. This contribution would also be quenched if the EMF intensity is greater than 10^{-6} nG, as expected away from voids. A lower EMF increases the amount of cascade emission reaching the observer in the GeV band, with a signature in the GLAST band for intensities $\sim 10^{-8}$ nG – but at the price of a hard intrinsic spectrum so as to fit the HESS observations.

References

Aharonian, F. A., Coppi, P. S., & Völk, H.J. 1994, ApJ, 423, L5
Aharonian, F. A., Timokhin, A. N., & Plyasheshnikov, A. V. 2002, A&A, 384, 834
Aharonian, F., Akhperjanian, A. G., Aye, K.-M., et al. 2005, A&A, 437, 95
Aharonian, F., Akhperjanian, A. G., Bazer-Bachi, A. R., et al. 2006, Nature, 440, 1018
Biller, S. D. 1995, Astropart. Phys., 3, 385
Cheng, L. X., & Cheng, K. S. 1996, ApJ, 459, L79
Dai, Z. G., Zhang, B., Gou, L. J., Mészáros, P., & Waxman, E. 2002, ApJ, 580, L7
Dole, H., Lagache, G., Puget, J.-L., et al. 2006, A&A, 446
Fan, Y. Z., Dai, Z. G., & Wei, D. M. 2003, A&A, 13
Gould, R. J., & Schréder, G. 1966, Phys. Rev. Lett., 16, 252
Jones, F. C. 1967, Phys. Rev., 167, 1159
Kronberg, P. P. 1994, Reports of Progress in Physics, 57, 325
Lagache, G., Dole, H., & Puget, J.-L. 2003, MNRAS, 338, 555
Neronov, A., & Semikoz, D. V. 2006, ArXiv Astrophysics e-prints
Patiri, S. G., Betancort-Rijo, J. E., Prada, F., Klypin, A., & Gottlöber, S. 2006, MNRAS, 369, 335
Peiris, H. V., Komatsu, E., Verde, L., et al. 2003, ApJS, 148, 213
Plaga, R. 1995, Nature, 374, 430
Primack, J. 2002, in COSPAR, Plenary Meeting
Primack, J. R., Bullock, J. S., Somerville, R. S., & MacMinn, D. 1999, Astropart. Phys., 11, 93
Primack, J. R., Bullock, J. S., & Somerville, R. S. 2005, in High Energy Gamma-Ray Astronomy, ed. F. A. Aharonian, H. J. Völk, & D. Horns, AIP Conf. Proc, 745, 23
Protheroe, R. J. 1986, MNRAS, 221, 769
Protheroe, R. J., & Stanev, T. 1993, MNRAS, 264, 191
Stecker, F. W., de Jager, O. C., & Salamon, M. H. 1992, ApJ, 390, L49
Vallée, J. P. 2004, New A. Rev., 48, 763
Widrow, L. M. 2002, Rev. Mod. Phys., 74, 775
Xu, C., Lonsdale, C. J., Shupe, D. L., O'Linger, J., & Masci, F. 2001, ApJ, 562, 179
Zdziarski, A. A. 1988, ApJ, 335, 786

If it was well known that high-energy γ-rays can be an interesting probe of the contents of the space they travel through, that they can also be a probe of space *itself* is a rather new and at least as interesting development. It appears that some models for quantum gravity predict an energy-dependence on the speed of light through Lorentz invariance violation[Amelino-Camelia et al., 1998], which can be probed when high-energy gamma-rays travel over cosmological distances. This has in turn been searched for by quantifying possible energy-dependent lags in AGN light curves (assuming no intrinsic time-effect cause), which has provided some of the most constraining upper limits to the energy scale at which this happens (for a review see, e.g., Wagner 2009).

Chapter 3

AGN Variability and the blazar PKS 2155-304: "Photons from a hotter hell"

Goodness, Gracious, Great Balls Of Fire!

Jerry Lee Lewis

Abstract

This section is based on what is to date one of the most iconic time series of VHE γ-ray outbursts measured by an ACT. PKS 2155−304 was being monitored routinely when it was noticed to be in an increasingly high flux state which prompted for increased observations on the night following July 25, 2006. When it was established that the source was at a multi-Crab level, the information was released to the community [Benbow, Costamante, & Giebels, 2006]. The subsequent days of observations have provided a remarkable data set, and have been to date the subject of five H.E.S.S. publications. The light curve of the night of July 26, called the "Big Flare" night, showed fluctuations up to 15 times the average flux of the Crab, with one of the fastest variability timescales ever established in the field of VHE γ-rayástronomy. The strong flux observed for multiple days allowed some of the shortest sampling time scales, which in turn allowed to probe for statistical properties hitherto reserved to the field of X-ray astrophysics. Evidence was found that the fluctuations possibly obey an underlying red noise power spectrum, which appears stronger with increasing energy, and a clear flux-r.m.s. correlation suggests that the process at play is a multiplicative phenomenon, given the clear flux-r.m.s. correlation which can be reproduced by a lognormal random process.

3.1 VHE γ-ray variability

One of the basic questions about the mechanism(s) which dissipates energy in an ultrarelativistic jet through γ-ray emission is the origin of the variability. Most of the extreme transient phenomena occuring in AGN are unpredictable, and catching those events with small field-of-view instruments requires some luck as well in the absence of any other indication from other wavelenghts that the source should be observed. That is why ACT observation strategy still involves the monitoring of a set of already detected AGN. Fermi being an almost all-sky instrument does not have such issues, but the very small effective area compared to that of ACTs does not allow to sample timescales $\leq 2-3\,\mathrm{hr}$ even on the brightest AGN (see e.g. the fastest doubling timescales in FSRQs with Fermi, Foschini et al. 2011).

Variability of a light curve is usually first defined as the negative outcome of a constant flux test: a χ^2 fit of a constant to the N data points $\Phi_i = \Phi(t = t_i), i = 1..N$ yields some kind of chisquare variability $P(\chi^2)$ which excludes at a given significance level that the statistical fluctuations are incompatible with that hypothesis. A few estimators exist to characterize the variability, once it is defined as being non-constant (see e.g. Zhang et al. 1999), such as

- the so-called 'doubling time scale' $T_2^{i,j} = |\frac{t_j - t_i}{\Phi_j - \Phi_i}| \frac{\Phi_i + \Phi_j}{2}$, which weighs the observed variability by its amplitude, is probably the most used equivalent of t_{var}. The smallest T_2 is often used as the most constraining "typical timescale" as measured by the experiment and used to derive physical values $t_{var} = T_2 = min(T_2^{i,j})$ (with t_{var} used as in §1.2.4). When some systematics are not fully understood it happens that the average of the N shortest doubling times is used ($N = 5$ in the case of Zhang et al. 1999). Sometimes the above definition of can be replaced by a more conservative variant $t_{var} = |\frac{t_j - t_i}{\ln \Phi_j - \ln \Phi_i}|$ [Burbidge et al., 1974].

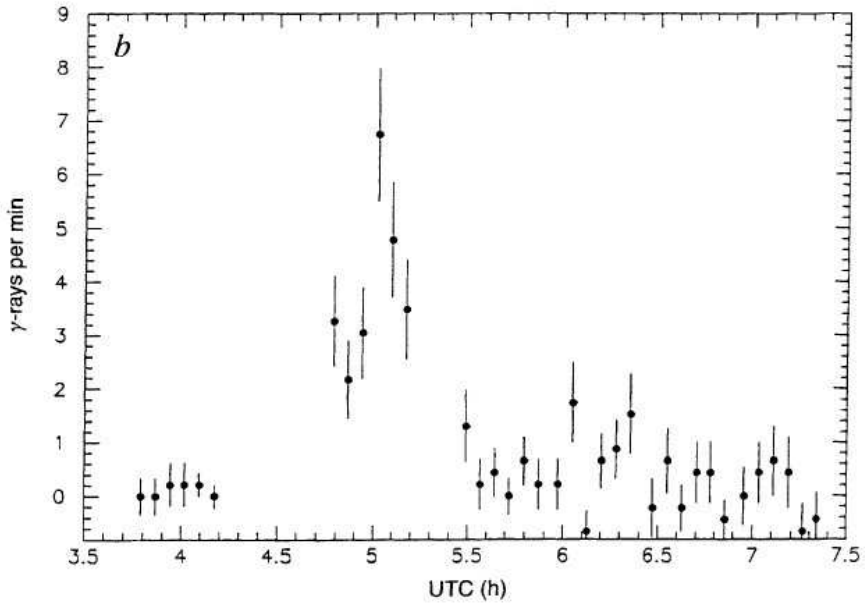

Figure 3.1: *Light curve of a VHE γ-ray flare from Mkn 421 as observed by the Whipple telescope in 1996. The time bins are 5' wide, and the flux can clearly be seen to double within that time during the peak of the emission. (Reproduced from Gaidos et al. 1996)*

- the excess variance σ_V and the excess rms σ_{XS}, defined as $\sigma_V = \sigma_{XS}^2 = \frac{1}{N}\sum_{i=1}^{i=N}[(\phi_i - \Phi)^2 - \sigma_i^2]$ which estimates the rms corrected for the Poisson noise,
- the fractional rms $F_{\rm var}$ defined as the excess rms normalized to the average flux $\bar{\Phi}$ such that $F_{\rm var} = \frac{\sigma_{XS}}{\Phi}$.

Note that σ_{XS} can be negative in the case that the average of the errors is larger than the measurements (in which case the time series will be considered as constant/non-variable in time), which can happen if the sample is small or when the errors on an otherwise non-variable flux are overestimated due to systematic errors. In the case of a constant signal, it can be useful (but is rarely done) that upper limits are set on the variability estimator using e.g. the method from Feldman & Cousins [1998]. This turned out to be very important in the case where two time series are compared and are searched for correlations: if one series shows significant correlation, but not the other, it can still be compatible with a correlation provided that the limit on the variance of the latter is similar or larger to the significant variability of the former (which is the case e.g. in the measurements of the article Aharonian et al. [2009c], further described in §4.6).

An issue here is however that these estimators can strongly depent on the observation length T and the interval Δt over which it is sampled since [van der Klis, 1989]

$$\sigma_V = \int_0^T (\Phi(t) - \overline{\Phi})^2 dt = \int_{1/T}^{1/\Delta t} P(\nu) d\nu$$

, where $P(\nu) = \frac{2T}{\overline{\Phi}^2 N^2}|\hat{F}(\nu)|^2$ is the power spectral density (PSD) normalized to the fractional rms, defined as in Uttley et al. [2002], so only if the bulk of $P(\nu)$ is within the boundaries of the integral do such estimators say something intrinsic about $P(\nu)$.

3.2 The PKS 2155-304 flares

While many of the first-generation ACTs observed high flux states with its associated variability, it was the Whipple observatory who got lucky during observations of one of the known VHE γ-ray emitters in the 1990's, the BL Lac object Mkn 421. The fluctuations seen in the light curve at the instrumental resolution limit (Figure 3.1) were the fastest ever recorded at any wavelength for such objects, and hailed as 'Photons from Hell' by Halzen [1992]. Until the flares observed by H.E.S.S. on PKS 2155−304 were observed these were the strongest constraint on VHE variability since the observed flux doubling timescales of $\leq 15\,\mathrm{min}$ allowed to use the opacity constraint and set a limit on the Doppler factor of $\delta \simeq \Gamma \geq 10$[Celotti et al., 1998].

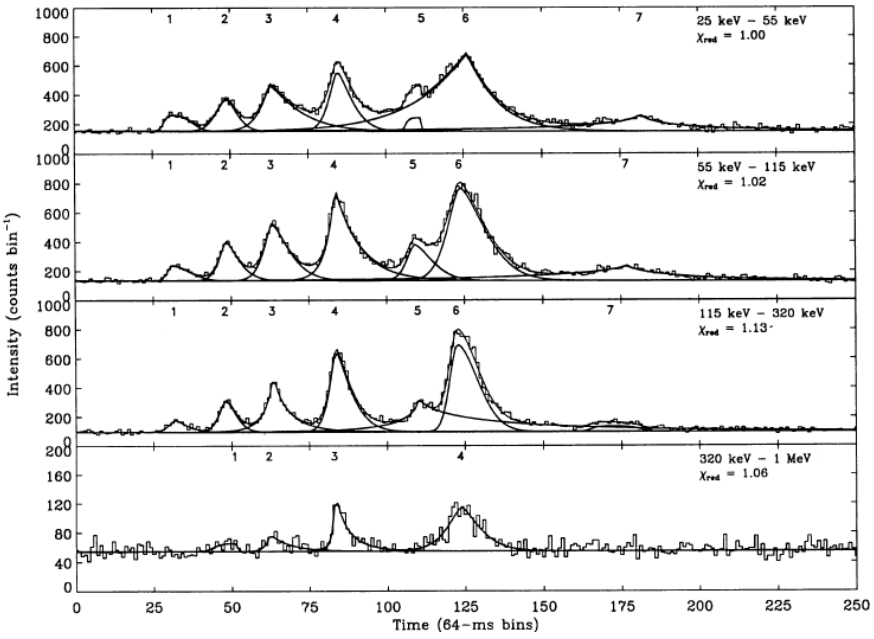

Figure 3.2: *A GRB as seen by BATSE in four different energy channels, which is permitted thanks to the tremendous count rates in this energy band. All the bursts are fitted by a generalized Gaussian shape. (Reproduced from Norris et al. 1996).*

Then on July 2006 there was an indication that the activity of PKS 2155−304 was increasing up to an unseen-before level. It was quickly decided to increase the observation time by a factor of 3 the following night, and one of the most spectacular series of outbursts was caught by H.E.S.S.and the observations were extended over the following nights for which a multi-wavelength campaign was triggered and, exceptionally, even the Chandra X-ray telescope allocated time for this event.

The flux on the night of MJD 53944 was high enough that 1-minute binning was possible throughout, which was still conservative given the multi-Crab flux levels as can be seen in Fig.3.3 for which the analysis details are given in §3.2.3. These results were however similar to those found in using light curves derived with $\Delta t = 20$s. The light curve however showed such substructures, with clear rising and decaying features strongly reminding of similar structures often seen in GRBs, that some shape model could possibly be used in defining them.

3.2.1 Impulsive analysis

Here it is assumed that the fast variability is produced by several individual emission regions, rather than fluctuations in one region, such that the observed γ-ray emission is the superposition of multiple and independent flares. Such features are often seen in the hard X-ray GRBs as seen by e.g. BATSE (Fig. 3.2), where it is often assumed to originate from shocks arising when multiple relativistic shells catch up with each other and collide [Rees & Meszaros, 1994], a physical model which has also been extended to AGN variability by Spada et al. 2001. During intense discussions then the relative merits of different functional forms such as exponential shapes (common in radio observations), Gaussians (which seemed too simple in this case given the sharp turnover features), and even triangles, were compared.

Since the features in the light curve seem well defined, and that the rising and decaying time for each burst appear quantifiable, the bursts were characterized by the slightly complex "generalized Gaussian" shape from Norris et al. [1996], where the total burst intensity is described by

$$I(t) = \sum_{i=1}^{n} A_i e^{-(|t-t_{\mathrm{max,i}}|/\sigma_{\mathrm{r_i,d_i}})^{\kappa,i}} + K$$

where $t_{\mathrm{max,i}}$ is the time of the i^{th} burst maximum intensity A_i; $\sigma_{\mathrm{r,i}}$ and $\sigma_{\mathrm{d,i}}$ are the rise ($t < t_{\mathrm{max,i}}$) and decay ($t > t_{\mathrm{max,i}}$) time constants, respectively; and κ, i is a measure of the i^{th} burst sharpness. The rise and decay times, from half to maximum amplitude, are $\tau_{r,d} = [\ln 2]^{1/\kappa,i}\sigma_{r,d}$. A peak finding tool, using a Markov chain algorithm [Morháč et al., 2000], selected five significant bursts, and these positions were used to initialize the value of t_{max} for each burst but left free in the fit. The

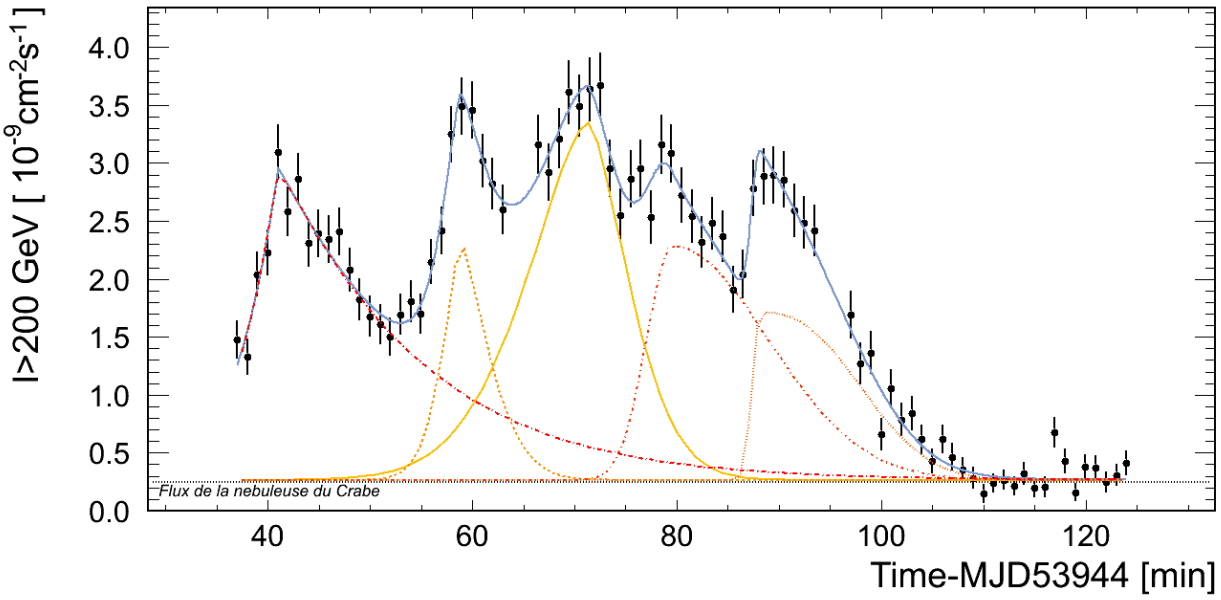

Figure 3.3: *Light curve of PKS 2155−304 during the Big Flare, sampled at* $\Delta t = 60\,\mathrm{s}$*, showing the integral flux above* $200\,\mathrm{GeV}$ *during approximately* $3\,\mathrm{h}$ *of observations of the source. The continuous line is the superposition of five underlying generalized Gaussians which are indicated in dashed lines (not shown in the original article), on top of a continuum at the Crab Nebula flux level. Two interruptions in the series are visible at 58 and 90 minutes, which are due to the dead time in between two runs. The measurement at about 118 minutes, which is about 3 standard deviations from the line, is actually still compatible with a 20% probability fluctuation for the 82 measurements.*

Table 3.1: *The results of the best* χ^2 *fit of the superposition of five bursts and a constant to the data shown in The constant term is* $0.27\pm0.03\times10^{-9}\,\mathrm{cm}^{-2}\,\mathrm{s}^{-1}$ *(1.1* $\mathrm{I}_{\mathrm{Crab}}$*). Note that here the timescales from half to maximum amplitude* τ *are given, related to the actual fitted parameters through* $\tau_{r,d} = (\ln 2)^{1/\kappa}\sigma_{r,d}$*.*

t_{max} [min]	A [$10^{-9}\,\mathrm{cm}^{-2}\,\mathrm{s}^{-1}$]	τ_r [s]	τ_d [s]	κ
41	2.7±0.2	173±28	610±129	1.07±0.20
59	2.1±0.9	116±53	178±146	1.43±0.83
71	3.1±0.3	404±219	269±158	1.59±0.42
80	2.0±0.8	178±55	657±268	2.01±0.87
88	1.5±0.5	67±44	620±75	2.44±0.41

best fit has a χ^2 probability of 20% and the fit parameters are shown in Table 3.1. Interestingly, there is a marginal trend for κ to increase with subsequent bursts, making them less sharp, as the flare progresses. The κ values are close to the bulk of those found by Norris et al. [1996] , but the time scales measured here are two orders of magnitude larger. Given the $\sim(1-2)\times10^9 M_\odot$ central black hole in the AGN of PKS 2155−304, these time scales are much shorter than the inferred dynamical timescale of the compact object $R_S/c = 2GM/c^3 \simeq 10-20\,\mathrm{hr}$ (which is the light crossing time of its horizon, assumed to be the fastest timescale in such a system), while in GRBs the timescales are much longer than the $10^{-3}\,\mathrm{s}$ dynamical timescale of heavy stellar mass objects. This has an important consequence, described in the next paragraph.

3.2.2 Doppler factor estimation

The logic used in §3.2.3 to derive the emitting γ-ray blob in PKS 2155−304 is slightly different from the more traditional opacity treatment. Here, it is assumed that the size R of the dissipative γ-ray emitting region is at least as large as the gravitational radius of the BH, a constraint used and assumed to be rather conservative by [Lyubarsky, 2010], but which can also be derived

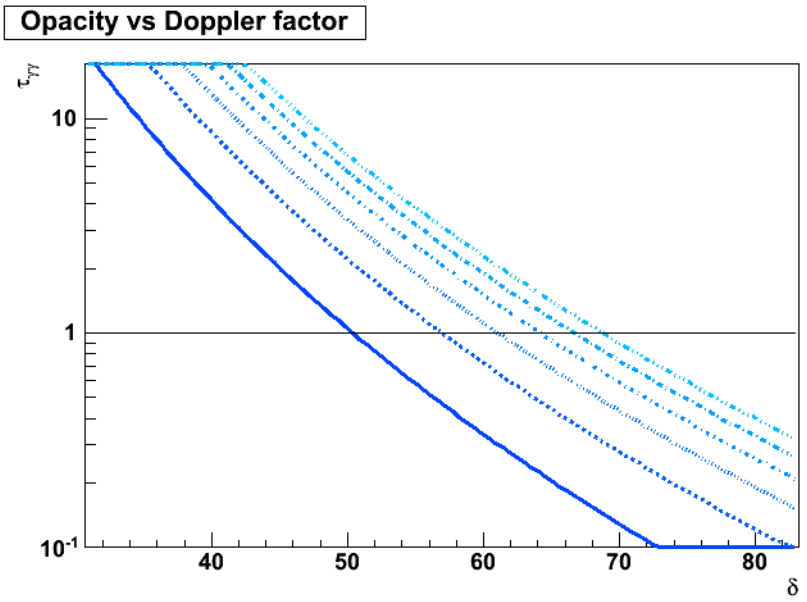

Figure 3.4: *The γ-ray opacity $\tau_{\gamma\gamma}$ derived for $t_{var} = 173$s variability for γ-ray energies of $E_\gamma = 0.5, 1, 1.5, 2, 2.5$ and 3 TeV (left to right, respectively). The comoving target density field was derived from scaling by a factor 10 the synchrotron emission of PKS 2155−304 in its quiescent state (which is consistent with what was measured for this object throughout the optical-to-X-ray spectrum in Aharonian et al. 2009b) and parametrized by a log-parabolic shape.*

from if the dissipative region has at least the size of the smallest radius in a jet (the $r_{0_{\rm min}}$ parameter in Blandford & Payne 1982). Assuming $R \sim R_{\rm S}$, and that $R\frac{1+z}{\delta} \leq ct_{var}$, one finds that the required Doppler factors are $\delta \geq (60-120)R/R_{\rm S}$ in order to match the initial hypothesis. Even larger emission regions would need Doppler factors matching those derived for GRBs, which would be a challenge to understand.

The more "traditional" Doppler factor limit computation, based on Eq. 1.1, uses the variability timescale to estimate the dissipative region size R, and needs the knowledge of the target field density. While Mattox et al. [1993] estimated the flux density at the energy $m_e^2c^4/E_\gamma\delta$ in extrapolating back the observed X-ray spectrum according to a power law, this can also be done in using an analytical form of the complete synchrotron shape. This was done in Fig.3.4 at 5 different γ-ray energies, and using a high-state SED of PKS 2155−304 to estimate the comoving target density. It can be seen that, for $E_\gamma = 500$ GeV photons to significantly escape the lower radiation field, the required Doppler factor is $\delta > 50$, and can be as high as $\delta > 70$ for $E_\gamma = 3$ TeV which is practically the last significant flux estimation in the spectrum of the Big Flare as shown in §3.2.3[1] These Doppler factors are among the highest derived for a blazar, and had important consequences which will be briefly described in §3.3, but it can already be mentioned that, as for a few other rapidly varying blazars for which high values of δ were derived in order for γ-rays to escape, Piner & Edwards [2004] did not find superluminal expansions on sub-parsec scales in VLBA images of the jet of PKS 2155−304, implying again that the dissipative region must be extremely close to the BH.

The bulk Lorentz factors implicated in GRB outflows are also deduced from arguments involving opacity to pair creation for the high energy photons and typically lie in the range $\Gamma \sim 10^2 - 10^3$ for long/soft bursts. A prominent recent example is GRB 080916C observed by Fermi, for which $\Gamma > 600$ has been inferred in this way [Abdo et al., 2009b].

3.2.3 " An Exceptional VHE Gamma-ray Flare from PKS 2155-304"

[1] Given the lenght of an Astrophysical Journal Letter this analysis was not included in the original paper.

The Astrophysical Journal, 664: L71–L74, 2007 August 1

AN EXCEPTIONAL VERY HIGH ENERGY GAMMA-RAY FLARE OF PKS 2155−304

F. Aharonian,[1,2,3] A. G. Akhperjanian,[4] A. R. Bazer-Bachi,[5] B. Behera,[6] M. Beilicke,[7] W. Benbow,[2] D. Berge,[2,8] K. Bernlöhr,[2,9] C. Boisson,[10] O. Bolz,[2] V. Borrel,[5] T. Boutelier,[11] I. Braun,[2] E. Brion,[12] A. M. Brown,[13] R. Bühler,[2] I. Büsching,[14] T. Bulik,[15] S. Carrigan,[2] P. M. Chadwick,[13] A. C. Clapson,[2] L.-M. Chounet,[16] G. Coignet,[17] R. Cornils,[7] L. Costamante,[2,18] B. Degrange,[16] H. J. Dickinson,[13] A. Djannati-Ataï,[19] W. Domainko,[2] L. O'C. Drury,[3] G. Dubus,[16] J. Dyks,[15] K. Egberts,[2] D. Emmanoulopoulos,[6] P. Espigat,[19] C. Farnier,[20] F. Feinstein,[20] A. Fiasson,[20] A. Förster,[2] G. Fontaine,[16] Seb. Funk,[9] S. Funk,[2] M. Füßling,[9] Y. A. Gallant,[20] B. Giebels,[16] J. F. Glicenstein,[12] B. Glück,[21] P. Goret,[12] C. Hadjichristidis,[13] D. Hauser,[2] M. Hauser,[6] G. Heinzelmann,[7] G. Henri,[11] G. Hermann,[2] J. A. Hinton,[2,6,22] A. Hoffmann,[23] W. Hofmann,[2] M. Holleran,[14] S. Hoppe,[2] D. Horns,[23] A. Jacholkowska,[20] O. C. de Jager,[14] E. Kendziorra,[23] M. Kerschhaggl,[9] B. Khélifi,[2,16] Nu. Komin,[20] K. Kosack,[2] G. Lamanna,[17] I. J. Latham,[13] R. Le Gallou,[13] A. Lemière,[19] M. Lemoine-Goumard,[16] J.-P. Lenain,[10] T. Lohse,[9] J. M. Martin,[10] O. Martineau-Huynh,[24] A. Marcowith,[20] C. Masterson,[3] G. Maurin,[19] T. J. L. McComb,[13] R. Moderski,[15] E. Moulin,[12,20] M. de Naurois,[24] D. Nedbal,[25] S. J. Nolan,[13] J-P. Olive,[5] K. J. Orford,[13] J. L. Osborne,[13] M. Ostrowski,[26] M. Panter,[2] G. Pedaletti,[6] G. Pelletier,[11] P.-O. Petrucci,[11] S. Pita,[19] G. Pühlhofer,[6] M. Punch,[19] S. Ranchon,[17] B. C. Raubenheimer,[14] M. Raue,[7] S. M. Rayner,[13] M. Renaud,[2] J. Ripken,[7] L. Rob,[25] L. Rolland,[12] S. Rosier-Lees,[17] G. Rowell,[2,27] B. Rudak,[15] J. Ruppel,[28] V. Sahakian,[4] A. Santangelo,[23] L. Saugé,[11] S. Schlenker,[9] R. Schlickeiser,[28] R. Schröder,[28] U. Schwanke,[9] S. Schwarzburg,[23] S. Schwemmer,[6] A. Shalchi,[28] H. Sol,[10] D. Spangler,[13] Ł. Stawarz,[26] R. Steenkamp,[29] C. Stegmann,[21] G. Superina,[16] P. H. Tam,[6] J.-P. Tavernet,[24] R. Terrier,[19] C. van Eldik,[2] G. Vasileiadis,[20] C. Venter,[14] J. P. Vialle,[17] P. Vincent,[24] M. Vivier,[12] H. J. Völk,[2] F. Volpe,[16] S. J. Wagner,[6] M. Ward,[13] and A. A. Zdziarski[15]

Received 2007 March 16; accepted 2007 June 5; published 2007 July 20

ABSTRACT

The high-frequency peaked BL Lac PKS 2155−304 at redshift $z = 0.116$ is a well-known VHE (>100 GeV) γ-ray emitter. Since 2002 its VHE flux has been monitored using the H.E.S.S. stereoscopic array of imaging atmospheric Cerenkov telescopes in Namibia. During the 2006 July dark period, the average VHE flux was measured to be more than 10 times typical values observed from the object. This article focuses solely on an extreme γ-ray outburst detected in the early hours of 2006 July 28 (MJD 53,944). The average flux observed during this outburst is $I(>200\ \mathrm{GeV}) = (1.72 \pm 0.05_{\mathrm{stat}} \pm 0.34_{\mathrm{syst}}) \times 10^{-9}\ \mathrm{cm}^{-2}\ \mathrm{s}^{-1}$, corresponding to ~7 times the flux, $I(>200\ \mathrm{GeV})$, observed from the Crab Nebula. Peak fluxes are measured with 1 minute timescale resolution at more than twice this average value. Variability is seen up to ~600 s in the Fourier power spectrum, and well-resolved bursts varying on timescales of ~200 s are observed. There are no strong indications for spectral variability within the data. Assuming the emission region has a size comparable to the Schwarzschild radius of a $\sim 10^9 M_\odot$ black hole, Doppler factors greater than 100 are required to accommodate the observed variability timescales.

Subject headings: BL Lacertae objects: individual (PKS 2155−304) — galaxies: active — gamma rays: observations

1. INTRODUCTION

Flux variability studies provide a strong probe into the physical processes of the innermost regions of active galactic nuclei (AGNs). Although the broadband emission from all AGNs is highly variable, the most extreme flux variability, i.e., largest magnitude and shortest timescale, is observed from a class of

[1] Correspondence and request for material should be addressed to Wystan.Benbow@mpi-hd.mpg.de and Berrie.Giebels@poly.in2p3.fr.
[2] Max-Planck-Institut für Kernphysik, Heidelberg, Germany.
[3] Dublin Institute for Advanced Studies, Ireland.
[4] Yerevan Physics Institute, Armenia.
[5] Centre d'Etude Spatiale des Rayonnements, CNRS/UPS, Toulouse, France.
[6] Landessternwarte, Universität Heidelberg, Königstuhl, Germany.
[7] Universität Hamburg, Institut für Experimentalphysik, Germany.
[8] Now at CERN, Geneva, Switzerland.
[9] Institut für Physik, Humboldt-Universität zu Berlin, Germany.
[10] LUTH, UMR 8102 du CNRS, Observatoire de Paris, Section de Meudon, France.
[11] Laboratoire d'Astrophysique de Grenoble, INSU/CNRS, Université Joseph Fourier, Grenoble, France.
[12] DAPNIA/DSM/CEA, CE Saclay, Gif-sur-Yvette, France.
[13] University of Durham, Department of Physics, UK.
[14] Unit for Space Physics, North-West University, Potchefstroom, South Africa.
[15] Nicolaus Copernicus Astronomical Center, Warsaw, Poland.
[16] Laboratoire Leprince-Ringuet, Ecole Polytechnique, CNRS/IN2P3, Palaiseau, France.
[17] Laboratoire d'Annecy-le-Vieux de Physique des Particules, CNRS/IN2P3, Annecy-le-Vieux, France.
[18] European Associated Laboratory for Gamma-Ray Astronomy, jointly supported by CNRS and MPG.
[19] APC, Paris, France.
[20] Laboratoire de Physique Théorique et Astroparticules, CNRS/IN2P3, Université Montpellier II, Montpellier, France.
[21] Universität Erlangen-Nürnberg, Physikalisches Institut, Germany.
[22] Now at University of Leeds, UK.
[23] Institut für Astronomie und Astrophysik, Universität Tübingen, Germany.
[24] LPNHE, IN2P3/CNRS, Universités Paris VI and VII, France.
[25] Institute of Particle and Nuclear Physics, Charles University, Prague, Czech Republic.
[26] Obserwatorium Astronomiczne, Uniwersytet Jagielloński, Kraków, Poland.
[27] Now at University of Adelaide, Australia.
[28] Institut für Theoretische Physik, Lehrstuhl IV: Weltraum und Astrophysik, Ruhr-Universität Bochum, Germany.
[29] University of Namibia, Windhoek, Namibia.

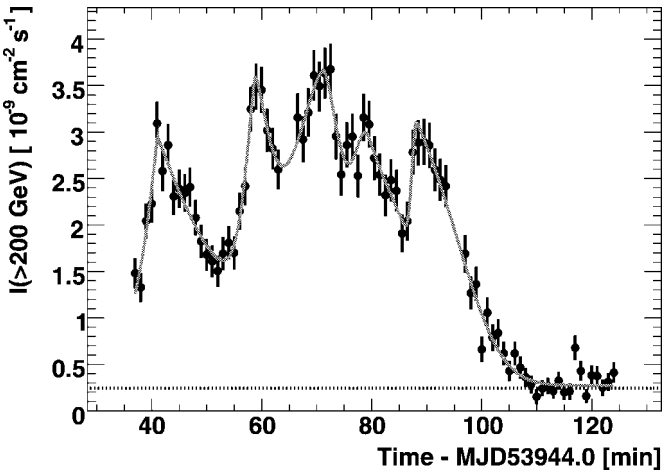

FIG. 1.—Integral flux above 200 GeV observed from PKS 2155−304 on MJD 53,944 vs. time. The data are binned in 1 minute intervals. The horizontal line represents I(>200 GeV) observed (Aharonian et al. 2006) from the Crab Nebula. The curve is the fit to these data of the superposition of five bursts (see text) and a constant flux.

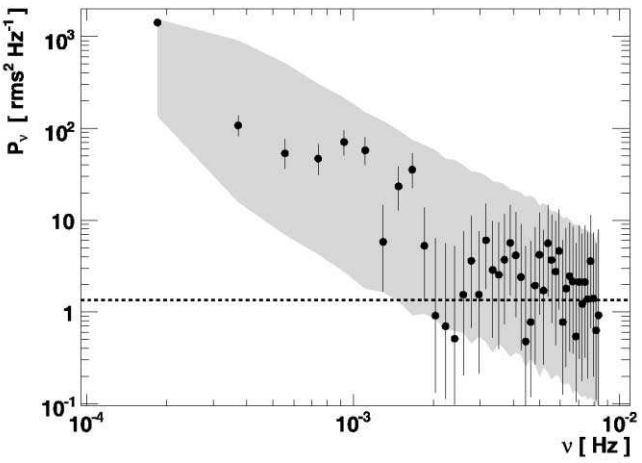

FIG. 2.—Fourier power spectrum of the light curve and associated measurement error. The gray shaded area corresponds to the 90% confidence interval for a light curve with a power-law Fourier spectrum $P_\nu \propto \nu^{-2}$. The horizontal line is the average noise level (see text).

AGNs known as blazars. As a result, blazar variability studies are crucial to unraveling the mysteries of AGNs. Over a dozen blazars have been detected so far at very high energies (VHEs). In the southern hemisphere, PKS 2155−304 is generally the brightest blazar at these energies and is probably the best studied at all wavelengths. The VHE flux observed (Aharonian et al. 2005a) from PKS 2155−304 is typically of the order ~15% of the Crab Nebula flux above 200 GeV. The highest flux previously measured in one night is approximately 4 times this value, and clear VHE-flux variability has been observed on daily timescales. The most rapid flux variability measured for this source is 25 minutes (Aharonian et al. 2005b) occurring at X-ray energies. The fastest variation published from any blazar, at any wavelength, is an event lasting ~800 s, where the X-ray flux from Mrk 501 varied by 30% (Xue & Cui 2005),[30] while at VHEs doubling timescales as fast as ~15 minutes have been observed from Mrk 421 (Gaidos et al. 1996).

The High Energy Stereoscopic System (H.E.S.S.; Hinton 2004) is used to study VHE γ-ray emission from a wide variety of astrophysical objects. As part of the normal H.E.S.S. observation program, the flux from known VHE AGNs is monitored regularly to search for bright flares. During such flares, the unprecedented sensitivity of H.E.S.S. (5 standard deviation, σ, detection in ~30 s for a Crab Nebula flux source at 20° zenith angle) enables studies of VHE flux variability on timescales of a few tens of seconds. During the 2006 July dark period, the average VHE flux observed by H.E.S.S. from PKS 2155−304 was more than 10 times its typical value. In particular, an extremely bright flare of PKS 2155−304 was observed in the early hours of 2006 July 28 (MJD 53,944). This article focuses solely on this particular flare. The results from other H.E.S.S. observations of PKS 2155−304 from 2004 through 2006 will be published elsewhere.

2. RESULTS FROM MJD 53,944

A total of three observation runs (~28 minutes each) were taken on PKS 2155−304 in the early hours[31] of MJD 53,944. These data entirely pass the standard H.E.S.S. data-quality selection criteria, yielding an exposure of 1.32 hr live time at a mean zenith angle of 13°. The standard H.E.S.S. calibration (Aharonian et al. 2004) and analysis tools (Benbow 2005) are used to extract the results shown here. As the observed signal is exceptionally strong, the event-selection criteria (Benbow 2005) are performed using the "loose cuts," instead of the "standard cuts," yielding an average postanalysis energy threshold of 170 GeV. The loose cuts are selected since they have a lower energy threshold and higher γ-ray and background acceptance. The higher acceptances avoid low-statistics issues by estimating the background and significance on short timescales, thus simplifying the analysis. The on-source data are taken from a circular region of radius $\theta_{\rm cut} = 0.2°$ centered on PKS 2155−304, and the background (off-source data) is estimated using the "Reflected-Region" method (Berge et al. 2007).

A total of 12,480 on-source events and 3296 off-source events are measured with an on-off normalization of 0.215. The observed excess is 11,771 events (~2.5 Hz), corresponding to a significance of 168 σ calculated following the method of equation (17) in Li & Ma (1983). It should be noted that use of the standard cuts also yields a strong excess (6040 events, 159 σ) and results (i.e., flux, spectrum, variability) consistent with those detailed later.

2.1. *Flux Variability*

The average integral flux above 200 GeV observed from PKS 2155−304 is $I(>200\ \text{GeV}) = (1.72 \pm 0.05_{\rm stat} \pm 0.34_{\rm syst}) \times 10^{-9}\ \text{cm}^{-2}\ \text{s}^{-1}$, equivalent to ~7 times the I(>200 GeV) observed from the Crab Nebula ($I_{\rm Crab}$; Aharonian et al. 2006). Figure 1 shows I(>200 GeV), binned in 1 minute intervals, versus time. The fluxes in this light curve range from $0.65 I_{\rm Crab}$ to $15.1 I_{\rm Crab}$, and their fractional rms variability amplitude (Vaughan et al. 2003) is $F_{\rm var} = 0.58 \pm 0.03$. This is ~2 times higher than archival X-ray variability (Zhang et al. 1999, 2005). The Fourier power spectrum calculated from Figure 1 is shown in Figure 2. The error on the power spectrum is the 90% confidence interval estimated from 10^4 simulated light curves. These curves are generated by adding a random constant to each individual flux point, where this constant is taken randomly from a Gaussian distribution with a dispersion equal to the error of the respective point. The average power expected when the measurement error dominates is shown as a dashed line (see the Appendix in

[30] Xue & Cui (2005) also demonstrate that a 60% X-ray flux increase in ~200 s observed (Catanese & Sambruna 2000) from Mrk 501 is likely an artifact.

[31] The three runs began at 00:35, 01:06, and 01:36 UTC, respectively.

Vaughan et al. 2003). There is power significantly above the measurement noise level up to 1.6×10^{-3} Hz (600 s). The power spectrum also shows that most of the power is at low frequencies. The gray shaded area shows the 90% confidence level obtained by simulating 10^4 light curves with a power-law Fourier spectrum $P_\nu \propto \nu^{-2}$ (Timmer & Koenig 1995) and a random Gaussian error as above. The power spectrum derived from the data is thus compatible with a light curve generated by a stochastic process with a power-law Fourier spectrum of index -2. An index of -1 produces too much power at high frequencies and is rejected. These power spectra are remarkably similar to those derived in X-rays (Zhang et al. 1999) from the same source.

Rapid variability is clearly visible in substructures that appear in the light curve, with even shorter rise and decay timescales than those found in the Fourier analysis. In order to quantify those timescales, the light curve is considered to be consisting of a series of bursts, which is common for AGNs and γ-ray bursts (GRBs). The "generalized Gaussian" shape from Norris et al. (1996) is used to characterize these bursts, where the burst intensity is described by $I(t) = A \exp\left[-(|t - t_{\max}|/\sigma_{r,d})^{\kappa}\right]$, where $t_{\max}$ is the time of the burst's maximum intensity (A); σ_r and σ_d are the rise ($t < t_{\max}$) and decay ($t > t_{\max}$) time constants, respectively; and κ is a measure of the burst's sharpness. The rise and decay times, from half to maximum amplitude, are $\tau_{r,d} = (\ln 2)^{1/\kappa}\, \sigma_{r,d}$. A peak finding tool, using a Markov chain algorithm (Morhac et al. 2000), selected five significant bursts. A function consisting of a superposition of an identical number of bursts plus a constant signal was fit[32] to the data. The best fit has a χ^2 probability of 20%, and the fit parameters are shown in Table 1. Interestingly, there is a marginal trend for κ to increase with subsequent bursts, making them less sharp, as the flare progresses. The κ values are close to the bulk of those found by Norris et al. (1996), but the timescales measured here are 2 orders of magnitude larger.

During both the first two bursts, there is clear doubling of the flux within τ_r. Such doubling is sometimes used as a characteristic timescale of flux variability. For compatibility with such estimators, the definition of doubling time, $T_2 = |I_{ij}\Delta T/\Delta I|$, from Zhang et al. (1999) was used.[33] Here $\Delta T = T_j - T_i$, $\Delta I = I_j - I_i$, $I_{ij} = (I_j + I_i)/2$, with T and I being the time and flux, respectively, of any pair of points in the light curve. The fastest $T_2 = 224 \pm 60$ s is compatible with the fastest significant timescale found by the Fourier transform. Averaging the five lowest T_2 values yields 330 ± 40 s.

The variability timescales of these bursts are among (see also Albert et al. 2007) the fastest ever seen in a blazar, at any wavelength, and are almost an order of magnitude smaller than those previously observed from this object. It should be noted that similar timescales are found with even smaller binning (e.g., 20 s) of the H.E.S.S. light curve and that many checks of the data quality were undertaken to ensure that the flux variations cannot be the result of background fluctuations, atmospheric events, etc. In addition, all the results have been verified using an independent calibration method and alternative analysis techniques.

2.2. *Spectral Analysis*

Figure 3 shows the time-averaged photon spectrum for these data. The data are well fit, $\chi^2 = 17.1$ for 13 degrees of freedom (dof), by a broken power-law function:

$$E < E_B: \frac{dN}{dE} = I_0 \left(\frac{E}{1\ \mathrm{TeV}}\right)^{-\Gamma_1},$$

$$E > E_B: \frac{dN}{dE} = I_0 \left(\frac{E_B}{1\ \mathrm{TeV}}\right)^{(\Gamma_2-\Gamma_1)} \left(\frac{E}{1\ \mathrm{TeV}}\right)^{-\Gamma_2},$$

where $I_0 = (2.06 \pm 0.16 \pm 0.41) \times 10^{-10}$ cm^{-2} s^{-1} TeV^{-1}, $E = 430 \pm 22 \pm 80$ GeV, $\Gamma_1 = 2.71 \pm 0.06 \pm 0.10$, and $\Gamma_2 = 3.53 \pm 0.05 \pm 0.10$. For each parameter, the two uncertainties are the statistical and systematic values, respectively. Fits to the data of either a simple power law ($\Gamma = 3.19 \pm 0.02 \pm 0.10$, $\chi^2 = 138$, 15 dof) or a power law with an exponential cutoff ($\chi^2 = 45$, 14 dof) are not acceptable. The time-averaged spectrum ($\Gamma = 3.32$) of PKS 2155−304 measured in 2003 (Aharonian et al. 2005a) multiplied by the ratio (48.7) of I(>200 GeV) from the respective data sets, is also shown in Figure 3. Despite a factor of ~50 change in flux, there is qualitatively little difference between the two spectra. Indeed, fitting a broken power law to the current data set, keeping Γ_1 and Γ_2 fixed to the values measured in 2003, yields a value for E_B consistent with that measured in 2003. The small difference is surprising since a change of the spectral shape with varying flux levels, typically hardening with increased flux, has often been observed from blazars at X-ray energies (see, e.g., Giommi et al. 1990), as well as in the VHE domain (see, e.g., Aharonian et al. 2002).

[32] The Markov chain burst positions were used to initialize $t_{\max}$ for each burst. All parameters are left free in the fit.

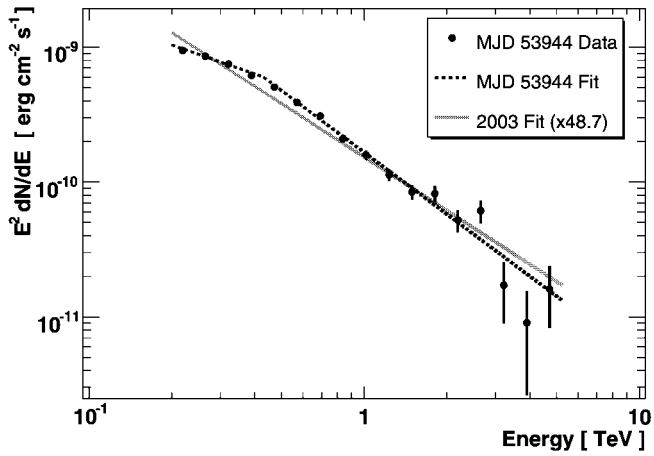

FIG. 3.—Time-averaged spectrum observed from PKS 2155−304 on MJD 53,944. The dashed line is the best χ^2 fit of a broken power law to the data. The solid line represents the fit to the time-averaged spectrum of PKS 2155−304 from 2003 (Aharonian et al. 2005a) scaled by 48.7. Neither spectrum is corrected (see, e.g., Aharonian et al. 2005b) for the absorption of VHE γ-rays on the extragalactic background light.

[33] Only values of T_2 with less than 30% uncertainty are considered.

TABLE 1

RESULTS OF THE BEST χ^2 FIT OF THE SUPERPOSITION OF FIVE BURSTS AND A CONSTANT TO THE DATA SHOWN IN FIGURE 1

$t_{\max}$ (minutes)	A (10^{-9} cm^{-2} s^{-1})	τ_r (s)	τ_d (s)	κ
41.0	2.7 ± 0.2	173 ± 28	610 ± 129	1.07 ± 0.20
58.8	2.1 ± 0.9	116 ± 53	178 ± 146	1.43 ± 0.83
71.3	3.1 ± 0.3	404 ± 219	269 ± 158	1.59 ± 0.42
79.5	2.0 ± 0.8	178 ± 55	657 ± 268	2.01 ± 0.87
88.3	1.5 ± 0.5	67 ± 44	620 ± 75	2.44 ± 0.41

NOTE.—The constant term is $(0.27 \pm 0.03) \times 10^{-9}$ cm^{-2} s^{-1} ($1.1 I_{\mathrm{Crab}}$).

The high flux observed from PKS 2155−304 allows the determination of accurate photon spectra on timescales of the order of minutes. Therefore, a simple search for temporal changes of the VHE spectral shape within these data was performed. Spectra were determined for consecutive data slices of 28 minutes (1 run), 10 minutes, and 5 minutes. Fitting the time-average spectral shape, allowing only the normalization (I_0) to vary, to these short-timescale spectra yields reasonable χ^2 probabilities. Thus, there are no strong indications of fast spectral variability. However, weak variations ($\Delta\Gamma < 0.2$) are not ruled out. A more sophisticated study of any fast spectral variations within these data is beyond the scope of this Letter and will be published elsewhere.

3. DISCUSSION

It is very likely that the electromagnetic emission in blazars is generated in jets that are beamed and Doppler-boosted toward the observer. Superluminal expansions observed with VLBI (Piner & Edwards 2004) provide evidence for moderate Doppler boosting in PKS 2155−304. Causality implies that γ-ray variability on a timescale $t_{\rm var}$, with a Doppler factor[34] (δ), is related to the radius (R) of the emission zone by $R \leq ct_{\rm var}\delta/(1+z)$. Conservatively using the best-determined rise time (i.e., τ_r with the smallest error) from Table 1 for $t_{\rm var} = 173 \pm 28$ s (note that this is similar to the fastest T_2) limits the size of the emission region to $R\delta^{-1} \leq 4.65 \times 10^{12}$ cm ≤ 0.31 AU.

The jets of blazars are believed to be powered by accretion onto a supermassive black hole (SMBH). Thus, accretion/ejection properties are usually presumed to scale with the Schwarzschild radius $R_{\rm S}$ of the SMBH, where $R_{\rm S} = 2GM/c^2$, which is the smallest, most-natural size of the system (see, e.g., Blandford & Payne 1982). Expressing the size R of the γ-ray–emitting region in terms of $R_{\rm S}$, the variability timescale limits its mass by $M \leq [c^3 t_{\rm var}\delta/2G(1+z)]\, R_{\rm S}/R \sim 1.6 \times 10^7\, M_\odot \delta R_{\rm S}/R$. The reported[35] host galaxy luminosity $M_R = -24.4$ (Kotilainen et al. 1998, Table 3) would imply a SMBH mass of order $(1–2) \times 10^9\, M_\odot$ (Bettoni et al. 2003) and therefore $\delta \geq (60–120)\, R/R_{\rm S}$. Emission regions of only a few $R_{\rm S}$ would require values of δ much greater than those typically derived for blazars ($\delta \sim 10$) and come close to those used for GRBs, which would be a challenge to understand. For example, the subparsec VHE γ-ray–emitting plasma would have to decelerate with a high efficiency to accommodate relatively small Lorentz factors observed at parsec scales (Piner & Edwards 2004). It is possible, however, that the SMBH mass is overestimated, reducing the δ constraint by the same factor, or that the variability has an origin (e.g., a geometric effect from jet bending as discussed in Wagner et al. 1993) unrelated to the black hole. Detailed modeling of the spectral energy distribution of PKS 2155−304, during the multiple VHE flares observed by H.E.S.S. in the 2006 July dark period, including simultaneous multifrequency data, will appear elsewhere.

The VHE variability observed in this particular flaring episode is the fastest ever observed from a blazar. While the variability is a factor of 5 times faster than that previously measured from Mrk 421 (Gaidos et al. 1996) in terms of the light-crossing time of the Schwarzschild radius, $R_{\rm S}/c$, the variability of PKS 2155−304 is another factor of ≈6–12 more constraining assuming a $10^{8.22}\, M_\odot$ for Mrk 421 (Woo et al. 2005). It should also be noted that the choice of a ∼3 minute variability timescale here is conservative and that the light curve is strongly oversampled, allowing for the first time in the VHE regime a detailed statistical analysis of a flare, which shows remarkable similarity to other longer duration events at X-ray energies. From such rapid variability one must conclude that either very large Doppler factors can be present in AGN jets, or that the observed variability is not connected to the central black hole, clearly showing the power of Cerenkov-telescope arrays in probing the internal mechanisms in BL Lac objects.

The support of the Namibian authorities and of the University of Namibia in facilitating the construction and operation of H.E.S.S. is gratefully acknowledged, as is the support by the German Ministry for Education and Research (BMBF), the Max Planck Society, the French Ministry for Research, the CNRS-IN2P3, and the Astroparticle Interdisciplinary Programme of the CNRS, the UK Particle Physics and Astronomy Research Council (PPARC), the IPNP of the Charles University, the Polish Ministry of Science and Higher Education, the South African Department of Science and Technology and National Research Foundation, and by the University of Namibia. We appreciate the excellent work of the technical support staff in Berlin, Durham, Hamburg, Heidelberg, Palaiseau, Paris, Saclay, and in Namibia in the construction and operation of the equipment.

[34] With δ defined in the standard way as $[\Gamma(1-\beta\cos\theta)]^{-1}$, where Γ is the bulk Lorentz factor of the plasma in the jet, $\beta = v/c$, and θ is the angle to the line of sight.

[35] See Wurtz et al. (1996) and $M_R > -23.1$ (for $h = 0.5$) showing the need for confirmation of this value.

REFERENCES

Aharonian, F., et al. 2002, A&A, 393, 89
———. 2004, Astropart. Phys., 22, 109
———. 2005a, A&A, 430, 865
———. 2005b, A&A, 442, 895
———. 2006, A&A, 457, 899
Albert, J., et al. 2007, ApJ, in press (astro-ph/0702008)
Benbow, W. 2005, in Towards a Network of Atmospheric Cherenkov Detectors VII, ed. B. Degrange & G. Fontaine (Palaiseau: Ecole Polytechnique), 163
Berge, D., Funk, S., & Hinton, J. 2007, A&A, 466, 1219
Bettoni, D., Falomo, R., Fasano, G., & Govoni, F. 2003, A&A, 399, 869
Blandford, R. D., & Payne, D. G. 1982, MNRAS, 199, 883
Catanese, M., & Sambruna, R. M. 2000, ApJ, 534, L39
Gaidos, J. A., et al. 1996, Nature, 383, 319
Giommi, P., et al. 1990, ApJ, 356, 432
Hinton, J. 2004, NewA Rev., 48, 331
Kotilainen, J. K., Falomo, R., & Scarpa, R. 1998, A&A, 336, 479
Li, T., & Ma, Y. 1983, ApJ, 272, 317
Morhac, M., et al. 2000, Nucl. Instrum. and Methods Phys. Res. A, 443, 108
Norris, J. P., et al. 1996, ApJ, 459, 393
Piner, B. G., & Edwards, P. G. 2004, ApJ, 600, 115
Timmer, J., & Koenig, M. 1995, A&A, 300, 707
Vaughan, S., Edelson, R., Warwick, R. S., & Uttley, P. 2003, MNRAS, 345, 1271
Wagner, S. J., et al. 1993, A&A, 271, 344
Woo, J.-H., et al. 2005, ApJ, 631, 762
Wurtz, R., Stocke, J. T., & Yee, H. K. C. 1996, ApJS, 103, 109
Xue, Y., & Cui, W. 2005, ApJ, 622, 160
Zhang, Y. H., et al. 1999, ApJ, 527, 719
———. 2005, ApJ, 629, 686

3.3 Data interpretation developments since publication

The observations of these flares were hailed - by Trevor Weekes this time - as "Photons from a Hotter Hell" [Weekes, 2007], and not to be outdone, it is probably an honour that Begelman et al. [2008] get the most citations when the high Doppler/Lorentz factor needed for these flares is mentioned in articles elsewhere. Their interpretation of the overall energetics leads them also to conclude that the γ-rays must originate from comptonization of an external field, since the Compton component clearly dominates the overall SED. The dazzling flares have triggered a great interest of the AGN community, and some new theoretical developments and phenomenological considerations have stemmed from them.

Using constraints from both a 1-zone SSC model fit and EBL attenuation, Finke et al. [2008] infer even larger values of $\delta = 80-170$ (see Kusunose & Takahara 2008 for equally high values) with unreasonable cooling time scales to match the variability, and conclude that, while other so-called "TeV blazars" such as Mkn 421 and Mkn 501 can usually be adequately fit by such models, it is not the case of PKS 2155−304 so they also indicate that more research needs to be done into adding external Compton components when modeling this kind of extreme events. Departing from 1-zone models, Giannios et al. [2009] derived their "mini-jets" model on small regions nested in the jet and powered by the reduction of the magnetic field through magnetic reconnections, quite similar to Ghisellini & Tavecchio [2008] who assume that the radiation could possibly come from small and fast $\delta > 50$ regions (called "needles") in a slower jet, and hence warn that this could bias the interpretation of the global jet, since such fast and bright events should not be used to derive general properties of the bulk jet motion. Boutelier et al. [2008]. Inhomogenous time-dependent models however seem to find a way out of the Doppler conundrum, perhaps at the price of a high complexity. Bulk Lorentz factors of $\Gamma \leq 15$ are sufficient in the stratified model of Boutelier et al. [2008] to reproduce both the spectral features and the fast variability, while also featuring other interesting properties such as the very low degree of correlation between optical and VHE fluxes (unlike most 1-zone models) or the strong correlation between the jet base radius and bulk jet speed which allows a comparison of the central BH mass.

On the other hand, Katarzyński et al. [2008] also successfully fit each of the flares with moderate $\delta \leq 30$ regions, but using longer timescales. A similar multi-zone model but with different emission properties (taking into account e.g. light-crossing time effects) by Graff et al. [2008] inferred $\delta = 20-40$. The properties of the Big Flare will probably remain of interest for still some time.. until a brighter and faster flare comes along! A question which hence naturally arises about such an intense flaring episode is whether it arises from a statistical fluctuation in an otherwise featureless noise-like power-law continuum, or if a different physical phenomenon comes into play.

3.3.1 Power Spectrum of PKS 2155−304

Perhaps one of the most interesting developments of densely sampled quasi-continuous light curves in the VHE domain is that it opens the possibility to actually probe the properties of the variablity itself at different frequencies ν in the time domain, i.e. to ask the question where most of the variability occurs, in establishing its power spectrum density $P(\nu)$. This has been frequently done in the X-ray domain, and precisely on PKS 2155−304 by Zhang et al. [1999] using BeppoSAX observations with a resolution of $\Delta t = 10$s and $2-3$d exposures which satellites allow. It is apparent in Fig. 3.5) that the Fourier power behaves as a power law $P(\nu) \propto \nu^{-\alpha}$, and since in this case the frequency leakage and aliasing (due to the finite observation time and windowing effects, see e.g. Deeming 1975; van der Klis 1989) are small enough, the α parameter can be in good approximation be directly estimated from a fit to the central points of the PSD, which would not be justified for irregularly sampled time series [Deeter, 1984] which are particularly affected by windowing effects which plague ACT-derived light curves at different levels. The power law behaviour of the PSD from Figure 3.5 indicates that the amplitude of the variability decreases when the variability timescale decreases.

Establishing constraints on α from multiple-night observations has hence to be done in a

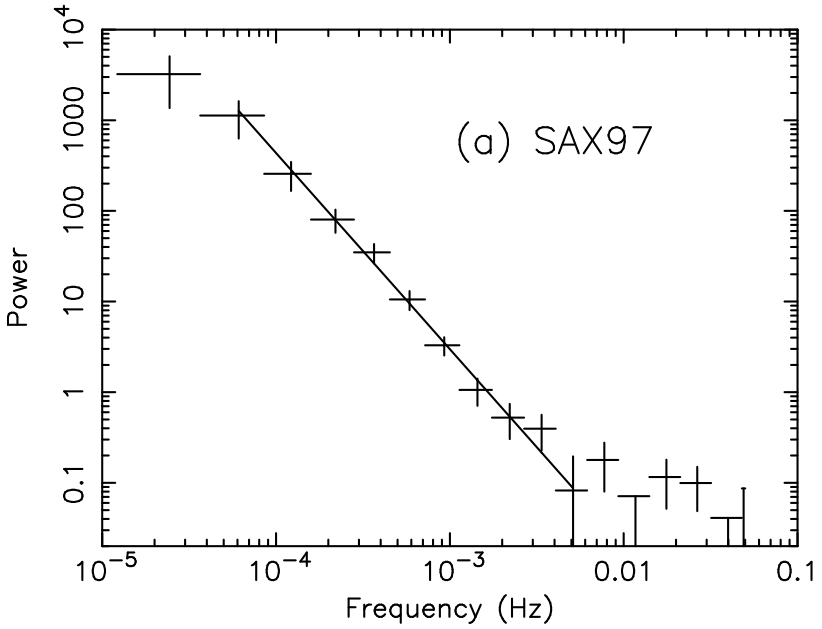

Figure 3.5: *The power spectrum of PKS 2155−304 derived by Zhang et al. [1999] using X-ray data, in the frequency domain* $10^{-2} - 10^{-4}$ Hz *similar to the VHE* γ*-ray PSD for the same object by H.E.S.S. (see Fig. 2 in §3.2.3).*

different way. Assuming that the observations are realizations of a red noise process, one can simulate time series generated by Fourier series using the prescription from Timmer & Koenig [1995] for inverting a Fourier spectrum and generate a time series. Many simulated light curves are then segmented into active periods and gaps of same durations as the experimental ones in order to account for windowing effects, and experimental errors are added to match the observations. This finally allows to compare properties of the measured light curve, as derived with techniques used to derive intrinsic properties, with the simulated ones. Note how this procedure is in some sense close to the energy spectrum forward folding method, where the observed spectrum is compared with a simulated intrinsic spectrum distorted by instrument response functions.

One such technique to establish the Fourier spectral index is the first order Kolmogorov structure function (SF) [Lindsey & Chie, 1976; Simonetti et al., 1985] $S(\tau)$ defined as $S(\tau) = \overline{\big(\Phi(t) - \Phi(t+\tau)\big)^2}$, where τ is a delay separating two measurements, and for which the mean difference in flux is calculated. The SF is particularly useful for non-periodic data analyses as it provides information similar to a PSD while being easy to compute. Also in the absence of windowing and other distorsions, $SF(\tau) \propto \tau^{1-\alpha}$ such that the slope of the SF in logarithmic representation provides the index of the underlying Fourier power law. Significant departures from the power law in the SF are used (just like features in a PSD) as an indication of a characteristic timescale in the light curve. Great care must be taken in the interpretation of such features though when the light curve has discontinuities, even at the smallest scales, since they can artificially induce such peaks and gaps as are visible in Fig. 13 of §3.4. Once the observation conditions are carefully taken into account and injected into multiple red noise simulations, one can derive the confidence countours for a specific index of α (shaded areas in Fig. 13 of §3.4 but also Fig. 2 in §3.2.3): the fitted slope of the SF (or even of the Fourier transform) can be significantly different from the underlying one! §3.4 describes how for the first time such methods are applied to a discontinuous VHE γ-ray light curve, through the use of a likelihood function of α (see Degrange, Superina, Giebels, & Volpe 2008 for more details) based on the structure function. The result was that the light curve of the 4 high flux nights including the "Big Flare" could be consistently described by a random process whose PSD is characterized by $\alpha = 2.06 \pm 0.21$.

A similar likelihood function of α can also be built on the PSD of the data set and the simulated light curves. In this case, the simulated light curves are subjected to the experimental conditions (run stops, daylight gaps, statistical errors) and their PSDs are normalized to a probability density per frequency interval $\Psi(\nu)$. The likelihood $\mathcal{L}(\Psi) = \Pi_i \mathcal{P}(P(\nu_i)|\Psi)$ is computed for all values of α and $\log\mathcal{L}$ is maximized as usual (Fig. 3.6). A χ^2 minimization was also attempted

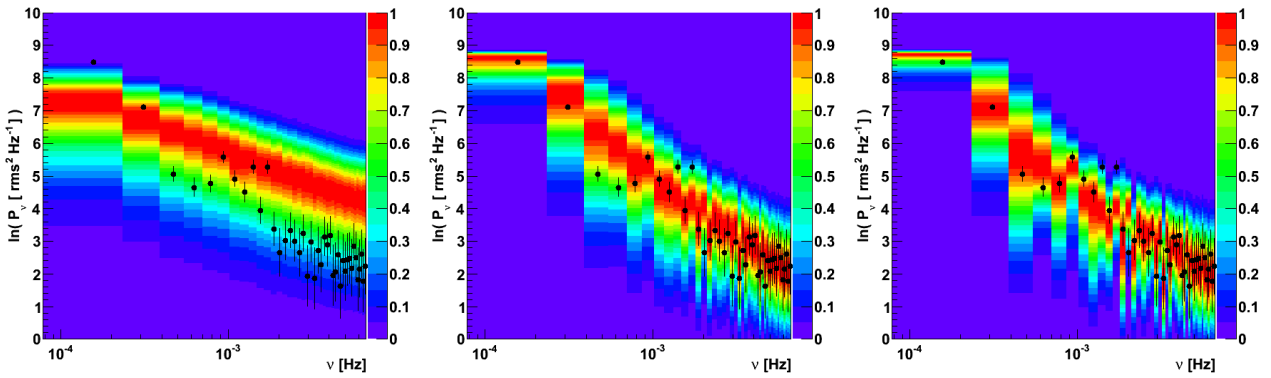

Figure 3.6: *Results of the application of the likelihood method to the light curve of the "Big Flare". The PSD of the observed data are the filled circles, where the errors are statistical only. The intensity levels reflect the probability density derived from* 10^4 *simulations of red noise light curves* $P(\nu) \propto \nu^{-\alpha}$ *and distorted by experimental effects. The likelihood is calculated for stepped values of* $3.5 < \alpha < 1.5$ *left:* $\alpha = 1.5$*, middle:*$\alpha = 2.5$*, right:*$\alpha = 3.5$*. The optimal value was found to be* $\alpha = 2.32 \pm 0.12$*, compatible with those found in the articles of §3.2.3 and §3.4.*

to derive an estimator of α but this introduced complicated biases which the likelihood method does not show.

Having established that the PSD has a power law slope, it raises the issue that dynamical (or thermal) timescales, or generally speaking any particular timescale at all, should be impossible to identify. Also the above-defined doubling timescale T_2 should be mostly meaningless when variability is identified as being scale invariant, as it can take any value [McHardy & Czerny, 1987] the instrumental sensitivity can provide.

3.3.2 Energy and Flux dependent variability

Energy dependent variability

The number of γ-ray counts during the high state was high enough that the time series could be separated into 3-4 energy channels (Fig. 9 in §3.4). The estimation of $F_{\rm var}$ for each channel resulted in an energy dependent variability $F_{\rm var}(E) \propto E^{0.19}$ indicating that higher energies have larger amplitudes as well. Only the VHE γ-ray source Mkn 501 has historically been in sufficiently high flux states that an energy dependence could be searched for. Albert et al. [2007] also showed an increase in $F_{\rm var}$ in such flares, sampled at slightly larger timescales than those mentioned here. The energy dependence is remarkably similar to that reported in X-rays for Mkn 421 [Giebels et al., 2007] and for PKS 2155−304 [Maraschi et al., 2002]. This phenomenon is not quite understood yet, and deserved further investigation. The existing SSC code was hence made time-dependent (without diffusion terms), and in order to check for achromatic variability across the complete electromagnetic spectrum, a time-dependent maxwellian electron injection function $Q(\gamma) = K\gamma^2 \exp(\frac{2\gamma}{\gamma_b(t)})$ (defined in Saugé & Henri [2004], and used to model the SED of Mkn 421 in Giebels et al. 2007) was used in which the parameter γ_b followed a red noise with an index of 2 [Sanchez, Giebels, & Dubus, 2008; Sanchez, 2010]. As can be seen in Figure 3.7, the fractional variability computed in small logarithmic intervals up to 10 TeV clearly shows an achromatic variability.

This spectral variability distribution (SVD) resembles the spectral energy distribution (SED), as it also shows two distributions clearly linked to the cooling mechanisms. The increasing slope up to the first inflexion point at the end of the synchrotron component around 100 keV can probably be explained by the characteristic synchrotron cooling timescale which is $\propto 1/B^2\gamma$ such that more energetic injections should cool faster and hence output a higher variance synchrotron flux. Between the optical and the X-ray bands, $F_{\rm var} \propto E^{\kappa}$ with an index $\kappa = 0.26 \pm 0.08$, in good agreement with data. In the Fermi range, $F_{\rm var}$ is less energy dependent but the model predicts an even higher variability above 200 GeV. While this work is still in development, it seems

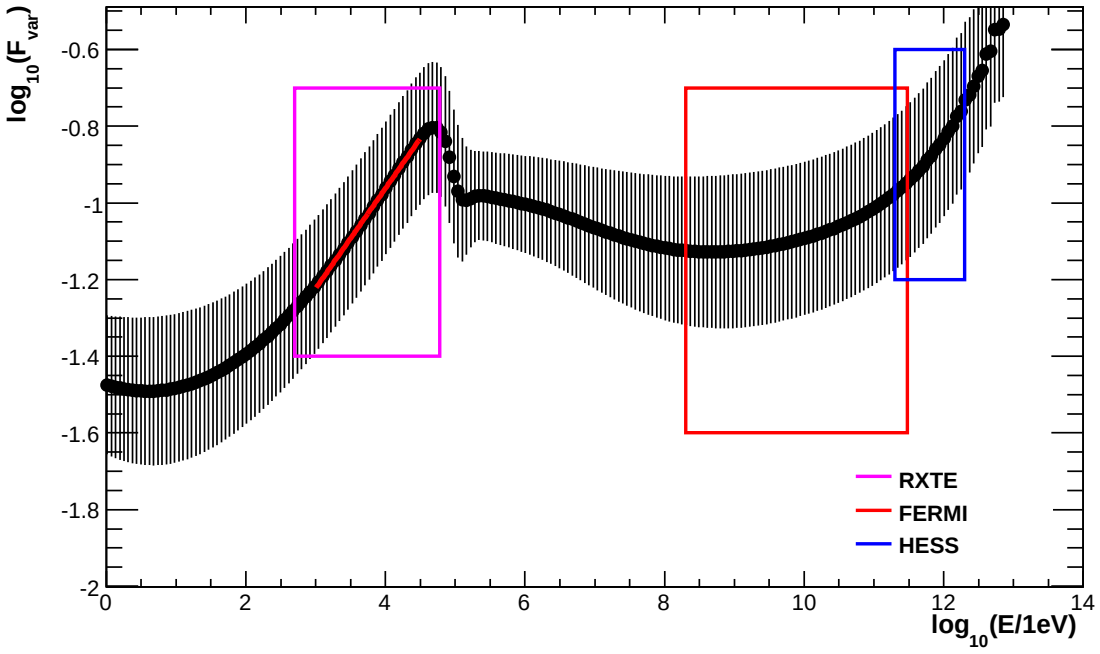

Figure 3.7: *The spectral variability distribution (SVD) using a time-dependent SSC model where a maxwellian electron distribution is injected using a red noise time profile.*

promising that accurate energy dependent estimations of the variability could constrain physical parameters in a model as well.

Flux dependent variability

Given the dense sampling, the light curve could be searched for evidence of a statistical property found in some accreting sources, called lognormality, found in X-rays time series of some classes of Galactic as well as extragalactic accreting sources which can be generated by a stationary process by taking the exponential of a Gaussian time series [Uttley et al., 2005]. In this case, fluxes are distributed as

$$f(\Phi)\mathrm{d}\Phi = \frac{1}{\sigma\sqrt{2\pi}} e^{-\frac{(\ln\Phi-\overline{\ln\Phi})^2}{2\sigma^2}} \mathrm{d}\ln\Phi$$

However,McHardy [2008] suggested that variations generated within the accretion disk can modulate the nonthermal jet emission. It is shown in Fig. 11 of §3.4) (see also Superina 2009 for further details) that the VHE γ-ray fluctuations of PKS 2155−304 are on average proportional to the flux itself which is characteristic of a lognormal flux. This suggests that the underlying physical variability process is multiplicative, rather than additive, since a multiplication of ≥ 3 independent random processes tends towards a lognormal distribution [Ioka & Nakamura, 2002]. This signature can relatively easily be searched for in astronomical sources with either long time series or short ones with ample count rates, but it is particularly difficult to find in the light curves of VHE blazars because they are relatively faint, causing the Poisson noise to be large, and usually densely sampled only on flaring occasions and for a few days, but even then fluxes remain modest compared to those of X-ray binaries. The sampling density is critical in order to apply Gaussian statistics to the variance measurements. This required also to adapt the underlying PSD characterization of §3.4 through the SF in using the difference of the logarithms of the fluxes, and not the fluxes themselves, i.e. $S(\tau) = \overline{(\ln\Phi(t) - \ln\Phi(t+\tau))^2}$.

Lognormal variability was also found in the most X-ray variable narrow-line Seyfert 1 galaxy IRAS 13244−3809 by Gaskell [2004], the only other known case of an extragalactic source exhibiting lognormal X-ray flux variations before Giebels & Degrange [2009] showed that the X-rays of BL Lacertae itself are also best characterized by a lognormal flux. We also note that a linear flux-rms relationship was found for Galactic accreting sources such as X-ray binaries

Cyg X-1 and SAX J 1808.4-3658 by Uttley & McHardy [2001]. A specific observation of Cyg X-1 exhibited a remarkable lognormal fit to its Xray flux distribution Uttley et al. [2005]. The origin of the linear flux-rms was interpreted by Uttley & McHardy [2001] as originating from the subdivision of magnetic reconnection energy release as an avalanche occuring on large scales in the corona (while Mineshige et al. [1994] show that avalanche-type cascades induced by instabilities in the accretion disk can in some cases also generate $\nu^{-\beta}$ fluctuations in the X-ray luminosity using an interesting sand-pile related self-organized criticality analogy). The same authors note that the radius-dependent fluctuations in the mass accretion rate in the model of Lyubarskii [1997] can also explain this relationship. It seems possible that the photon breeding mechanism (Stern & Poutanen 2008, and references therein), which generates highly non-linear light curves in relativistic jets and operates in sites that are not necessarily directly connected to accretion properties, could be an alternative explanation of lognormal blazar variability, but this remains to be investigated since the statistical properties of the photon luminosity from this model are not known at this point. These striking similarities suggest that the variability mechanism causing the VHE modulation of the flares is independent of the emission mechanism, and could indeed originate in the disk as suggested by the energetics of the source (as some theoreticians speculated in §3.3), rather than in the jet, provided these lognormal fluctuations are indeed present in the disk. Note that the SSC and EC mechanisms do not provide a way to generate lognormal variability if one of the parameters affecting the predicted flux (e.g., magnetic field, Doppler factor, injection rate) does not have a lognormal time dependence itself. If fluctuations in the disk are indeed the origin of the lognormal radiation in PKS 2155−304, then the most appropriate hypothesis would be one in which lognormal fluctuations in the accretion rate yield an injection rate with similar properties. If however external photons are at least partly responsible for the cooling of the X-ray emitting electrons, then lognormal fluctuations in the disk luminosity would have a similar result. A link with disk thermal emission fluctuations is difficult to find in VHE γ-ray AGN because of the dominance of the nonthermal radiation [Perlman et al., 2008], complicating further the study of the link between accretion and jet physics in these objects.

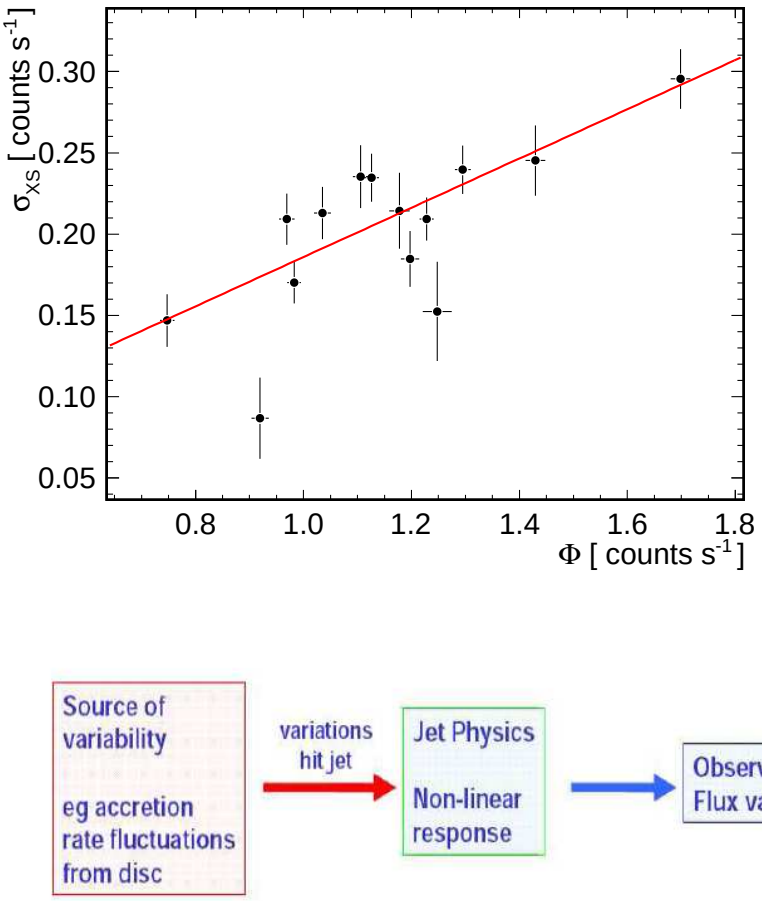

Figure 3.8: *Top: The excess variance σ_{XS} versus the flux average in the X-ray flux of the blazar BL Lacertae [Giebels & Degrange, 2009], showing a linear correlation between both, as is also apparent for the VHE γ-ray flux of PKS 2155−304 in Fig. 11 of HESS Collaboration et al. 2010 (see §3.4). Bottom: The origin of a flux-rms relationship scenario which finds its origin in the disk rather than in the jet. (Reproduced from McHardy 2008).*

An ambitious observation programme targeting other γ-ray bright blazars (or fainter blazars but with a much better sensitivity - perhaps that of the CTA project, discussed further in §4), over similar time scales, and with a similar sampling quality, would allow us to search for lognormal variability, and perhaps solve an important piece in the puzzle about blazar variability.

3.4 "VHE γ-ray emission of PKS 2155−304: spectral and temporal variability"

A&A 520, A83 (2010)
DOI: 10.1051/0004-6361/201014484

Astronomy & Astrophysics

VHE γ-ray emission of PKS 2155–304: spectral and temporal variability

HESS Collaboration, A. Abramowski[4], F. Acero[15], F. Aharonian[1,13], A. G. Akhperjanian[2], G. Anton[16], U. Barres de Almeida[8,⋆], A. R. Bazer-Bachi[3], Y. Becherini[12], B. Behera[14], W. Benbow[1], K. Bernlöhr[1,5], A. Bochow[1], C. Boisson[6], J. Bolmont[19], V. Borrel[3], J. Brucker[16], F. Brun[19], P. Brun[7], R. Bühler[1], T. Bulik[29], I. Büsching[9], T. Boutelier[17], P. M. Chadwick[8], A. Charbonnier[19], R. C. G. Chaves[1], A. Cheesebrough[8], L.-M. Chounet[10], A. C. Clapson[1], G. Coignet[11], J. Conrad[31], L. Costamante[1,34], M. Dalton[5], M. K. Daniel[8], I. D. Davids[22,9], B. Degrange[10], C. Deil[1], H. J. Dickinson[8], A. Djannati-Ataï[12], W. Domainko[1], L. O'C. Drury[13], F. Dubois[11], G. Dubus[17], J. Dyks[24], M. Dyrda[28], K. Egberts[1,30], P. Eger[16], P. Espigat[12], L. Fallon[13], C. Farnier[15], S. Fegan[10], F. Feinstein[15], M. V. Fernandes[4], A. Fiasson[11], A. Förster[1], G. Fontaine[10], M. Füßling[5], S. Gabici[13], Y. A. Gallant[15], L. Gérard[12], D. Gerbig[21], B. Giebels[10], J. F. Glicenstein[7], B. Glück[16], P. Goret[7], D. Göring[16], D. Hampf[4], M. Hauser[14], S. Heinz[16], G. Heinzelmann[4], G. Henri[17], G. Hermann[1], J. A. Hinton[33], A. Hoffmann[18], W. Hofmann[1], P. Hofverberg[1], M. Holleran[9], S. Hoppe[1], D. Horns[4], A. Jacholkowska[19], O. C. de Jager[9], C. Jahn[16], I. Jung[16], K. Katarzyński[27], U. Katz[16], S. Kaufmann[14], M. Kerschhaggl[5], D. Khangulyan[1], B. Khélifi[10], D. Keogh[8], D. Klochkov[18], W. Kluźniak[24], T. Kneiske[4], Nu. Komin[7], K. Kosack[7], R. Kossakowski[11], G. Lamanna[11], J.-P. Lenain[6], T. Lohse[5], C.-C. Lu[1], V. Marandon[12], A. Marcowith[15], J. Masbou[11], D. Maurin[19], T. J. L. McComb[8], M. C. Medina[6], J. Méhault[15], R. Moderski[24], E. Moulin[7], M. Naumann-Godo[10], M. de Naurois[19], D. Nedbal[20], D. Nekrassov[1], N. Nguyen[4], B. Nicholas[26], J. Niemiec[28], S. J. Nolan[8], S. Ohm[1], J.-F. Olive[3], E. de Oña Wilhelmi[1], B. Opitz[4], K. J. Orford[8], M. Ostrowski[23], M. Panter[1], M. Paz Arribas[5], G. Pedaletti[14], G. Pelletier[17], P.-O. Petrucci[17], S. Pita[12], G. Pühlhofer[18], M. Punch[12], A. Quirrenbach[14], B. C. Raubenheimer[9], M. Raue[1,34], S. M. Rayner[8], O. Reimer[30], M. Renaud[12], R. de los Reyes[1], F. Rieger[1,34], J. Ripken[31], L. Rob[20], S. Rosier-Lees[11], G. Rowell[26], B. Rudak[24], C. B. Rulten[8], J. Ruppel[21], F. Ryde[32], V. Sahakian[2], A. Santangelo[18], R. Schlickeiser[21], F. M. Schöck[16], A. Schönwald[5], U. Schwanke[5], S. Schwarzburg[18], S. Schwemmer[14], A. Shalchi[21], I. Sushch[5], M. Sikora[24], J. L. Skilton[25], H. Sol[6], Ł. Stawarz[23], R. Steenkamp[22], C. Stegmann[16], F. Stinzing[16], G. Superina[10], A. Szostek[23,17], P. H. Tam[14], J.-P. Tavernet[19], R. Terrier[12], O. Tibolla[1], M. Tluczykont[4], K. Valerius[16], C. van Eldik[1], G. Vasileiadis[15], C. Venter[9], L. Venter[6], J. P. Vialle[11], A. Viana[7], P. Vincent[19], M. Vivier[7], H. J. Völk[1], F. Volpe[1,10], S. Vorobiov[15], S. J. Wagner[14], M. Ward[8], A. A. Zdziarski[24], A. Zech[6], and H.-S. Zechlin[4]
(Affiliations can be found after the references)

Received 22 March 2010 / Accepted 14 May 2010

ABSTRACT

Context. Observations of very high-energy γ-rays from blazars provide information about acceleration mechanisms occurring in their innermost regions. Studies of variability in these objects lead to a better understanding of the mechanisms in play.
Aims. To investigate the spectral and temporal variability of VHE (>100 GeV) γ-rays of the well-known high-frequency-peaked BL Lac object PKS 2155−304 with the HESS imaging atmospheric Cherenkov telescopes over a wide range of flux states.
Methods. Data collected from 2005 to 2007 were analyzed. Spectra were derived on time scales ranging from 3 years to 4 min. Light curve variability was studied through doubling timescales and structure functions and compared with red noise process simulations.
Results. The source was found to be in a low state from 2005 to 2007, except for a set of exceptional flares that occurred in July 2006. The quiescent state of the source is characterized by an associated mean flux level of $(4.32 \pm 0.09_{\rm stat} \pm 0.86_{\rm syst}) \times 10^{-11}$ cm^{-2} s^{-1} above 200 GeV, or approximately 15% of the Crab Nebula, and a power-law photon index of $\Gamma = 3.53 \pm 0.06_{\rm stat} \pm 0.10_{\rm syst}$. During the flares of July 2006, doubling timescales of ∼2 min are found. The spectral index variation is examined over two orders of magnitude in flux, yielding different behavior at low and high fluxes, which is a new phenomenon in VHE γ-ray emitting blazars. The variability amplitude characterized by the fractional rms $F_{\rm var}$ is strongly energy-dependent and is $\propto E^{0.19\pm0.01}$. The light curve rms correlates with the flux. This is the signature of a multiplicative process that can be accounted for as a red noise with a Fourier index of ∼2.
Conclusions. This unique data set shows evidence of a low-level γ-ray emission state from PKS 2155−304 that possibly has a different origin than the outbursts. The discovery of the light curve lognormal behavior might be an indicator of the origin of aperiodic variability in blazars.

Key words. gamma rays: general – galaxies: active – galaxies: jets – BL Lacertae objects: individual: PKS 2155−304

1. Introduction

The BL Lacertae (BL Lac) category of active galactic nuclei (AGN) represents the vast majority of the population of energetic

⋆ Supported by CAPES Foundation, Ministry of Education of Brazil.

and extremely variable extragalactic very high-energy γ-ray emitters. Their luminosity varies in unpredictable, highly irregular ways, by orders of magnitude and at all wavelengths across the electromagnetic spectrum. The very high-energy (VHE, $E \geq 100$ GeV) γ-ray fluxes vary often on the shortest timescales that can be seen in this type of object, with large amplitudes that can dominate the overall output. It thus indicates that the understanding of this energy domain is the most important one for understanding the underlying fundamental variability and emission mechanisms in play in high flux states.

It has been difficult, however, to ascertain whether γ-ray emission is present only during high flux states or also when the source is in a more stable or quiescent state but with a flux that is below the instrumental limits. The advent of the current generation of atmospheric Cherenkov telescopes with unprecedented sensitivity in the VHE regime gives new insight into these questions.

The high-frequency-peaked BL Lac object (HBL) PKS 2155−304, located at redshift $z = 0.117$, initially discovered as a VHE γ-ray emitter by the Mark 6 telescope (Chadwick et al. 1999), has been detected by the first HESS telescope in 2002−2003 (Aharonian et al. 2005b). It has been frequently observed by the full array of four telescopes since 2004, either sparsely during the HESS monitoring program or intensely during dedicated campaigns, such as described in Aharonian et al. (2005c), showing mean flux levels of ∼20% of the Crab Nebula flux for energies above 200 GeV. During the summer of 2006, PKS 2155−304 exhibited unprecedented flux levels accompanied by strong variability (Aharonian et al. 2007a), making temporal and spectral variability studies possible on timescales on the order of a few minutes. The VHE γ-ray emission is usually thought to originate from a relativistic jet, emanating from the vicinity of a supermassive black hole (SMBH). The physical processes in play are still poorly understood, but the analysis of the γ-ray flux spectral and temporal characteristics is well-suited to providing deeper insight.

For this goal, the data set of HESS observations of PKS 2155−304 between 2005 and 2007 is used. After describing the observations and the analysis chain in Sect. 2, the emission from the "quiescent", i.e. nonflaring, state of the source is characterized in Sect. 3. Section 4 explains the spectral variability related to the source intensity. Section 5 describes the temporal variability during the highly active state of the source and its possible energy dependence. Section 6 illustrates the observed variability phenomenon by a random stationary process, characterized by a simple power density spectrum. Section 7 shows how limits on the characteristic time of the source can be derived. The multi-wavelength aspects from the high flux state will be presented in a second paper.

2. Observations and analysis

HESS is an array of four imaging atmospheric Cherenkov telescopes situated in the Khomas Highland of Namibia (23°16′18″ South, 16°30′00″ East), at an elevation of 1800 m above sea level (see Aharonian et al. 2006). PKS 2155−304 was observed by HESS each year after 2002; results of observations in 2002, 2003, and 2004 can be found in Aharonian et al. (2005b), Aharonian et al. (2005c) and Giebels et al. (2005). The data reported here were collected between 2005 and 2007. In 2005, 12.2 h of observations were taken. A similar observation time was scheduled in 2006, but following the strong flare of July 26 (Aharonian et al. 2007a), it was decided to increase this observation time significantly. Ultimately, from June to October 2006, this source was observed for 75.9 h, with a further 20.9 h in 2007.

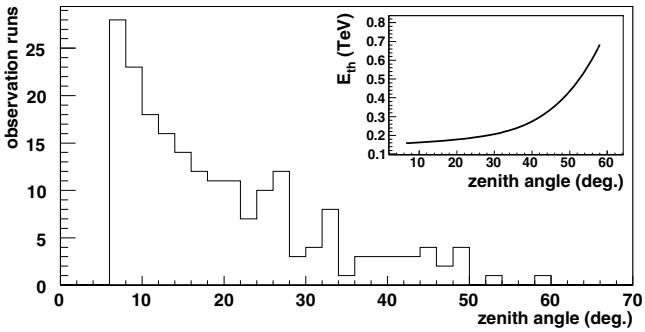

Fig. 1. Zenith angle distribution for the 202 4-telescopes observation runs from 2005 to 2007. The inset shows, for each zenith angle, the energy threshold associated with the analysis presented in Sect. 2.

Table 1. Summary of observations for each year.

Year	T	n_{on}	n_{off}	Excess	σ	$\sigma/\sqrt{T}$
2005	9.4	7282	27 071	1868	21.8	7.1
2006	66.1	123 567	203 815	82 804	288.4	35.5
2007	13.8	11 012	40 065	2999	28.6	7.7
Total	89.2	141 861	270 951	87 671	275.6	29.2

Notes. T represents the live-time (hours), n_{on} the number of on-source events, n_{off} the number of off-source events (from a region five times larger than for the on-source events), and σ the significance of the corresponding excess, given in units of standard deviations.

The data were recorded during runs of 28 min nominal duration, with the telescopes pointing at 0.5° from the source position in the sky to enable a simultaneous estimate of the background. This offset was taken alternatively in both right ascension and declination (with both signs), in order to minimize systematics. Only the runs passing the HESS data-quality selection criteria were used for the analyses presented below. These criteria imply good atmospheric conditions and checks that the hardware state of the cameras is satisfactory. The number of runs thus selected is 22 for 2005, 153 for 2006, and 35 for 2007, corresponding to live-times of 9.4, 66.1, and 13.8 h respectively. During these observations, zenith angles were between 7 and 60 degrees, resulting in large variations in the instrument energy threshold (E_{th}, see Fig. 1) and sensitivity. This variation has been accounted for in the spectral and temporal variability studies presented below.

The data have been analyzed following the prescription presented in Aharonian et al. (2006), using the *loose* set of cuts that are well adapted for bright sources with moderately soft spectra, and the *Reflected-Region* method for the definition of the on-source and off-source data regions. A year-wise summary of the observations and the resulting detections are shown in Table 1. A similar summary is given in Appendix A for the 67 nights of data taken, showing that the emission of PKS 2155−304 is easily detected by HESS almost every night. For 66 nights out of 67, the significance per square root of the live-time ($\sigma/\sqrt{T}$, where T is the observation live-time) is at least equal to $3.6\sigma/\sqrt{h}$, the only night with a lower value – MJD 53705 – corresponding to a very short exposure. In addition, for 61 nights out of 67 the source emission is high enough to enable a detection of the source with 5σ significance in one hour or less, a level usually required in this domain to firmly claim a new source detection. In 2006 the source exhibits very strong activity (38 nights,

Table 2. The various data sets used in the paper, referred to in the text by the labels presented in this table.

Label	Period	Runs	T(hours)	Excess	σ	Section	Additional criteria
D	2005–2007	165	69.7	67 654	237.4	4, 7	–
$D_{\rm QS}$	2005–2007	115	48.1	12 287	60.5	3.2, 3.4, 3.3, 7	July 2006 excluded
$D_{\rm QS-2005}$	2005	19	8.0	1816	22.6	3.4	–
$D_{\rm QS-2006}$	2006	61	26.3	7472	48.4	3.4	July 2006 excluded
$D_{\rm QS-2007}$	2007	35	13.8	2999	28.6	3.4	–
$D_{\rm JULY06}$	July 2006	50	21.6	55,367	281.8	4, 5, 6, 7	–
$D_{\rm FLARES}$	July 2006 (4 nights)	27	11.8	46 036	284.1	4, 5, 6, 7	–

Notes. Only runs with the full array of four telescopes in operation (202 runs over 210) and an energy threshold lower than 200 GeV (165 runs over 202) are considered. The corresponding period of the observations, the number of runs, the live-time T (hours), the number of γ excess events and its significance σ are shown. The column *section* indicates the sections of the paper in which each data set is discussed. Additional criteria for the data set definitions are indicated in the last column.

between MJD 53916−53999) with a nightly $\sigma/\sqrt{T}$ varying from 3.6 to 150, and being higher than $10\sigma/\sqrt{h}$ for 19 nights. The activity of the source climaxes on MJD 53944 and 53946 with statistical significances that are unprecedented at these energies, the rate of detected γ-rays corresponding to 2.5 and 1.3 Hz, with 150 and $98\sigma/\sqrt{h}$ respectively.

For subsequent spectral analysis, an improved energy reconstruction method with respect to the one described in Aharonian et al. (2006) was applied. This method is based on a look-up table determined from Monte-Carlo simulations, which contains the relation between an image's amplitude and its reconstructed impact parameter as a function of the true energy, the observation zenith angle, the position of the source in the camera, the optical efficiency of the telescopes (which tend to decrease due to the aging of the optical surfaces), the number of triggered telescopes and the reconstructed altitude of the shower maximum. Thus, for a given event, the reconstructed energy is determined by requiring the minimal χ^2 between the image amplitudes and those expected from the look-up table corresponding to the same observation conditions. This method yields a slightly lower energy threshold (shown in Fig. 1 as a function of zenith angle), an energy resolution that varies from 15% to 20% over all the energy range, and biases in the energy reconstruction that are smaller than 5%, even close to the threshold. The systematic uncertainty in the normalization of the HESS energy scale is estimated to be as large as 15%, corresponding for such soft spectrum source to 40% in the overall flux normalization as quoted in Aharonian et al. (2009).

All the spectra presented in this paper have been obtained using a forward-folding maximum likelihood method based on the measured energy-dependent on-source and off-source distributions. This method, fully described in Piron et al. (2001), performs a global deconvolution of the instrument functions (energy resolution, collection area) and the parametrization of the spectral shape. Two different sets of parameters, corresponding to a power law and to a power law with an exponential cut-off, are used for the spectral shape, with the following equations:

$$\phi(E) = \phi_0 \left(\frac{E}{E_0}\right)^{-\Gamma} \quad (1)$$

$$\phi(E) = \phi_0 \exp\left(\frac{E_0}{E_{\rm cut}}\right)\left(\frac{E}{E_0}\right)^{-\Gamma} \exp\left(-\frac{E}{E_{\rm cut}}\right) \quad (2)$$

ϕ_0 represents the differential flux at E_0 (chosen to be 1 TeV), Γ is the power-law index and $E_{\rm cut}$ the characteristic energy of the exponential cut-off. The maximum likelihood method provides the best set of parameters corresponding to the selected hypothesis, and the corresponding error matrix.

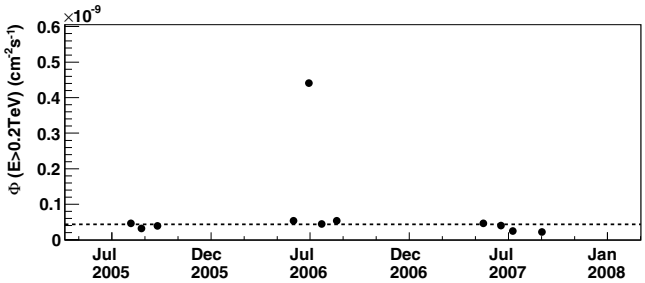

Fig. 2. Monthly averaged integral flux of PKS 2155−304 above 200 GeV obtained from data set D (see Table 2). The dotted line corresponds to 15% of the Crab Nebula emission level (see Sect. 3.2).

Finally, various data sets have been used for subsequent analyses. These are summarized in Table 2.

3. Characterization of the quiescent state

As can be seen in Fig. 2, with the exception of the high state of July 2006 PKS 2155−304 was in a low state during the observations from 2005 to 2007. This section explores the variability of the source during these periods of low-level activity, based on the determination of the run-wise integral fluxes for the data set $D_{\rm QS}$, which excludes the flaring period of July 2006 and also those runs whose energy threshold is higher than 200 GeV (see 3.1 for justification). As for Sects. 5 and 6, the control of systematics in such a study is particularly important, especially because of the strong variations of the energy threshold throughout the observations.

3.1. Method and systematics

The integral flux for a given period of observations is determined in a standard way. For subsequent discussion purposes, the formula applied is given here:

$$\Phi = N_{\rm exp} \frac{\int_{E_{\rm min}}^{E_{\rm max}} S(E){\rm d}E}{T \int_0^\infty \int_{E_{\rm min}}^{E_{\rm max}} A(E)R(E,E')S(E){\rm d}E'{\rm d}E} \quad (3)$$

where T represents the corresponding live-time, $A(E)$ and $R(E, E')$ are, respectively, the collection area at the true energy E and the energy resolution function between E and the measured energy E', and $S(E)$ the shape of the differential energy spectrum as defined in Eqs. (1) and (2). Finally, $N_{\rm exp}$ is the number of measured events in the energy range $[E_{\rm min}, E_{\rm max}]$.

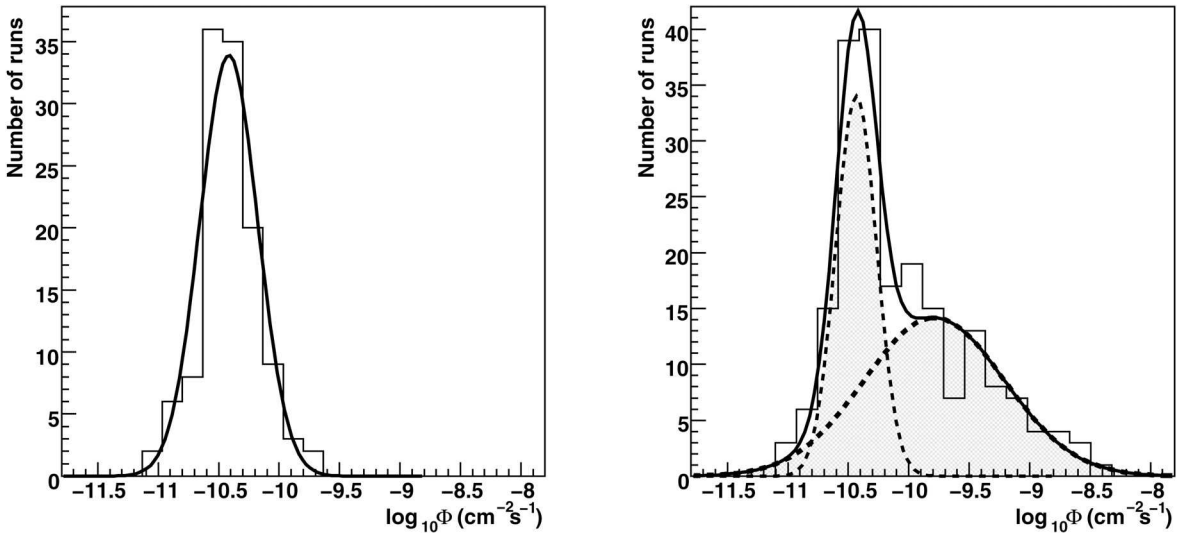

Fig. 3. Distributions of the logarithms of integral fluxes above 200 GeV in individual runs. *Left*: from 2005 to 2007 except the July 2006 period (data set D_{QS}), fitted by a Gaussian. *Right*: all runs from 2005 to 2007 (data set D), where the solid line represents the result of a fit by the sum of 2 Gaussians (dashed lines). See Table 4 for details.

In the case that $S(E)$ is a power law, an important source of systematic error in the determination of the integral flux variation with time comes from the value chosen for the index Γ. The average 2005−2007 energy spectrum yields a very well determined power-law index[1]. However, in Sect. 4 it will be shown that this index varies depending on the flux level of the source. Moreover, in some cases the energy spectrum of the source shows some curvature in the TeV region, giving slight variations in the fitted power-law index depending on the energy range used.

For runs whose energy threshold is lower than E_{min}, a simulation performed under the observation conditions corresponding to the data shows that an index variation of $\Delta\Gamma = 0.1$ implies a flux error at the level of $\Delta\Phi \sim 1\%$, this relation being quite linear up to $\Delta\Gamma \sim 0.5$. However, this relation no longer holds when the energy threshold is above E_{min}, as the determination of Φ becomes much more dependent on the choice of Γ. For this reason, only runs whose energy threshold is lower than E_{min} will be kept for the subsequent light curves. The value of E_{min} is chosen as 200 GeV, which is a compromise between a low value which maximizes the excess numbers used for the flux determinations and a high value which maximizes the number of runs whose energy threshold is lower than E_{min}.

3.2. Run-wise distribution of the integral flux

From 2005 to 2007, PKS 2155−304 is almost always detected when observed (except for two nights for which the exposure was very low), indicating the existence, at least during these observations, of a minimal level of activity of the source. Focussing on data set D_{QS} (which excludes the July 2006 data where the source is in a high state), the distribution of the integral fluxes of the individual runs above 200 GeV has been determined for the 115 runs, using a spectral index $\Gamma = 3.53$ (the best value for this data set, as shown in 3.4). This distribution has an asymmetric shape, with mean value $(4.32 \pm 0.09_{stat}) \times 10^{-11}$ cm^{-2} s^{-1} and root mean square (rms) $(2.48 \pm 0.11_{stat}) \times 10^{-11}$ cm^{-2} s^{-1}, and is very well described with a lognormal function. Such a behavior implies that the logarithm of fluxes follows a normal distribution, centered on the logarithm of $(3.75 \pm 0.11_{stat}) \times 10^{-11}$ cm^{-2} s^{-1}. This is shown in the left panel of Fig. 3, where the solid line represents the best fit obtained with a maximum-likelihood method, yielding results independent of the choice of the intervals in the histogram. It is interesting to note that this result can be compared to the fluxes measured by HESS from PKS 2155−304 during its construction phase, in 2002 and 2003 (see Aharonian et al. 2005b,c). As shown in Table 3, these flux levels extrapolated down to 200 GeV were close to the value corresponding to the peak shown in the left panel of Fig. 3.

Table 3. Integral fluxes and their statistical errors from 2002 and 2003 observations of PKS 2155−304 during the HESS construction phase.

Month	Year	Φ [10^{-11} cm^{-2} s^{-1}]
July	2002	16.4 ± 4.7
Oct.	2002	8.9 ± 5.2
June	2003	5.8 ± 1.4
July	2003	2.9 ± 0.5
Aug.	2003	3.5 ± 0.5
Sep.	2003	4.9 ± 1.2
Oct.	2003	5.2 ± 0.5

Notes. These values are taken from Aharonian et al. (2005b,c) and, correspond to flux extrapolations to above 200 GeV.

The right panel of Fig. 3 shows how the flux distribution is modified when the July 2006 data are taken into account (data set D in Table 2): the histogram can be accounted for by the superposition of two Gaussian distributions (solid curve). The results, summarized in Table 4, are also independent of the choice of the intervals in the histogram. Remarkably enough, the characteristics of the first Gaussian obtained in the first step (left panel) remain quite stable in the double Gaussian fit.

This leads to two conclusions. First, the flux distribution of PKS 2155−304 is well described considering a low state and a high state, for each of which the distribution of the logarithms

[1] The resulting spectral index is $\Gamma = 3.37 \pm 0.02_{stat}$. The alternative hypothesis with a curvature in the spectrum (Eq. (2)) is favored at 8.4σ, yelding a harder index ($\Gamma = 3.05 \pm 0.05_{stat}$) with an exponential cut-off at $E_{cut} = 1.76 \pm 0.27_{stat}$ TeV. As the integral flux is dominated by the low-energy part of the spectrum, the choice of the model has a little effect on the integral flux values above 200 GeV.

Table 4. The distribution of the flux logarithm.

	"Quiescent" regime	Flaring regime
$\langle \log_{10} \Phi \rangle$	–10.42 ± 0.02	–9.79 ± 0.11
rms of $\log_{10} \Phi$	0.24 ± 0.02	0.58 ± 0.04

Notes. First column: distribution as fitted by a single Gaussian law for the "quiescent" regime (data set D_{QS}). Second column: distribution fitted by two Gaussian laws, one for the "quiescent" regime, the other for the flaring regime (data set D). Decimal logarithms are quoted to make the comparison with the left panel of Fig. 3 easier and the flux is expressed in cm^{-2} s^{-1}. In the first line the average of fluxes is reported, while in the second line their rms.

of the fluxes follows a Gaussian distribution. The characteristics of the lognormal flux distribution for the high state are given in Sects. 5–7. Secondly, PKS 2155−304 has a level of minimal activity that seems to be stable on a several-year time-scale. This state will henceforth be referred to as the "quiescent state" of the source.

3.3. Width of the run-wise flux distribution

In order to determine if the measured width of the flux distribution (left panel of Fig. 3) can be explained as statistical fluctuations from the measurement process a simulation has been carried out considering a source that emits an integral flux above 200 GeV of 4.32×10^{-11} cm^{-2} s^{-1} with a power-law spectral index $\Gamma = 3.53$ (as determined in the next section). For each run of the data set D_{QS} the number n_γ expected by convolving the assumed differential energy spectrum with the instrument response corresponding to the observation conditions is determined. A random smearing around this value allows statistical fluctuations to be taken into account. The number of events in the off-source region and also the number of background events in the source region are derived from the measured values n_{off} in the data set. These are also smeared in order to take into account the expected statistical fluctuations.

10 000 such flux distributions have been simulated, and for each one its mean value and rms (which will be called below RMSD) are determined. The distribution of RMSD thus obtained, shown in Fig. 4, is well described by a Gaussian centred on 0.98×10^{-11} cm^{-2} s^{-1} (which represents a relative flux dispersion of 23%) and with a σ_{RMSD} of 0.07×10^{-11} cm^{-2} s^{-1}.

It should be noted that here the effect of atmospheric fluctuations in the determination of the flux is only taken into account at the level of the off-source events, as these numbers are taken from the measured data. But the effect of the corresponding level of fluctuations on the source signal is very difficult to determine. If a conservative value of 20% is considered[2] that is added in the simulations as a supplementary fluctuation factor for the number of events expected from the source, a RMSD distribution centred on 1.30×10^{-11} cm^{-2} s^{-1} with a σ_{RMSD} of 0.09×10^{-11} cm^{-2} s^{-1} is obtained. Even in this conservative case, the measured value for the flux distribution rms ($(2.48 \pm 0.11_{stat}) \times 10^{-11}$ cm^{-2} s^{-1}) is very far (more than 8 standard deviations) from the simulated value. All these elements strongly suggest the existence of an intrinsic variability associated with the quiescent state of PKS 2155−304.

[2] A similar procedure has been carried out on the Crab Nebula observations. Assuming this source is perfectly stable, it allows the derivation of an upper limit to the fluctuations of the Crab signal due to the atmosphere. Nonetheless, this value, ∼10%, is linked to the observations' epoch and zenith angles, and to the source spectral shape.

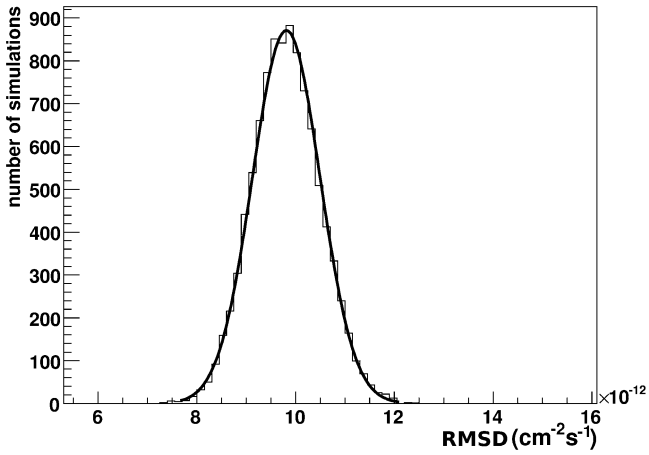

Fig. 4. Distribution of RMSD obtained when the instrument response to a fixed emission ($\Phi = 4.32 \times 10^{-11}$ cm^{-2} s^{-1} and $\Gamma = 3.53$) is simulated 10 000 times with the same observation conditions as for the 115 runs of the left part of Fig. 3.

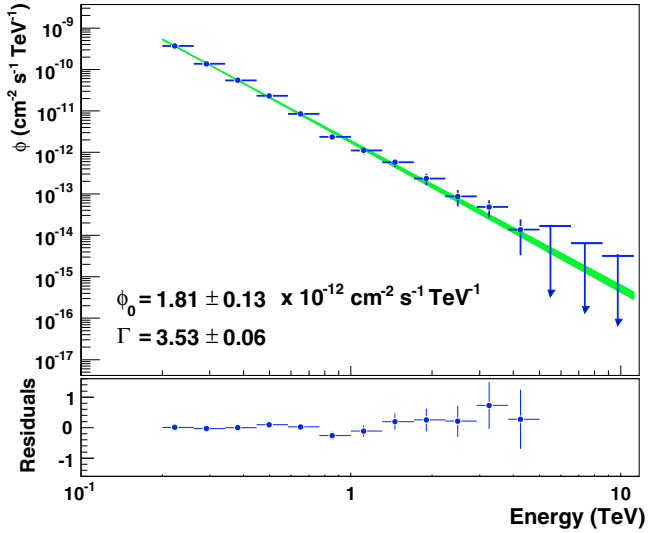

Fig. 5. Energy spectrum of the quiescent state for the period 2005–2007. The green band correponds to the 68% confidence-level provided by the maximum likelihood method. Points are derived from the residuals in each energy bin, only for illustration purposes. See Sect. 3.4 for further details.

3.4. Quiescent-state energy spectrum

The energy spectrum associated with the data set D_{QS}, shown in Fig. 5, is well described by a power law with a differential flux at 1 TeV of $\phi_0 = (1.81 \pm 0.13_{stat}) \times 10^{-12}$ cm^{-2} s^{-1} TeV^{-1} and an index of $\Gamma = 3.53 \pm 0.06_{stat}$. The stability of these values for spectra measured separately for 2005, 2006 (excluding July), and 2007 is presented in Table 5. The corresponding average integral flux is $(4.23 \pm 0.09_{stat}) \times 10^{-11}$ cm^{-2} s^{-1}, which is as expected in very good agreement with the mean value of the distribution shown in the left panel of Fig. 3.

Bins above 2 TeV correspond to γ−ray excesses lower than 20 γ and significances lower than 2σ. Above 5 TeV excesses are even less significant (∼1σ or less) and 99% upper-limits are

Table 5. Parametrization of the differential energy spectrum of the quiescent state of PKS 2155−304, determined in the energy range 0.2−10 TeV, first for the 2005–2007 period and also separately for the 2005, 2006 (excluding July) and 2007 periods.

Year	Data set	ϕ_0	Γ	Φ
2005–2007	$D_{\rm QS}$	1.81 ± 0.13	3.53 ± 0.06	4.23 ± 0.09
2005	$D_{\rm QS-2005}$	1.59 ± 0.32	3.56 ± 0.16	3.83 ± 0.21
2006	$D_{\rm QS-2006}$	1.87 ± 0.18	3.59 ± 0.08	4.65 ± 0.13
2007	$D_{\rm QS-2007}$	1.84 ± 0.24	3.43 ± 0.11	3.78 ± 0.16

Notes. Corresponding data sets are those of Table 2. ϕ_0 (10^{-12} cm^{-2} s^{-1} TeV^{-1}) is the differential flux at 1 TeV, Γ the photon index and Φ (10^{-11} cm^{-2} s^{-1}) the integral flux above 0.2 TeV. Errors are statistical.

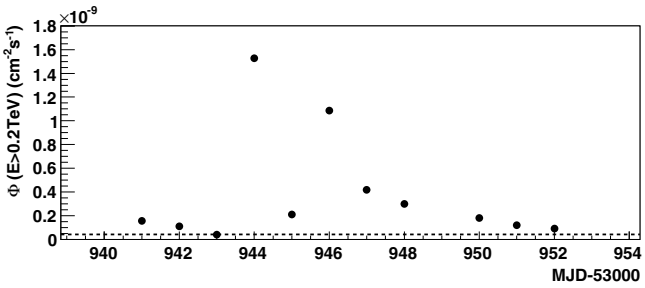

Fig. 6. Integral flux above 200 GeV measured each night during late July 2006 observations. The horizontal dashed line corresponds to the quiescent state emission level defined in Sect. 3.2.

used. There is no improvement of the fit when a curvature is taken into account.

4. Spectral variability

4.1. Variation of the spectral index for the whole data set 2005–2007

The spectral state of PKS 2155−304 has been monitored since 2002. The first set of observations (Aharonian et al. 2005b), from July 2002 to September 2003, shows an average energy spectrum well described by a power law with an index of $\Gamma = 3.32 \pm 0.06_{\rm stat}$, for an integral flux (extrapolated down to 200 GeV) of $(4.39 \pm 0.40_{\rm stat}) \times 10^{-11}$ cm^{-2} s^{-1}. No clear indication of spectral variability was seen. Consecutive observations in October and November 2003 (Aharonian et al. 2005c) gave a similar value for the index, $\Gamma = 3.37 \pm 0.07_{\rm stat}$, for a slightly higher flux of $(5.22 \pm 0.54_{\rm stat}) \times 10^{-11}$ cm^{-2} s^{-1}. Later, during HESS observations of the first (MJD 53944, Aharonian et al. 2007a) and second (MJD 53946, Aharonian et al. 2009) exceptional flares of July 2006, the source reached much higher average fluxes, corresponding to $(1.72 \pm 0.05_{\rm stat}) \times 10^{-9}$ cm^{-2} s^{-1} and $(1.24 \pm 0.02_{\rm stat}) \times 10^{-9}$ cm^{-2} s^{-1}[3] respectively. In the first case, no strong indications for spectral variability were found and the average index $\Gamma = 3.19 \pm 0.02_{\rm stat}$ was close to those associated with the 2002 and 2003 observations. In the second case, clear evidence of spectral hardening with increasing flux was found.

The observations of PKS 2155−304 presented in this paper also include the subsequent flares of 2006 and the data of 2005 and 2007. Therefore, the evolution of the spectral index is studied for the first time for a flux level varying over two orders of magnitude. This spectral study has been carried out over the fixed energy range 0.2−1 TeV in order to minimize both systematic effects due to the energy threshold variation and the effect of the curvature observed at high energy in the flaring states. The maximal energy has been chosen to be at the limit where the spectral curvature seen in high flux states begins to render the power law or exponential curvature hypotheses distinguishable. As flux levels observed in July 2006 are significantly higher than in the rest of the data set (see Fig. 6), the flux-index behavior is determined separately first for the July 2006 data set itself ($D_{\rm JULY06}$) and secondly for the 2005-2007 data excluding this data set ($D_{\rm QS}$).

On both data sets, the following method was applied. The integral flux was determined for each run assuming a power law shape with an index of $\Gamma = 3.37$ (average spectral index for the whole data set), and runs were sorted by increasing flux. The set of ordered runs was then divided into subsets containing at least an excess of 1500 γ above 200 GeV and the energy spectrum of each subset was determined[4].

The left panel of Fig. 7 shows the photon index versus integral flux for data sets $D_{\rm QS}$ (grey crosses) and $D_{\rm JULY06}$ (black points). Corresponding numbers are summarized in Appendix B. While a clear hardening is observed for integral fluxes above a few 10^{-10} cm^{-2} s^{-1}, a break in this behavior is observed for lower fluxes. Indeed, for the data set $D_{\rm JULY06}$ (black points) a linear fit yields a slope $d\Gamma/d\Phi = (3.0 \pm 0.3_{\rm stat}) \times 10^8$ cm^2 s, whereas the same fit for data set $D_{\rm QS}$ (grey crosses) yields a slope $d\Gamma/d\Phi = (-3.4 \pm 1.9_{\rm stat}) \times 10^9$ cm^2 s. The latter corresponds to a χ^2 probability $P(\chi^2) = 71\%$; a fit to a constant yields $P(\chi^2) = 33\%$ but with a constant fitted index incompatible with a linear extrapolation from higher flux states at a 3σ level. This is compatible with conclusions obtained either with an independent analysis or when these spectra are processed following a different prescription. In this prescription the runs were sorted as a function of time in contiguous subsets with similar photon statistics, rather than as a function of increasing flux.

The form of the relation between the index versus integral flux is unprecedented in the TeV regime. Prior to the results presented here, spectral variability has been detected only in two other blazars, Mrk 421 and Mrk 501. For Mrk 421, a clear hardening with increasing flux appeared during the 1999/2000 and 2000/2001 observations performed with HEGRA (Aharonian et al. 2002) and also during the 2004 observations performed with HESS (Aharonian et al. 2005a). In addition, the Mrk 501 observations carried out with CAT during the strong flares of 1997 (Djannati-Ataï et al. 1999) and also the recent observation performed by MAGIC in 2005 (Albert et al. 2007) have shown a similar hardening. In both studies, the VHE peak has been observed in the νF_ν distributions of the flaring states of Mrk 501.

4.2. Variation of the spectral index for the four flaring nights of July 2006

In this section, the spectral variability during the flares of July 2006 is described in more detail. A zoom on the variation of the integral flux (4-min binning) for the four nights containing the flares (nights MJD 53944, 53945, 53946, and 53947, called the "flaring period") is presented in the top panel of Fig. 8. This figure shows two exceptional peaks on MJD 53944 and MJD 53946 that climax respectively at fluxes higher than 2.5×10^{-9} cm^{-2} s^{-1} and 3.5×10^{-9} cm^{-2} s^{-1} (~9 and ~12 times the

[3] Corresponding to data set T200 in Aharonian et al. (2009).

[4] Even for lower fluxes, the significance associated with each subset is always higher than 20 standard deviations.

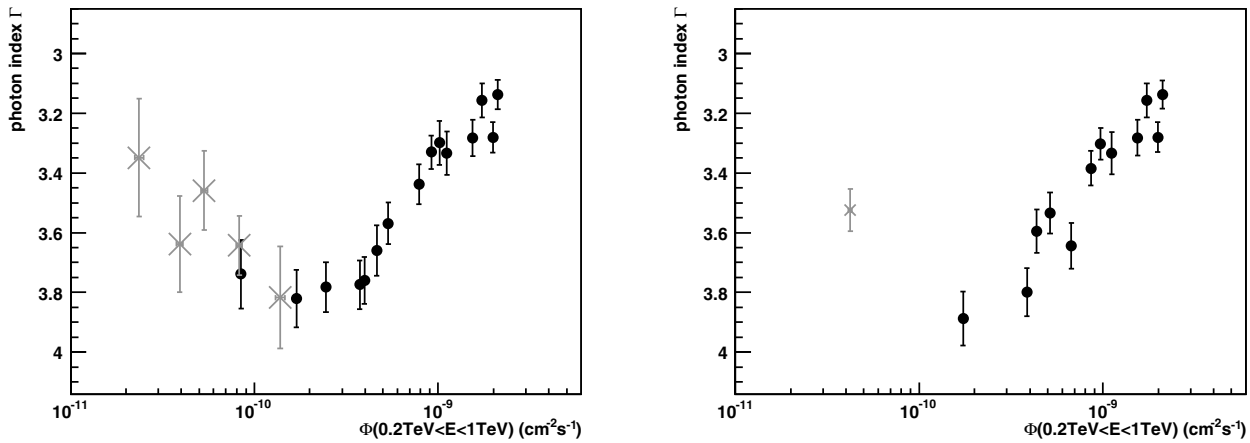

Fig. 7. Evolution of the photon index Γ with increasing flux Φ in the 0.2−1 TeV energy range. *The left panel* shows the results for the July 2006 data (black points, data set D_{JULY06}) and for the 2005−2007 period excluding July 2006 (grey points, data set D_{QS}). *The right panel* shows the results for the four nights flaring period of July 2006 (black points, data set D_{FLARES}) and one point corresponding to the quiescent state average spectrum (grey point, again data set D_{QS}). See text in Sects. 4.1 (*left panel*) and 4.2 (*right panel*) for further details on the method.

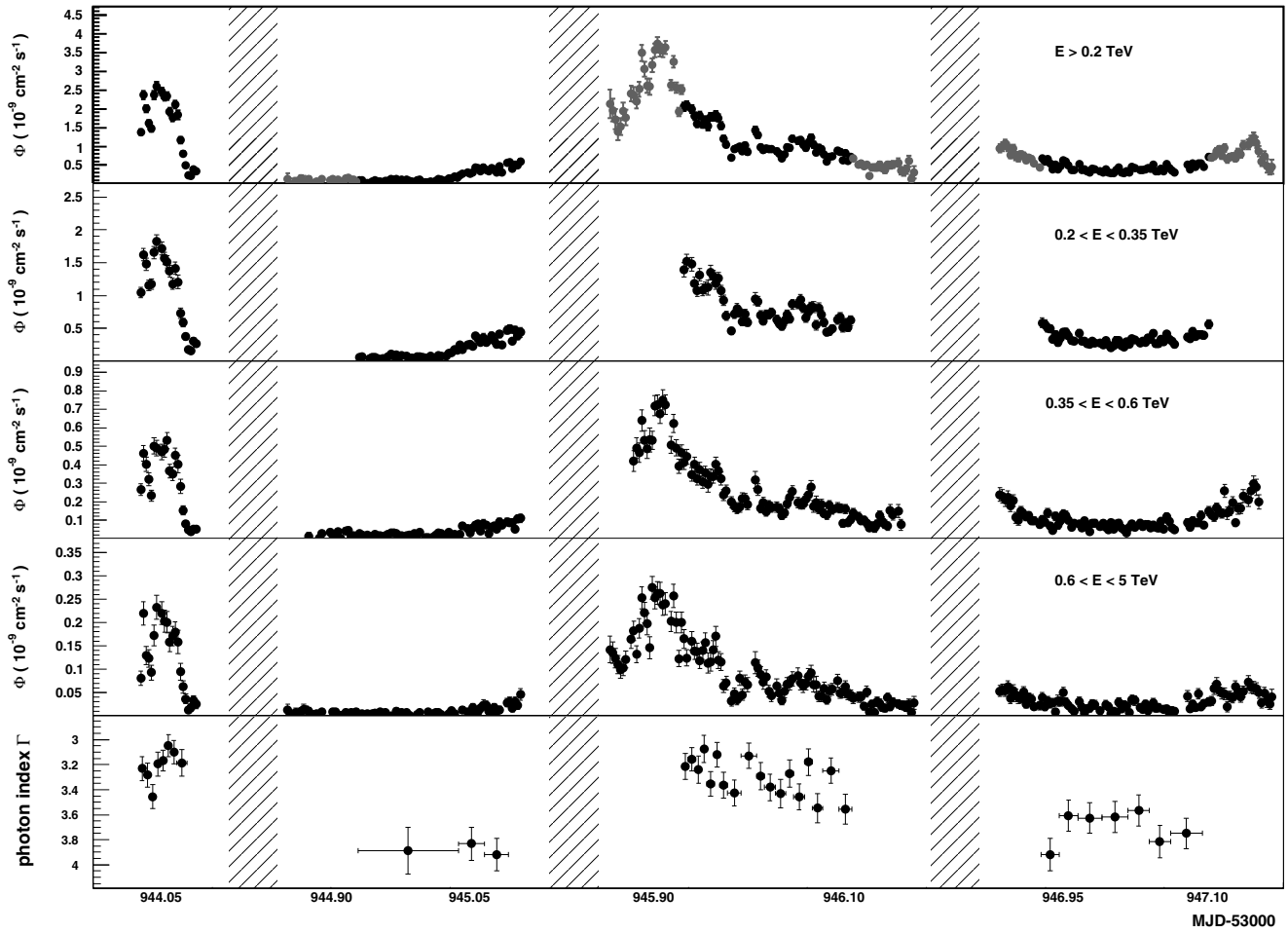

Fig. 8. Integrated flux versus time for PKS 2155−304 on MJD 53944–53947 for four energy bands and with a 4-min binning. *From top to bottom*: >0.2 TeV, 0.2−0.35 TeV, 0.35−0.6 TeV and 0.6−5 TeV. These light curves are obtained using a power law spectral shape with an index of $\Gamma = 3.37$, also used to derive the flux extrapolation down to 0.2 TeV when the threshold is above that energy in *the top panel* (grey points). Because of the high dispersion of the energy threshold of the instrument (see Sect. 2, Fig. 1), and following the prescription described in 3.1, the integral flux has been determined for a time bin only if the corresponding energy threshold is lower than E_{min}. The fractional rms for the light curves are respectively, $0.86 \pm 0.01_{\mathrm{stat}}$, $0.79 \pm 0.01_{\mathrm{stat}}$, $0.89 \pm 0.01_{\mathrm{stat}}$ and $1.01 \pm 0.02_{\mathrm{stat}}$. The last plot shows the variation of the photon index determined in the 0.2−1 TeV range. See Sect. 4.2 and Appendix B.4 for details.

Crab Nebula level above the same energy), both about two orders of magnitude above the quiescent state level.

The variation with time of the photon index is shown in the bottom panel of Fig. 8. To obtain these values, the γ excess

above 200 GeV has been determined for each 4-min bin. Then, successive bins have been grouped in order to reach a global excess higher than 600 γ. Finally, the energy spectrum of each data set has been determined in the 0.2−1 TeV energy range, as before (corresponding numbers are summarized in Appendix Table B.4). There is no clear indication of spectral variability within each night, except for MJD 53946 as shown in Aharonian et al. (2009). However, a variability can be seen from night to night, and the spectral hardening with increasing flux level already shown in Fig. 7 is also seen very clearly in this manner.

It is certainly interesting to directly compare the spectral behavior seen during the flaring period with the hardness of the energy spectrum associated with the quiescent state. This is shown in the right panel of Fig. 7, where black points correspond to the four flaring nights; these were determined in the same manner as for the left panel (see 4.1 for details). A linear fit here yields a slope $d\Gamma/d\Phi = (2.8 \pm 0.3_{stat}) \times 10^8$ cm^2 s. The grey cross corresponds to the integral flux and the photon index associated with the quiescent state (derived in a consistent way in the energy range from 0.2−1 TeV), showing a clear rupture with the tendancy at higher fluxes (typically above 10^{-10} cm^{-2} s^{-1}).

These four nights were further examined to search for differences in the spectral behavior between periods in which the source flux was clearly increasing and periods in which it was decreasing. For this, the first 16 min of the first flare (MJD 53944) are of special interest because they present a very symmetric situation: the flux increases during the first half, and then decreases to its initial level. The averaged fluxes are similar in both parts ($\sim 1.8 \times 10^{-9}$ cm^{-2} s^{-1}), and the observation conditions (and thus the instrument response) are almost constant – the mean zenith angle of each part being respectively 7.2 and 7.8 degrees. Again, the spectra have been determined in the 0.2−1 TeV energy range, giving indices of $\Gamma = 3.27 \pm 0.12_{stat}$ and $\Gamma = 3.27 \pm 0.09_{stat}$ respectively. To further investigate this question and avoid potential systematic errors from the spectral method determination, the hardness ratios were derived (defined as the ratio of the excesses in different energy bands), using for this the energy (TeV) bands [0.2−0.35], [0.35−0.6] and [0.6−5.0]. For any combination, no differences were found beyond the 1σ level between the increasing and decreasing parts. A similar approach has been applied – when possible – for the rest of the flaring period. No clear dependence has been found within the statistical error limit of the determined indices, which is distributed between 0.09 and 0.20.

Finally, the persistence of the energy cut-off in the differential energy spectrum along the flaring period has been examined. For this purpose, runs were sorted again by increasing flux and grouped into subsets containing at least an excess of 3000 γ above 200 GeV[5]. For the seven subsets found, the energy spectrum has been determined in the 0.2−10 TeV energy range both for a simple power law and a power law with an exponential cut-off. This last hypothesis was found to be favoured systematically at a level varying from 1.8 to 4.6σ compared to the simple power law and is always compatible with a cut-off in the 1−2 TeV range.

5. Light curve variability and correlation studies

This section is devoted to the characterization of the temporal variability of PKS 2155−304, focusing on the flaring period observations. The high number of γ-rays available not only enabled minute-level time scale studies, such as those presented for MJD 53944 in Aharonian et al. (2007a), but also to derive detailed light curves for three energy bands (Fig. 8): 0.2−0.35 TeV, 0.35−0.6 TeV and 0.6−5 TeV.

The variability of the energy-dependent light curves of PKS 2155−304 is in the following quantified through their fractional rms F_{var} defined in Eq. (4) (Nandra et al. 1997; Edelson et al. 2002). In addition, possible time lags between light curves in two energy bands are investigated.

5.1. Fractional rms F_{var}

All fluxes in the energy bands of Fig. 8 show a strong variability that is quantified through their fractional rms F_{var} (which depends on observation durations and their sampling). Measurement errors $\sigma_{i,err}$ on each of the N fluxes ϕ_i of the light curve are taken into account in the definition of F_{var}:

$$F_{var} = \frac{\sqrt{S^2 - \sigma_{err}^2}}{\overline{\phi}} \tag{4}$$

where S^2 is the variance

$$S^2 = \frac{1}{N-1} \sum_{i=1}^{N} (\phi_i - \overline{\phi})^2, \tag{5}$$

and where σ_{err}^2 is the mean square error and $\overline{\phi}$ is the mean flux.

The energy-dependent variability $F_{var}(E)$ has been calculated for the flaring period according to Eq. (4) in all three energy bands. The uncertainties on $F_{var}(E)$ have been estimated according to the parametrization derived by Vaughan et al. (2003b), using a Monte Carlo approach which accounts for the measurement errors on the simulated light curves.

Figure 9 shows the energy dependence of F_{var} over the four nights for a sampling of 4 min where only fluxes with a significance of at least 2 standard deviations were considered. There is a clear energy-dependence of the variability (a null probability of $\sim 10^{-16}$). The points in Fig. 9 are fitted according to a power law showing that the variability follows $F_{var}(E) \propto E^{0.19 \pm 0.01}$.

This energy dependence of F_{var} is also perceptible within each individual night. In Table 6 the values of F_{var}, the relative mean flux and the observation duration, are reported night by night for the flaring period. Because of the steeply falling spectra, the low-energy events dominate in the light curves. This lack of statistics for high energy prevents to have a high fraction of points with a significance more than 2 standard deviation in light curves night by night for the three energy bands previously considered. On the other hand, the error contribution dominates, preventing the estimation of the F_{var} in all these three energy bands. Therefore, only two energy bands were considered: low (0.2−0.5 TeV) and high (0.5−5 TeV). As can be seen in Table 6 also night by night the high-energy fluxes seem to be more variable than those at lower energies.

5.2. Doubling/halving timescale

While F_{var} characterizes the mean variability of a source, the shortest doubling/halving time (Zhang et al. 1999) is an important parameter in view of finding an upper limit on a possible physical shortest time scale of the blazar.

If Φ_i represents the light curve flux at a time T_i, for each pair of Φ_i one may calculate $T_2^{i,j} = |\Phi \Delta T / \Delta \Phi|$, where $\Delta T = T_j - T_i$,

[5] To be significant, the determination of an energy cut-off needs a higher number of γ than for a power-law fit.

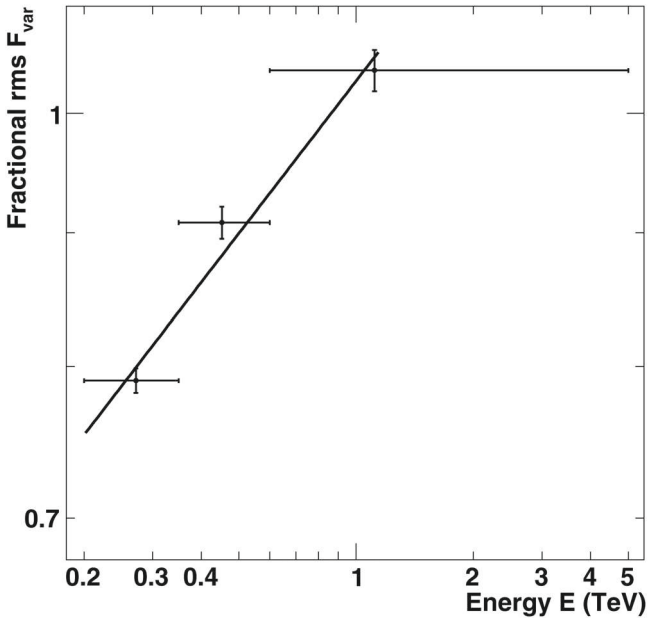

Fig. 9. Fractional rms F_{var} versus energy for the observation period MJD 53944–53947. The points are the mean value of the energy in the range represented by the horizontal bars. The line is the result of a power law fit where the errors on F_{var} and on the mean energy are taken into account, yielding $F_{var}(E) \propto E^{0.19\pm0.01}$.

Table 6. Mean Flux and the fractional rms F_{var} night by night for MJD 53944–53947.

MJD	Duration (min)	Energy (TeV)	$\overline{\Phi}$ (10^{-10} cm^{-2} s^{-1})	F_{var}
53944	88			
		all	15.44 ± 0.87	0.56 ± 0.01
		0.2–0.5	13.28 ± 0.85	0.55 ± 0.01
		0.5–5.0	1.94 ± 0.24	0.61 ± 0.03
53945	244			
		all	2.40 ± 0.41	0.67 ± 0.03
		0.2–0.5	2.35 ± 0.42	0.64 ± 0.03
		0.5–5.0	0.34 ± 0.12	–
53946	252			
		all	11.39 ± 0.80	0.35 ± 0.01
		0.2–0.5	10.02 ± 0.79	0.33 ± 0.01
		0.5–5.0	1.39 ± 0.20	0.43 ± 0.02
53947	252			
		all	4.26 ± 0.52	0.22 ± 0.02
		0.2–0.5	4.02 ± 0.52	0.22 ± 0.02
		0.5–5.0	0.37 ± 0.11	0.13 ± 0.09

Notes. The values refers to light curves with 4 min bins and respectively in three energy bands: >0.2 TeV, 0.2−0.5 TeV, 0.5−5.0 TeV. Since a significant fraction (≈40%) of the points in the light curve of MJD 53945 in the energy band 0.5−5.0 TeV have a significance of less than 2 standard deviations, its F_{var} is not estimated.

$\Delta\Phi = \Phi_j - \Phi_i$ and $\Phi = (\Phi_j + \Phi_i)/2$. Two possible definitions of the doubling/halving are proposed by Zhang et al. (1999): the smallest doubling time of all data pairs in a light curve (T_2), or the mean of the 5 smallest $T_2^{i,j}$ (in the following indicated as $\tilde{T}_2$). One should keep in mind that, according to Zhang et al. (1999), these quantities are ill defined and strongly depend on the length of the sampling intervals and on the signal-to-noise ratio in the observation.

Table 7. Doubling/Halving times for the high intensity nights MJD 53944 and MJD 53946 estimated with two different samplings, using the two definitions explained in the text.

MJD	Bin size	T_2[min]	$\tilde{T}_2$[min]	Fraction of pairs
53944	1 min	1.65 ± 0.38	2.27 ± 0.77	0.53
53944	2 min	2.20 ± 0.60	4.45 ± 1.64	0.62
53946	1 min	1.61 ± 0.45	5.72 ± 3.83	0.25
53946	2 min	4.55 ± 1.19	9.15 ± 4.05	0.38

Notes. The final column corresponds to the fraction of flux pairs kept to estimate the doubling times.

This quantity was calculated for the two nights with the highest fluxes, MJD 53944 and MJD 53946, considering light curves with two different binnings (1 and 2 min). Bins with flux significances more than 2σ and flux ratios with an uncertainty smaller than 30% were required to estimate the doubling time scale. The uncertainty on T_2 was estimated by propagating the errors on the Φ_i, and a dispersion of the 5 smallest values was included in the error for $\tilde{T}_2$.

In Table 7, the values of T_2 and $\tilde{T}_2$ for the two nights are shown. The dependence with respect to the binning is clearly visible for both observables. In this table, the last column shows that the fraction of pairs in the light curves that are kept in order to estimate the doubling times is on average ∼45%. Moreover, doubling times T_2 and $\tilde{T}_2$ have been estimated for two sets of pairs in the light curves where $\Delta\Phi = \Phi_j - \Phi_i$ is increasing or decreasing respectively. The values of the doubling time for the two cases are compatible within 1σ, therefore no significant asymmetry has been found.

It should be noted that these values are strongly dependent on the time binning and on the experiment's sensitivity, so that the typical fastest doubling timescale should be conservatively estimated as being less than ∼2 min, which is compatible with the values reported in Aharonian et al. (2007a) and in Albert et al. (2007), the latter concerning the blazar Mrk 501.

5.3. Cross-correlation analysis as a function of energy

Time lags between light curves at different energies can provide insight into acceleration, cooling and propagation effects of the radiative particles.

The discrete correlation function (DCF) as a function of the delay (White & Peterson 1984; Edelson & Krolik 1988) is used here to search for possible time lags between the energy-resolved light curves. The uncertainty on the DCF has been estimated using simulations. For each delay, 10^5 light curves (in both energy bands) have been generated within their errors, assuming a Gaussian probability distribution. A probability distribution function (PDF) of the correlation coefficients between the two energy bands has been estimated for each set of simulated light curves. The rms of these PDF are the errors related to the DCF at each delay. Figure 10 shows the DCF between the high and low-energy bands for the four-night flaring period (with 4 min bins) and for the second flaring night (with 2 min bins). The gaps between each 28 min run have been taken into account in the DCF estimation.

The position of the maximum of the DCF has been estimated by a Gaussian fit that shows no time lag between low and high energies for either the 4 or 2 min binned light curves. This sets a limit of 14 ± 41 s from the observation of MJD 53946. A detailed study on the limit on the energy scale on which quantum

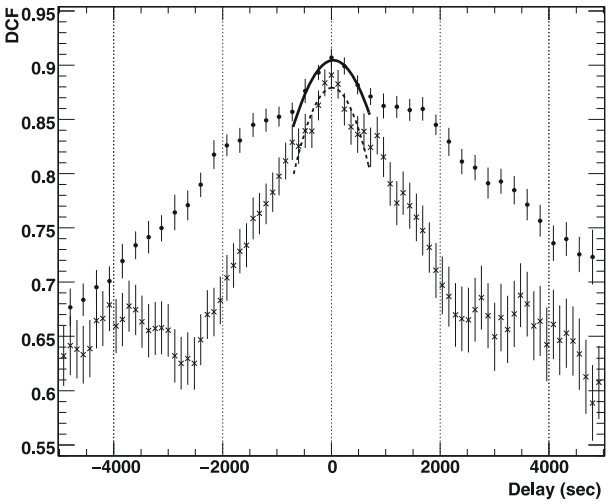

Fig. 10. DCF between the light curves in the energy ranges 0.2−0.5 TeV and 0.5−5 TeV and Gaussian fits around the peak. Full circles represent the DCF for MJD 53944–53947 4-min light curve and the solid line is the Gaussian fit around the peak with mean value of 43 ± 51 s. Crosses represent the DCF for MJD 53946 with a 2-min light curve binning, and the dashed line in the Gaussian fit with a peak centred at 14 ± 41 s.

gravity effects could become important, using the same data set, are reported in Aharonian et al. (2008a).

5.4. Excess rms-flux correlation

Having defined the shortest variability time scales, the nature of the process that generates the fluctuations is investigated, using another estimator: the excess rms. It is defined as the variance of a light curve (Eq. (5)) after subtracting the measurement error:

$$\sigma_{\rm xs} = \sqrt{(S^2 - \sigma_{\rm err}^2)}. \quad (6)$$

Figure 11 shows the correlation between the excess rms of the light curve and the flux, where the flux here considered are selected with an energy threshold of 200 GeV. The excess variance is estimated for 1- and 4-min binned light curves, using 20 consecutive flux points Φ_i that are at least at the 2σ significance level (81% of the 1 min binned sample). The correlation factors are $r_1 = 0.60^{+0.21}_{-0.25}$ and $r_4 = 0.87^{+0.10}_{-0.24}$ for the 1 and 4 min binning, excluding an absence of correlation at the 2σ and 4σ levels respectively, implying that fluctuations in the flux are probably proportional to the flux itself, which is a characteristic of lognormal distributions (Aitchinson & Brown 1963). This correlation has also been investigated extending the analysis to a statistically more significant data set including observations with a higher energy threshold in which the determination of the flux above 200 GeV requires an extrapolation (grey points in the top panel in Fig. 8). In this case the correlations found are compatible ($r_1 = 0.78^{+0.12}_{-0.14}$ and $r_4 = 0.93^{+0.05}_{-0.15}$ for the 1 and 4 min binning, respectively) and also exclude an absence of correlation with a higher significance (4σ and 7σ, respectively).

Such a correlation has already been observed for X-rays in the Seyfert class AGN (Edelson et al. 2002; Vaughan et al. 2003a,b; M$^{\rm c}$Hardy et al. 2004) and in X-ray binaries (Uttley & M$^{\rm c}$Hardy 2001; Uttley 2004; Gleissner et al. 2004), where it is considered as evidence for an underlying stochastic multiplicative process (Uttley et al. 2005), as opposed to an additive process. In additive processes, light curves are considered as the sum of individual flares "shots" contributing from several zones (multi-zone models) and the relevant variable that has a Gaussian distribution (namely Gaussian variable) is the flux. For multiplicative (or cascade) models the Gaussian variable is the logarithm of the flux. Therefore, this first observation of a strong rms-flux correlation in the VHE domain fully confirms the lognormality of the flux distribution presented in Sect. 3.2.

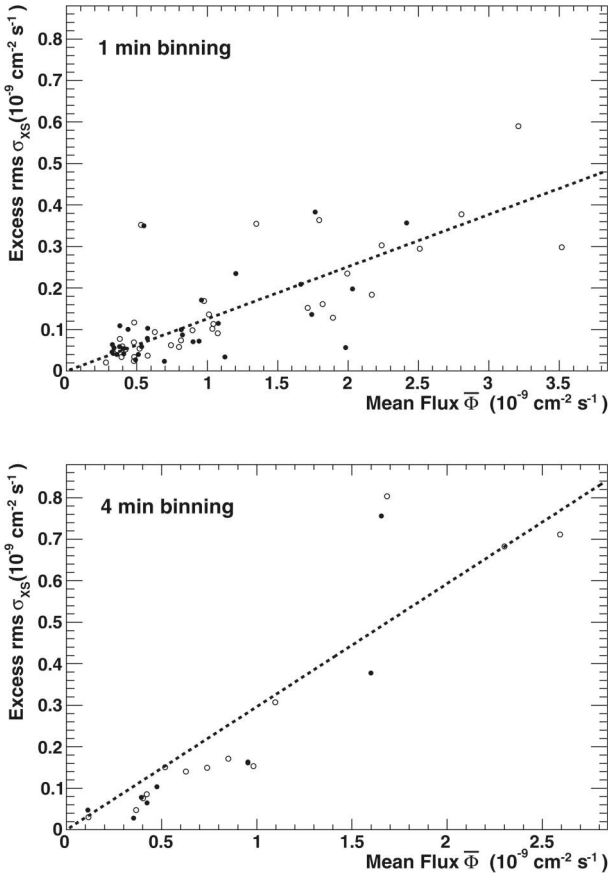

Fig. 11. The excess rms $\sigma_{\rm xs}$ vs. mean flux $\bar{\Phi}$ for the observation in MJD 53944–53947 (Full circles). The open circles are the additional points obtained when also including the extrapolated flux points – see text). *Top*: $\sigma_{\rm xs}$ estimated with 20 min time intervals and a 1 min binned light curve. *Bottom*: $\sigma_{\rm xs}$ estimated with 80 min time intervals and a 4 min binned light curve. The dotted lines are a linear fit to the points, where $\sigma_{\rm xs} \propto 0.13 \times \bar{\Phi}$ for the 1 min binning and $\sigma_{\rm xs} \propto 0.3 \times \bar{\Phi}$ for the 4 min binning. Fits to the open circles yield similar results.

6. Characterization of the lognormal process during the flaring period

This section investigates whether the variability of PKS 2155−304 in the flaring period can be described by a random stationary process, where, as shown in Sect. 5.4, the Gaussian variable is the logarithm of the flux. In this case the variability can be characterized through its Power Spectral Density (PSD) (van der Klis 1997), which indicates the density of variance as function of the frequency ν. The PSD is an intrinsic indicator of the variability, usually represented in large frequency intervals by power laws ($\propto \nu^{-\alpha}$) and is often used to define different "states" of variable objects (see e.g., Paltani et al. 1997; and Zhang et al. 1999, for the PSD of PKS 2155−304 in the optical and X-rays). The PSD of the light curve of one single night (MJD 53944) was given in Aharonian et al. (2007a) between 10^{-4} and 10^{-2} Hz, and was found to be compatible

with a red noise process ($\alpha \geq 2$) with ~10 times more power as in archival X-ray data (Zhang et al. 1999), but with a similar index. This study implicitely assumed the γ-ray flux to be the Gaussian variable. In the present paper, the PSD is determined using data from 4 consecutive nights (MJD 53944–53947) and assuming a lognormal process. Since direct Fourier analysis is not well adapted to light curves extending over multiple days and affected by uneven sampling and uneven flux errors, the PSD will be further determined on the basis of parametric estimation and simulations.

In the hypothesis where the process is stationary, i.e., the PSD is time-independent, a power-law shape of the PSD was assumed, as for X-ray emitting blazars. The PSD was defined as depending on two parameters and as follows: $P(\nu) = K(\nu_{\rm ref}/\nu)^{\alpha}$, where α is the variability spectral index and K denotes the "power" (i.e., the variance density) at a reference frequency $\nu_{\rm ref}$. This latter was conventionally chosen to be 10^{-4} Hz, where the two parameters α and K are found to be decorrelated. Since a lognormal process is considered, $P(\nu)$ is the density of variance of the Gaussian variable $\ln \Phi$. The *natural* logarithm of the flux is conveniently used here, since its variance over a given frequency interval[6] is close to the corresponding value of $F_{\rm var}^2$, at least for small fluctuations. For a given set of α and K, it is possible to simulate many long time series and to modify them according to experimental effects, namely those of background events and of flux measurement errors. Light curve segments are further extracted from this simulation, with exactly the same time structure (observation and non-observation intervals) and the same sampling rates as those of real data. The distributions of several observables obtained from simulations for different values of α and K will be compared to those determined from observations, thus allowing these parameters to be determined from a maximum-likelihood fit.

The simulation characteristics will be described in Sect. 6.1. Sections 6.2–6.4 will be devoted to the determination of α and K by three methods, each of them based on an experimental result: the excess rms-flux correlation, the Kolmogorov first-order structure function (Rutman 1978; Simonetti et al. 1985) and doubling-time measurements.

6.1. Simulation of realistic time-series

For practical reasons, simulated values of $\ln \Phi$ were calculated from Fourier series, thus with a discrete PSD. The fundamental frequency $\nu_0 = 1/T_0$ that corresponds to an elementary bin $\delta\nu \equiv \nu_0$ in frequency, must be much lower than $1/T$ if T is the duration of the observation. The ratio T_0/T was chosen to be of the order of 100, in such a way that the influence of a finite value of T_0 on the average variance of a light curve of duration T would be less than about 2%. Taking $T_0 = 9 \times 10^5$ s, this condition is fulfilled for the following studies. With this approximation, the simulated flux logarithms are given by:

$$\ln \Phi(t) = a_0 + \sum_{n=1}^{N_{\rm max}} a_n \cos(2n\pi\nu_0 t + \varphi_n) \qquad (7)$$

where $N_{\rm max}$ is chosen in such a way that $T_0/N_{\rm max}$ is less than the time interval between consecutive measurements (i.e., the sampling interval). According to the definition of a Gaussian random process, the phases φ_n are uniformly distributed between 0 and 2π and the Fourier coefficients a_n are normally distributed with mean 0 and variances given by $P(\nu)\,\delta\nu/2$ with $\nu = n\,\delta\nu = n\,\nu_0$.

From the long simulated time-series, light curve segments were extracted with the same durations as the periods of continuous data taking and with the same gaps between them. The simulated fluxes were further smeared according to measurement errors, according to the observing conditions (essentially zenith angle and background rate effects) in the corresponding data set.

[6] If σ^2 is the variance of $\ln \Phi$, $F_{\rm var} = \sqrt{\exp(\sigma^2) - 1}$.

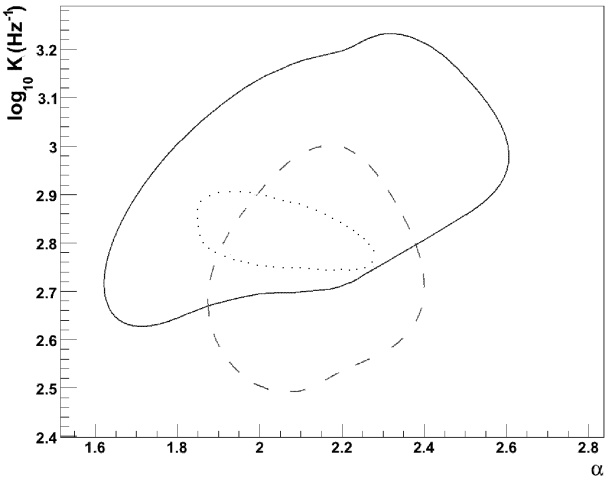

Fig. 12. 95% confidence domains for α and K at $\nu_{\rm ref} = 10^{-4}$ Hz obtained by a maximum-likelihood method based on the $\sigma_{\rm xs}$-flux correlation from 500 simulated light curves. The dashed contour refers to light curve segments of 20 min duration, sampled every minute. The solid contour refers to light curve segments of 80 min duration, sampled every 4 min. The dotted contour refers to the method based on the structure function, as explained in Sect. 6.3.

6.2. Characterization of the lognormal process by the excess rms-flux relation

For a fixed PSD, characterized by a set of parameters $\{\alpha, K\}$, 500 light curves were simulated, reproducing the observing conditions of the flaring period (MJD 53944–53947), according to the procedure explained in Sect. 6.1.

For each set of simulated light curves, segments of 20 min duration sampled every minute (and alternatively segments of 80 min duration sampled every 4 min) were extracted and, for each of them, the excess rms $\sigma_{\rm xs}$ and the mean flux $\bar{\Phi}$ were calculated as explained in Sect. 5.4. For a wide range of values of α and K, simulated light curves reproduce well the high level of correlation found in the measured light curves. On the other hand, the fractional variability $F_{\rm var}$ and $\bar{\Phi}$ are essentially uncorrelated and will be used in the following. A likelihood function of α and K was obtained by comparing the simulated distributions of $F_{\rm var}$ and $\bar{\Phi}$ to the experimental ones. An additional observable that is sensitive to α and K is the fraction of those light curve segments for which $F_{\rm var}$ cannot be calculated because large measurement errors lead to a negative value for the excess variance. The comparison between the measured value of this fraction and those obtained from simulations is also taken into account in the likelihood function. The 95% confidence contours for the two parameters α and K obtained from the maximum likelihood method are shown in Fig. 12 for both kinds of light curve segments. The two selected domains in the $\{\alpha, K\}$ plane have a large overlap which restricts the values of α to the interval (1.9, 2.4).

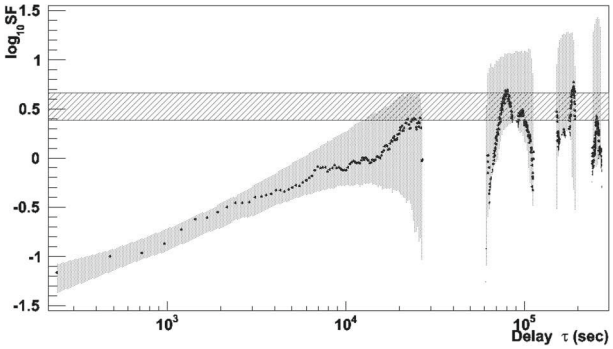

Fig. 13. First order structure function SF for the observations carried out in the period MJD 53944–53947 (circles). The shaded area corresponds to the 68% confidence limits obtained from simulations for the lognormal stationary process characterized by $\alpha = 2$ and $\log_{10}(K/\mathrm{Hz}^{-1}) = 2.8$. The superimposed horizontal band represents the allowed range for the asymptotic value of the SF as obtained in Sect. 7.

6.3. Characterization of the lognormal process by the structure function analysis

Another method for determining α and K is based on Kolmogorov structure functions (SF). For a signal $X(t)$, measured at N pairs of times separated by a delay τ, $\{t_i, t_i + \tau\}$ $(i = 1, ..., N)$, the first-order structure function is defined as (Simonetti et al. 1985):

$$\mathrm{SF}(\tau) = \frac{1}{N}\sum_{i=1}^{N}[X(t_i) - X(t_i+\tau)]^2 = \frac{1}{N}\sum_{i=1}^{N}[\ln\Phi(t_i) - \ln\Phi(t_i+\tau)]^2. \quad (8)$$

In the present analysis, $X(t)$ represents the variable whose PSD is being estimated, namely $\ln\Phi$. The structure function is a powerful tool for studying aperiodic signals (Rutman 1978; Simonetti et al. 1985), such as the luminosity of blazars at various wavelengths. Compared to the direct Fourier analysis, the SF has the advantage of being less affected by "windowing effects" caused by large gaps between short observation periods in VHE observations. The first-order structure function is adapted to those PSDs whose variability spectral index is less than 3 (Rutman 1978), which is the case here, according to the results of the preceding section.

Figure 13 shows the first-order SF estimated for the flaring period (circles) for $\tau < 60$ h. At fixed τ, the distribution of $\mathrm{SF}(\tau)$ expected for a given set of parameters $\{\alpha, K\}$ is obtained from 500 simulated light curves. As an example, taking $\alpha = 2$ and $\log_{10}(K/\mathrm{Hz}^{-1}) = 2.8$, values of $\mathrm{SF}(\tau)$ are found to lie at 68% confidence level within the shaded region in Fig. 13.

In the case of a power law PSD with index α, the SF averaged over an ensemble of light curves is expected show a variation as $\tau^{\alpha-1}$ (Kataoka et al. 2001). However, this property does not take into account the effect of measurement errors, nor of the limited sensitivity of Cherenkov telescopes at lower fluxes. For the present study, it was preferable to use the distributions of $\mathrm{SF}(\tau)$ obtained from realistic simulations including all experimental effects. Using such distributions expected for a given set of parameters $\{\alpha, K\}$, a likelihood function can be obtained from the experimental SF and further maximized with respect to these two parameters. Furthermore, the likelihood fit was restricted to values of τ lower than 10^4 s, for which the expected fluctuations are not too large and are well-controlled. The 95% confidence region in the $\{\alpha, K\}$ plane thus obtained is indicated by the dotted line in Fig. 12. It is in very good agreement with those based on the excess rms-flux correlation and give the best values for α and K:

$$\alpha = 2.06 \pm 0.21 \quad \text{and} \quad \log_{10}(K/\mathrm{Hz}^{-1}) = 2.82 \pm 0.08. \quad (9)$$

The variability index α at VHE energies is found to be remarkably close to those measured in the X-ray domain on PKS 2155−304, Mrk 421, and Mrk 501 (Kataoka et al. 2001).

Table 8. Confidence interval at 68% c.l. for T_2 and $\tilde{T}_2$ predicted by simulations for $\alpha = 2$ and $\log_{10}(K/(\mathrm{Hz}^{-1})) = 2.8$ for the two high-intensity nights MJD 53944 and MJD 53946, with two different sampling intervals (1 and 2 min).

MJD	Bin size	T_2[min]	$\tilde{T}_2$[min]
53944	1 min	0.93–1.85	1.60–2.60
53944	2 min	3.01–4.28	4.52–6.40
53946	1 min	1.8–2.3	1.96–2.41
53946	2 min	5.3–9.1	6.6–12.1

6.4. Characterization of the lognormal process by doubling times

Simulations were also used to investigate if the estimator T_2 can be used to constrain the values of α and K. However, for α less than 2, no significant constraints on those parameters are obtained from the values of T_2. For higher values of α, doubling times only provide loose confidence intervals on K that are compatible with the values reported above. This can be seen in Table 8, showing the 68% confidence intervals predicted for T_2 and $\tilde{T}_2$ for a lognormal process with $\alpha = 2$ and $\log_{10}(K/(\mathrm{Hz}^{-1})) = 2.8$, as obtained from simulation. Therefore, the variability of PKS 2155−304 during the flaring period can be consistently described by the lognormal random process whose PSD is characterized by the parameters given by Eq. (9).

7. Limits on characteristic time of PKS 2155−304

In Sect. 5.2 the shortest variability time scale of PKS 2155−304 using estimators like doubling times have been estimated. This corresponds to exploring the high-frequency behavior of the PSD. In this section the lower ($<10^{-4}$ Hz) frequency part of the PSD will be considered, aiming to set a limit on the timescale above which the PSD, characterized in Sect. 6, starts to steepen to $\alpha > 2$. A break in the PSD is expected to avoid infrared divergences and the time at which this break occurs can be considered as a characteristic time, from which physical mechanisms occurring in AGN could be inferred.

Clearly the description of the source variability during the flaring period by a stationary lognormal random process is in good agreement with the flux distributions shown in Fig. 3. Considering the second Gaussian fit in the right panel of Fig. 3, the excess variance in the flaring regime reported in Table 9, although affected by a large error, is an estimator of the intrinsic variance of the stationary process. It has been demonstrated that $2\sigma_{\mathrm{xs}}^2$ represents the asymptotic value of the first-order structure function for large values of the delay τ (Simonetti et al. 1985). On the other hand, as already mentioned, a PSD proportional to $\nu^{-\alpha}$ with $\alpha \approx 2$ cannot be extrapolated to arbitrary low frequencies; equivalently, the average structure function cannot rise as $\tau^{\alpha-1}$ for arbitrarily long times. Therefore, by setting a 95% confidence interval on $\log_{10}\mathrm{SF}_{\mathrm{asympt}} = \log_{10}(2\sigma_{\mathrm{xs}}^2)$

Table 9. Variability estimators (definitions in Sect. 5.1) relative to $\ln\Phi$ both for the "quiescent" and flaring regime, as defined in Sect. 3.2.

	"Quiescent" regime	Flaring regime
$\sigma^2_{\rm exp}$ of $\ln\Phi$	0.304 ± 0.040	1.78 ± 0.27
$\sigma^2_{\rm err}$ of $\ln\Phi$	0.169 ± 0.053	0.022 ± 0.005
$\sigma^2_{\rm xs}$ of $\ln\Phi$	0.135 ± 0.067	1.758 ± 0.273

Notes. Experimental variance (line 1), error contribution to the variance (line 2), and excess variance (line 3). The latter is directly comparable to $F^2_{\rm var}$.

of $[0.38, 0.66]$ from Table 9, it is possible to evaluate a confidence interval on a timescale above which the average value of the structure function cannot be described by a power law. Taking account of the uncertainties on α and K given by Eq. (9), leads to the 95% confidence interval for this characteristic time $T_{\rm char}$ of the blazar in the flaring regime:

$$3\ {\rm h} < T_{\rm char} < 20\ {\rm h}.$$

This is compatible with the behavior of the experimental structure function at times $\tau > 10^4$ s (Fig. 13), although the large fluctuations expected in this region do not allow a more accurate estimation. In the X-ray domain, characteristic times of the order of one day or less have been found for several blazars including PKS 2155−304 (Kataoka et al. 2001). The results presented here suggest a strong similarity between the PSDs for X-rays and VHE γ-rays during flaring periods.

8. Discussion and conclusions

This data set, which exhibits unique features and results, is the outcome of a long-term monitoring program and dedicated, dense, observations. One of the main results here is the evidence for a VHE γ-ray quiescent-state emission, where the variations in the flux are found to have a lognormal distribution. The existence of such a state was postulated by Stecker & Salamon (1996) in order to explain the extragalactic γ-ray background at 0.03−100 GeV detected by EGRET (Fichtel 1996; Sreekumar et al. 1998) as coming from quiescent-state unresolved blazars. Such a background has not yet been detected in the VHE range, as it is technically difficult with the atmospheric Cherenkov technique to find an isotropic extragalactic emission and even more to distinguish it from the cosmic-ray electron flux (Aharonian et al. 2008b). In addition, the EBL attenuation limits the distance from which ∼TeV γ-rays can propagate to ∼1 Gpc (Aharonian et al. 2007b). As pointed out by Cheng et al. (2000), emission mechanisms might be simpler to understand during quiescent states in blazars, and they are also the most likely state to be found observationally. In the X-ray band, the existence of a steady underlying emission has also been invoked for two other VHE emitting blazars (Mrk 421, Fossati et al. 2000; and 1ES 1959+650, Giebels et al. 2002). Being able to separate, and detect, flaring and nonflaring states in VHE γ-rays is thus important for such studies.

The observation of the spectacular outbursts of PKS 2155–304 in July 2006 represents one of the most extreme examples of AGN variability in the TeV domain, and allows spectral and timing properties to be probed over two orders of magnitude in flux. For the flaring states a clear hardening of the spectrum with increasing flux above a few 10^{-10} cm^{-2} s^{-1} is observed, as was seen for the blazars Mrk 421 and Mrk 501. In contrast, for the quiescent state of PKS 2155−304 an indication of a softening is noted. If confirmed, this is a new and intruiging observation in the VHE regime of blazars. The blazar PKS 0208−512 (of the FSRQ class) also shows such initial softening and subsequent hardening with flux in the MeV range, but no general trend could be found for γ-ray blazars (Nandikotkur et al. 2007). In the framework of synchrotron self-Compton scenarios, VHE spectral softening with increasing flux can be associated with, for example, an increase in magnetic field intensity, emission region size, or the power law index of the underlying electron distribution, keeping all other parameters constant. A spectral hardening can equally be obtained by increasing the maximal Lorentz factor of the electron distribution or the Doppler factor (see e.g. Fig. 11.7 in Kataoka 1999). A better understanding of the mechanisms in play would require multi-wavelength observations to be taken over a similar time span and with similar sampling density as the data set presented here.

It is shown that the variability time scale $t_{\rm var}$ of a few minutes are only upper limits for the intrinsic lowest characteristic time scale. Doppler factors of $\delta \geq 100$ of the emission region are derived by Aharonian et al. (2007a) using the $\sim 10^9\ M_\odot$ black hole (BH) Schwarzschild radius light crossing time as a limit, while Begelman et al. (2008) argue that such fast time scales cannot be linked to the size of the BH and must occur in regions of smaller scales, such as "needles" of matter moving faster than average within a larger jet (Ghisellini & Tavecchio 2008), small components in the jet dominating at TeV energies (Katarzyński et al. 2008), or jet "stratification" (Boutelier et al. 2008). Levinson (2007) attributes the variability to dissipation in the jet coming from radiative deceleration of shells with high Lorentz factors.

The flaring period allowed the study of light curves in separated energy bands and the derivation of a power law dependence of $F_{\rm var}$ with the energy ($F_{\rm var} \propto E^{\sim 0.2}$). This dependence is comparable to that reported in Giebels et al. (2007), Lichti et al. (2008), Maraschi et al. (2002), where $F_{\rm var}(E) \propto E^{\sim 0.2}$ between the optical and X-ray energy bands was found for Mrk 421 and PKS 2155−304, respectively. An increase with the energy of the flux variability has been found for Mrk 501 (Albert et al. 2007) in VHE γ-rays on timescales comparable to those observed here.

The flaring period showed for the first time that the intrinsic variability of PKS 2155−304 increases with the flux, which can itself be described by a lognormal process, indicating that the aperiodic variability of PKS 2155−304 could be produced by a multiplicative process. The flux in the "quiescent regime", which is on average 50 times lower than in the flaring period and has a 3 times lower $F_{\rm var}$, also follows a lognormal distribution, suggesting similarities between these two regimes.

It has been possible to characterize a power spectral density of the flaring period in the frequency range 10^{-4}–10^{-2} Hz, resulting in a power law of index $\alpha = 2.06 \pm 0.21$ valid for frequencies down to ∼1/day. The description of the rapid variability of a TeV blazar as a random stationary process must be taken into account by time-dependent blazar models. For PKS 2155−304 the evidence of this log-normality has been found very recently in X-rays (Giebels & Degrange 2009) and as previously mentioned, X-ray binaries and Seyfert galaxies also show lognormal variability, which is thought to originate from the accretion disk (M$^{\rm c}$Hardy et al. 2004; Lyubarskii et al. 1997; Arévalo & Uttley 2006), suggesting a connection between the disk and the jet. This variability behavior should therefore be searched for in existing blazar light curves, independently of the observed wavelength.

Acknowledgements. The support of the Namibian authorities and of the University of Namibia in facilitating the construction and operation of HESS is

gratefully acknowledged, as is the support by the German Ministry for Education and Research (BMBF), the Max Planck Society, the French Ministry for Research, the CNRS-IN2P3 and the Astroparticle Interdisciplinary Programme of the CNRS, the UK Science and Technology Facilities Council (STFC), the IPNP of the Charles University, the Polish Ministry of Science and Higher Education, the South African Department of Science and Technology and National Research Foundation, and by the University of Namibia. We appreciate the excellent work of the technical support staff in Berlin, Durham, Hamburg, Heidelberg, Palaiseau, Paris, Saclay, and in Namibia in the construction and operation of the equipment.

Appendix A: Observations summary

The journal of observations for the 2005-2007 is presented in Table A.1.

Table A.1. Summary of the 2005 to 2007 observations.

MJD	θ_z	T	n_{on}	n_{off}	Excess	σ	$\sigma/\sqrt{T}$
53618	16.9	0.87	860	3202	219.6	7.5	8.0
53637	16.6	1.09	788	2673	253.4	9.2	8.8
53638	14.7	2.18	1694	6029	488.2	12.0	8.1
53665	22.6	0.87	618	2487	120.6	4.7	5.1
53666	26.3	1.31	857	3406	175.8	5.9	5.1
53668	23.3	1.30	926	3793	167.4	5.3	4.7
53669	19.6	0.86	1027	2939	439.2	14.7	15.8
53705	55.6	0.88	512	2542	3.6	0.1	0.2
53916	13.7	0.88	993	3317	329.6	10.7	11.5
53917	11.8	0.88	933	3163	300.4	10.1	10.7
53918	10.2	1.32	1491	4596	571.8	15.5	13.5
53919	10.9	1.32	1477	4638	549.4	14.9	13.0
53941	14.4	1.31	2445	4844	1476.2	35.0	30.6
53942	13.7	1.76	2453	5766	1299.8	29.5	22.3
53943	9.8	1.33	1142	3627	416.6	12.8	11.1
53944	13.2	1.33	12 762	3563	12 049.4	172.9	149.7
53945	23.9	5.23	8037	16 352	4766.6	62.0	27.1
53946	27.7	6.61	35 874	19 881	31,897.8	251.3	97.7
53947	25.1	5.89	17 158	17 006	13 756.8	142.6	58.8
53948	27.7	2.75	5366	7957	3774.6	64.6	38.9
53950	26.6	3.51	5108	11 955	2717.0	42.8	22.9
53951	28.4	2.51	3275	8421	1590.8	30.6	19.3
53952	35.8	1.76	1786	5395	707.0	17.7	13.3
53953	44.1	0.89	670	2285	213.0	8.4	8.9
53962	27.6	0.89	534	2088	116.4	4.9	5.3
53963	19.4	1.75	1613	6145	384.0	9.5	7.1
53964	10.3	1.49	1057	4146	227.8	6.9	5.6
53965	15.7	1.57	1584	5662	451.6	11.4	9.1
53966	18.6	0.88	719	2844	150.2	5.5	5.8
53967	24.3	0.86	481	1801	120.8	5.5	5.9
53968	19.1	0.86	479	1974	84.2	3.7	4.0
53969	21.2	1.29	1738	4368	864.4	23.0	20.2
53970	20.9	0.88	690	2759	138.2	5.1	5.5
53971	19.8	1.32	1449	4313	586.4	16.3	14.2
53972	16.5	1.30	683	2499	183.2	7.0	6.1
53973	14.5	1.32	1157	4311	294.8	8.6	7.5
53974	16.2	1.76	1504	5925	319.0	8.1	6.1
53975	15.8	0.88	804	3059	192.2	6.7	7.2
53976	13.8	0.89	727	2544	218.2	8.2	8.7
53977	12.0	0.88	832	2745	283.0	10.1	10.8
53978	13.3	0.89	687	2317	223.6	8.7	9.3
53995	21.4	1.75	1712	5989	514.2	12.6	9.5
53996	25.3	1.33	680	2834	113.2	4.2	3.6
53997	26.3	1.32	1113	4382	236.6	7.0	6.1
53998	26.1	1.32	1247	4082	430.6	12.6	11.0
53999	21.4	1.32	1107	4262	254.6	7.5	6.6

Table A.1. continued.

MJD	θ_z	T	n_{on}	n_{off}	Excess	σ	$\sigma/\sqrt{T}$
54264	8.5	0.13	109	449	19.2	1.8	5.0
54265	8.5	1.05	920	3513	217.4	7.1	6.9
54266	9.3	1.39	1129	4553	218.4	6.3	5.4
54267	9.2	1.32	1095	4176	259.8	7.8	6.7
54268	10.2	0.32	261	1040	53.0	3.2	5.6
54269	9.1	0.89	908	2491	409.8	14.7	15.6
54270	10.8	0.44	565	1266	311.8	14.9	22.4
54271	7.6	0.36	308	983	111.4	6.6	11.0
54294	7.7	0.44	447	1337	179.6	9.0	13.5
54296	7.2	0.44	350	1289	92.2	4.9	7.4
54297	9.8	0.44	344	1265	91.0	4.9	7.4
54299	7.6	0.44	347	1232	100.6	5.5	8.2
54300	7.3	0.44	343	1245	94.0	5.1	7.6
54302	7.7	0.44	358	1234	111.2	6.0	9.0
54304	7.9	0.88	680	2765	127.0	4.7	5.0
54319	8.9	0.88	692	2650	162.0	6.1	6.5
54320	8.0	0.89	553	2199	113.2	4.7	5.0
54329	11.7	0.44	297	1258	45.4	2.5	3.8
54332	7.0	0.16	100	391	21.8	2.1	5.3
54375	9.4	1.27	811	3124	186.2	6.4	5.7
54376	7.9	0.68	395	1605	74.0	3.6	4.4

Notes. For each night MJD is the Modified Julian Date, θ_z the mean observation zenith angle (degrees), T the total observation live-time (hours), n_{on} the number of on-source events, n_{off} the number of off-source events (from a region five times larger than for the on-source events). The final three columns are the corresponding excess, significance (given in units of standard deviations), and the significance per square root of the live-time.

Appendix B: Spectral variability

The numerical information associated with Fig. 7 is given in Tables B.1 (left panel, grey points), B.2 (left panel, black points) and B.3 (right panel). In addition, numerical information associated with Fig. 8 is given in Table B.4.

Table B.1. Integral flux (10^{-11} cm^{-2} s^{-1}) in the 0.2−1 TeV energy range versus photon index corresponding to grey points in the left panel of Fig. 7.

Φ	Index Γ
2.36 ± 0.13	3.345 ± 0.20
3.92 ± 0.17	3.64 ± 0.16
5.33 ± 0.22	3.46 ± 0.13
8.29 ± 0.30	3.64 ± 0.10
13.82 ± 0.82	3.82 ± 0.17

Notes. Errors are statistical. See Sect. 4.1 for more details.

Table B.2. Integral flux (10^{-11} cm^{-2} s^{-1}) in the 0.2−1 TeV energy range versus photon index corresponding to black points in the left panel of Fig. 7.

Φ	Index Γ
8.4 ± 0.3	3.74 ± 0.11
16.9 ± 0.5	3.82 ± 0.10
24.5 ± 0.7	3.78 ± 0.08
37.4 ± 1.0	3.77 ± 0.08
39.7 ± 1.1	3.76 ± 0.08
46.4 ± 1.1	3.66 ± 0.08
53.5 ± 1.3	3.57 ± 0.07
78.6 ± 1.9	3.44 ± 0.06
91.8 ± 1.9	3.33 ± 0.06
101.6 ± 2.8	3.30 ± 0.07
111.7 ± 3.0	3.33 ± 0.07
154.1 ± 3.5	3.28 ± 0.06
173.1 ± 3.8	3.16 ± 0.06
198.5 ± 3.8	3.28 ± 0.05
210.9 ± 3.9	3.14 ± 0.05

Notes. Errors are statistical. See Sect. 4.1 for more details.

Table B.3. Integral flux (10^{-11} cm^{-2} s^{-1}) in the 0.2−1 TeV energy range versus photon index corresponding to the right panel of Fig. 7.

Φ	Index Γ
4.2 ± 0.1	3.52 ± 0.07
17.3 ± 0.5	3.89 ± 0.09
38.6 ± 1.1	3.80 ± 0.08
43.6 ± 1.1	3.60 ± 0.07
51.5 ± 1.3	3.53 ± 0.07
67.2 ± 1.9	3.64 ± 0.07
86.1 ± 1.9	3.38 ± 0.06
97.0 ± 1.9	3.30 ± 0.05
111.7 ± 3.0	3.33 ± 0.07
154.1 ± 3.5	3.28 ± 0.06
173.1 ± 3.8	3.16 ± 0.06
198.5 ± 3.8	3.28 ± 0.05
210.9 ± 3.9	3.14 ± 0.04

Notes. Errors are statistical. See Sect. 4.1 for more details.

Table B.4. MJD, integral flux (10^{-11} cm^{-2} s^{-1}) in the 0.2−1 TeV energy range, and photon index corresponding to the entries of Fig. 8.

MJD	Φ	Index Γ
53944.02742 ± 0.00277	188.6 ± 30.6	3.22 ± 0.09
53944.03298 ± 0.00277	184.1 ± 30.9	3.28 ± 0.09
53944.03854 ± 0.00277	191.7 ± 32.6	3.45 ± 0.09
53944.04409 ± 0.00277	252.4 ± 40.5	3.19 ± 0.09
53944.04965 ± 0.00277	237.5 ± 33.8	3.16 ± 0.08
53944.05520 ± 0.00277	212.8 ± 30.8	3.04 ± 0.08
53944.06076 ± 0.00277	190.9 ± 30.0	3.09 ± 0.09
53944.06909 ± 0.00555	99.5 ± 17.5	3.18 ± 0.10
53944.98298 ± 0.05277	9.2 ± 3.1	3.89 ± 0.18
53945.04965 ± 0.01388	34.2 ± 8.3	3.83 ± 0.13
53945.07604 ± 0.01250	42.6 ± 10.2	3.92 ± 0.13
53945.93020 ± 0.00277	206.9 ± 34.9	3.2 ± 0.10
53945.93715 ± 0.00416	190.9 ± 28.6	3.15 ± 0.09
53945.94409 ± 0.00277	171.0 ± 30.5	3.23 ± 0.10
53945.94965 ± 0.00277	161.2 ± 28.2	3.06 ± 0.10
53945.95659 ± 0.00416	173.9 ± 28.9	3.35 ± 0.09
53945.96354 ± 0.00277	179.1 ± 29.4	3.11 ± 0.10
53945.97048 ± 0.00416	127.8 ± 22.6	3.36 ± 0.10
53945.98159 ± 0.00694	91.9 ± 16.5	3.42 ± 0.10
53945.99687 ± 0.00833	101.6 ± 16.9	3.12 ± 0.10
53946.00937 ± 0.00416	104.4 ± 19.7	3.28 ± 0.11
53946.01909 ± 0.00555	92.2 ± 17.1	3.37 ± 0.10
53946.03020 ± 0.00555	79.5 ± 15.9	3.42 ± 0.11
53946.03992 ± 0.00416	105.6 ± 19.3	3.26 ± 0.10
53946.04965 ± 0.00555	114.7 ± 20.9	3.45 ± 0.10
53946.05937 ± 0.00416	110.2 ± 19.6	3.17 ± 0.10
53946.06909 ± 0.00555	97.2 ± 19.9	3.54 ± 0.11
53946.08298 ± 0.00833	75.1 ± 12.8	3.24 ± 0.10
53946.09826 ± 0.00694	75.1 ± 15.5	3.55 ± 0.12
53946.93437 ± 0.00972	58.1 ± 13.5	3.92 ± 0.13
53946.95381 ± 0.00972	50.7 ± 11.2	3.6 ± 0.12
53946.97604 ± 0.01250	39.7 ± 8.7	3.62 ± 0.12
53947.00242 ± 0.01388	34.0 ± 7.5	3.62 ± 0.12
53947.02742 ± 0.01111	40.4 ± 8.8	3.56 ± 0.12
53947.04965 ± 0.01111	43.5 ± 10.3	3.82 ± 0.13
53947.07742 ± 0.01666	45.8 ± 10.1	3.75 ± 0.12

Notes. Only points associated with an energy threshold lower than 200 GeV are considered. Errors are statistical. See Sect. 4.2 for more details.

References

Aharonian, F., Akhperjanian, A., Beilicke, M., et al. (HEGRA. Collaboration) 2002, A&A, 393, 89
Aharonian, F., Akhperjanian, A. G., Aye, K.-M., et al. (HESS Collaboration) 2005a, A&A, 437, 95
Aharonian, F., Akhperjanian, A. G., Aye, K.-M., et al. (HESS Collaboration) 2005b, A&A, 430, 865
Aharonian, F., Akhperjanian, A. G., Bazer-Bachi, A. R., et al. (HESS Collaboration) 2005c, A&A, 442, 895
Aharonian, F., Akhperjanian, A. G., Bazer-Bachi, A. R., et al. (HESS Collaboration) 2006, A&A, 457, 899
Aharonian, F., Akhperjanian, A. G., Bazer-Bachi, A. R., et al. (HESS Collaboration) 2007a, ApJ, 664, L71
Aharonian, F., Akhperjanian, A. G., Barres de Almeida, U., et al. (HESS Collaboration) 2007b, A&A, 475, L9
Aharonian, F., Akhperjanian, A. G., Barres de Almeida, U., et al. (HESS Collaboration) 2008a, Phys. Rev. Lett., 101, 170402
Aharonian, F., Akhperjanian, A. G., Barres de Almeida, U., et al. (HESS Collaboration) 2008b, Phys. Rev. Lett, 101, 261104
Aharonian, F., Akhperjanian, A. G., Anton, G., et al. (HESS Collaboration) 2009, A&A, 502, 749
Aitchinson, J., & Brown, J. A. C. 1963, The Lognormal Distribution (Cambridge: Cambridge University Press)
Albert, J., Aliu, E., Anderhub, H., et al. (MAGIC Collaboration) 2007, ApJ, 669, 862
Arévalo, P., & Uttley, P. 2006, MNRAS, 367, 801
Begelman, M. C., Fabian, A. C., & Rees, M. J. 2008, MNRAS, 384, L19
Boutelier, T., Henri, G., & Petrucci, P. O. 2008, MNRAS, 390, 73
Chadwick, P. M., Lyons, K., McComb, T. J. L., et al. 1999, ApJ, 513, 161
Cheng, K. S., Zhang, X., & Zhang, L. 2000, ApJ, 537, 80
Djannati-Ataï, A., Piron, F., Barrau, A., et al. 1999, A&A, 350, 17
Edelson, R. A., & Krolik, J. H. 1988, ApJ, 333, 646
Edelson, R., Turner, T. J., Pounds, K., et al. 2002, ApJ, 568, 610
Fichtel, C. 1996, A&AS, 120, 23
Fossati, G., Celotti, A., Chiaberge, M., et al. 2000, ApJ, 541, 153
Ghisellini, G., & Tavecchio, F. 2008, MNRAS, 386, 28
Giebels, B., & Degrange, B. 2009, A&A, 503, 797
Giebels, B., Bloom, E. D., Focke, W., et al. 2002, ApJ, 571, 763
Giebels, B., et al. (HESS Collaboration) 2005, Proc. Annual meeting of the French Society of Astronomy and Astrophysics (Strasbourg), 527
Giebels, B., Dubus, G., & Khelifi, B. 2007, A&A, 462, 29
Gleissner, T., Wilms, J., Pottschmidt, K., et al. 2004, A&A, 414, 1091
Katarzyński, K., Lenain, J.-P., Zech, A., Boisson, C., & Sol, H. 2008, MNRAS, 390, 371
Kataoka, J. 1999, X-ray Study of Rapid Variability in TeV Blazars and the Implications on Particle Acceleration in Jets, ISAS RN 710
Kataoka, J., Takahashi, T., Wagner, S. J., et al. 2001, ApJ, 560, 659
Lemoine-Goumard, M., Degrange, B., & Tluczykont, M. 2006, Astropart. Phys., 25, 195
Levinson, A. 2007, ApJ, 671, L29
Lichti, G. G., Bottacini, E., Ajello, M., et al. 2008, A&A, 486, 721
Lyubarskii, Y. E. 1997, MNRAS, 292, 679
Maraschi, L., et al. 2002, Proc. Symposium "New Visions of the X-ray Universe in the XMM-Newton and Chandra Era", ESTEC 2001 [arXiv:0202418v1]
M^{c}Hardy, I. M., Papadakis, I. E., Uttley, P., Page, M. J., & Mason, K. O. 2004, MNRAS, 348, 783
Nandikotkur, G., Jahoda, K. M., Hartman, R. C., et al. 2007, ApJ, 657, 706
Nandra, K., George, I. M., Mushotzky, R. F., Turner, T. J., & Yaqoob, T. 1997, ApJ, 476, 70
Paltani, S., Courvoisier, T. J.-L., Blecha, A., & Bratschi, P. 1997, A&A, 327, 539
Piron, F., Djannati-Atai, A., Punch, M., et al. 2001, A&A, 374, 895
Poutanen, J., & Stern, B. E. 2008, Int. J. Mod. Phys., 17, 1619
Rutman, J. 1978, Proc. IEEE, 66, 1048
Simonetti, J. H., Cordes, J. M., & Heeschen, D. S. 1985, ApJ, 296, 46
Sreekumar, P., Bertsch, D. L., Dingus, B. L., et al. 1998, ApJ, 494, 523
Stecker, F. W., & Salamon, M. H. 1996, ApJ, 464, 600
Stern, B. E. 2003, MNRAS, 345, 590
Stern, B. E., & Poutanen, J. 2006, MNRAS, 372, 1217
Spada, M., Ghisellini, G., Lazzati, D., & Celotti, A. 2001, MNRAS, 325, 1559
Takahashi, T., Kataoka, J., Madejski, G., et al. 2000, ApJ, 542, L105
Uttley, P. 2004, MNRAS, 347, L61
Uttley, P., & M^{c} Hardy, I. M. 2001, MNRAS, 323, L26
Uttley, P., M^{c} Hardy, I. M., & Vaughan, S. 2005, MNRAS, 359, 345
van der Klis, M. 1997, Proc. Conf. Statistical Challenges in Modern Astronomy II, Pennsylvania State University (Berlin: Springer-Verlag), 321
Vaughan, S., Fabian, A. C., & Nandra, K. 2003a, MNRAS, 339, 1237
Vaughan, S., Edelson, R., Warwick, R. S., & Uttley, P. 2003b, MNRAS, 345, 1271
White, R. J., & Peterson, B. M. 1994, PASP, 106, 879
Zhang, Y. H., Celotti, A., Treves, A., et al. 1999, ApJ, 527, 719

[1] Max-Planck-Institut für Kernphysik, PO Box 103980, 69029 Heidelberg, Germany
e-mail: francesca.volpe@mpi-hd.mpg.de; volpe@llr.in2p3.fr
[2] Yerevan Physics Institute, 2 Alikhanian Brothers St., 375036 Yerevan, Armenia
[3] Centre d'Étude Spatiale des Rayonnements, CNRS/UPS, 9 Av. du Colonel Roche, BP 4346, 31029 Toulouse Cedex 4, France
[4] Universität Hamburg, Institut für Experimentalphysik, Luruper Chaussee 149, 22761 Hamburg, Germany
[5] Institut für Physik, Humboldt-Universität zu Berlin, Newtonstr. 15, 12489 Berlin, Germany
[6] LUTH, Observatoire de Paris, CNRS, Université Paris Diderot, 5 place Jules Janssen, 92190 Meudon, France
[7] CEA Saclay, DSM/IRFU, 91191 Gif-Sur-Yvette Cedex, France
[8] University of Durham, Department of Physics, South Road, Durham DH1 3LE, UK
[9] Unit for Space Physics, North-West University, Potchefstroom 2520, South Africa
[10] Laboratoire Leprince-Ringuet, École Polytechnique, CNRS/IN2P3, 91128 Palaiseau, France
[11] Laboratoire d'Annecy-le-Vieux de Physique des Particules, Université de Savoie, CNRS/IN2P3, 74941 Annecy-le-Vieux, France
[12] Astroparticule et Cosmologie (APC), CNRS, Université Paris 7 Denis Diderot, 10 rue Alice Domon et Léonie Duquet, 75205 Paris Cedex 13, France UMR 7164 (CNRS, Université Paris VII, CEA, Observatoire de Paris)
e-mail: santiago.pita@apc.univ-paris7.fr
[13] Dublin Institute for Advanced Studies, 5 Merrion Square, Dublin 2, Ireland
[14] Landessternwarte, Universität Heidelberg, Königstuhl, 69117 Heidelberg, Germany
[15] Laboratoire de Physique Théorique et Astroparticules, Université Montpellier 2, CNRS/IN2P3, CC 70, Place Eugène Bataillon, 34095 Montpellier Cedex 5, France
[16] Universität Erlangen-Nürnberg, Physikalisches Institut, Erwin-Rommel-Str. 1, 91058 Erlangen, Germany
[17] Laboratoire d'Astrophysique de Grenoble, INSU/CNRS, Université Joseph Fourier, BP 53, 38041 Grenoble Cedex 9, France
[18] Institut für Astronomie und Astrophysik, Universität Tübingen, Sand 1, 72076 Tübingen, Germany
[19] LPNHE, Université Pierre et Marie Curie Paris 6, Université Denis Diderot Paris 7, CNRS/IN2P3, 4 place Jussieu, 75252 Paris Cedex 5, France
[20] Charles University, Faculty of Mathematics and Physics, Institute of Particle and Nuclear Physics, V Holešovičkách 2, 180 00 Prague 8, Czech Republic
[21] Institut für Theoretische Physik, Lehrstuhl IV: Weltraum und Astrophysik, Ruhr-Universität Bochum, 44780 Bochum, Germany
[22] University of Namibia, Department of Physics, Private Bag 13301, Windhoek, Namibia
[23] Obserwatorium Astronomiczne, Uniwersytet Jagielloński, ul. Orla 171, 30-244 Kraków, Poland
[24] Nicolaus Copernicus Astronomical Center, ul. Bartycka 18, 00-716 Warsaw, Poland
[25] School of Physics & Astronomy, University of Leeds, Leeds LS2 9JT, UK
[26] School of Chemistry & Physics, University of Adelaide, Adelaide 5005, Australia
[27] Toruń Centre for Astronomy, Nicolaus Copernicus University, ul. Gagarina 11, 87-100 Toruń, Poland
[28] Instytut Fizyki Jądrowej PAN, ul. Radzikowskiego 152, 31-342 Kraków, Poland
[29] Astronomical Observatory, The University of Warsaw, Al. Ujazdowskie 4, 00-478 Warsaw, Poland
[30] Institut für Astro- und Teilchenphysik, Leopold-Franzens-Universität Innsbruck, 6020 Innsbruck, Austria
[31] Oskar Klein Centre, Department of Physics, Stockholm University, Albanova University Center, 10691 Stockholm, Sweden
[32] Oskar Klein Centre, Department of Physics, Royal Institute of Technology (KTH), Albanova, 10691 Stockholm, Sweden
[33] Department of Physics and Astronomy, The University of Leicester, University Road, Leicester, LE1 7RH, UK
[34] European Associated Laboratory for Gamma-Ray Astronomy, jointly supported by CNRS and MPG

Chapter 4
Two Multi-wavelength studies of PKS 2155-304

The people grow tired of a confusion whose end is not in sight.
Alexis de Tocqueville, 'Democracy in America'

Abstract

The interest of multi-wavelength observations (MWL) of VHE γ-ray emitters, and not just AGN, spans the whole electromagnetic spectrum, from radio wave observations around $\sim 100\,\mathrm{neV}$ up to $10-100\,\mathrm{TeV}$ γ-rays. This is mainly a consequence from the fact that (i) broad energetic particle distributions are expected from cosmic accelerators, creating a broad radiative spectrum as well and (ii) the intrinsic photon fields have to be defined in order to estimate the characteristics of the underlying particle distribution which interacts with these "calorimetric" fields. The accurate description of the SED, and how the various continua are related over time, is of paramount importance to test theoretical scenarios which necessarily model the emission over many decades in energy. It yields often bewildering data sets where expected correlations disappear, new ones appear, and official interpretations seem only limited by imagination and journal referees. MWL observations are also sometimes the only available means to infer the nature of unidentified γ-ray sources, either through the characterization of the SED, or when a brighter counterpart is found, to search for features such as variability in its flux. ACT arrays now often dedicate a significant amount of their limited observation time to MWL campaigns, mostly on already known VHE emitters, which come with additional constraints compared to observational programs aiming at discovering new sources. These are either triggered by an unusual activity of a known source at a wavelength of interest as in §4.3, or planned well in advance to ensure the availability of the needed observational resources independently of what the target's state will be (as in §4.6).

4.1 Introduction

The characterization of the SED, as simultaneously as possible, tells us what the relative importance is of the emitted continua, and the correlation of the variability of the various continua gives insights into how they are related. As described in §1, the X-rays are one of the most important bands in the SED of VHE emitters. The X-ray counterparts of VHE emitters have usually steep spectra ($\Gamma_X > 2$) which do not connect with the VHE part of the spectrum when extrapolated. X-rays are hence thought to be synchrotron emission of the most energetic electrons in the jet, providing constraints in emission models on the maximal Lorentz factor of the underlying distribution. The X-rays are also the lowest energetic emission taken unanimously seriously into consideration as constraint when fitting a SED with a model, since (i) sub-keV fluxes have not (yet) been seen to correlate with more energetic counterparts (further discussed in §4.1.2) and (ii) the lack of such correlations (or fit mismatches) can be easily hand-waved away through invoking larger, extended unresolved structures and/or complications arising from possible unresolved thermal components or host galaxy emission. X-ray observations are not guaranteed, as they require to submit proposals during calls for specific instruments which have oversubscription factors of $5-20$. Still the H.E.S.S. collaboration managed to secure $O(500\,\mathrm{ksec})$ of observations with *RXTE*, $O(50\,\mathrm{ksec})$ with *Swift* and slightly less on more constrained X-ray telescopes such as *XMM*.

4.1.1 VHE γ-ray /X-ray correlations

Since all the VHE γ-ray emitting BL Lacs are X-ray selected objects, the correlations between the two energy bands are a prime investigation tool since they show the interplay between

the two competing cooling mechanisms. X-rays are also a relatively accessible energy range immediately below the VHE γ-rays, given the wide variety of space-based instruments available for that purpose[1], and RXTE has been the working horse in that respect. Needless to say that the outcome of such joint studies with *Fermi*, are eagerly awaited , though its observational power is its wide field of view and duty cycle, since its effective area does not allow time series to be established at timescales of minutes for HBLs.

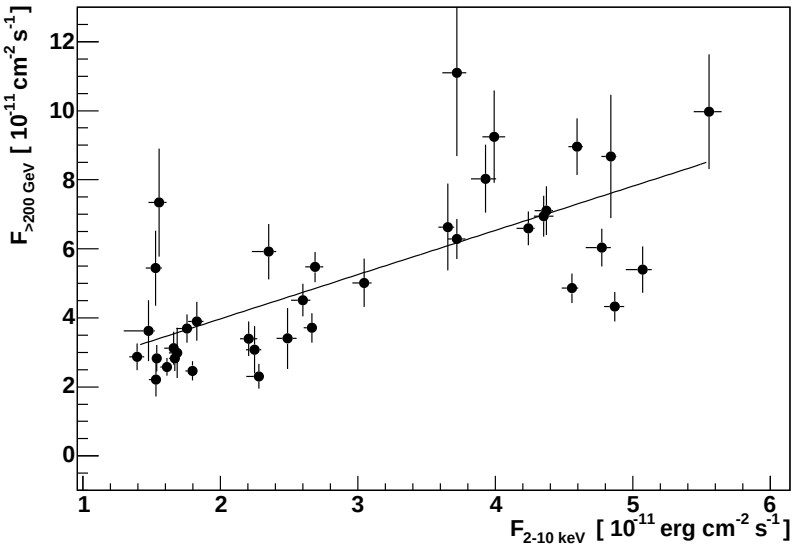

Figure 4.1: *Correlation plot of simultaneous observations of PKS 2155−304 in the VHE γ-ray flux (E > 200 GeV) measured by H.E.S.S. and the 2-10 keV flux measured by RXTE, for the 2004 MWL campaign. The correlation factor is* $\rho = 0.71 \pm 0.05$. *This was the first correlated H.E.S.S. VHE/X-ray data set, and was only the 4th VHE AGN for which this was observed.*

VHE/X-ray flux correlations during flares have been rather ubiquitous in all of the simultaneous campaigns where VHE γ-ray flux variations of order unity occur [Katarzyński et al., 2005], except for a single case (known as Orphan flares [Krawczynski et al., 2004]). Correlation factors between a VHE and an X-ray lightcurve are usually high (with Pearson's correlation $\rho \geq 0.7$, e.g. Figure 4.1 for a correlation observed in a high VHE state in PKS 2155−304.) for flares. Time lags in time series have been a very powerful tool to put additional constraints on the parameters that define radiative cooling. For instance, energy-resolved time lags within the synchrotron radiation, which is due to the energy-dependent cooling timescale, sets a specific constraint [Takahashi et al., 1999; Giebels et al., 2002] between the magnetic field B and the doppler factor δ. The homogenous SSC model implies a lag of the comptonized emission of the order of $R/c\delta$ since the synchrotron emission has to fill the emission region of size R with photon targets, such that an upper limit on a lag can in some cases provide slightly stronger constraints on that parameter. Thus the investigation of correlated flux and spectral correlations between the X-rays and the γ-rays through multiwavelength studies is of paramount importance, and are mostly carried out simultaneously with RXTE and/or Swift, and a few constraints have to be obeyed to in order to get a meaningful result such as truly overlapping exposures and obtaining a significant measurement in all bands; the ACTs involved in such observations are usually the most constrained instruments in almost all aspects, so their limitations drive the observation strategy. Only a few of the currently known VHE γ-ray emitters are sufficiently bright for all high-energy instruments involved to get a well-defined and unambiguous SED.

4.1.2 VHE γ-ray -optical correlations

Besides the available ground-based optical telescopes, the most recent X-ray observatories have integrated an optical telescope into their platform, avoiding the need for ground-based optical observations, with their inherent limitations, during simultaneous multi-wavelength campaigns. There is so far no evidence for a lagged or non-lagged correlation between the optical and

[1] However the solar and anti-solar region exclusion constraints for a.o. XMM, INTEGRAL and Suzaku make them very ineffective for simulaneous observations with ground-based instruments. Future missions are likely to follow a similar path..

the X-ray/γ-ray regime on timescales up to ∼24 h in all VHE γ-ray emitting blazars, despite intense monitoring campaigns. A few examples of such campaigns on some specific HBL with no evidence for short timescale optical correlations are those on 1ES 1959+650 [Krawczynski et al., 2004]; Mrk 421 [Giebels et al., 2007; Acciari et al., 2009b]; or Mrk 501 [Albert et al., 2007]). Given the rich history provided by the archival campaigns with negative results on this search, a claim of evidence for an optical correlation with higher energy radiation should be taken with more than a grain of salt since its statistical significance would need to take into account trial factors at this point..

This lack of correlation is at odds with the single radiative population model for the whole SED, and suggests that there is a either a low-energy cutoff in the electron distribution, or that there is more than one radiative population associated with the optical emission. Estimating the optical contribution of the non-thermal radiation is however challenging since the host galaxy contribution, and probably other extended sources, have to be subtracted. Therefore the lack of optical correlation has generally been downplayed in the context of SED modelling by single-zone models. This should however be where time-dependent jet models become important, since higher order statistical moments could be probes for their time-dependent predictions; the model described in Boutelier et al. [2008] is interesting in that context as it does not predict rapid correlations but rather a slow onset due to the pileup of optical emitting electrons from previous injections.

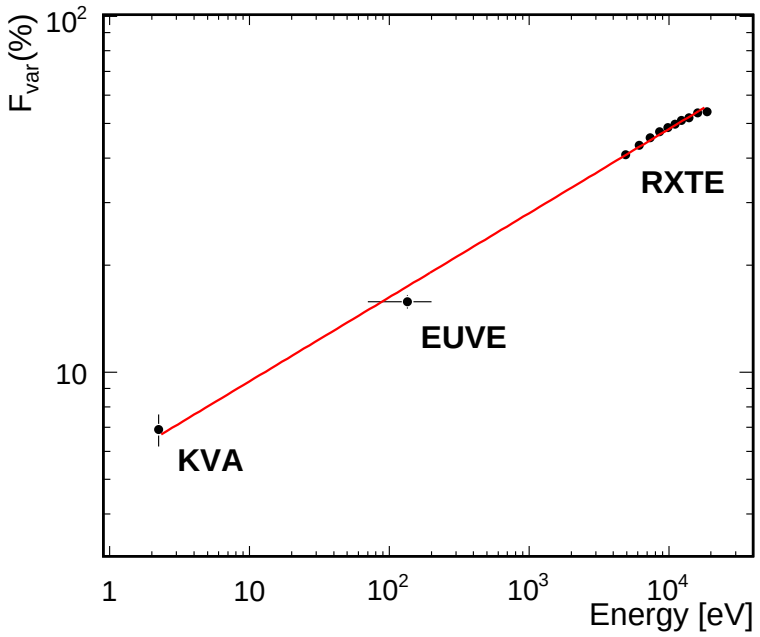

Figure 4.2: *Energy-dependency of the normalized excess variance F_{var} of Mrk 421 during a MWL campaign, showing a clear correlation from the optical up to the X-rays. The proportionality has a power law behaviour $F_{var} \propto E^{0.25}$.*

Interestingly however, there seems to be a clear energy-dependent variability correlation in at least two sources. The excess variance in PKS2155-304 Maraschi et al. [2002] and in Mrk 421 Giebels et al. [2007]; Acciari et al. [2009b] (Figure 4.2) seems to follow a power law. This would suggest that if the fluxes are not correlated between these two components, their fluctuations might be. This requires more investigation in future campaigns with improved spectrophotometry such as millimagnitude photometry in order to measure a significant excess variance, or a lack thereof, at the levels of a few percent for relatively faint sources.

4.2 Spectral Energy Distributions: PKS 2155-304

The first MWL campaign carried out by H.E.S.S. was based on the detection of PKS 2155−304 at the 5σ level within 1h. With our current knowledge, this turns out to be its low/quiescent state, but at that time it was taken as a probable high flux state. Optical (ROTSE) and X-ray (RXTE) observations were subsequently carried out over 2 viewing periods for a total of 16

good observation nights. At that time, only 2 objects were known to exhibit X-ray/VHE γ-ray correlations.

From all the observed wavebands, no clear correlations were apparent (Fig. 4 in §4.3), despite some significant variability in e.g. the X-ray fluxes. During a high flux state recorded in 2004 by H.E.S.S. and RXTE, the fluxes appeared indeed to correlate (Fig. 4.1, from Giebels & the Hess collaboration 2007). The significant scatter in the data points make the correlation appear only at high amplitudes of the VHE emission.

The SED clearly indicated that both the X-rays and the optical measurement were well below the highest archival values, and mostly compatible with the lowest fluxes ever seen in those wavebands. This brought up the conclusion that PKS 2155−304 was at that point in a low/quiescent state, and that the VHE emission was hence also that of a non-flaring state, which was not a usual notion at that time and one of the main results here. The existence of such a state was postulated by Stecker & Salamon [1996] in order to explain the extragalactic γ-ray background at 0.03-100 GeV detected by EGRET (Fichtel 1996; Sreekumar et al. 1998 but see the less intense and softer Fermi spectrum derived in Abdo et al. 2010c) as coming from quiescent-state unresolved blazars. Such a background has not yet been detected in the VHE range, as it is technically difficult with the atmospheric Čerenkov technique to find an isotropic extragalactic emission and even more to distinguish it from the cosmic-ray electron flux [Aharonian et al., 2008b].

As pointed out by Cheng et al. [2000] emission mechanisms might be simpler to understand during quiescent states in blazars, and they are also the most likely state to be found observationally. In the X-ray band, the existence of a steady underlying emission has also been invoked for two other VHE emitting blazars (Mrk 421, Fossati et al. 2000; and 1ES 1959+650, Giebels et al. 2002). Being able to separate, and detect, flaring and nonflaring states in VHE γ-rays is probably more important for such studies than is currently stated. The evidence of the existence of a lowest flux emission level in PKS 2155−304 presented in §3.4 (while the current sensitivity of the H.E.S.S. array is not sufficient to establish the statistical nature of the fluctuations seen in that state), corroborated this notion, as well as the fact that most of the HE light curves of VHE emitters are not variable [Abdo et al., 2009c].

4.3 "Multi-wavelength observations of PKS 2155−304 with H.E.S.S."

A&A 442, 895–907 (2005)
DOI: 10.1051/0004-6361:20053353

Astronomy & Astrophysics

Multi-wavelength observations of PKS 2155-304 with HESS

F. Aharonian[1], A. G. Akhperjanian[2], A. R. Bazer-Bachi[3], M. Beilicke[4], W. Benbow[1], D. Berge[1], K. Bernlöhr[1,5], C. Boisson[6], O. Bolz[1], V. Borrel[3], I. Braun[1], F. Breitling[5], A. M. Brown[7], P. M. Chadwick[7], L.-M. Chounet[8], R. Cornils[4], L. Costamante[1,20], B. Degrange[8], H. J. Dickinson[7], A. Djannati-Ataï[9], L. O'C. Drury[10], G. Dubus[8], D. Emmanoulopoulos[11], P. Espigat[9], F. Feinstein[12], G. Fontaine[8], Y. Fuchs[13], S. Funk[1], Y. A. Gallant[12], B. Giebels[8], S. Gillessen[1], J. F. Glicenstein[14], P. Goret[14], C. Hadjichristidis[7], M. Hauser[11], G. Heinzelmann[4], G. Henri[13], G. Hermann[1], J. A. Hinton[1], W. Hofmann[1], M. Holleran[15], D. Horns[1], A. Jacholkowska[12], O. C. de Jager[15], B. Khélifi[1], Nu. Komin[5], A. Konopelko[1,5], I. J. Latham[7], R. Le Gallou[7], A. Lemière[9], M. Lemoine-Goumard[8], N. Leroy[8], T. Lohse[5], J. M. Martin[6], O. Martineau-Huynh[16], A. Marcowith[3], C. Masterson[1,20], T. J. L. McComb[7], M. de Naurois[16], S. J. Nolan[7], A. Noutsos[7], K. J. Orford[7], J. L. Osborne[7], M. Ouchrif[16,20], M. Panter[1], G. Pelletier[13], S. Pita[9], G. Pühlhofer[1,11], M. Punch[9], B. C. Raubenheimer[15], M. Raue[4], J. Raux[16], S. M. Rayner[7], A. Reimer[17], O. Reimer[17], J. Ripken[4], L. Rob[18], L. Rolland[16], G. Rowell[1], V. Sahakian[2], L. Saugé[13], S. Schlenker[5], R. Schlickeiser[17], C. Schuster[17], U. Schwanke[5], M. Siewert[17], H. Sol[6], D. Spangler[7], R. Steenkamp[19], C. Stegmann[5], J.-P. Tavernet[16], R. Terrier[9], C. G. Théoret[9], M. Tluczykont[8,20], G. Vasileiadis[12], C. Venter[15], P. Vincent[16], H. J . Völk[1], and S. J. Wagner[11]

[1] Max-Planck-Institut für Kernphysik, Heidelberg, Germany; [2] Yerevan Physics Institute, Armenia; [3] Centre d'Étude Spatiale des Rayonnements, CNRS/UPS, Toulouse, France; [4] Universität Hamburg, Institut für Experimentalphysik, Germany; [5] Institut für Physik, Humboldt-Universität zu Berlin, Germany; [6] LUTH, UMR 8102 du CNRS, Observatoire de Paris, Section de Meudon, France; [7] University of Durham, Department of Physics, UK; [8] Laboratoire Leprince-Ringuet, IN2P3/CNRS, École Polytechnique, Palaiseau, France, e-mail: berrie@poly.in2p3.fr; [9] APC, Paris, France⋆; [10] Dublin Institute for Advanced Studies, Ireland; [11] Landessternwarte, Königstuhl, Heidelberg, Germany; [12] Laboratoire de Physique Théorique et Astroparticules, IN2P3/CNRS, Université Montpellier II, France; [13] Laboratoire d'Astrophysique de Grenoble, INSU/CNRS, Université Joseph Fourier, France; [14] DAPNIA/DSM/CEA, CE Saclay, Gif-sur-Yvette, France; [15] Unit for Space Physics, North-West University, Potchefstroom, South Africa; [16] Laboratoire de Physique Nucléaire et de Hautes Énergies, IN2P3/CNRS, Universités Paris VI & VII, Paris, France; [17] Institut für Theoretische Physik, Lehrstuhl IV: Weltraum und Astrophysik, Ruhr-Universität Bochum, Germany; [18] Institute of Particle and Nuclear Physics, Charles University, Prague, Czech Republic; [19] University of Namibia1, Windhoek, Namibia;[20] European Associated Laboratory for Gamma-Ray Astronomy, jointly supported by CNRS and MPG

Received 2 May 2005 / Accepted 22 June 2005

ABSTRACT

The High Energy Stereoscopic System (HESS) has observed the high-frequency peaked BL Lac object PKS 2155−304 in 2003 between October 19 and November 26 in Very High Energy (VHE) γ-rays ($E \geq 160$ GeV for these observations). Observations were carried out simultaneously with the Proportional Counter Array (PCA) on board the Rossi X-ray Timing Explorer satellite (RXTE), the Robotic Optical Transient Search Experiment (ROTSE) and the Nançay decimetric radiotelescope (NRT). Intra-night variability is seen in the *VHE* band, the source being detected with a high significance on each night it was observed. Variability is also found in the X-ray and optical bands on kilosecond timescales, along with flux-dependent spectral changes in the X-rays. A transient X-ray event with a 1500 s timescale is detected, making this the fastest X-ray flare seen in this object. No correlation can be established between the X-ray and the γ-ray fluxes, or any of the other wavebands, over the small range of observed variability. The average HESS spectrum shows a very soft power law shape with a photon index of $3.37 \pm 0.07_{\rm stat} \pm 0.10_{\rm sys}$. The energy outputs in the 2–10 keV and in the VHE γ-ray range are found to be similar, with the X-rays and the optical fluxes at a level comparable to some of the lowest historical measurements, indicating that PKS 2155−304 was in a low or quiescent state during the observations. Both a leptonic and a hadronic model are used to derive source parameters from these observations. These parameters are found to be sensitive to the model of Extragalactic Background Light (EBL) that attenuates the VHE signal at this source's redshift ($z = 0.117$).

Key words. galaxies: active – gamma rays: observations – X-rays: galaxies – radiation mechanisms: non thermal

⋆ UMR 7164 (CNRS, Université Paris VII, CEA, Observatoire de Paris).

1. Introduction

The innermost regions of active galactic nuclei, where the largest part of their luminosity is emitted, can be probed through observations of their flux variability at different wavelengths. The physical processes in their central engines and jets are usually considered the main candidates for the origin of the observed variability. Measurements of correlated variability, spectral variations and time lags across the broad-band observations allow modelling of particle distributions and their radiation processes, as well as probing the acceleration mechanisms that are involved.

PKS 2155−304 is probably the most prominent and best-studied blazar-type Active Galactic Nuclei (AGN) in the Southern Hemisphere. The emission of PKS 2155−304, its possible variability patterns, as well as correlations across all wavebands, have been studied exhaustively over the past 20 years (see e.g. Urry et al. 1997). Its first detection at *VHE* γ-rays by the Durham Mk VI telescopes (Chadwick et al. 1999) classified it as a TeV blazar, like the northern hemisphere BL Lac objects Mkn 421, Mkn 501, H 1426+428, or 1ES 1959+650. Its redshift of $z = 0.117$ makes it the second most distant confirmed TeV blazar after H 1426+428 ($z = 0.129$). PKS 2155−304 was the brightest BL Lac object in the EUVE all-sky survey (Marshall et al. 1995). This source was confirmed as a high energy γ-ray emitter by HESS (Aharonian et al. 2005, AH04 hereafter) at the 45σ significance level, when strong detections were reported for each of the dark periods of observations.

Here we report on simultaneous HESS VHE γ-ray, RXTE/PCA X-ray, ROTSE optical, and NRT decimetric observations of PKS 2155−304 during the dark periods of October and November 2003. No simultaneous multi-wavelength campaign had before included an Atmospheric Cherenkov Telescope (ACT) that could sample the evolution of the high energy component of the spectral energy distribution (SED) of this object. We also include EGRET archival data, and other archival radio through X-ray data obtained from the NASA/IPAC Extragalactic Database (NED). Details of the observations and data reduction/analysis are given in Sect. 2. Light curves and spectra are described in Sect. 3. The attenuation of the HESS spectrum by the EBL and an interpretation of the data using a leptonic and a hadronic model are discussed in Sect. 4.

2. Observations and data analysis

2.1. HESS

2.1.1. HESS detector

In its first phase, the HESS array consists of four atmospheric Cherenkov telescopes operating in stereoscopic mode. However, the data shown here were taken during the construction of the system, initially with two telescopes, with one more as of mid-September, 2003. The fourth and final telescope was added to the array in December 2003, subsequent to the data presented here. Each telescope has a tessellated 13 m-diameter (107 m^2 surface area) mirror which focuses the Cherenkov light from the showers of secondary particles created by the interaction of γ-rays in the atmosphere onto a camera in the focal plane. This camera consists of 960 photomultipliers, each with a pixel size of 0.16°, giving a field of view of 5°. For the data sets presented here the γ-ray trigger threshold is ≈100 GeV and the spectral threshold is 160 GeV with an energy resolution ≃15%. The experiment is located in the Khomas highlands in Namibia, (23° S, 15° E, 1800 m a.s.l.). A detailed description of the layout and the components of the telescope optical systems, including the segmented mirror with its support structure, the mirror facets for each telescope and the Winston cone light concentrators in front of the PMT camera can be found in Bernlöhr et al. (2003), and a description of the mirror alignment is given in Cornils et al. (2003). For details on the camera calibration see Aharonian et al. (2004a). The trigger system is described in Funk et al. (2004). Early reports of HESS have been given elsewhere (see e.g. Hofmann 2002).

2.1.2. Observations

In the beginning of the observation period of October 2003, a single 5σ detection by HESS achieved in 1 h, triggered an approved RXTE ToO (Target of Opportunity) on this target. The results presented here are based on observations carried out in 2003 between October 19 and November 26.

The data were taken in the *Wobble* mode where the source direction is positioned ±0.5° in declination relative to the centre of the field of view of the camera during observations. This allows for both on-source observations and simultaneous estimation of the background induced by charged cosmic rays. The data reported here are selected and analyzed with the "standard analysis" described in Sect. 4 of AH04. The background is estimated here by using all events passing cuts in a ring around the source, as described in Sect. 4.3 in AH04. The runs passing the quality selection criteria total 32.4 h of livetime on the source. The total two-dimensional significance sky map is shown in Fig. 1, along with a graph showing the θ^2 distribution (where θ^2 is the square of the angular difference between the reconstructed shower position and the source position) of the 1764 excess events observed. This yields a detection at the 34.3σ level, at the average rate of $0.91\gamma/$ min and a significance of $6.0\sigma/\sqrt{\text{h}}$.

The methods used here for reconstructing the energy of each event and for determining a spectrum are described in Sect. 6 of AH04. The measured time-average spectrum is fitted by a power law of the form $\mathrm{d}N/\mathrm{d}E = I_0(E/1\ \text{TeV})^{-\Gamma}$ with I_0 the flux normalization at 1 TeV and Γ the photon index. The photon index obtained from the time-averaged spectrum is then used as a fixed parameter to estimate the integral flux above 300 GeV for each run. This integrated flux takes into account the effective area and threshold variations due to the source moving through the sky, giving more reliable variability information than counting rates in units of γ-rays/min. Overall systematic errors are estimated to be 20% for the integral flux and ≃0.1 for the photon index.

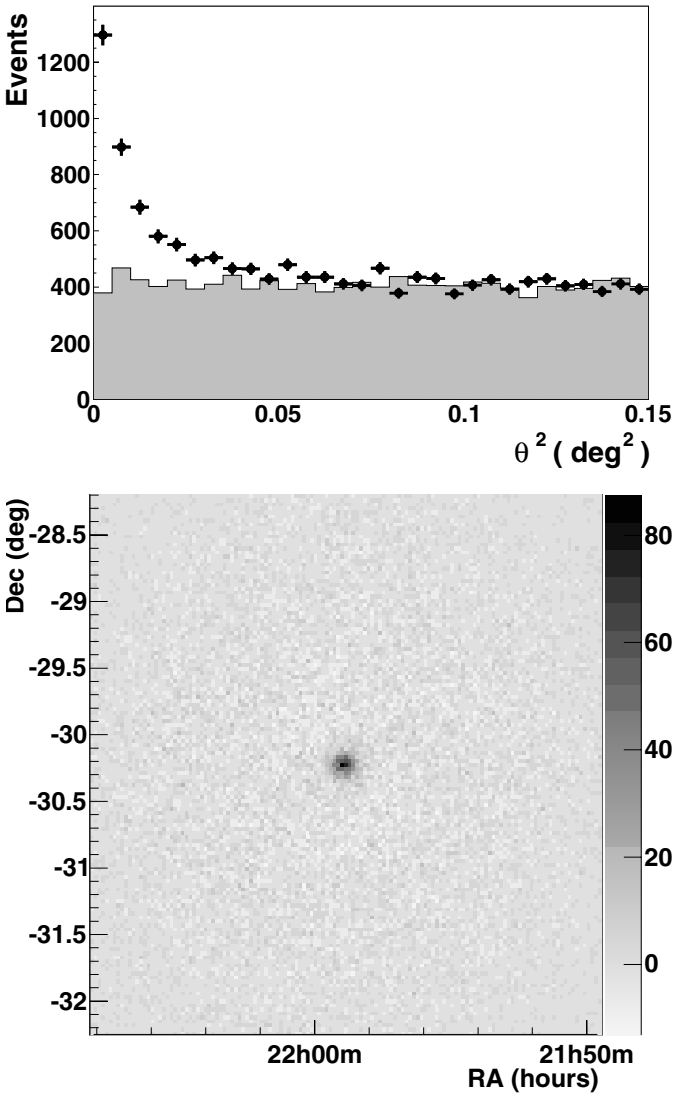

Fig. 1. *Top*: the distribution of θ^2 for on-source events (points) and normalized off-source events (shaded) for the observations in October and November 2003. *Bottom*: the two-dimensional distribution of excess events observed in the direction of PKS 2155-304. The bins are not correlated and represent the actual distribution of observed γ-rays on the sky. The right hand scale is the number of counts.

2.2. RXTE

The PCA (Jahoda et al. 1996) units of RXTE observed PKS 2155−304 between October 22 and November 23 of 2003 with exposures of typically 10 ks in October and ≃1 ks in November. The STANDARD2 data were extracted using the ftools in the HEASOFT 5.3.1 analysis software package provided by NASA/GSFC and filtered using the RXTE Guest Observer Facility (GOF) recommended criteria. The changing Proportional Counter Units (PCU0/2/3) configuration throughout the observations was taken into account in the data reduction, and only the signals from the top layer (X1L and X1R) were used. When reducing the PCUs individually to establish the time-averaged spectrum, the average spectral fit parameters are similar within error bars but with a systematically higher χ^2 for spectral fits performed on PCU0 data alone. On shorter timescales this effect becomes negligible and PCU0 contributes to the statistical significance of the flux measurement. Therefore all PCUs were kept for the overall light curve which is binned in 400 s bins, but only PCU2 and PCU3 are used for the analysis of data segments that are simultaneous with HESS runs and for the time-averaged spectrum.

The average spectrum used in the SED is derived by combining PCU2 and PCU3 spectra using the `addspec` tool weighted by the counts information delivered by `fstatistic` and then the corresponding response matrices were combined with `addrmf`. The faint-background model was used and only the 3–40 PHA channel range was kept in `XSPEC v. 11.3.1`, or approximately 2–20 keV.

To build a light curve in units of integrated flux in the 2–10 keV band, spectral data were derived from 400 s bins to probe short timescales with adequate statistical accuracy. These segments are then fitted by a power law in XSPEC with PCU configuration-dependent response matrices generated by the ftool `pcarsp v. 10.1` and a fixed column density of $N_{\rm H} = 1.7 \times 10^{20}\,{\rm cm}^{-2}$ obtained from PIMMS[1]. This yields the flux and the error (corresponding to the 1σ confidence level) on the flux reported in the light curves in Fig. 2, in units of $10^{-11}\,{\rm erg\,cm^{-2}\,s^{-1}}$ in the 2–10 keV band. The fits did not improve by using a broken power-law for the 400 s binned observations.

2.3. ROTSE

The ROTSE-III array is a worldwide network of four 0.45 m robotic, automated telescopes built for fast (≈6 s) response to GRB triggers from satellites such as HETE-2 (High Energy Transient Explorer 2) and Swift. The ROTSE-III telescopes have a wide (1.85°×1.85°) field of view imaged onto a Marconi 2048 × 2048 pixel back-illuminated thinned CCD and are operated without filters. The ROTSE-III systems are described in detail in Akerlof et al. (2003). At the time of the observations of PKS 2155−304 in October and November 2003, two ROTSE-III telescopes were operational in the Southern hemisphere: ROTSE-IIIa located at the Siding Spring Observatory, Australia and ROTSE-IIIc at the HESS site. The ROTSE-IIIc telescope is located in the centre of the HESS telescope array. A 30% share of the total observation time is available to the HESS collaboration, which has been used to perform an automated monitoring programme of blazars, including objects that are being observed with the HESS telescopes. Both telescopes participated in the observation campaign on PKS 2155−304 in October and November 2003.

The telescopes observed PKS 2155−304 typically 10 times per night taking sequences of 2 frames with 60 s exposures with a slight dithering of the pointing to reduce the impact of individual noisy pixels. The typical limiting magnitude, depending on the sky conditions, is $18.5^{\rm mag}$. Overall, 323 bias-subtracted and flat-fielded frames have passed visual inspection and are used to produce a light curve. A total of 6 frames were rejected due to the presence of stray light from Jupiter.

[1] See `http://legacy.gsfc.nasa.gov/Tools/w3pimms.html`

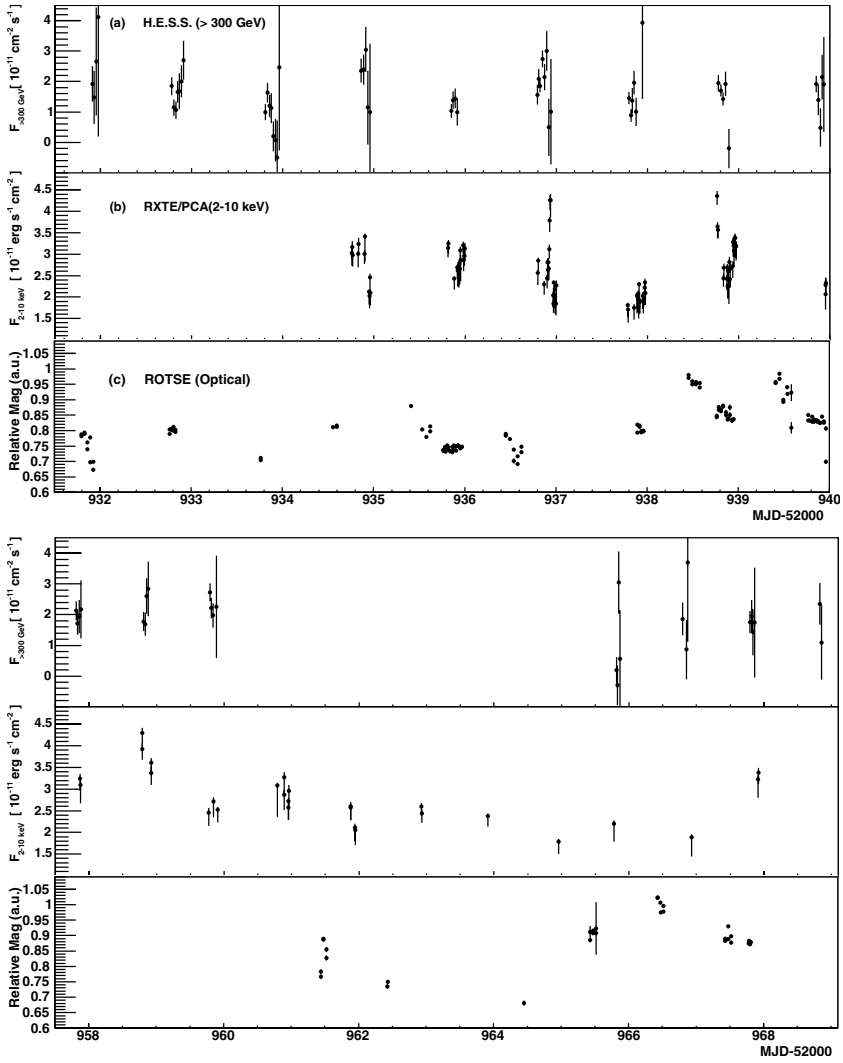

Fig. 2. *Top*: **a)** October 2003 Light curve from HESS binned in run lengths averaging 28 min each, in units of integral flux above 300 GeV; **b)** light curve expressed as flux in the 2–10 keV band for the RXTE observations, in 400 s bins; **c)** light curve derived from the ROTSE optical data. *Bottom*: same as above but for the November 2003 data. Note that the RXTE observations were much shorter than in the previous month.

Using an overlay of 50 isolated comparison stars with similar brightness ($12^{\rm mag}$–$14^{\rm mag}$) and co-located with PKS 2155−304 (<15 arcmin), a two-dimensional Gaussian is fit to the intensity distribution characterising the point-spread function by $\sigma_{\rm psf}$.

To estimate the local sky-background for the reference stars and the target object, an annulus with inner radius $2 \times \sigma_{\rm psf}$ and an outer radius $6 \times \sigma_{\rm psf}$ is chosen. Based upon a reference frame which is derived from co-adding 30 individual frames, a mask is calculated for each object excluding regions where faint objects coincide with the annulus; pixels exceeding 3 standard deviations of the local sky background are excluded. Using the local sky background, the intensity and error of each object is calculated. Using the 50 reference stars, a relative intensity and statistical error with respect to a reference frame is calculated.

The absolute flux values are obtained by calculating a relative R magnitude by comparing the instrumental magnitude with the USNO catalogue as described in Akerlof et al. (2000). The procedure has been checked by comparing the average R magnitude of a sample of 70 BL Lac type objects determined with ROTSE observations carried out over one year of operation with the V magnitude listed in the 10th Veron Cetty & Veron catalogue of BL Lac type objects. The average $V - R$ of 0.5 that is found is consistent with the average value for $V-R$ obtained from cross-checking the colours with the 2MASS catalogued value for the BL Lac type objects.

Finally, the host galaxy has been resolved in optical (Falomo 1996) and NIR (Kotilainen et al. 1998, KFS98 hereafter) and found to be a typical giant elliptical with $M(R) = -24.4$ which translates into an apparent $m(R) = 15.1$ (here the distance moduli given by KFS98 have been used to calculate the apparent magnitude based upon the absolute magnitude quoted). The ROTSE measurements have as maximum and minimum $m(R, \min) = 13.3$ and $m(R, \max) = 13.7$ which corresponds to 10 mJy for the maximum observed flux and 6.7 mJy for the minimum flux taking the contribution of the host galaxy into account. These values are considerably lower than the retrieved archival data indicating that PKS 2155−304 was in a low state at the moment of the observations.

2.4. NRT

The Nançay radiotelescope is a single-dish antenna with a collecting area of 200×34.56 m^2 equivalent to that of a 94 m-diameter parabolic dish (van Driel et al. 1996). The half-power beam width at 11 cm is 1.9 arcmin (EW) $\times$ 11.5 arcmin (NS) (at zero declination), and the system temperature is about 45 K in both horizontal and vertical polarizations. The point source efficiency is 0.8 K Jy^{-1}, and the chosen filter bandwidth was 12.5 MHz for each polarization, split into two sub-bands of 6.25 MHz each. Between 4 and 14 individual 1-min drift scans were performed for each observation, and the flux was calibrated using a calibrated noise diode emission for each drift scan. Data processing has been done with the Nançay local software NAPS and SIR.

A monitoring programme with this telescope on extragalactic sources visible by both the NRT and HESS is in place since 2001. For the campaign described here it consisted of a measurement at 11 cm every two or three days. The average flux for the 8 measurements in October and November 2003 was 0.30 ± 0.01 Jy with possible marginal variability.

3. Results

3.1. Light curves

The October and November 2003 light curves of all the HESS, RXTE and ROTSE observations are shown in Fig. 2. The HESS light curve is binned in run-length times averaging 28 min each. The flux is in units of 10^{-11} photons cm^{-2} s^{-1} above 300 GeV, derived using the average photon index 3.37 obtained in Sect. 3.3. Spectra could not be derived on a run-by-run basis due to the weak signal. As for the observations reported in AH04, the overall light curve is inconsistent with a constant flux. A χ^2 fit of the data to a constant yields a 3.4×10^{-10} χ^2 probablility. The intra-night VHE flux on MJD 52 936 (Fig. 3) exhibits an increase of a factor of 1.9 ± 0.6 in 0.11 d. On MJD 52 932 the peak-to-peak flux shows an increase of a factor of 2.5 ± 0.9 within 0.09 d. These timescales are longer than the 30 min doubling time reported in AH04. For these two extreme cases of VHE variability observed during this campaign only the second had a limited RXTE coverage.

The 2–10 keV X-ray flux in this campaign ranges from $F_{2-10\,\mathrm{keV}} = 2.0 \times 10^{-11}$ erg cm^{-2} s^{-1} to 4.4×10^{-11} erg cm^{-2} s^{-1}. The maximum is lower than the 20 November 1997 measurement of 2.3×10^{-10} erg cm^{-2} s^{-1} (Vestrand & Sreekumar 1999) indicating that the X-ray state seen here is not exceptionally high. The minimum seen here is consistent with historically low fluxes (Zhang et al. 2002). The intra-night variability is also obvious here, but no flare was completely resolved.

A 60% flux variability in $t_{\mathrm{var}} \approx 1.5$ ks on MJD 52 936 is the best marked transient episode in the observations reported here (bottom panel b) in Fig. 3 for which the HESS observations were made at the end of the transit inducing a large associated error on the flux estimation due to the high zenith angle of the source. This timescale is comparable to those reported by Gaidos et al. (1996) where doubling times as short as 15 min from Mkn 421 were observed in the *VHE* band.

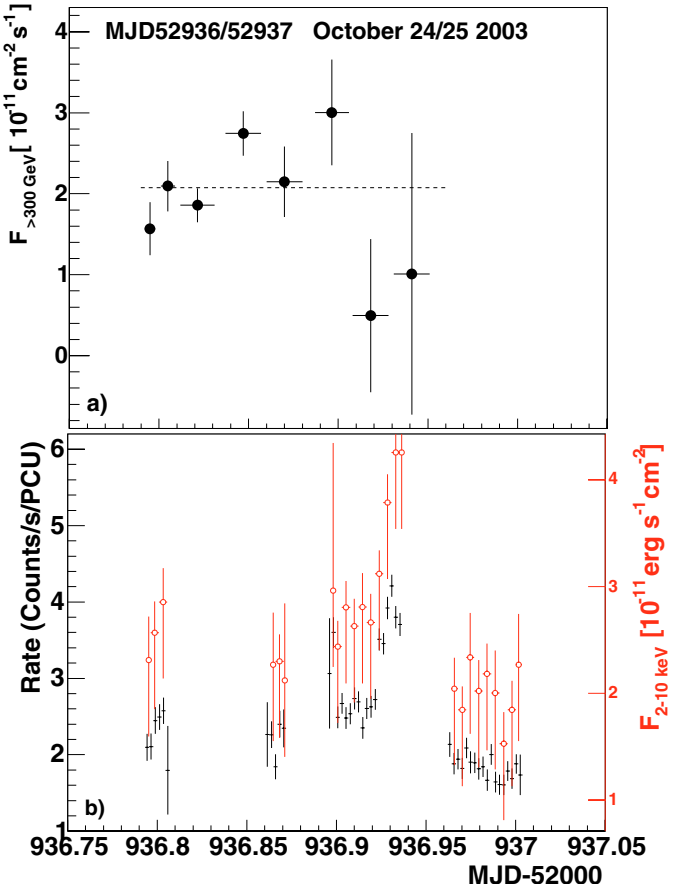

Fig. 3. a) The VHE light curve derived run by run on MJD 52 936. The horizontal error bars are the length of the run from which the flux is derived. The dashed line is the result of a χ^2 fit of the data to a constant, which yields a χ^2 of 15 for 7 degrees of freedom, corresponding to a 0.04 χ^2 probability which is evidence for the variability seen here. **b)** The 2–10 keV X-ray flux (*open circles, right scale*) and counting rate normalized to 1 PCU (*lines, left scale*) showing the fast transient.

This flare is the fastest rise seen in this object to date since BeppoSAX saw a 5×10^4 s rise timescale (Zhang et al. 2002) and Kataoka et al. (2000) observed a doubling timescale of 3×10^4 s with the ASCA satellite. So far the fastest rise in this type of object was observed in Mkn 501 with a 60% increase in less than 200 s (Catanese & Sambruna 2000) though Xue & Cui (2004) claims that this flare is likely to be an artifact.

The optical emission of PKS 2155−304 is dominated by the nucleus which outshines the host galaxy by a factor of ≈4 given in KFS98. The observed variability amplitude is therefore not biased by the constant emission of the host galaxy and mainly due to the activity of the nucleus. The peak-to-peak amplitude of variability is moderate compared to the variability amplitude at shorter wavelengths and typically 0.1^{mag} peak-to-peak. The object has been monitored over longer time-scales with the ROTSE-IIIc telescopes showing variations with amplitudes close to 1^{mag}.

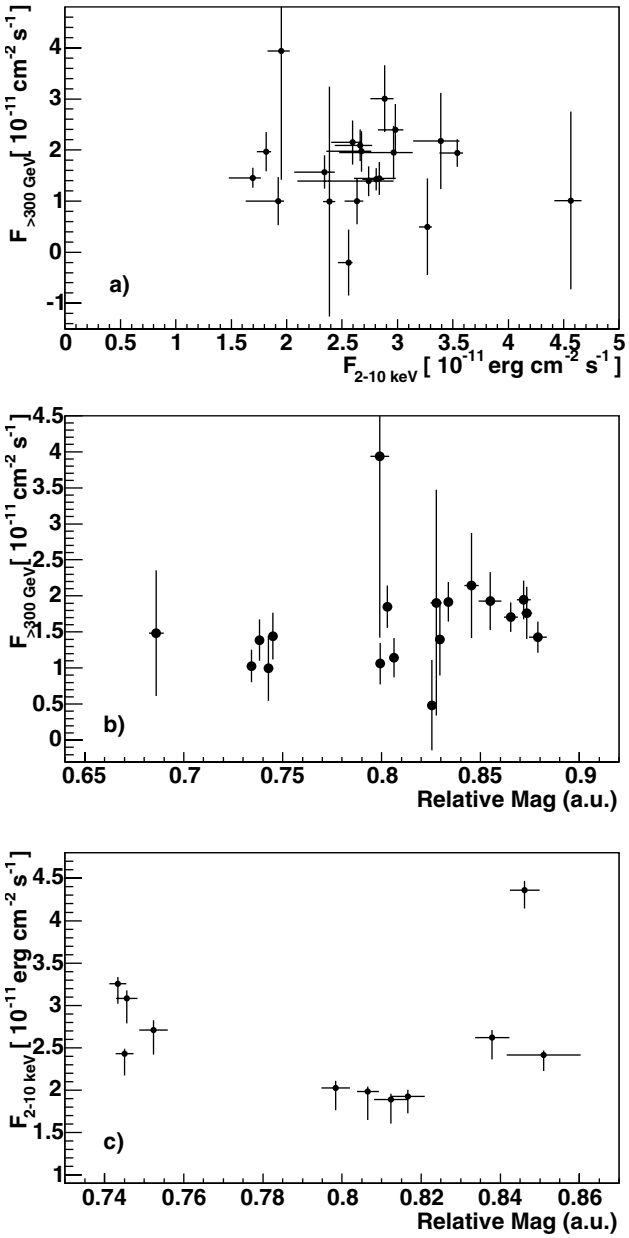

Fig. 4. Correlation plots between different wavebands. No clear correlation is found between any of the simultaneous measurements. **a)** Correlation plot for the 23 X-ray data segments that overlapped exactly with a HESS observation. **b)** Simultaneous HESS and ROTSE observations. **c)** Simultaneous RXTE and ROTSE observations. The optical data were binned to the 400 s long RXTE segments, which are overlapping on 6 different days.

3.2. Correlation analysis

In order to quantitatively look for correlated variability between the *VHE*, X-ray and optical bands, the measured fluxes are plotted against each other in Fig. 4 for all the observations carried out during this campaign. For correlated *VHE*/X-ray variability, the RXTE analysis was slightly modified: only observation segments that happen exactly within a HESS run are reduced and analyzed (using only PCU2, PCU3 and combinations thereof). This provides 23 simultaneous data segments for the whole campaign for which the fluxes are represented in Fig. 4. There is no obvious correlation for those observations (correlation factor $r = 0.37 \pm 0.13$). For correlated optical/*VHE* variability, ROTSE observations that happen within a HESS run are averaged and their errors summed quadratically. No correlation ($r = 0.24 \pm 0.27$) is found for these observations. Also no correlation was found between the optical and X-ray band ($r = -0.02 \pm 0.05$).

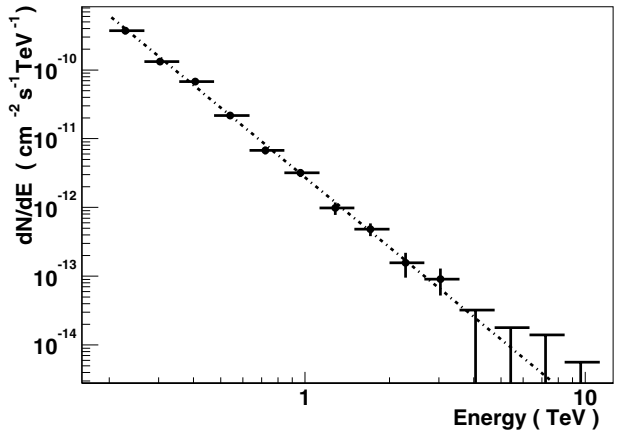

Fig. 5. Time-averaged spectrum derived from the October and November 2003 HESS data along with a fit to a powerlaw.

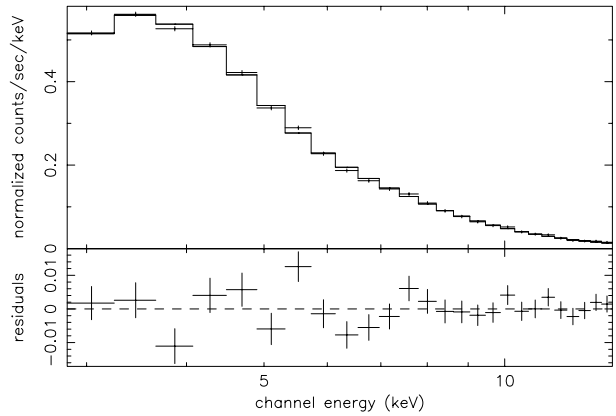

Fig. 6. X-ray spectrum derived from the summed October and November 2003 data, using PCU2 and PCU3, fitted by a broken power law. *The top panel* shows the data and folded model, *the bottom panel* shows the residuals between the data and the model.

3.3. Spectra

The October and November 2003 HESS data were all combined for the spectrum shown in Fig. 5. The best-fitting power law ($\chi^2 = 7$ for 8 degrees of freedom) is given by:

$$\frac{\mathrm{d}N}{\mathrm{d}E} = (2.73 \pm 0.17) \times 10^{-12} \left(\frac{E}{\mathrm{TeV}}\right)^{-3.37 \pm 0.07 \pm 0.10} \mathrm{cm}^{-2}\,\mathrm{s}^{-1}\,\mathrm{TeV}^{-1} \quad (1)$$

which is comparable to $\Gamma = 3.32 \pm 0.06$ and $I_0 = (1.96 \pm 0.12) \times 10^{-12}\,\mathrm{cm}^{-2}\,\mathrm{s}^{-1}\,\mathrm{TeV}^{-1}$ previously reported in AH04.

The result of the broken power law fit for the combined RXTE PCU2 and PCU3 spectrum is shown in Fig. 6. It yields an unabsorbed flux in the 2–10 keV band of

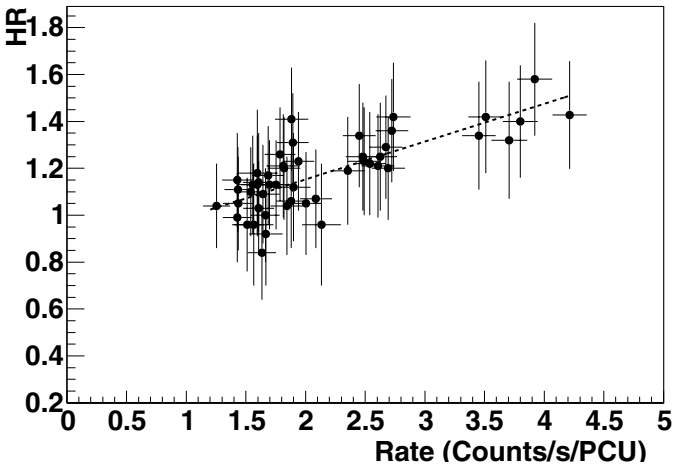

Fig. 7. Plot of the hardness ratio HR versus the counting rate normalized to 1 PCU.

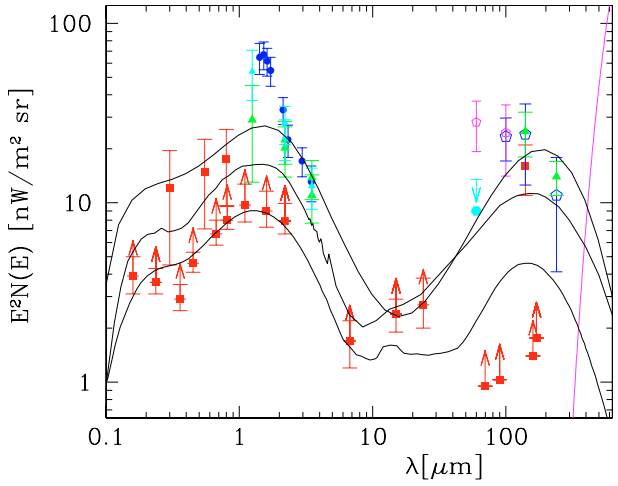

Fig. 8. Spectral energy distribution of the Extragalactic Background Light (EBL). It is thought to be characterized by two distinct bumps, around 1–2 and 100–200 μm, produced by the redshifted stellar light and re-radiated thermal dust emission, respectively. The compilation of measurements have been taken from Hauser & Dwek (2001) and Aharonian et al. (2003). Lower limits are from HST and ISO source counts (Madau & Pozzetti 2000; Elbaz et al. 2002; Gardner et al. 2000). Above 400 μm, the contribution of the CMB starts to dominate. The three continuous lines represent the "Primack-type" EBL shapes: from higher to lower fluxes (at 1 μm), Phigh, Primack01 and Primack04 models (see text). The steep line starting at 300 μm is the onset of the CMBR.

$F_{2-10\,\mathrm{keV}} = (2.66 \pm 0.04) \times 10^{-11}\,\mathrm{erg\,cm^{-2}\,s^{-1}}$ ($\chi^2 = 41$, 31 degrees of freedom), a lower index of $\Gamma_L = 2.81 \pm 0.05$, a break energy of $E_\mathrm{b} = 4.9 \pm 0.8$ keV and a higher index of $\Gamma_\mathrm{H} = 2.95 \pm 0.04$. A single power law fit to the same data yields $F_{2-10\,\mathrm{keV}} = (2.69 \pm 0.03) \times 10^{-11}\,\mathrm{erg\,cm^{-2}\,s^{-1}}$ ($\chi^2 = 51$, 34 degrees of freedom) and an index of $\Gamma = 2.88 \pm 0.13$, a poorer fit than the broken power law, but the index still provides information that can be used for comparison with historical measurements. Indeed, the derived index is close to those measured by the BeppoSAX satellite (Giommi et al. 1998), GINGA (Sembay et al. 1993) and well within the range observed by EXOSAT (Treves et al. 1989). The statistics above 10 keV in our RXTE observations are too poor to check the existence of a possible hard tail above 20 keV (Giommi et al. 1998) which might be the signature of the onset of a high-energy component.

In order to look for flux dependent spectral variability, the RXTE data subset used in Fig. 3 is divided into two energy bands, the PHA channels 0–9 (soft band) and 10–27 (hard band), corresponding to approximately 1–4 keV and 4–11 keV, respectively. A hardness ratio (HR), shown in Fig. 7, is the ratio of the counting rate in the hard band over the soft band. There is a clear correlation of the HR with the rate, peaking when the rate is highest. The correlation factor between the rate and the HR is $r = 0.76 \pm 0.12$. Even though the variability timescale here is much smaller, this behavior is compatible with the hardening reported in Chiappetti et al. (1999).

3.4. EBL corrected spectrum

For objects at non-negligible redshifts, the large, energy-dependent opacities can cause the emitted spectrum to be greatly modified both in shape and intensity (see e.g. Stecker et al. 1992; Biller 1995; Coppi & Aharonian 1999; Vassiliev 2000). Unfortunately, at present the knowledge of the EBL still has large uncertainties, for both direct measurements and models, as summarized in Primack et al. (2001). In order to estimate the intrinsic *VHE* spectrum, and thus to locate the Inverse Compton (IC) peak of the blazar's SED, we have used three EBL models (Fig. 8) as representatives of three different flux levels for the stellar peak component. This is the EBL energy range which mostly affects the HESS spectrum: with data up to 3–3.5 TeV, the peak of the $\gamma - \gamma$ cross section is reached for soft photons with wavelengths $\lesssim 5\,\mu$m.

The three models used here are (in order from higher to lower fluxes): the phenomenological shape used in Aharonian et al. (2003), which is based on the original Primack et al. (2001) calculation but smoothed and scaled up to match the data points below 1 μm and at 2–3.5 μm (hereafter *Phigh*); the original Primack et al. (2001) calculation for a Salpeter initial mass function (hereafter Primack01); and the new 2004 calculation (Primack et al. 2004, hereafter Primack04), which takes advantage of the recent improvements in the knowledge of the cosmological parameters and of the local luminosity function of galaxies.

The opacities are calculated from the EBL SED shapes taking into account only the cosmology ($H_0 = 70\,\mathrm{km\,s^{-1}\,Mpc^{-1}}$, $\Omega_\mathrm{Mat} = 0.3$ and $\Omega_\Lambda = 0.7$). To treat all three shapes similarly, no evolution has been introduced at this point. This corresponds to a "maximum absorption" hypothesis (i.e., for increasing z, constant instead of decreasing EBL comoving energy density). But at these redshifts (~0.1) and, for example, assuming the evolution given in Primack et al. (2001), the difference is still small (variation in the photon index $\Delta\Gamma < 0.1$ in the range 0.3–1 TeV), and negligible compared to the differences between models.

The resulting absorption-corrected spectra are shown in Fig. 9, together with the observed spectrum. The intrinsic spectra are all well fitted by a single power-law model, with a hard

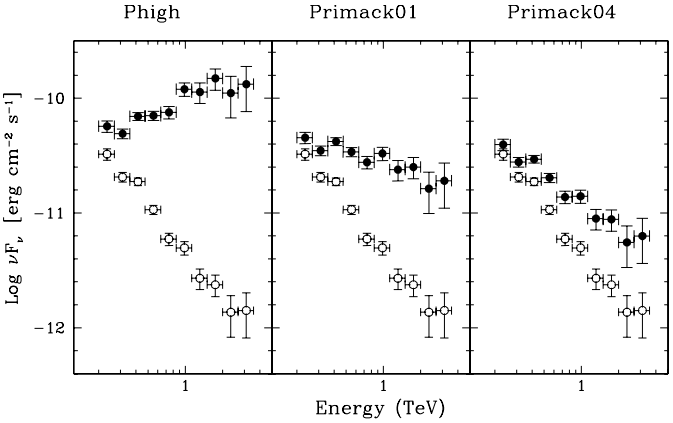

Fig. 9. PKS 2155−304 absorption-corrected spectra, along with the observed spectrum, for each EBL model considered and in a νF_ν plot (i.e. a zoom in the blazar's SED). Open dots: HESS observed spectrum. Filled dots: reconstructed intrinsic spectrum. All spectra from "Primack-type" models are compatible with a power-law shape, with different slopes: hard (Phigh) and soft (Primack01, Primack04), locating the intrinsic SED peak for the high component above 1–2 TeV or below 200 GeV, respectively.

spectrum for Phigh ($\Gamma \approx 1.5$), and soft spectra for Primack01 and Primack04 models ($\Gamma \approx 2.3$ and $\Gamma \approx 2.8$, respectively). This effect is directly related to the different flux levels of the stellar peak component, which imprint a different amount of softening onto the original spectrum. This direct link thus yields two simple scenarios for the location of the blazar's high energy peak, with the dividing line represented by the EBL flux which gives $\Gamma = 2.0$ (1.3 times the Primack01 model). Models with stellar peak fluxes above this (such as Phigh, and generally all those in agreement with the direct estimates of the fluxes between 2 and 3.5 μm) imply a hard intrinsic spectrum ($\Gamma < 2$), and thus an IC peak above 1–2 TeV. EBL models with lower fluxes (such as the Primack01 and Primack04) imply instead a soft spectrum ($\Gamma > 2$), locating the IC peak below the observed energy range (<200 GeV). In the following, we will discuss both scenarios for the SED modelling, using the Phigh and Primack2004 curves as the two ends of the possible range of values for the "Primack-type" shape (i.e., between the claimed EBL direct measurements at few microns and the lower limits from galaxy counts).

4. SED modelling

The broadband spectral morphology of PKS 2155−304 is typical of the BL Lac type, with a double-humped structure in νF_ν representation, exhibiting a low-energy and a high-energy component. Its broadband emission is usually attributed to emission from a beamed relativistic jet, oriented in a direction close to the line of sight (Begelman et al. 1984; Blandford & Königl 1979). The spectral energy distribution in units of power per logarithmic bandwidth $E^2\mathrm{d}N/\mathrm{d}E$ versus energy E is shown in Fig. 10. The EGRET measurements, between the HESS and RXTE points, are from the third EGRET catalog (Hartman 1999) and from a very high γ-ray state described in Vestrand et al. (1995). There is a difference in spectral states, since in the former case the power law photon index is 1.71 ± 0.24 whereas it is 2.34 ± 0.26 in the latter which most likely consists of a mix of low and high activity state observations. The historical EGRET spectra are therefore unlikely to represent the state of PKS 2155−304 during the campaign presented here and are not used to put stringent constraints on the modelling. Considering the archival data and the steep X-ray spectrum in Fig. 10, the peak of the low-energy component occurs in the 2–2000 eV range. The archival BeppoSAX data from a high state analyzed by Chiappetti et al. (1999), and represented here above our RXTE data, show a peak at ≈0.1 keV. The absorbed VHE peak location is clearly below 300 GeV, with its exact location depending on the spectrum in the EGRET range.

Whereas the current models seem to agree that the low-energy component is dominated by synchrotron radiation coming from nonthermal electrons emitted in collimated jets, the high-energy emission is assumed to be either inverse Compton scattering off the synchrotron photons (Synchrotron Self-Compton, SSC, see e.g. Maraschi et al. 1999; Bicknell & Wagner 2002) or by external photons (see e.g. Sikora et al. 1994). This kind of leptonic model will be discussed in Sect. 4.2. A hadronic origin of the VHE emission using the Synchrotron-Proton Blazar (SPB) model with a dominating proton synchrotron component at high energies in a proton-electron plasma is also able to produce a double humped SED and is discussed in Sect. 4.3. The lack of correlation between the RXTE and HESS fluxes (and possibly also between the optical and the VHE emission) within the small variability range may indicate a different spatial origin, or a different underlying particle distribution. In the proton synchrotron model a lack of correlated variability between γ-ray emission and the low energy electron synchrotron component could arise if the electrons and protons are not co-accelerated.

The high-energy component above ≈100 GeV is attenuated by interactions with the EBL and is a lower limit for the intrinsic spectrum. The energy budget in X-rays and VHE γ-rays is comparable, though the maximum output at the peak energy in the high-energy component is likely to be lower than that in the lower-energy component. Interpolating between the high-state EGRET archival data and VHE data would lead to a maximum located above 10 GeV, which is surprising since the observations reported here indicate a low state. Extrapolating the EGRET catalogue spectrum to VHE energies with a power law falls below the HESS data and therefore requires two inflexion points in the SED. Simultaneous observations in the MeV–GeV range with the upcoming satellite GLAST will be crucial to constrain the high-energy component shape.

4.1. Doppler boosting and synchrotron/Compton derived parameters

The electromagnetic emission in blazars is very likely to be Doppler-boosted (or beamed) toward the observer. In the radio regime, the evidence for Doppler boosting in PKS 2155−304 comes from superluminal expansions observed with VLBI (Piner & Edwards 2004). Relativistic beaming is also required in order to avoid absorption of GeV photons by

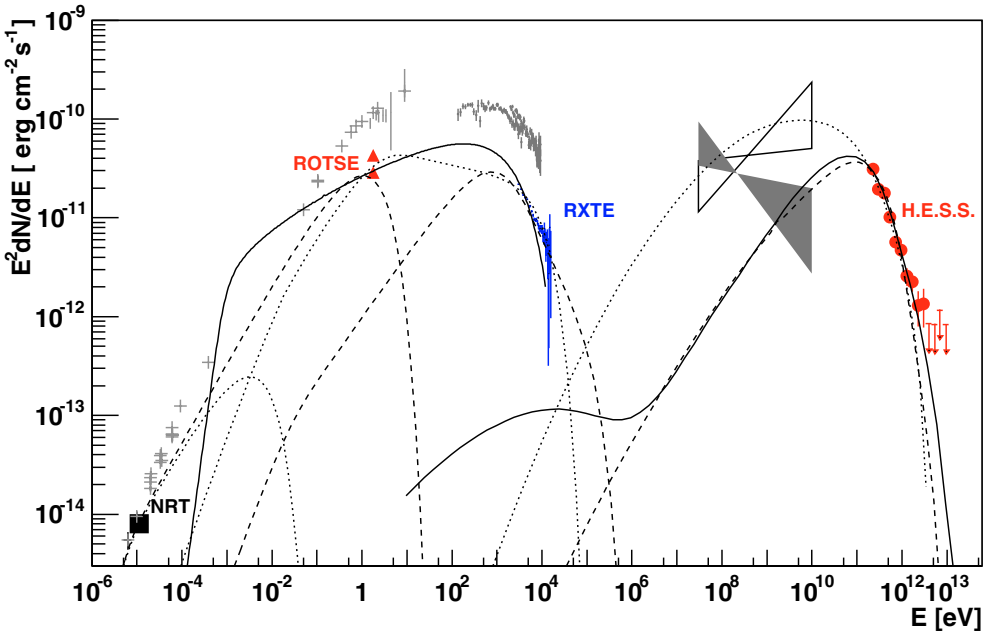

Fig. 10. Spectral energy distribution of PKS2155−304. Only simultaneous measurements are labeled. Non contemporaneous data are in grey symbols. The HESS spectrum is derived from October and November 2003 data (*filled circles*) as is the RXTE spectrum. The NRT radio point (*filled square*) is the average value for the observations carried out during this period. The two triangles are the highest and lowest ROTSE measurements for the Oct.–Nov. observations. Archival SAX data represent the high state observed in 1997 from Chiappetti et al. (1999). Archival EGRET data are from the third EGRET catalogue (shaded bowtie), Hartman (1999) and from a very high γ-ray state described in Vestrand et al. (1995) (open bowtie). 1995 *UBVRI* data are from Paltani et al. (1997) where the mean flux and flux deviation is used here. IUE data from Urry et al. (1993) at 2800 Å and 1400 Å are included here with an error bar corresponding to the spread of the measured fluxes. Other data are NED archival data. The solid line is the hadronic model described in Sect. 4.3. The dotted and dashed lines are the same leptonic model with different assumptions described in Sect. 4.2: the dotted line assumes a common origin for the optical and X-ray synchrotron emission, while the dashed line is the case where the optical emission emanates from the VLBI core; for both cases the lowest frequency hump is the predicted VLBI core emission. All the VHE emission in the models are absorbed according to the Primack04 model discussed in Sect. 3.4.

X-ray photons via the e^+/e^- pair-production process (see e.g. Maraschi et al. 1992). It is thus possible to use the γ-ray variability to establish a limit for the Doppler factor δ, with δ defined in the standard way as $[\Gamma(1-\beta\cos\theta)]^{-1}$, where Γ is the bulk Lorentz factor of the plasma in the jet, $\beta = v/c$, and θ is the angle to the line of sight.

Following Dondi & Ghisellini (1995), the size of the γ-ray emission zone R is derived from the time-scale of variability $t_{\rm var}$ (supposing the timescale of intrinsic variability is negligible compared to the light crossing time) by $R \leq ct_{\rm var}\delta/(1+z)$. In this case (assuming a time scale $t_{\rm var} \approx 2$ ks from Sect. 3) the size of the emission region is

$$R\delta^{-1} \leq 5 \times 10^{13}\,{\rm cm}. \quad (2)$$

Since for γ-rays in the 300 GeV–3 TeV range the opacity $\tau_{\gamma\gamma}$ cannot significantly exceed 1, independently of the emission mechanisms, another constraint on the minimum value of the Doppler factor can be derived by estimating how much Doppler boosting is necessary for photons with observed energy E_γ to escape from a source with radius R and a flux density $F(E_t)$, where $E_t = (m_{\rm e}c^2)^2\delta^2/E_\gamma(1+z)^2$. At this point one can follow Mattox et al. (1993) and especially Eq. (3.7) in Dondi & Ghisellini (1995), writing that the opacity is

$$\tau_{\gamma\gamma} \approx \frac{\sigma_{\rm T}}{5}\frac{1}{hc}\frac{d_L^2}{R}\frac{1}{\delta^3(1+z)}F(E_t). \quad (3)$$

Imposing that $\tau_{\gamma\gamma} < 1$ for photons with observed energy $E_\gamma = 1$ TeV yields a lower limit on δ for given R that can be derived numerically from the observed SED. For PKS 2155−304 this yields

$$R^{-1}\delta^{-6.4} \leq 5.6 \times 10^{-24}\,{\rm cm}^{-1}. \quad (4)$$

The minimum allowable boost δ comes from combining Eqs. (2) and (4) and yields

$$\delta \geq 19 \quad (5)$$

which is higher than the limit obtained in a similar way in Tavecchio et al. (1998), but at the lower end of the range usually obtained from SSC modelling as in Kataoka et al. (2000). It is useful to stress that this constraint is valid under the usual assumption that the region emitting the SED optical flux (i.e., the target photons) is cospatial with (or at least embeds) the high energy emitting region. The models used later in this paper are therefore essentially single zone models.

If the observed X-rays are synchrotron radiation from non-thermal electrons then the mean observed energy $\langle E\rangle$ of an electron with Lorentz factor $\gamma_{\rm e}$ is given by

$$\langle E\rangle \approx \frac{\delta}{1+z}\frac{21\hbar\gamma_{\rm e}^2 qB}{15\sqrt{3}m_{\rm e}}.$$

Using $\langle E\rangle = 10$ keV here yields

$$B\delta\gamma_{\rm e}^2 = 1.1 \times 10^{12}\,{\rm G}. \quad (6)$$

In the SSC scenario the same electrons can Comptonize ambient photons up to the VHE regime, thus

$$\frac{\delta}{1+z}\gamma_e m_e c^2 \geq 3\,\mathrm{TeV}. \quad (7)$$

Combining Eqs. (6) and (7) yields

$$B\delta^{-1} \leq 1.1\times10^{12}\,\mathrm{G}\times\left(\frac{3\,\mathrm{TeV}}{m_e c^2}\right)^{-2}(1+z)^{-2}. \quad (8)$$

A numerical application yields

$$B\delta^{-1} \leq 0.03\,\mathrm{G} \quad (9)$$

and hence the Lorentz factor is constrained to $\gamma_e \geq 1.3\times10^6$ which is higher than that calculated as above for Mkn 421 by Takahashi et al. (1996) who derived $\gamma_e > 5\times10^5$ (and $B \approx 0.2$ G) but lower than $\gamma_e \approx 10^7$ found in a similar way in 1ES1959+650 (Giebels et al. 2002).

The X-ray data presented above imply that the X-ray spectrum of PKS 2155−304 hardens as the source brightens. This is often measured in BL Lac objects; a hardening of the spectrum when flares occur, and a blueward shift of the peak of the synchrotron emission ν_{sync} (and presumably higher energy inverse-Compton emission) by factors that can be as large as 100 were measured in the cases of Mkn 501 (Pian et al. 1998), 1ES 1426+428 and PKS 0548−322 (Costamante et al. 2001). In the case of PKS 2005−489 (Perlman et al. 1999), a more moderate shift of a factor of 3 or less of the synchrotron emission was found. The archival data suggest that ν_{sync} lies in the UV band for PKS 2155−304, but no data were taken simultaneously in this campaign at that wavelength.

The lack of indication for correlated X-ray/VHE variability does not imply that PKS 2155−304 behaves differently from VHE sources such as Mkn 421, for which VHE/X-ray correlation has been established on a much higher variability basis (see e.g. Cui et al. 2004) with dynamical ranges of 30 in both energy bands. Limiting those observations to the same dynamical range as observed here would not allow any claim for correlation. Future observations of PKS 2155−304 with a higher variability amplitude would bring more insight into this.

4.2. Leptonic interpretation

Interpretation with a single zone SSC model of the SED of PKS 2155−304 has already been proposed in the literature using two different assumptions. In Kataoka et al. (2000) the low energy tail of the SSC model is used to account for the low-energy component up to the optical in the SED. That component is decomposed into two sub-components by Chiappetti et al. (1999) where the radio to optical emission has another origin than the X-rays, which are assumed to come from the jet. These two different interpretations are used here in the context of the leptonic model described in Katarzyński et al. (2001) which has already been applied to Mkn 501 and Mkn 421 (Katarzyński et al. 2003). To constrain this model, only the simultaneous data are used, since the archival data reported in the SED of Fig. 10 are likely to not represent the state of this source (note for example the difference in optical flux and the ROTSE measurement).

When using the Primack04 absorption, the model used here can reproduce the X-ray through VHE part of the SED, but the HESS spectrum constrains it such that the radio measurement can not be included in the synchrotron bump predicted by the single-zone model. As for Mkn 421 and Mkn 501, adding a more extended component than the VHE emitting zone can provide an explanation for this. The origin is probably the compact VLBI core which has a radio core to lobe ratio of ≈1 (Laurent-Muehleisen et al. 1993; Piner & Edwards 2004) and a typical size of 10^{18} cm, more than two orders of magnitude larger than the VHE emitting zone. This VLBI feature dominates the spectrum at low energy and is included in the SED modelling here. An uncertainty remains which is the high frequency cutoff of this VLBI component. The host galaxy contribution to the optical flux is estimated to be $\approx10^{-11}$ erg cm^{-2} s^{-1}, deduced from the magnitudes given by KFS98 and assuming a low-redshift solar metallicity elliptical galaxy of age equal to 13 Gyr ($R - H = 2.4$), corresponding to a mass of $5\times10^{11}\,M_\odot$ (Fioc & Rocca-Volmerange 1997). So even at the measured low activity state of PKS 2155−304 the host galaxy is not contributing much in the optical range.

The ROTSE measurement can be ascribed here to either the high-energy tail of the VLBI component or to the synchrotron part of the SSC model. Assuming a common origin for the X-rays and the optical emission, and using a variability time scale of 0.1 d to constrain the emitting zone, the model tends to predict a high IC flux, as shown in Fig. 10. However, the lack of correlation between the X-rays and the optical emission in our measurements – also suggested by Dominici et al. (2004) based on less sensitive RXTE/ASM measurements – indicates that the optical emission could originate from the VLBI component, which is modelled by a slight increase in the maximal Lorentz factor of the emitting electrons. This in turn lessens the constraint on the simultaneous SSC fit of the X-ray and VHE part and allows a better fit of the VHE spectrum for smaller sizes of the emitting zone. Detailed parameters of the two hypotheses are given in Table 1.

If the absorption correction is well described by the Phigh model, the slope of HESS data at high energy implies that the peak of the TeV emission bump is located above 4 TeV (or 10^{27} Hz). Such a high frequency peak emission imposes a strong constraint for the single-zone SSC scenario, especially since the peak of the synchrotron bump has to remain below 1 keV (or $10^{17.5}$ Hz) as required by the slope of the RXTE data. High values of both the jet Doppler factor and the maximal Lorentz factor of radiating particles are required to reach the necessary energy for the IC bump, that is $\gamma_{\max}\delta > 8\times10^6$. On the other hand, to keep the synchrotron peak below 1 keV imposes an upper limit to the magnetic field. Within these constrains, the best fit we obtain is shown in Fig. 11. We can note that none of the high energy tails are well accounted for. The set of parameters for the best fit is given in Table 1. This fit marginally reproduces the observed X-ray and γ-ray data, but is not as satisfactory than that obtained with the Primack04 absorption correction, and in any case it is impossible to take into account the ROTSE optical point. The main changes in parameters between the two fits consist in enhancing the boosting,

Table 1. Parameters for the SED fit with the assumption that the optical and X-ray emission are part of the jet synchrotron emission (Model 1 in the table, dotted line in Fig. 10) or that the optical emission emanates from the VLBI emission zone (Model 2 in the table, dashed lines in the same figure). The parameters are described in Katarzyński et al. (2001).

Parameter	Model 1	Model 2	Model 2 Phigh
$R_{\rm blob}(10^{15}$ cm)	6.5	1.5	1.5
B(G)	0.15	0.25	0.02
$\delta_{\rm b}$	25	25	50
K(cm^{-3})	160	2.0×10^3	240
$\gamma_{\rm break}(10^3)$	7.5	100	300
$\gamma_{\rm max}(10^5)$	3.8	9.0	5.0
α_1	1.4	1.7	1.6
α_2	3.2	4.65	4.5
$R_{\rm jet}(10^6$ cm)	1.0	1.0	1.0
$L_{\rm jet}$(pc)	55	55	55
$\delta_{\rm jet}$	2	2	2
$K_{\rm jet}$(cm^{-3})	40	40	40
$B_{\rm jet}$(G)	0.04	0.04	0.04
$\gamma_{\rm break,jet}(10^3)$	2.5	45	45

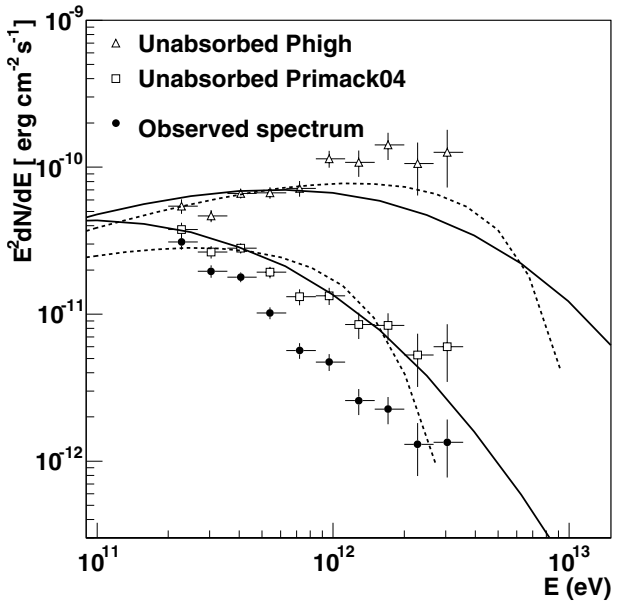

Fig. 11. Estimations of the intrinsic PKS 2155−304 *VHE* spectrum, corrected for either the Phigh or Primack04 models, along with the associated intrinsic (i.e. before absorption) SSC model (dashed lines) and SPB model (solid lines).

which then becomes quite extreme, while reducing the density and magnetic field for the Phigh absorption correction.

The constraints on δ derived here from either simple opacity arguments or from the one-zone model parametrisation of the SED are in the range of Doppler factors usually derived with such assumptions or models for other VHE emitters. As pointed out by Chiaberge et al. (2000) such high values are however at odds with attempts to unify the BL Lac population with the family of FR I sources (Urry & Padovani 1995), the latter being possibly an unbeamed since off-axis viewed case of the former. The same authors suggest that models where velocity structures in the jet, such as the "spine-sheath" model (see e.g. Sol et al. 1989) or the decelerating flow model (Georganopoulos & Kazanas 2003; Georganopoulos & Kazanas 2004) allow lower bulk Lorentz factors. Another option from Pelletier et al. (2004) is to cope with the pair creation catastrophe implied by smaller Doppler factors in their "two-flow" solution. Comparing the SED with such models, which make the BL Lac – FR-I connection more plausible, is an interesting task but beyond the scope of this paper.

4.3. Hadronic models

Generally, the leptonic models constitute the preferred concept for TeV blazars, essentially because of two attractive features: (i) the capability of the (relatively) well understood shocks to accelerate electrons to TeV energies (Sikora & Madejski 2001; Pelletier 2001) and (ii) the effective conversion of the kinetic energy of these relativistic electrons into the X-ray and VHE γ-ray emission components through the synchrotron and inverse Compton radiation channels. The hadronic models are generally lack these virtues. They assume that the observed γ-ray emission is initiated by accelerated protons interacting with ambient matter (Bednarek 1993; Dar & Laor 1997; Pohl & Schlickeiser 2000), photon fields (PIC model, Mannheim 2000), magnetic fields (Aharonian et al. 2002) or both (Mücke & Protheroe 2000).

The models of TeV blazars involving interactions of protons with photon and B-fields require particle acceleration to extreme energies exceeding 10^{19} eV which is possible if the acceleration time is close to $t_{\rm acc} = r_{\rm g}/c$ ($r_{\rm g}$ is the gyro-radius). This corresponds (independent of a specific acceleration mechanism) to the maximum (theoretically possible) acceleration rates (Aharonian et al. 2002) which can only be achieved by the conventional diffusive shock acceleration in the Bohm diffusion regime.

On the other hand, the condition of high efficiency of radiative cooling of accelerated particles requires extreme parameters characterizing the sub-parsec jets and their environments, in particular very high densities of the thermal plasma, radiation and/or B-fields. In particular, the proton-synchrotron models of TeV blazars require highly magnetized ($B \gg 10$ G) condensations of γ-ray emitting clouds containing Extremely High Energy (EHE) protons, where the magnetic pressure dominates over the pressure of relativistic protons (Aharonian 2000).

Below we use the hadronic SPB model (Mücke & Protheroe 2000, 2001) to model the average spectral energy distribution (SED) of PKS 2155−304 in October-November 2003. A detailed description of the model, and its implementation as a (time-independent) Monte-Carlo/numerical code, has been given in Mücke et al. (2003) and Reimer et al. (2004).

Considering the rather quiet activity state of PKS 2155−304 in Oct.–Nov. 2003, we use the 3EG catalog spectrum, since it is the best determined EGRET spectrum

from this source to date, as an upper limit for modelling purposes.

Flux variability provides an upper limit for the size of the emission region. To allow for a comparative study between leptonic and hadronic models we fix here the comoving emission region to $R \sim ct_{\rm var}\delta = 5 \times 10^{13}\delta$ cm deduced from the X-ray variability. We assume that the optical through X-ray emission and the γ-ray output stem from the same region of size R.

A reasonable model representation for the simultaneous data assuming a Primack04 model for the VHE absorption is found for the following parameters: magnetic field $B = 40$ G, Doppler factor $\delta = 20$, injection electron spectral index $\alpha_{\rm e} = 1.6$, assumed to be identical to the injection proton spectral index $\alpha_{\rm p}$, maximum proton energy of order $\gamma_{\rm p,max} \sim 4 \times 10^9$, e/p-ratio of 0.15 and a near-equipartition proton energy density of $u_{\rm p} = 27\,{\rm erg\,cm^{-3}}$. The required total jet power is of the order $L_{\rm jet} \sim 1.6 \times 10^{45}\,{\rm erg\,s^{-1}}$. When using the Phigh EBL model, a reasonable representation of the data may be achieved by increasing the maximum injected proton energy to $\gamma_{\rm p,max} = 10^{10}$ and simultaneously increasing the e/p-ratio to 0.24, while all other parameters remain unchanged. Note that here the maximum proton gyro-radius approaches the size of the emission region. Alternatively, a doubling of the magnetic field to 80 G together with an increase of $\gamma_{\rm p,max}$ to 8×10^9 and a e/p-ratio of unity (leading to $u_B \approx 50u_{\rm p}$) represents the SED-data equally well. In conclusion, none of the "Primack-type" EBL models can explicitly be ruled out in the framework of the SPB-model by the HESS data presented here. In all cases, proton synchrotron emission dominates the (sub-)TeV radiative output. Depending on the Doppler factor, part of the proton synchrotron radiation produced may be reprocessed to lower energies. Contributions from the muon and pion cascades are always lower than the proton synchrotron component. The low energy component is dominated by synchrotron radiation from the primary electrons, with a negligible contribution of synchrotron radiation from secondary electrons (produced by the p- and $\mu^{\pm}$-synchrotron cascade).

On the other hand, the synchrotron radiation of secondary electrons resulting from interactions of VHE γ-rays with external low-energy photons with a modest $\gamma\gamma \rightarrow {\rm e}^+/{\rm e}^-$ opacity ($\tau_{\gamma\gamma} \leq 1$) may lead to significant X-ray emission with a luminosity comparable to the luminosity of the primary VHE emission (Aharonian 2000).

Models involving meson production inevitably predict neutrino emission due to the decay of charged mesons. The SPB-model for PKS 2155−304 explains the high energy emission dominantly as proton synchrotron radiation, making the neutrino flux completely negligible.

5. Conclusions

This paper reports multi-wavelength observations of the BL Lac object PKS 2155−304 in 2003. Although the source appeared variable in the VHE, X-rays and optical bands, the latter two indicate that PKS 2155−304 was in a state close to historically low measurements, even though it was easily detectable by HESS in all nights of observations since the beginning of the detector operation (see AH04 for the observation history up to August 2003). An extreme case of VHE variability shows a peak-to-peak increase of a factor of 2.5 ± 0.9 in 0.09 d. Variability on the timescale of a few ks in the 2–10 keV band and of the order of 0.1 d for energies > 300 GeV were observed by RXTE and HESS The X-ray data show a correlation of the flux with the spectrum, which becomes harder when the source is brighter. At the level of the simultaneously observed modest variability, no correlation between the VHE γ-rays, the X-rays and optical was seen. Observations with greater variability and better coverage are needed before it can be asserted that the VHE/X-ray pattern in PKS 2155−304 is different from other known VHE-emitting AGN. Since the source was in a low emission state in both the optical and X-rays compared to archival measurements, this lack of correlation has yet to be established for a higher emission state. Simultaneous observations in the X-rays/optical band and VHE γ-rays had never previously been performed on this scale. Its continual VHE detection makes PKS 2155−304 unique in the TeV BL Lac category, and probably indicates that HESS has achieved the sensitivity level where it can detect the quiescent state of PKS 2155−304 at any time. A time-averaged energy spectrum is determined for the 2 observation periods and fits to a power law ($\Gamma = 3.37 \pm 0.07$) in the VHE γ-rays, and to a broken power law ($\Gamma_L = 2.81 \pm 0.05$, $E_{\rm b} = 4.9 \pm 0.8$ keV, $\Gamma_{\rm H} = 2.95 \pm 0.04$) in the X-rays.

A comparison of the intrinsic spectrum with predictions from existing one-zone leptonic and one-zone hadronic models is attempted to give a plausible estimation of underlying physical parameters. The values of the parameters are in line with those inferred for other VHE-emitting blazars. In these models the VHE emission is attenuated according to two different EBL levels. This changes mainly the Doppler boosting in the leptonic model, but the high level EBL decreases the agreement significantly. In the hadronic model, the maximum injected proton energy can be changed to accomodate different EBL levels and can therefore not significantly constrain any of the EBL models used here.

Acknowledgements. The authors would like to thank the anonymous referee for his correction and useful comments that improved this paper. The support of the Namibian authorities and of the University of Namibia in facilitating the construction and operation of HESS is gratefully acknowledged, as is the support by the German Ministry for Education and Research (BMBF), the Max-Planck-Society, the French Ministry for Research, the CNRS-IN2P3 and the Astroparticle Interdisciplinary Programme of the CNRS, the UK Particle Physics and Astronomy Research Council (PPARC), the IPNP of the Charles University, the South African Department of Science and Technology and National Research Foundation, and by the University of Namibia. We appreciate the excellent work of the technical support staff in Berlin, Durham, Hamburg, Heidelberg, Palaiseau, Paris, Saclay, and in Namibia in the construction and operation of the equipment.
The authors acknowledge the support of the ROTSE III collaboration and the sharing of observation time with the Australian ROTSE IIIa telescope operated by A. Phillips and M. C. B. Ashley from the School of Physics, Department of Astrophysics and Optics, University of New South Wales, Sydney, Australia. Special thanks also to R. Quimby from the University of Texas for providing tools for data-reduction.
H. Sol and C. Boisson thank K. Katarzyński for his SSC code.
This research has made use of the NASA/IPAC Extragalactic Database

(NED) which is operated by the Jet Propulsion Laboratory, California Institute of Technology, under contract with the National Aeronautics and Space Administration. We thank the RXTE team for their prompt response to our ToO request and the professional interactions that followed.

References

Aharonian, F. 2000, New Astron., 5, 377

Aharonian, F., Belyanin, A. A., Derishev, E. V., & Kocharovsky, V. V. 2002, Phys. Rev. D, 66, 023 005

Aharonian, F. A., Akhperjanian, A., Beilicke, M., et al. 2003, A&A, 403, 523

Aharonian, F. A., Akhperjanian, A. G., Aye, K.-M., et al. 2004, APh, 22, 109

Aharonian, F. A., et al. 2005, A&A, 430, 865

Akerlof, C. W., Balsano, R., Barthelmy, S., et al. 2000, ApJ, 542, 251

Akerlof, C. W., Kehoe, R. L., McKay, T. A., et al. 2003, PASP, 115, 132

Bednarek, W. 1993, ApJ, 402, L29

Begelman, M. C., Blandford, R. D., & Rees, M. J. 1984, Rev. Mod. Phys., 56, 255

Bernlöhr, K., Carrol, O., Cornils, R., et al. 2003, APh, 20, 111

Bicknell, G. V., & Wagner, S. J. 2002, PASA, 19, 129

Biller, S. D. 1995, APh, 3, 385

Blandford, R. D., & Königl, A. 1979, ApJ, 232, 34

Catanese, M., & Sambruna, R. M. 2000, ApJ, 534, L39

Chadwick, P. M., Lyons, K., McComb, T. J. L., et al. 1999, ApJ, 513, 161

Chiaberge, M., Celotti, A., Capetti, A., & Ghisellini, G. 2000, A&A, 358, 104

Chiappetti, L., Maraschi, L., Tavecchio, F., et al. 1999, ApJ, 521, 522

Coppi, P. S., & Aharonian, F. A. 1999, APh, 11, 35

Cornils, R., Gillessen, S., Jung, I., et al. 2003, APh, 20, 129

Costamante, L., Ghisellini, G., Tagliaferri, G., et al. 2001, A&A, 371, 512

Costamante, L., Aharonian, F., Horns, D., & Ghisellini, G. 2004, NewAR, 48, 469

Cui, W., et al. 2004, AIP Conf. Proc. [arXiv:astro-ph/0410160]

Dominici, T. P., Abraham, Z., Teixeira, R., & Benevides-Soares, P. 2004, AJ, 128, 47

Dondi, L., & Ghisellini, G. 1995, MNRAS, 273, 583

Elbaz, D., Cesarsky, C. J., Chanial, P., et al. 2002, A&A, 384, 848

Falomo, R., Bersanelli, M., Bouchet, P., & Tanzi, E. G. 1993, AJ, 106, 11

Falomo, R. 1996, MNRAS, 283, 241

Fioc, M., & Rocca-Volmerange, B. 1997, A&A, 326, 950

Funk, S., Hermann, G., Hinton, J., et al. 2004, APh, 22, 285

Gardner, J. P., Brown, T. M., Ferguson, H. C., et al. 2000, ApJ, 542, L79

Gaidos, J. A., Akerlof, C. W., Biller, S. D., et al. 1996, Nature, 383, 319

Georganopoulos, M., & Kazanas, D. 2003, ApJ, 594, L27

Georganopoulos, M., & Kazanas, D. 2004, NewAR, 48, 403

Giebels, B., Bloom, E. D., Focke, W., et al. 2002, ApJ, 571, 763

Giommi, P., Fiore, F., Guainazzi, M., et al. 1998, A&A, 333, L5

Hartman, R. C., Bertsch, D. L., Bloom, S. D., et al. 1999, ApJS, 123, 79

Hauser, M. G., & Dwek, E. 2001, ARA&A, 39

Hofmann, W. 2002, HESS project in The Universe Viewed in Gamma-rays, September 25, Kashiwa, Japan

Jahoda, K., et al. 1996, in EUV, X-ray, and Gamma-ray Instrumentation for Astronomy VII, SPIE Proc., 2808, 59

Kataoka, J., Takahashi, T., Makino, F., Inoue, S., et al. 2000, ApJ, 528, 243

Katarzyński, K., Sol, H., & Kus., A. 2001, A&A, 367, 809

Katarzyński, K., Sol, H., & Kus., A. 2003, A&A, 410, 101

Kirk, J. G., & Mastichiadis, A. 1999, APh, 11, 45

Kotilainen, J. K., Falomo, R., & Scarpa, R. 1998, A&A, 336, 479

Dar, A., & Laor, A. 1997, ApJ, 478, L5

Laurent-Muehleisen, S. A., Kollgaard, R. I., Moellenbrock, G. A., & Feigelson, E. D. 1993, AJ, 106, 875

Madau, P., & Pozzetti, L. 2000, MNRAS, 312, L9

Mannheim, K. 2000, A&A, 269, 67

Madejski, G., Takahashi, T., Tashiro, M., et al. 1996, ApJ, 459, 156

Maraschi, L., Ghisellini, G., & Celotti, A. 1992, ApJ, 397, L5

Maraschi, L., Fossati, G., Tavecchio, F., et al. 1999, ApJ, 526, L81

Marshall, H. L., Fruscione, A., & Carone, T. E. 1995, ApJ, 439, 90

Mattox, J. R., Bertsch, D. L., Chiang, J., et al. 1993, ApJ, 410, 609

Mücke, A., & Protheroe, R. J. 2000, AIP Conf. Proc., 515, 149

Mücke, A., & Protheroe, R. J. 2001, APh, 15, 121

Mücke, A., Protheroe, R. J., Protheroe, R. J., et al. 2003, APh, 18, 593

Paltani, S., Courvoisier, T. J.-L., Protheroe, R. J., Blecha, A., & Bratschi, P. 1997, A&A, 327, 539

Pelletier, G. 2001, AIP Conf. Proc., 558, 289

Pelletier, G., et al. 2004, AIP Conf. Proc., 745, 34

Perlman, E. S., Madejski, G., Stocke, J. T., & Rector, T. A. 1999, ApJ, 523, L11

Pian, E., Vacanti, G., Tagliaferri, G., et al. 1998, ApJ, 492, L17

Piner, G. P., & Edwards, P. G. 2004, ApJ, 600, 115

Pohl, M., & Schlickeiser, R. 2000, A&A, 354, 395

Primack, J., et al. 2001, AIP Conf. Proc., 558, 463

Primack, J., Bullock, J., & Somerville, R. 2004, Observational Gamma-Ray Cosmology, Proc. of the Conf. Gamma 2004 Heidelberg, 26–30 July, Germany

Reimer, A., Protheroe, R. J., & Donea, A.-C. 2004, A&A, 419, 89

Rybicki, G. B., & Lightman, A. P. 1979, Radiative Processes in Astrophysics (New York: Wiley)

Sembay, S., Warwick, R. S., Urry, C. M., et al. 1993, ApJ, 404, 112

Sikora, M., Begelman, M. C., & Rees, M. J. 1994, ApJ, 421,153

Sol, H., Pelletier, G., & Asseo, E. 1989, MNRAS, 237, 411

Stecker, F. W., de Jager, O. C., & Salamon, M. H., et al. 1992, ApJ, 390, L49

Sikora, M., & Madejski, G. 2001, AIP Conf. Proc., 558, 275

Takahashi, T., Tashiro, M., Madejski, G., et al. 1996, ApJ, 470, L89

Tavecchio, F., et al. 1998, A&A, 509, 608

Treves, A., Morini, M., Chiappetti, L., et al. 1989, ApJ, 341, 733

Urry, C. M., & Padovani, P. 1995, PASP, 107, 803

Urry, C. M., Maraschi, L., Edelson, R., et al. 1993, ApJ, 411, 614

Urry, C. M., et al. 1997, ApJ, 486, 770

van Driel, W., Pezzani, J., & Gérard, E. 1996, in High sensitivity radio astronomy, ed. N. Jackson, & R. J. Davis (Cambridge Univ. Press), 229

Vassiliev, S. D. 2000, APh, 12, 217

Vestrand, W. T., Stacy, J. G., & Sreekumar, P. 1995, ApJ, 454, L93

Vestrand, W. T., & Sreekumar, P. 1999, APh, 11, 197

Xue, Y., & Cui, W. 2004, ApJ, in press [arXiv:astro-ph/0412226]

Zhang, Y. H., Treves, A., et al. 2002, ApJ, 572, 762

4.4 Preparations for the VHE-Fermi MWL observations

However a crucial part of the spectrum was still missing in the HE MeV-GeV energy range, critical enough to not allow us to disentangle the three emission models used in that study. The situation was also rather confusing at the time given the significant difference between the two published EGRET photon indices of $\Gamma_{HE} = 1.71 \pm 0.24$ [Vestrand et al., 1995] in a high flux state, and $\Gamma_{HE} = 2.35 \pm 0.26$ in the 3rd EGRET catalog[Hartman et al., 1999]. While the high-state flux could easily accomodate the observed H.E.S.S. spectrum, the SED of the previous MWL campaign indicated that PKS 2155−304 was in a low flux state, and therefore the second photon index should be the relevant one. The issue here is that the soft EGRET spectrum does not directly connect with the low-state H.E.S.S. spectrum, which would hence require an inflexion point in the Compton spectrum or, in other words, a second VHE component. This prompted for the preparation before the launch of Fermi of simultaneous MWL campaigns, not only on PKS 2155−304 but on the brightest VHE AGN of interest for the ACT community, which was achieved by a few dedicated people within the multiwavelength working group [Paneque, Chiang, Giebels, Lonjou, Lott, & Madejski, 2008]. Thanks to Fermi-LAT's large field of view, the whole sky is covered within 3h so that virtually any celestial source can be monitored down to that time scale without requiring repointing of the instrument. This provides observers a unique opportunity to conduct simultaneous multi-wavelength observations because Fermi γ-ray observations are granted to happen at any time.

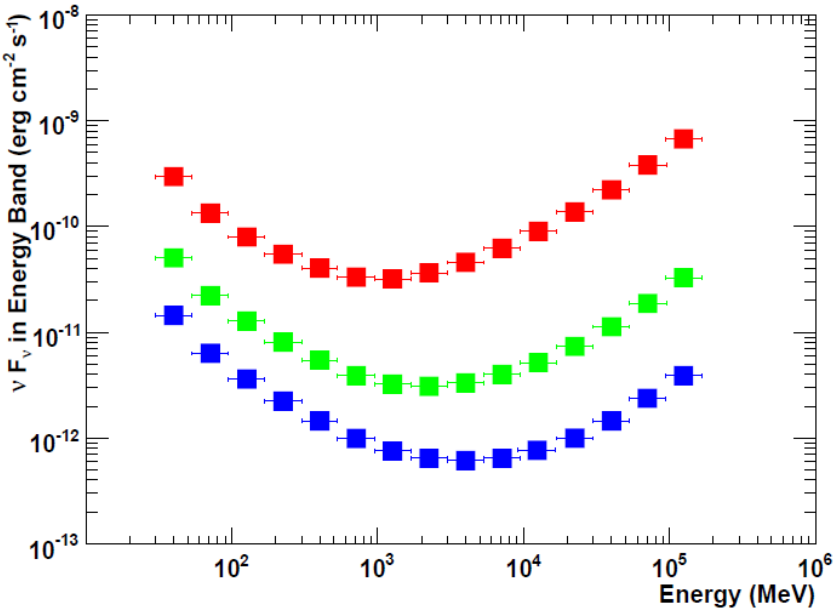

Figure 4.3: *Differential LAT sensitivity used to derive the potential of the LAT to detect bright VHE sources. The points are defined as the flux level over an energy interval of 1/4 of a decade over which the statistical significance is 2 standard deviations in 1 day (red), 1 month (green) and 1 year (blue). Note that the sensitivity of LAT is best in the energy range 0.1-10 GeV, with the "sweet spot" point moving slightly towards higher energies as the observing time increases. as shown in Paneque, Chiang, Giebels, Lonjou, Lott, & Madejski [2008] .*

In the study of the potential outcome of these observations were used only the sensitivity of the instrument after 1 day, 1 month and 1 year of observation (Fig. 4.3. LAT capabilities were estimated on the relatively nearby and bright VHE blazars Mrk 421 (z = 0.031), Mrk 501 (z = 0.034) 1ES 1959+650 ($z = 0.047$), and PKS2155-304 (z = 0.117) about which very little was known in the GeV range. Mrk 421 and PKS2155-304 are in the 3rd EGRET catalog [Hartman et al., 1999], yet Mrk 501 and 1ES 1959+650 are not. The EGRET source 3EG J1959+6342 is located ∼1.5 degrees away from 1ES 1959+650, and its HE flux can be considered as an upper limit for the average emission of this blazar. As far as Mrk 501, the only EGRET detection is reported in Kataoka et al. [1999]; the source was detected at 5 standard deviations (s.d.) during a flaring episode. It was however not detected during 1997, when the source underwent into a extremely high state at TeV energies. Archival measurements of these sources, along with a variety of model fits, are displayed in Figure 4.4, along with simple estimates for the expected $F_{\rm HE}$ flux in the 0.1-10 GeV range according to the the model fits. The required times

to achieve a 5σ detection of those fluxes are reported in Table 4.1. As we know by now, the Fermi-LAT sensitivity permits the detection of these sources in observing times as low as a day, which is more than one order of magnitude better than EGRET.

Spectral Flux	$T_{\rm obs}$	$\Delta F_{\rm HE}$	$\Delta\Gamma$
(day)	(%)	(%)	
Mrk 421:f1	0.6	60	14
Mrk 421:f2	0.2	56	14
Mrk 501:f1	7	62	13
Mrk 501:f2	0.7	63	13
Mrk 501:f3	0.2	68	13
1ES 1959:f1	33	62	12
1ES 1959:f2	17	66	13
1ES 1959:f3	10	28	8
PKS 2155:f1	4	58	12
PKS 2155:f2	5	34	9
PKS 2155:f3	0.5	52	13

Table 4.1: *Required observation times $T_{\rm obs}$ for a 5σ detection (or a TS=25) of the spectra $f_{1,2,3}$ depicted in Figure 4.4. These estimates are valid for survey mode operation, in which Fermi scans the entire sky every 3 hours. The statistical uncertainties $\Delta F_{\rm HE}$ in the flux above $100\,{\rm MeV}$ and the spectral index $\Delta\Gamma$ for those observation times are also reported.*

4.5 The H.E.S.S. and *Fermi* observation campaign of PKS 2155-304

One of those campaigns subsequently aimed at PKS 2155−304 since the predictions made for Fermi in this study were optimistic, but for which the H.E.S.S. observation window happened to be uncomfortably close to the launch date, and for which valuable X-ray observation time (first RXTE, then Swift as well) was allocated. This scheduled MWL campaign nevertheless happened, and is described in §4.6. H.E.S.S. observed PKS 2155−304 for 10 days, and when the source was close to its quiescent flux level with little but significant variability, the Fermi observations revealed a rather bright emission but with no significant flux variability. These were the first multiwaveband observations that include simultaneous coverage in the 100 MeV-300 GeV band, and provided new, more stringent constraints on models of jet emission in this source, including a direct measurement of the apparent overall luminosity of the high energy component of the SED. The X-ray and VHE data show significant variability on the 1–2 day time scale, even though the source remained in a relatively low state in the VHE for the duration of the campaign. The time-averaged LAT and H.E.S.S. data are roughly consistent with a single inverse-Compton component for the high energy part of the overall SED, but the flux and spectral variability seen in the X-ray, HE, and VHE bands on shorter time scales are more surprising.

The time averaged SED was adjusted with a standard one zone synchroton self-Compton (SSC) model, for which the electron density is described by three power laws $dn/d\gamma \propto \gamma^{-p_i}\,(i=1-3)$. Note that the variability time scale used to constain R/δ in this model was the observed one of 2-3 days in the VHE γ-rays, and not the extremely fast ones from the 2006 outbursts. This model reproduced the observed SED quite well. Another interesting fact was that such a model can naturally explain why the variable X-ray flux did not correlate with the VHE γ-ray flux, very much like the results from the previous MWL campaign on PKS 2155−304. This might actually be a natural outcome of strong Klein-Nishina suppression for X-ray radiating electrons; the imprint of IC cooling on the VHE emission could be so imperceptible that even the largest X-ray variability might not produce detectable VHE variability (see Fig. 2 in §4.6, but also Sanchez & Giebels 2009; Sanchez 2010)! What this means in turn is that the position of the IC peak position representation is very likely due to KN effects and not to a cutoff at high energy in the electron spectrum. A resounding consequence is that X-ray detectors are, for this

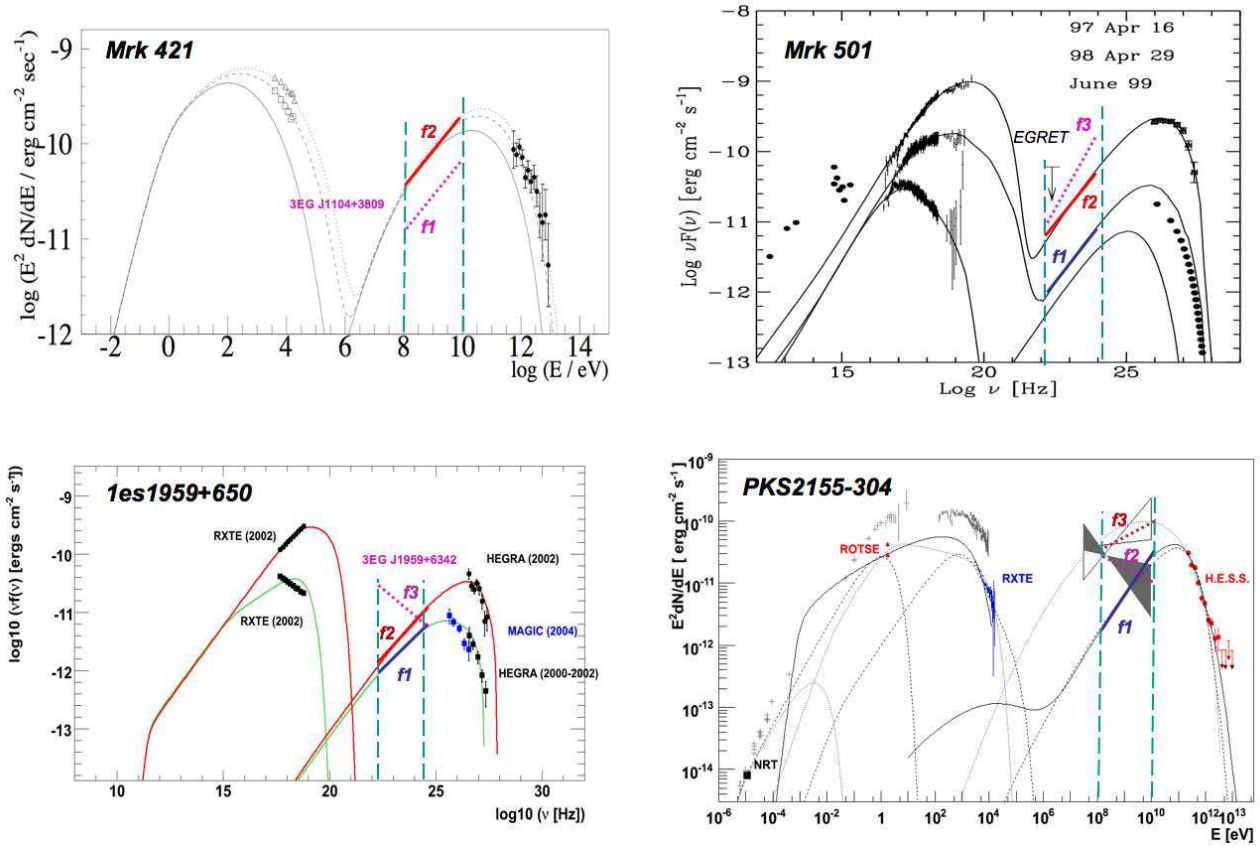

Figure 4.4: *The SEDs of the four main VHE emitters with two to three power law segments ($f_{1,2,3}$) used to estimate a year before launch the Fermi-LAT sensitivity for a MWL campaign [Paneque, Chiang, Giebels, Lonjou, Lott, & Madejski, 2008]. **Top left**: Observed and modeled SEDs for Mrk 421. Squares and triangles show the RXTE spectra measured from MJD 51581.1048-51581.1148 and 51581.3557-51581.3652, respectively. Filled circles show the HEGRA data measured during MJD 51581.0702-51581.2119; which included the first RXTE pointing. Solid, dashed and dotted lines show the SSC model predictions for the low-flux spectrum before the flare, and during the first and the second RXTE pointing, respectively (Reproduced from Krawczynski et al. 2001). The pink dotted line corresponds to the flux of the EGRET source 3EG J1104+3809, which is positionally coincident with Mrk 421 (reproduced from Hartman et al. 1999).**Top right**: Observed and modeled SEDs for Mrk 501. The X-ray data are from observations with BeppoSAX performed on 1997 April, 1998 April, and 1999 June. The squares are data from CAT recorded in 1997 April [Djannati-Atai et al., 1999], and the filled circles are data from HEGRA recorded in 1998- 1999 [Aharonian et al., 2001]. The solid lines show several SSC model predictions for the different flaring states (reproduced from Tavecchio et al. 2001). The pink dotted line corresponds to the only detection (∼5 sigma) of Mrk501 with EGRET obtained during a flare in 1996 [Kataoka et al., 1999]. **Bottom left**: Observed and modeled SED of 1ES 1959+650 obtained during various epochs. The X-ray points are RXTE data taken during June 14th 2002 [Krawczynski et al., 2004]. The black square points are data from HEGRA during the observing campaign 2000-2001 (∼100 hours). Data extracted from [14]. The blue circles are data from MAGIC during the observing campaign of 2004 (∼ 7 hours). (Data extracted from Aharonian et al. 2003a). In both occasions, the source was in quiescent state. The VHE spectra are corrected for EBL extinction using the "Low" EBL model described in Kneiske et al. [2004]. The one zone SSC modeling of the spectra was performed with the code presented in Krawczynski et al. [2004]. The pink dotted line corresponds to the EGRET source 3EG J1959+6342, which is located ∼1.5 degrees away from 1ES 1959+650, and can be considered as an upper limit for the average emission of this blazar. **Bottom right**: Observed and modeled SED of PKS2155-304 in a low state, with 3 different emission models from Aharonian et al. [2005] (or §4.3), two leptonic and one hadronic. The bowties and corresponding red and pink dotted lines are a high state seen by EGRET, and the average spectrum from the 3rd EGRET catalog.*

kind of extreme object, more sensitive to fluctuations in the most energetic electrons in the jet than the VHE γ-rays.

One of the surprises came from the optical/VHE correlation (Fig. 4.5), and it is interesting because it is seen in a *quiescent* state, as opposed to most of the non-correlations seen usually in a *high* state. This certainly has to be confirmed in future observations of PKS 2155−304 but should also be searched for in other BL Lac objects in a low state.

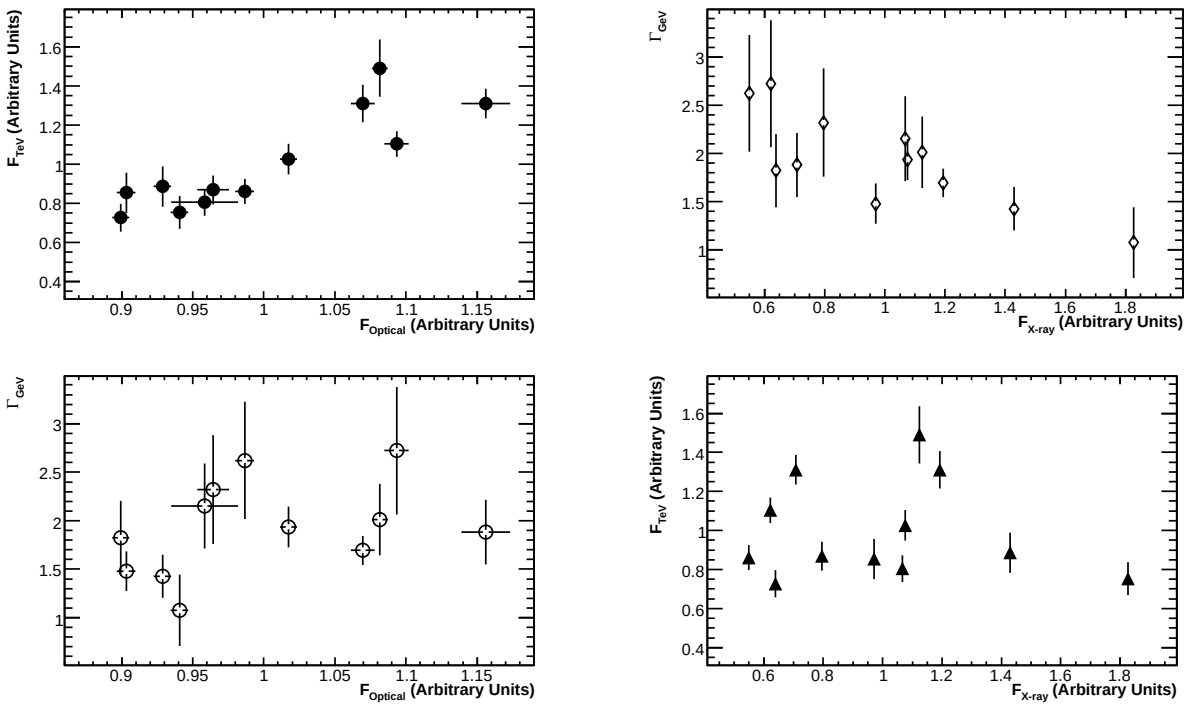

Figure 4.5: *All four correlation patterns extracted from the 2008 MWL campaign on PKS 2155−304 with a.o. H.E.S.S. and Fermi. A surprising VHE γ-ray /optical flux correlation was found (top left), while there was no X-ray/VHE correlation (bottom right), a behaviour also reported afterwards for Mkn 421 by Acciari et al. 2009b.*

Another opportunity to test this hypothesis came with a study of the peculiar HBL PG 1553+113 [Abdo et al., 2010a]. With one of the flattest light curves in the HE band with over 6 months of Fermi observations, PG 1553+113 has also not been variable in the VHE band for most of the observations carried out by ACTs. (Indeed, its declination makes it visible for all current major ACTs.) Interestingly, this object has such a steep VHE spectrum that its very hard HE spectrum makes Fermi's $\sim 2\mathrm{d}$ sampling time scale shorter than those of MAGIC and HESS. The archival X-ray observations however show an amplitude of about an order of magnitude in the flux, with however a spectral index which remains compatible during such different X-ray flux states. Interestingly, the same SSC model can be parametrized such that huge swings in the X-ray emitting electrons of the highest energies still yield a rather steady IC flux, exactly as for PKS 2155−304 (Fig. 4.6). This behaviour is an indication that the hard X-ray flux of BL Lacs can change significantly without resulting in detectable activity in the gamma-ray regime, except for at the peak of the SED at these energies, i.e., that X-ray variability can be accompanied by VHE gamma-ray quiescence and a measurable shift in the spectrum at the peak of the Fermi energy regime. In such a scenario, the electrons producing the variable X-ray emission are at higher energies than those upscattering the bulk of the synchrotron photons to the VHE gamma-ray regime; the scatterings of the variable hardest X-rays are suppressed mostly due to the Klein-Nishina regime scattering effects but also because of the decreasing target photon density at these energies. This effect is demonstrated for the extreme case in Figure 4.6 where the black dashed curve shows the broadband spectrum when the high-energy electron component is omitted. It can be seen that the difference between it and the curves in which

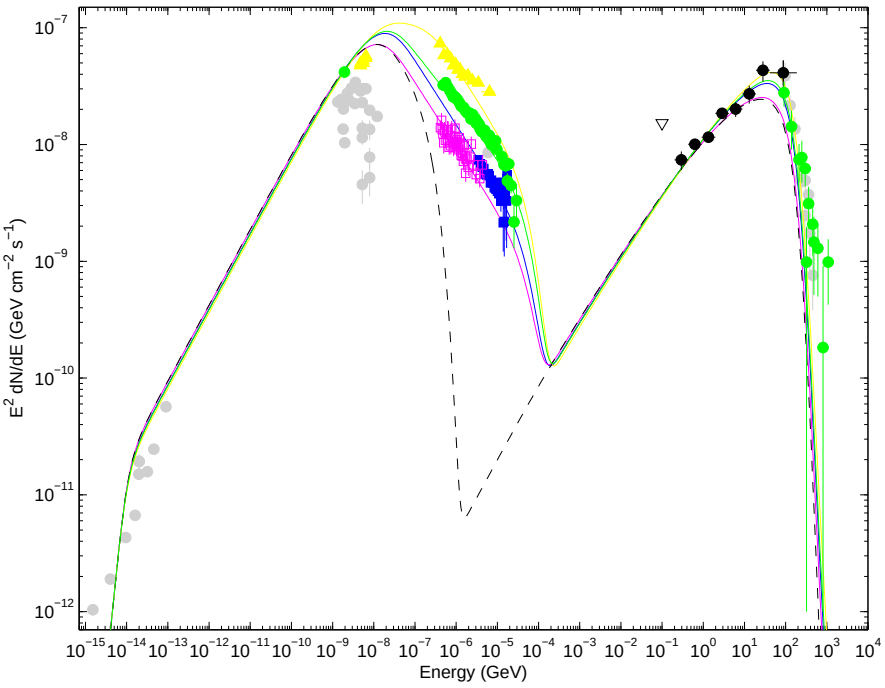

Figure 4.6: *The SED of PG 1553+113 fit with the same SSC model as in §4.6. By altering only the distribution of the electrons that produce the synchrotron emission, a good fit to the overall SED was found for each of the X-ray flux states; and for all of these model realizations, the VHE component of the SED did not change significantly: the magnitude of the changes in the SED above ∼200 GeV are on the order of the VHE statistical measurement uncertainties. This consistency of spectral shape implies that the gamma-ray flux could remain consistent with the state seen by H.E.S.S. and MAGIC during the observations of 2005-2006, even in the presence of the large changes in the X-ray flux level that have been detected.*

the highest energy electrons are included is still on the order of the statistical measurement uncertainties in the VHE regime.

In the framework of this model, the X-ray and VHE γ-ray fluxes would be correlated during γ-ray flaring states while during the more common gamma-ray quiescent states changes in the X-ray flux would not lead to detectable changes in the gamma-ray flux, except for at the high-energy peak in the SED. The simple, one-zone SSC model employed here allows for such a scenario accounting for the X-ray flux variations observed historically while not requiring detectable changes in the VHE gamma-ray flux state.

4.6 "Simultaneous observations of PKS 2155−304 with H.E.S.S., Fermi, RXTE and ATOM: Spectral energy distributions and variability in a low state"

The Astrophysical Journal, 696:L150–L155, 2009 May 10 doi:10.1088/0004-637X/696/2/L150

SIMULTANEOUS OBSERVATIONS OF PKS 2155−304 WITH HESS, *FERMI*, *RXTE*, AND ATOM: SPECTRAL ENERGY DISTRIBUTIONS AND VARIABILITY IN A LOW STATE

F. Aharonian[1,2], A. G. Akhperjanian[3], G. Anton[4], U. Barres de Almeida[5,76], A. R. Bazer-Bachi[6], Y. Becherini[7,8], B. Behera[9], K. Bernlöhr[1,10], C. Boisson[11], A. Bochow[1], V. Borrel[6], E. Brion[12], J. Brucker[4], P. Brun[12], R. Bühler[1], T. Bulik[13], I. Büsching[14], T. Boutelier[15], P. M. Chadwick[5], A. Charbonnier[16], R. C. G. Chaves[1], A. Cheesebrough[5], L.-M. Chounet[17], A. C. Clapson[1], G. Coignet[18], M. Dalton[10], M. K. Daniel[5], I. D. Davids[14,19], B. Degrange[17], C. Deil[1], H. J. Dickinson[5], A. Djannati-Ataï[7,8], W. Domainko[1], L. O'C. Drury[2], F. Dubois[18], G. Dubus[15], J. Dyks[13], M. Dyrda[20], K. Egberts[1], D. Emmanoulopoulos[9], P. Espigat[7,8], C. Farnier[21], F. Feinstein[21], A. Fiasson[21], A. Förster[1], G. Fontaine[17], M. Füssling[10], S. Gabici[2], Y. A. Gallant[21], L. Gérard[7,8,77], B. Giebels[17,77], J. F. Glicenstein[12], B. Glück[4], P. Goret[12], D. Göhring[4], D. Hauser[9], M. Hauser[9], S. Heinz[4], G. Heinzelmann[22], G. Henri[15], G. Hermann[1], J. A. Hinton[23], A. Hoffmann[24], W. Hofmann[1], M. Holleran[14], S. Hoppe[1], D. Horns[22], A. Jacholkowska[16], O. C. de Jager[14], C. Jahn[4], I. Jung[4], K. Katarzyński[25], U. Katz[4], S. Kaufmann[9], E. Kendziorra[24], M. Kerschhaggl[10], D. Khangulyan[1], B. Khélifi[17], D. Keogh[5], W. Kluźniak[13], Nu. Komin[12], K. Kosack[1], G. Lamanna[18], J.-P. Lenain[11], T. Lohse[10], V. Marandon[7,8], J. M. Martin[11], O. Martineau-Huynh[16], A. Marcowith[21], D. Maurin[16], T. J. L. McComb[5], M. C. Medina[11], R. Moderski[13], E. Moulin[12], M. Naumann-Godo[17], M. de Naurois[16], D. Nedbal[26], D. Nekrassov[1], J. Niemiec[20], S. J. Nolan[5], S. Ohm[1], J-F. Olive[6], E. de Oña Wilhelmi[7,8,78], K. J. Orford[5], M. Ostrowski[27], M. Panter[1], M. Paz Arribas[10], G. Pedaletti[9], G. Pelletier[15], P.-O. Petrucci[15], S. Pita[7,8], G. Pühlhofer[9], M. Punch[7,8], A. Quirrenbach[9], B. C. Raubenheimer[14], M. Raue[1,77], S. M. Rayner[5], M. Renaud[1,7,8], F. Rieger[1,77], J. Ripken[22], L. Rob[26], S. Rosier-Lees[18], G. Rowell[28], B. Rudak[13], C. B. Rulten[5], J. Ruppel[29], V. Sahakian[3], A. Santangelo[24], R. Schlickeiser[29], F. M. Schöck[4], R. Schröder[29], U. Schwanke[10], S. Schwarzburg[24], S. Schwemmer[9], A. Shalchi[29], M. Sikora[13], J. L. Skilton[23], H. Sol[11], D. Spangler[5], Ł Stawarz[27], R. Steenkamp[19], C. Stegmann[4], G. Superina[17], A. Szostek[27,15], P. H. Tam[9], J.-P. Tavernet[16], R. Terrier[7,8], O. Tibolla[1,9], C. van Eldik[1], G. Vasileiadis[21], C. Venter[14], L. Venter[11], J. P. Vialle[18], P. Vincent[16], M. Vivier[12], H. J. Völk[1], F. Volpe[1,17,77], S. J. Wagner[9], M. Ward[5], A. A. Zdziarski[13], A. Zech[11] (The HESS Collaboration), A. A. Abdo[30], M. Ackermann[31], M. Ajello[31], W. B. Atwood[32], M. Axelsson[33,34], L. Baldini[35], J. Ballet[36], G. Barbiellini[37,38], M. G. Baring[39], D. Bastieri[40,41], M. Battelino[33,42], B. M. Baughman[43], K. Bechtol[31], R. Bellazzini[35], B. Berenji[31], E. D. Bloom[31], E. Bonamente[44,45], A. W. Borgland[31], J. Bregeon[35], A. Brez[35], M. Brigida[46,47], P. Bruel[17], G. A. Caliandro[46,47], R. A. Cameron[31], P. A. Caraveo[48], J. M. Casandjian[36], E. Cavazzuti[49], C. Cecchi[44,45], E. Charles[31], A. Chekhtman[50,30], A. W. Chen[48], C. C. Cheung[51], J. Chiang[31,76], S. Ciprini[44,45], R. Claus[31], J. Cohen-Tanugi[21], S. Colafrancesco[49], J. Conrad[33,42,52], L. Costamante[31], S. Cutini[49], C. D. Dermer[30], A. de Angelis[53], F. de Palma[46,47], S. W. Digel[31], E. do Couto e Silva[31], P. S. Drell[31], R. Dubois[31], G. Dubus[15], D. Dumora[54,55], C. Farnier[21], C. Favuzzi[46,47], S. J. Fegan[17], E. C. Ferrara[51], P. Fleury[17], W. B. Focke[31], M. Frailis[53], Y. Fukazawa[56], S. Funk[31], P. Fusco[46,47], F. Gargano[47], D. Gasparrini[49], N. Gehrels[51,57], S. Germani[44,45], B. Giebels[17,77], N. Giglietto[46,47], F. Giordano[46,47], M.-H. Grondin[55,58], J. E. Grove[30], L. Guillemot[55,58], S. Guiriec[21], Y. Hanabata[56], A. K. Harding[51], M. Hayashida[31], E. Hays[51], D. Horan[17], G. Jóhannesson[31], A. S. Johnson[31], R. P. Johnson[32], W. N. Johnson[30], M. Kadler[59,60,61,62], T. Kamae[31], H. Katagiri[56], J. Kataoka[63], M. Kerr[64], J. Knödlseder[6], F. Kuehn[43], M. Kuss[35], J. Lande[31], L. Latronico[35], S.-H. Lee[31], M. Lemoine-Goumard[55,58], F. Longo[37,38], F. Loparco[46,47], B. Lott[55,58], M. N. Lovellette[30], G. M. Madejski[31], A. Makeev[30,50], M. N. Mazziotta[47], J. E. McEnery[51], C. Meurer[33,52], P. F. Michelson[31], W. Mitthumsiri[31], T. Mizuno[56], A. A. Moiseev[60], C. Monte[46,47], M. E. Monzani[31], A. Morselli[65], I. V. Moskalenko[31], S. Murgia[31], P. L. Nolan[31], E. Nuss[21], T. Ohsugi[56], N. Omodei[35], E. Orlando[66], J. F. Ormes[67], D. Paneque[31], J. H. Panetta[31], D. Parent[55,58], V. Pelassa[21], M. Pepe[44,45], M. Pesce-Rollins[35], F. Piron[21], T. A. Porter[32], S. Rainò[46,47], M. Razzano[35], A. Reimer[31], O. Reimer[31], T. Reposeur[55,58], S. Ritz[51,57], A. Y. Rodriguez[68], F. Ryde[33,42], H. F.-W. Sadrozinski[32], D. Sanchez[17,77], A. Sander[43], J. D. Scargle[69], T. L. Schalk[32], A. Sellerholm[33,52], C. Sgrò[35], M. Shaw[31], D. A. Smith[55,58], G. Spandre[35], P. Spinelli[46,47], J.-L. Starck[36], M. S. Strickman[30], H. Tajima[31], H. Takahashi[56], T. Takahashi[70], T. Tanaka[31], J. G. Thayer[31], D. J. Thompson[51], L. Tibaldo[40,41], D. F. Torres[68,71], G. Tosti[44,45], A. Tramacere[31,72], Y. Uchiyama[31], T. L. Usher[31], N. Vilchez[6], M. Villata[73], V. Vitale[65,74], A. P. Waite[31], K. S. Wood[30], T. Ylinen[33,42,75], and M. Ziegler[32] (The *Fermi*–LAT Collaboration)

[1] Max-Planck-Institut für Kernphysik, P.O. Box 103980, D-69029 Heidelberg, Germany
[2] Dublin Institute for Advanced Studies, 5 Merrion Square, Dublin 2, Ireland
[3] Yerevan Physics Institute, 2 Alikhanian Brothers Street, 375036 Yerevan, Armenia
[4] Universität Erlangen-Nürnberg, Physikalisches Institut, Erwin-Rommel-Str. 1, D-91058 Erlangen, Germany
[5] University of Durham, Department of Physics, South Road, Durham DH1 3LE, UK
[6] Centre d'Étude Spatiale des Rayonnements, CNRS/UPS, BP 44346, F-31028 Toulouse Cedex 4, France
[7] Astroparticule et Cosmologie (APC), CNRS, Universite Paris 7 Denis Diderot, 10, rue Alice Domon et Leonie Duquet, F-75205 Paris Cedex 13, France; lucie.gerard@apc.univ-paris7.fr
[8] UMR 7164 (CNRS, Université Paris VII, CEA, Observatoire de Paris), Paris, France
[9] Landessternwarte, Universität Heidelberg, Königstuhl, D-69117 Heidelberg, Germany
[10] Institut für Physik, Humboldt-Universität zu Berlin, Newtonstr. 15, D-12489 Berlin, Germany
[11] LUTH, Observatoire de Paris, CNRS, Université Paris Diderot, 5 Place Jules Janssen, 92190 Meudon, France
[12] IRFU/DSM/CEA, CE Saclay, F-91191 Gif-sur-Yvette, Cedex, France

[13] Nicolaus Copernicus Astronomical Center, ul. Bartycka 18, 00-716 Warsaw, Poland
[14] Unit for Space Physics, Northwest University, Potchefstroom 2520, South Africa
[15] Laboratoire d'Astrophysique de Grenoble, INSU/CNRS, Université Joseph Fourier, BP 53, F-38041 Grenoble Cedex 9, France
[16] LPNHE, Université Pierre et Marie Curie Paris 6, Université Denis Diderot Paris 7, CNRS/IN2P3, 4 Place Jussieu, F-75252, Paris Cedex 5, France
[17] Laboratoire Leprince-Ringuet, École polytechnique, CNRS/IN2P3, Palaiseau, France; berrie@in2p3.fr, sanchez@poly.in2p3.fr
[18] Laboratoire d'Annecy-le-Vieux de Physique des Particules, CNRS/IN2P3, 9 Chemin de Bellevue-BP 110 F-74941 Annecy-le-Vieux Cedex, France
[19] University of Namibia, Private Bag 13301, Windhoek, Namibia
[20] Instytut Fizyki Jądrowej PAN, ul. Radzikowskiego 152, 31-342 Kraków, Poland
[21] Laboratoire de Physique Théorique et Astroparticules, Université Montpellier 2, CNRS/IN2P3, Montpellier, France
[22] Universität Hamburg, Institut für Experimentalphysik, Luruper Chaussee 149, D-22761 Hamburg, Germany
[23] School of Physics & Astronomy, University of Leeds, Leeds LS2 9JT, UK
[24] Institut für Astronomie und Astrophysik, Universität Tübingen, Sand 1, D-72076 Tübingen, Germany
[25] Toruń Centre for Astronomy, Nicolaus Copernicus University, ul. Gagarina 11, 87-100 Toruń, Poland
[26] Institute of Particle and Nuclear Physics, Charles University, V Holesovickach 2, 180 00 Prague 8, Czech Republic
[27] Obserwatorium Astronomiczne, Uniwersytet Jagielloński, ul. Orla 171, 30-244 Kraków, Poland
[28] School of Chemistry & Physics, University of Adelaide, Adelaide 5005, Australia
[29] Institut für Theoretische Physik, Lehrstuhl IV, Weltraum und Astrophysik, Ruhr-Universität Bochum, D-44780 Bochum, Germany
[30] Space Science Division, Naval Research Laboratory, Washington, DC 20375, USA
[31] W. W. Hansen Experimental Physics Laboratory, Kavli Institute for Particle Astrophysics and Cosmology, Department of Physics and Stanford Linear Accelerator Center, Stanford University, Stanford, CA 94305, USA; jchiang@slac.stanford.edu
[32] Santa Cruz Institute for Particle Physics, Department of Physics and Department of Astronomy and Astrophysics, University of California at Santa Cruz, Santa Cruz, CA 95064, USA
[33] The Oskar Klein Centre for Cosmo Particle Physics, AlbaNova, SE-106 91 Stockholm, Sweden
[34] Stockholm Observatory, Albanova, SE-106 91 Stockholm, Sweden
[35] Istituto Nazionale di Fisica Nucleare, Sezione di Pisa, I-56127 Pisa, Italy
[36] Laboratoire AIM, CEA-IRFU/CNRS/Université Paris Diderot, Service d'Astrophysique, CEA Saclay, 91191 Gif sur Yvette, France
[37] Istituto Nazionale di Fisica Nucleare, Sezione di Trieste, I-34127 Trieste, Italy
[38] Dipartimento di Fisica, Università di Trieste, I-34127 Trieste, Italy
[39] Rice University, Department of Physics and Astronomy, MS-108, P.O. Box 1892, Houston, TX 77251, USA
[40] Istituto Nazionale di Fisica Nucleare, Sezione di Padova, I-35131 Padova, Italy
[41] Dipartimento di Fisica "G. Galilei," Università di Padova, I-35131 Padova, Italy
[42] Department of Physics, Royal Institute of Technology (KTH), AlbaNova, SE-106 91 Stockholm, Sweden
[43] Department of Physics, Center for Cosmology and Astro-Particle Physics, The Ohio State University, Columbus, OH 43210, USA
[44] Istituto Nazionale di Fisica Nucleare, Sezione di Perugia, I-06123 Perugia, Italy
[45] Dipartimento di Fisica, Università degli Studi di Perugia, I-06123 Perugia, Italy
[46] Dipartimento di Fisica "M. Merlin" dell'Università e del Politecnico di Bari, I-70126 Bari, Italy
[47] Istituto Nazionale di Fisica Nucleare, Sezione di Bari, 70126 Bari, Italy
[48] INAF-Istituto di Astrofisica Spaziale e Fisica Cosmica, I-20133 Milano, Italy
[49] Agenzia Spaziale Italiana (ASI) Science Data Center, I-00044 Frascati (Roma), Italy
[50] George Mason University, Fairfax, VA 22030, USA
[51] NASA Goddard Space Flight Center, Greenbelt, MD 20771, USA
[52] Department of Physics, Stockholm University, AlbaNova, SE-106 91 Stockholm, Sweden
[53] Dipartimento di Fisica, Università di Udine and Istituto Nazionale di Fisica Nucleare, Sezione di Trieste, Gruppo Collegato di Udine, I-33100 Udine, Italy
[54] Université de Bordeaux, Centre d'Études Nucléaires Bordeaux Gradignan, UMR 5797, Gradignan 33175, France
[55] Department of Physical Science and Hiroshima Astrophysical Science Center, Hiroshima University, Higashi-Hiroshima 739-8526, Japan
[56] University of Maryland, College Park, MD 20742, USA
[57] CNRS/IN2P3, Centre d'Études Nucléaires Bordeaux Gradignan, UMR 5797, Gradignan 33175, France
[58] Dr. Remeis-Sternwarte Bamberg, Sternwartstrasse 7, D-96049 Bamberg, Germany
[59] Center for Research and Exploration in Space Science and Technology (CRESST), NASA Goddard Space Flight Center, Greenbelt, MD 20771, USA
[60] Erlangen Centre for Astroparticle Physics, D-91058 Erlangen, Germany
[61] Universities Space Research Association (USRA), Columbia, MD 21044, USA
[62] Department of Physics, Tokyo Institute of Technology, Meguro City, Tokyo 152-8551, Japan
[63] Department of Physics, University of Washington, Seattle, WA 98195-1560, USA
[64] Istituto Nazionale di Fisica Nucleare, Sezione di Roma "Tor Vergata," I-00133 Roma, Italy
[65] Max-Planck Institut für Extraterrestrische Physik, 85748 Garching, Germany
[66] Department of Physics and Astronomy, University of Denver, Denver, CO 80208, USA
[67] Institut de Ciencies de l'Espai (IEEC-CSIC), Campus UAB, 08193 Barcelona, Spain
[68] Space Sciences Division, NASA Ames Research Center, Moffett Field, CA 94035-1000, USA
[69] Institute of Space and Astronautical Science, JAXA, 3-1-1 Yoshinodai, Sagamihara, Kanagawa 229-8510, Japan
[70] Institució Catalana de Recerca i Estudis Avançats (ICREA), Barcelona, Spain
[71] Consorzio Interuniversitario per la Fisica Spaziale (CIFS), I-10133 Torino, Italy
[72] INAF, Osservatorio Astronomico di Torino, I-10025 Pino Torinese (TO), Italy
[73] Dipartimento di Fisica, Università di Roma "Tor Vergata," I-00133 Roma, Italy
[74] School of Pure and Applied Natural Sciences, University of Kalmar, SE-391 82 Kalmar, Sweden
Received 2009 January 26; accepted 2009 March 16; published 2009 April 24

ABSTRACT

We report on the first simultaneous observations that cover the optical, X-ray, and high-energy gamma-ray bands of the BL Lac object PKS 2155−304. The gamma-ray bands were observed for 11 days, between 2008 August 25 and 2008 September 6 (MJD 54704−54715), jointly with the *Fermi Gamma-ray Space Telescope* and the HESS atmospheric Cherenkov array, providing the first simultaneous MeV–TeV spectral energy distribution (SED) with the new generation of γ-ray telescopes. The ATOM telescope and the *RXTE* and *Swift* observatories provided optical and

X-ray coverage of the low-energy component over the same time period. The object was close to the lowest archival X-ray and very high energy (VHE; >100 GeV) state, whereas the optical flux was much higher. The light curves show relatively little (∼30%) variability overall when compared to past flaring episodes, but we find a clear optical/VHE correlation and evidence for a correlation of the X-rays with the high-energy spectral index. Contrary to previous observations in the flaring state, we do not find any correlation between the X-ray and VHE components. Although synchrotron self-Compton models are often invoked to explain the SEDs of BL Lac objects, the most common versions of these models are at odds with the correlated variability we find in the various bands for PKS 2155−304.

Key words: BL Lacertae objects: individual (PKS 2155−304) – galaxies: active – gamma rays: observations

1. INTRODUCTION

The underlying particle distributions of blazars are usually studied by matching broadband observations with predictions from radiative models. Since these sources are highly variable, simultaneous observations are essential. The most energetic BL Lac spectra extend up to TeV energies, and positive detections have usually indicated flaring states. However, with their improved sensitivity, the new generation of Atmospheric Cherenkov Telescopes (ACTs), which has more than quadrupled[79] the number of known extragalactic very high energy (VHE) sources, finds a few of these sources in marginally variable states with consistent detections after short exposures. One of these objects, the blazar PKS 2155−304 at $z = 0.116$, is an ideal target for such studies. Crucial information is expected from the *Fermi* Gamma-ray Space Telescope, since its improved sensitivity over EGRET would constrain dramatically the existing models that predict a wide variety of fluxes in the 100 MeV–10 TeV energy range. Since the HESS experiment detects this source in a low state within ∼1 hr, significant daily detections were guaranteed and the source was targeted for an 11-day multiwavelength campaign.

2. OBSERVATIONS AND ANALYSIS RESULTS

The HESS observations of PKS 2155−304 took place during MJD 54701−54715, for a total of 42.2 hr. After applying the standard HESS data-quality selection criteria, an exposure of 32.9 hr live time remains (MJD 54704−54715), at a mean zenith angle of 18.°3. The data set has been calibrated using the standard HESS calibration method (Aharonian et al. 2004). The analysis tools and the event-selection criteria used for the VHE analysis are presented in F. Aharonian et al. (2009, in preparation). The events have been selected using "loose cuts," preferred for their lower energy threshold of 200 GeV and higher γ-ray acceptance. A 0.°2 radius circular region centered on PKS 2155−304 was defined to collect the on-source events. The background was estimated using the "Reflected Region" method (Aharonian et al. 2006b). Those observations yield an excess of 8800 events, a signal with a significance of 55.7σ calculated following Li & Ma (1983). Using standard cuts an excess of 3612 events with a significance of 68.7σ is found. An independent analysis and calibration (Benbow 2005) yields similar results.

The data from the Large Area Telescope (LAT; Atwood et al. 2008) have been analyzed by using `ScienceTools` version 9.7, which will be publicly available from the *HEASARC* in the future. Events having the highest probability of being photons (class 3, called "diffuse") and coming from zenith angles $< 105^\circ$ (to avoid Earth's albedo) were selected. The diffuse emission along the plane of the Milky Way, mainly due to cosmic-ray interactions with the Galactic interstellar matter, has been modeled using the `54_59Xvarh7S` model prepared with the *GALPROP* code (Strong et al. 2004a, 2004b) which has been refined with *Fermi*–LAT data taken during the first three months of operation. The extragalactic diffuse emission and the residual instrumental background have been modeled as an isotropic power-law component and included in the fit. Photons were extracted from a region with 10° radius centered on the coordinates of PKS 2155−304 and analyzed with an unbinned maximum likelihood technique (Cash 1979; Mattox et al. 1996) using the `Likelihood` analysis software provided by the LAT team. Because of calibration uncertainties at low energies, data in the 0.2–300 GeV energy band were selected.

A total of 75 ks of exposure was taken with *RXTE*, spread over 10 days coinciding with the HESS observations, and a 6.4 ks exposure with *Swift* was made toward the end of the campaign. The data taken with the Proportional Counter Array (PCA; Jahoda et al. 1996) and the X-ray Telescope (XRT; Burrows et al. 2005) instruments were analyzed using the *HEASOFT 6.5.1* package using the Guest Observer Facility recommended criteria. The XRT data were extracted from a 56″ slice, both for the source and the background. Since the rate was less than 10 Hz, no pile-up is expected in the Windowed Timing (WT) mode.

During the multiwavelength campaign, a total of 106 observations were taken with the 0.8 m ATOM optical telescope (Hauser et al. 2004) located on the HESS site. Integration times between 60 s and 200 s in the Bessel *BVR* filter bands were used. Photometric accuracy is typically between 0.01 and 0.02 mag for *BVR*.

2.1. Spectral Analyses

The HESS time-averaged photon spectrum is derived using a forward-folding maximum likelihood method (Piron et al. 2001). The VHE data are well described by a power law of the form $dN/dE = I_0(E/E_0)^{-\Gamma}$, with a differential flux at $E_0 = 350$ GeV (the fit decorrelation energy) of $I_0 = 10.4 \pm 0.24_{\rm stat} \pm 2.08_{\rm sys} \times 10^{-11}$ cm^{-2} s^{-1} TeV^{-1} and a spectral index $\Gamma = 3.34 \pm 0.05_{\rm stat} \pm 0.1_{\rm sys}$. As before, during nonflaring states of PKS 2155−304, the spectrum, measured with limited event statistics, shows no indication of curvature. The spectral index is similar to that previously measured by HESS when the source was at a comparable flux level, in 2003 (Aharonian et al. 2005a, 2005b) and between 2003 and 2005 (F. Aharonian et al. 2009, in preparation). The VHE spectrum is affected by interactions with the extragalactic background light (EBL) which modifies the intrinsic shape and intensity. Using

[75] Supported by CAPES Foundation, Ministry of Education of Brazil.
[76] Authors to whom any correspondence should be addressed.
[77] European Associated Laboratory for Gamma-Ray Astronomy, jointly supported by CNRS, and MPG.
[78] National Research Council Research Associate.
[79] See, e.g., the online TeVCat catalog http://tevcat.uchicago.edu, which has 22 sources at the time of the writing of this Letter.

the $P0.45$ model (Aharonian et al. 2006a), the intrinsic spectral index is derived to be $\Gamma_{\rm int} \approx 2.5$.

The average *Fermi* spectra over the duration of the campaign are fitted by a simple power law for which $I_0 = (2.42 \pm 0.33_{\rm stat} \pm 0.16_{\rm sys}) \times 10^{-11}$ cm^{-2} s^{-1} MeV^{-1}, $\Gamma = 1.81 \pm 0.11_{\rm stat} \pm 0.09_{\rm sys}$, and $E_0 = 943$ MeV is the energy at which the correlation between the fitted values of Γ and I_0 is minimized. The total exposure is 7.7×10^8 cm^2 s. There is no statistical preference for a broken power law in this data set. The light curve derived for *Fermi* data between MJD 54682−54743 shows a similar state on average as during this campaign, so in order to increase the photon statistics for the spectral fits, those data were included, resulting in an increase of the exposure by a factor of 3.6. The longer data set is then fit by a broken power-law spectrum, which is preferred over the single power law with a significance of 97% using the likelihood ratio test. We obtain a low-energy photon index of $\Gamma_L = 1.61 \pm 0.16_{\rm stat} \pm 0.17_{\rm sys}$, a break energy of $E_{\rm br} = 1.0 \pm 0.3$ GeV, a high-energy index of $\Gamma_H = 1.96 \pm 0.08_{\rm stat} \pm 0.08_{\rm sys}$, and a 0.2–300 GeV flux of $(1.13 \pm 0.05_{\rm stat} \pm 0.11_{\rm sys}) \times 10^{-7}$ cm^{-2} s^{-1}. The *Fermi* spectrum is consistent with the hard photon index of 1.71 ± 0.24 during a flaring episode detected by EGRET (Vestrand et al. 1995), but it differs from the Third EGRET Catalog spectrum (Hartman et al. 1999) where the index is 2.35 ± 0.26.

The 4–10 keV PCA and 0.5–9 keV XRT data were analyzed simultaneously with XSPEC version 12.4.0 (Arnaud 1996), using a broken power-law model and taking into account the uncertainty in the cross-calibrations, as well as the variability across the nonsimultaneous observations, by using a multiplicative factor for each instrument (fixed to 1 for the PCA data) as in Falanga et al. (2006). Using a fixed Galactic hydrogen column of $N_{\rm H} = 1.48 \times 10^{-20}$ cm^{-2}, we obtain a low-energy photon index of $\Gamma_1 = 2.36 \pm 0.01$, a break energy of $E_{\rm br} = 4.44 \pm 0.48$ keV, and a high-energy index of $\Gamma_2 = 2.67 \pm 0.01$, for an unabsorbed 2–10 keV flux of 4.99×10^{-11} erg cm^{-2} s^{-1}, which is approximately two times higher than during the 2003 campaign (Aharonian et al. 2006a). This is similar to the VHE flux increase reported above, while still being well below the high state fluxes reported by Vestrand et al. (1995).

2.2. Light Curves

The light curves from HESS, *Fermi*, *RXTE*, and ATOM are shown in Figure 1, where the HESS runs (∼28 minutes) were combined to derive nightly flux values. The average integrated flux above 200 GeV $(5.56 \pm 0.13_{\rm stat} \pm 1.11_{\rm sys}) \times 10^{-11}$ ph cm^{-2} s^{-1}, corresponds to ∼20% $F_{\rm Crab>200\,GeV}$, or ∼50% higher than the quiescent state of 2003 (Aharonian et al. 2006a) and 70 times lower than its peak flaring flux (Aharonian et al. 2007). The positive excess variance $\sigma_{\rm XS}^2$, indicating variability, allows a fractional rms of $F_{\rm var,VHE} = 23\% \pm 3\%$ (see Vaughan et al. 2003 for definitions of $\sigma_{\rm XS}^2$ and $F_{\rm var}$) to be derived, which is three times less than the high state flaring variability reported by Aharonian et al. (2007). A spectrum was obtained for each night when possible, otherwise two or three nights were combined. No indication of spectral variability was found during those observations, with a limit on the nightly index variations of $\Delta\Gamma < 0.2$.

The *Fermi* light curve shows the photon fluxes for the high energy (HE) range, 0.2–300 GeV, and the photon spectral indices for each interval. Each bin is the result of a power-law fit, using the background values found on the overall time-averaged fit, and centered on the HESS observations. The light curve fit to a constant has a χ^2 probability of $p(\chi^2) = 0.95$, clearly consistent with a constant flux. The normalized excess variance of -0.16 ± 0.09 sets a 90% confidence level limit of $F_{\rm var,HE} \leqslant 20\%$ on the fractional variance (Feldman & Cousins 1998).

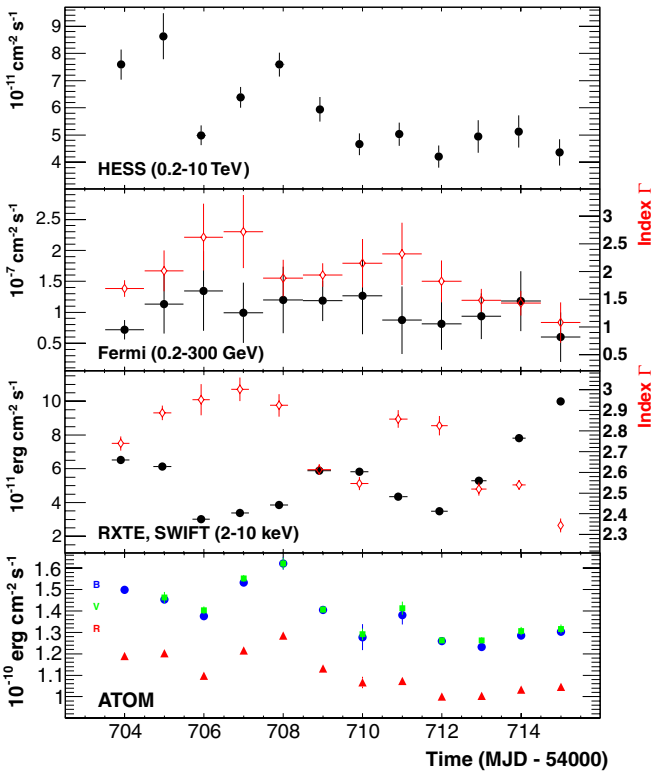

Figure 1. Light curves from (top to bottom): HESS, *Fermi*, *RXTE/Swift*, and ATOM. The *Fermi* and *RXTE/Swift* panels also show the spectral index measurements (red) for each night. Vertical bars show statistical errors only. Horizontal bars represent the integration time and are apparent only for the *RXTE* and *Fermi* data. The ATOM bands are *B* (blue circles), *V* (green squares), and *R* (red squares).

The X-ray light curve, derived from spectral fits of the nightly *RXTE* (and *Swift*) data sets, shows flux doubling episodes on timescales of days, similar to the optical and VHE measurements. The lowest fluxes of ∼3–6 $\times 10^{-11}$ erg cm^{-2} s^{-1} are at the same level as those seen in the low state (Aharonian et al. 2005b) but with larger fluctuations, $F_{\rm var,X} = 35\% \pm 0.05\%$. The time history of the fitted spectral indices in Figure 1 show clearly that the X-ray spectrum hardens significantly, $\Delta\Gamma_x \approx 0.5$, as the 2–10 keV flux increases.

The ATOM fluxes are ∼5 times higher than the low state found in Aharonian et al. (2005b), but the *V*-band magnitudes reported here are in the range 12.7–13 which is well on the lower side of the measurements of PKS 2155−304 reported by Foschini et al. (2008) when the source was quoted to be in a low state with *V*-band magnitudes in the range 12–12.7. The host galaxy flux is estimated to be $\approx 10^{-11}$ erg cm^{-2} s^{-1} (Kotilainen et al. 1998), hence most of the optical flux can be attributed to the central AGN. The average fractional rms over all bands is $F_{\rm var,opt} \sim 8\% \pm 0.5\%$. The $B - R$ light curve is compatible with a constant, $p(\chi^2) = 0.66$, indicating little or no optical spectral variability.

3. DISCUSSION

The two-component broadband spectra of high energy-peaked BL Lac objects (HBLs) are typically modeled with syn-

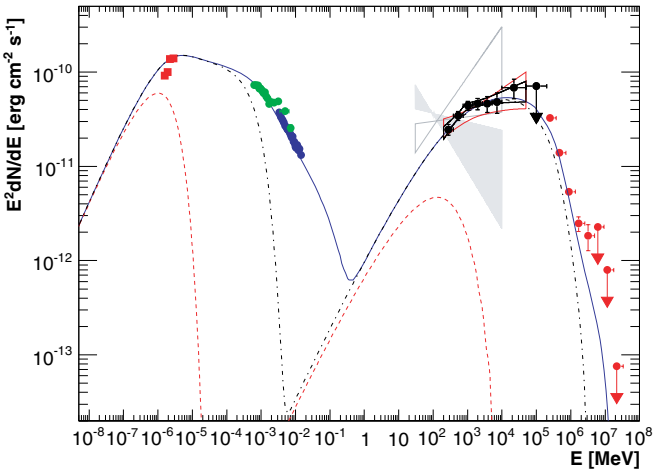

Figure 2. SED of PKS 2155−304. The red butterfly is the *Fermi* spectrum restricted to the MJD 54704−54715 period, while the black butterfly covers MJD 54682−54743. As a cross check of the fit robustness, the differential flux was estimated in eight limited energy bins by a power-law fit (black circles) and are found to be consistent within 1σ of the global fit, including a clear spectral break at ∼1 GeV. The gray points are archival NED data, and the two gray butterflies are EGRET measurements. The solid line is a one-zone SSC model. The dashed and the dot-dashed lines are the same model without electrons above γ_1 and γ_2, respectively. The VHE part is absorbed with the *P*0.45 extragalactic background model described in Aharonian et al. (2006a).

chrotron self-Compton (SSC) scenarios (e.g., Band & Grindlay 1985). Despite the simplicity of these models, they have been successful in reproducing many blazar spectral energy distributions (SEDs) and make definite predictions for the flux and spectral variability that should be seen in the two components. In particular, for typical parameters, the electrons responsible for the X-ray emission also produce the VHE emission; and if the underlying particle distributions were to vary, the resulting flux and spectral changes in the VHE band should be related to variations in the X-rays. In fact, for the 2006 July flare, a nonlinear relationship was seen between the X-ray and VHE bands, though the observed variability patterns do not quite fit the simple SSC model in detail (Costamante 2008).

In Figure 2, we overlay a model SSC calculation that roughly fits the time-averaged SED. The electron distribution model parameters, a three-component power law with indices $p_0 = 1.3$, $p_1 = 3.2$, $p_2 = 4.3$ ($dn/d\gamma \propto \gamma^{-p_i}$), minimal and maximal Lorentz factors $\gamma_{\rm min} = 1$ and $\gamma_{\rm max} = 10^{6.5}$, break electron Lorentz factors $\gamma_1 = 1.4\times10^4$, $\gamma_2 = 2.3\times10^5$, and total electron number $N_{\rm tot} = 6.8 \times 10^{51}$, have been set to reproduce the shape of the lower energy component of the SED. The overall SED is then adjusted with the remaining parameters: radius of the emitting region in the comoving frame, $R = 1.5 \times 10^{17}$ cm; bulk Doppler factor, $\delta = 32$; magnetic field, $B = 0.018$ G. Even though we regard this fit as a "straw-man" model, it is perhaps reassuring that the joint *Fermi*–HESS time-averaged spectra can be reasonably well described as SSC emission. Katarzyński et al. (2008) found similar values for R, B, and δ in their SSC description of a steady large jet component in the SED of PKS 2155−304.

Some features of this model calculation are particularly noteworthy. The electrons that produce the synchrotron X-ray emission have Lorentz factors $> \gamma_2$. When the power-law component for those electrons is omitted from the calculation, the dot-dashed curve in Figure 2 results. For this particular set of parameters, the electrons that produce the X-rays have higher energies than the electrons that produce the VHE emission. Furthermore, the lack of a significant impact on the shape of the SSC component when those electrons are removed indicates that Klein–Nishina effects suppress any significant contribution by those electrons to the emission at ∼TeV energies.

These features of this calculation allow that there need not be a correlation between the X-ray and VHE fluxes; and in fact, this is what is observed. In contrast with the 2006 July flare, we do not find any evidence of flux correlation between the X-ray and HESS bands with a Pearson's r of 0.12 ± 0.1 between these bands. Furthermore, the 2–10 keV X-ray spectra show spectral variability consistent with an underlying electron distribution for which the cooling timescales are of order the flux variability timescales, i.e., the spectra are softer when the flux is lower, with changes in photon index of $\Delta\Gamma_x \approx 0.5$ (Figure 1); whereas, the VHE emission shows no evidence for significant spectral variability despite flux variations of a factor of 2. Since radiative cooling timescales vary inversely with electron energy, this supports the conclusion that the electrons responsible for the synchrotron emission in the X-ray band have higher energies than the electrons that produce the inverse-Compton emission in the VHE range, assuming they are part of the same overall nonthermal distribution.

Even though this all fits in with our straw-man SED calculation, the variability patterns in the optical, X-ray, HE, and VHE bands suggest a much more complex situation. In the absence of spectral variability, the mechanisms that would produce the observed flux variability in the VHE band are rather constrained. Increases in flux could be driven by injection of particles with a constant spectral shape, and decreases in flux could be caused by particle escape from the emitting region or by expansion (adiabatic) losses, assuming those latter two processes can operate independent of particle energy. However, since the electrons that produce the VHE emission must be in the weak radiative cooling regime, a more natural mechanism for the flux variability would be that changes in the seed photon density are driving the variability. Comparing the daily flux values in the optical and the VHE bands, we find indications of fairly strong correlations that suggest that the optical emission provides the target photons for the IC emission. In the B, V, and R bands, the correlations with the HESS fluxes have Pearson's r values in the range 0.77–0.86 with uncertainties $\leqslant 0.09$. This correlated behavior is readily apparent in the light curves shown in Figure 1, and these results provide the first quantitative evidence of correlated variability between the optical and VHE bands on these timescales for an HBL.[80] Confirmation of this behavior, not only from this source but also from other VHE emitting blazars in a low state, would provide important constraints on emission models for these objects.

In the context of a single-zone SSC model, we would expect that any flux variability in the optical bands should also appear as variability in the *Fermi*–LAT energy range. To illustrate this, we plot, as the dashed curve in Figure 2, the SED that results if we omit contributions from electrons with energies $> \gamma_1$. For the original model parameters, the electrons that produce the optical-soft X-ray emission also produce the bulk of the IC component, including the HE and VHE emission. Since we do not find any indication of a correlation between the optical and HE fluxes, this suggests that the optical emission may arise from a separate population of electrons than those responsible for the

[80] Donnarumma et al. (2008) mention possible correlated variability in the recent 2008 June flare of Mrk 421 in a high state.

HE and VHE emission. If so, then these electrons probably also occupy a distinct physical region with different physical parameters (magnetic field, size scale, bulk Lorentz factor). Multizone SSC models of this kind have already been proposed to account for the "orphan" γ-ray flare in 1ES 1959+650 during 2002 May (Krawczynski et al. 2004).

Although the 0.2–300 GeV photon fluxes measured by *Fermi* are consistent with being constant, we find more significant variations of the photon spectral index in the daily analyses ($p(\chi^2) = 0.19$). The fitted values range from fairly soft, $\Gamma = 2.7 \pm 0.7$, to extremely hard, $\Gamma = 1.1 \pm 0.4$. These values, along with the constant, intrinsic VHE index of $\Gamma_{\rm VHE} \approx 2.5$ derived from the HESS data, imply spectral breaks between the HE and VHE bands of $\Delta\Gamma$ as large as 1.4. Very sharp spectral breaks ($\Delta\Gamma \gtrsim 1$) would require rather narrow electron distributions and would therefore pose difficulties in fitting a broad lower energy component in the context of a single-zone model. Interestingly, we find a significant anticorrelation between the nightly X-ray fluxes and the *Fermi*–LAT spectral indices of $r_{X\Gamma} = -0.80 \pm 0.15$. A fit to a linear model is preferred over a constant at the 2.6σ level, with a slope of -0.14 ± 0.05. If the electrons that produce the X-rays are at higher energies than those that produce the TeV emission, the cause for such a correlation would be difficult to understand. An important caveat in considering these results is that the *Fermi* coverage for PKS 2155−304 was relatively uniform over each 24 hr period, whereas the optical, X-ray, and VHE observations were restricted to 4–6 hr intervals each night. Hence, the *Fermi* observations are not strictly simultaneous with the other measurements, so it is possible that some of the observed HE spectral variability occurred outside of the nightly observing windows.

As the first multiwavelength campaign of an HBL that includes *Fermi* and an ACT instrument, these observations have yielded results that strongly challenge the standard models for these sources. Having caught PKS 2155−304 in a low state, we see that its spectral and variability properties are significantly different than its flaring, high state behavior. The variability patterns, in particular, defy easy explanation by the usual SSC models and should provide valuable constraints for models that attempt to describe the emission mechanisms in blazar jets.

The full HESS and *Fermi*–LAT acknowledgements can be found on Web sites http://www.mpi-hd.mpg.de/hfm/HESS/acknowledgements and http://www-glast.stanford.edu/acknowledgements.

REFERENCES

Aharonian, F., et al. (HESS Collaboration) 2004, Astropart. Phys., 22, 109
Aharonian, F., et al. (HESS Collaboration) 2005a, A&A, 430, 865
Aharonian, F., et al. (HESS Collaboration) 2005b, A&A, 442, 895
Aharonian, F., et al. (HESS Collaboration) 2006a, Nature, 440, 20
Aharonian, F., et al. (HESS Collaboration) 2006b, A&A, 457, 899
Aharonian, F., et al. (HESS Collaboration) 2007, ApJ, 664, L71
Arnaud, K. A. 1996, in ASP Conf. Ser. 101, Astronomical Data Analysis Software and Systems V, ed. G. H. Jacoby & J. Barnes (San Francisco, CA: ASP), 17
Atwood, W. B., et al. 2008, ApJ, submitted (arXiv:0902.1089)
Band, D. L., & Grindlay, J. E. 1985, ApJ, 298, 128
Benbow, W. 2005, Proc. Towards a Network of Atmospheric Cherenkov Detectors VII (Palaiseau), 163
Burrows, D. N., et al. 2005, Space Sci. Rev., 120, 165
Cash, W. 1979, ApJ, 228, 939
Costamante, L. (HESS Collaboration) 2008, Int. J. Mod. Phys. D, 17, 1449
Donnarumma, I., et al. 2008, ApJ, 691, 13
Falanga, M., Belloni, T., & Campana, S. 2006, A&A, L5, 456
Feldman, G. J., & Cousins, R. D. 1998, Phys. Rev. D, 57, 3873
Foschini, L., et al. 2008, A&A, 484, 35
Hartman, R. C., et al. 1999, ApJS, 123, 79
Hauser, M., et al. 2004, Astron. Nachr., 325, 659
Jahoda, K., et al. 1996, Proc. SPIE, 2808, 59
Katarzyński, K., Lenain, J.-P., Zech, A., Boisson, C., & Sol, H. 2008, MNRAS, 390, 371
Kotilainen, J. K., Falomo, R., & Scarpa, R. 1998, A&A, 336, 479
Krawczynski, H., et al. 2004, ApJ, 601, 151
Li, T.-P., & Ma, Y.-Q. 1983, ApJ, 272, 317L
Mattox, J. R., et al. 1996, ApJ, 461, 396
Piron, F., et al. 2001, A&A, 374, 895
Strong, A. W., Moskalenko, I. V., & Reimer, O. 2004a, ApJ, 613, 962
Strong, A. W., Moskalenko, I. V., Reimer, O., Digel, S., & Diehl, R. 2004b, A&A, 422, L47
Vaughan, S., Edelson, R., Warwick, R. S., & Uttley, P. 2003, MNRAS, 345, 1271
Vestrand, W. T., Stacy, J. G., & Sreekumar, P. 1995, ApJ, 454, 93

4.7 Conclusions

So what have we learned in discovering all these new VHE extragalactic sources? A clear global trend as of now is that more and more sources are discovered with little excess variability in their light curves, which could be interpreted as seeing them in their quiescent level. This is corroborated with the fact that (quasi) contemporaneous observations of the synchrotron component show fluxes that are often comparable to the lowest levels from archival observations (when those are available). Observations of low X-ray fluxes are the most convincing fact, since VHE γ-ray variability correlates best with X-rays (with one notable exception).

As pointed out by Cheng et al. [2000] emission mechanisms might be simpler to understand during quiescent states in blazars, and they are also the most likely state to be found observationally. In the X-ray band, the existence of a steady underlying emission has also been invoked for two other VHE emitting blazars (Mrk 421, Fossati et al. 2000; and 1ES 1959+650, Giebels et al. 2002). Being able to separate, and detect, flaring and nonflaring states in VHE γ-rays is probably more important for such studies than is currently stated. The evidence of the existence of a lowest flux emission level in PKS 2155−304 presented in §3.4 (while the current sensitivity of the H.E.S.S. array is not sufficient to establish the statistical nature of the fluctuations seen in that state), corroborated this notion, as well as the fact that most of the HE light curves of VHE emitters are not variable [Abdo et al., 2009c].

The statement from Gaskell & Klimek [2003] stipulating that "[He] believe[s] that variability probably poses the biggest challenge to understanding how AGNs work. A theory must not only explain the steady-state spectrum of an AGN, but it must also be able to explain how and why the continua vary", can in this case be inverted for VHE γ-ray emitters, where most models stem from the initial discovery conditions where the source was in a flaring state: the quiescent state might well pose a big challenge to understanding how blazars work, such that a theory must not only explain the variable state of a blazar, but it must also be ablo to explain the steady/quiescent component.

The monitoring of blazars with the current and upcoming generations of ACTs could yield other surprises, the radically different spectral and timing behaviour of PKS 2155-304,Mrk 501 and Mrk 421, the best studied AGN at this time, has yet to be fully understood.

Chapter 5

Perspectives

> The important thing in science is not so much to obtain new facts as to discover new ways of thinking about them.
>
> Sir William Bragg

5.1 Future AGN studies with H.E.S.S.-1,2 and Fermi

The immediate future looks quite γ-ray bright for H.E.S.S. with an ongoing mirror upgrade, and plenty of VHE candidates communicated by the *Fermi* team: the list from Table 1.3 is unlikely to saturate in the short term. Also the *Fermi* sensitivity is continuously improving - at the current time, it is probably slightly better than 40 h of H.E.S.S. observations for a hard blazar (with photon index ~ 1.5), as demonstrates the 38 hours H.E.S.S. exposure to detect SHBL J001355.9-185406 [Hofmann, 2010], and of which no *Fermi* counterpart was found in the 1FGL catalog but was subsequently announced at approximately 7σ with 2 years of *Fermi* data by Sanchez & Fegan [2010]. It is now likely that with 3 years of data the *Fermi* limit for the hardest blazars will reach the canonical $50\,\mathrm{h}$ of ACT observations such that all BL Lacs within a *reasonable* exposure should be known (provided the bulk of them are indeed not variable).

With some luck as well, we might catch another major PKS 2155−304 flare with *Fermi* as well this time, which would allow to find whether these variability properties can change with time. Finding an outburst of a similar southern hemisphere blazar of the same class in an extremely high state would allow to search for similar variability properties, and perhaps establish whether they are a property of a specific source class. Also very interesting would be to catch a flaring blazar from a different class, such as an LBL. With the discovery of VHE γ-rays from the LBL AP Librae this might now be possible, and hence find if these variability properties are class-dependent.

With the upcoming H.E.S.S. 2 telescope, a 28 m dish ACT in the middle of the current H.E.S.S. array, a huge improvement in performance is expected. The threshold should be lowered well below $100\,\mathrm{GeV}$ when the large telescope is used in stand-alone, with however the inconvenience of an expected worse background rejection. The use of both the large and smaller telescope, called the hybrid mode, should set a threshold $\sim 100\,\mathrm{GeV}$ with a moderately improved

Figure 5.1: *The HESS2 telescope in a photo-montage on the current H.E.S.S. site.*

sensitivity due to an improved background rejection thanks to better defined shower images. This should allow to e.g.:

- Define the statistical nature of the quiescent state flux of the brightest blazar PKS 2155−304, whether it behaves also a red noise, if its fluctuations are lognormal, and what its energy dependence might be at even lower energies. It has also yet to be seen what happens to the X-ray/γ-ray correlations in the quiescent state on timescales $\Delta t < 1\,\mathrm{h}$ which is the current limit for H.E.S.S. when PKS 2155−304 is in its low flux state: this could provide us with indications on how different the high state and low state emission regions are;
- Perform spectrally resolved burst analyses on high states of PKS 2155−304 when/if similar outbursts to those of §2 occur again, since the sensitivity of H.E.S.S. cannot constrain these significantly enough . While the fast burst behaviour of PKS 2155−304 is clearly different than those seen by VERITAS on e.g. Mkn 421, the latter has the clear advantage that the much slower rise and decay timescales allow more precise spectral measurements of these phases in a burst.
- Significantly improve the spectral characteristics, and the sampling rate at which the source is resolved, on extragalactic sources with intrinsic very soft spectra such as the HBLs PKS 2005-489 ($\Gamma \sim 4$) or bright HE sources with a large EBL induced cutoff such as PG 1553+113. While detections of the FSRQ class of AGN should become more frequent with HESS-2, it remains to be seen if it will be possible to do so on timescales similar to the 2-3 h timescale from Fermi.
- improve the $\Delta\Gamma = f(z)$ diagram (Fig. 2.2) for the relatively more distant sources at $z \geq 0.2$ since they have almost by definition steep VHE spectra with larger errors on Γ_{TeV}.

5.2 The Cherenkov Telescope Array

5.2.1 The next generation of ACTs

Paraphrasing Simon Swordy [Swordy, 2007], the path to progress goes either through (i) the use of existing instrumentation and methods on a significantly larger scale than before, or (ii) a technological breakthrough which provides a significant enhancement in sensitivity or the ease of constructing instruments. Some developments in the latter direction can be cited:

- Improving the quantum efficiency of the detector elements in ACTs would lower the energy threshold, and research on this is currently done by many groups. One of the HEGRA $9.5\,m^2$ telescopes has been equipped with a Geiger-mode Avalanche Photodiodes (G-APD, also called silicone photomultiplier - SiPM) camera to become the FACT (First G-APD Cherenkov Telescope) experiment [Anderhub et al., 2010]. G-APDs have a peak quantum efficiency $\sim 80\% - 90\%$ average efficiency (about ~ 3 times higher than the $\sim 20\% - 30\%$ quantum efficiency of PMTs such as the XP2020, one of the ACT workhorses), and can be operated at voltages $\leq 100\,\mathrm{V}$. They have however also a few drawbacks such as a high temperature dependency of the gain, small detection area, significant cross-talk, significant dark currents and a higher cost than PMTs; such difficulties have to be overcome before they can replace PMTs in the currently existing ACTs.
- Increasing the field of view of ACTs significantly beyond the current $2^\circ - 4^\circ$ range inherent to the prime-focus Davies-Cotton design would allow more efficient sky surveys [Krennrich, 2009], increase the rate of serendipitous source discoveries, and not miss transient events such as the PKS 2155−304 bursts from §2 when they occur! Extending the fov with prime-focus instruments seems difficult [Schliesser & Mirzoyan, 2005] so the attention has shifted to feasability studies of two-mirror systems. Difficulties here reside in the increased complexity in the telescope design, astigmatism for shower images at large angles and the loss of isochronicity. Developments in this direction include e.g. Schmidt type telescope designs allowing a 15° fov [Mirzoyan & Andersen, 2009] where a Fresnel lens is used as

corrector plate for the inherent spherical aberration, and the Schwarzschild-Couder design [Vassiliev et al., 2007] which allows a $\geq 12^\circ$ fov. The latter design might be used for a specific telescope type in the CTA observatory.

A significant development of VHE γ-ray astronomy is expected from the extension of the currently existing setups to much larger scales. Since the IACT technique, and the technologies, are quite robust, there would be little risk in a large scale replica of currently existing facilities.

5.2.2 Configuration

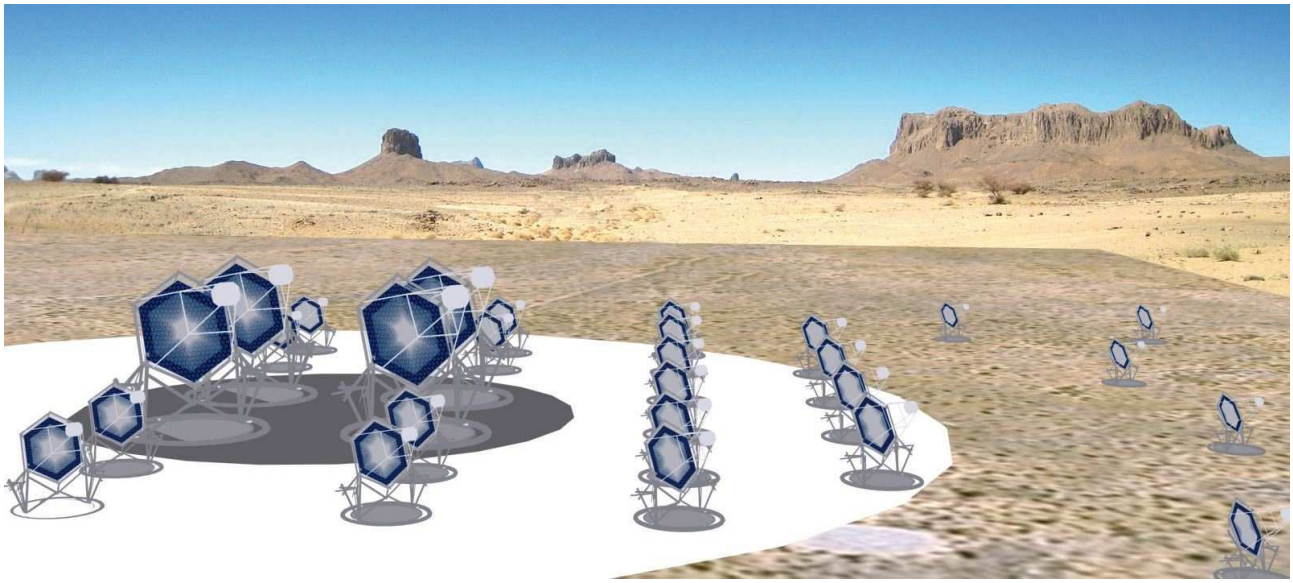

Figure 5.2: *The HESS2 telescope in a photo-montage on the current H.E.S.S. site. (Reproduced from CTA Consortium 2010).*

From this has emerged the Cherenkov Telescope Array (CTA), which is currently a consortium involving the main ACT collaborations, including H.E.S.S. VERITAS and MAGIC. The most complete documentation up to date is in the CTA Design Report [CTA Consortium, 2010] where the global science case and design concepts are presented. The telescope layout would consist of a few very large HESS-2/MAGIC class telescopes (which enables a low energy threshold of a few tens of GeV with a background-dominated sensitivity limit), surrounded by large HESS1/VERITAS 12 m class telescopes (providing the bulk of the sensitivity increase at $1\,\mathrm{TeV}$ with $O(100\,\mathrm{GeV})$ thresholds) in an array which will be larger than the Čerenkov light pool, and even more 3-4 m wide angle small class telescopes (Figure 5.2). This should achieve extensions to both low and high energies in the sensitivity, which might reach the mCrab level around $1\,\mathrm{TeV}$. The angular resolution has a goal of 0.02° at the highest energies, which is about 5 times better than the current performances (see e.g. Hofmann 2006 for the physical limitations to the ACT performances).

5.2.3 The PKS2155-304 flares as seen by CTA

While CTA will undoubtly increase the amount of known VHE emitters, both Galactic and extragalactic, it is considered here what CTA would improve on a known source such as PKS 2155−304. The model for the fluctuations of Figure 3.3, i.e. the parameters of Table 3.1 are here used as intrinsic flux. In order to correctly estimate the integrated flux $\Phi_>$ above $50\,\mathrm{GeV}$, the spectral behaviour $F(E)$ of the SSC fit from §4.6 was used and multiplied with the effective area (from configuration D in the CTA Design Report [CTA Consortium, 2010] which has the best γ-ray yield for a SED as PKS 2155−304.), which yields a number of photons N_γ. The choice of Δt is such that the measured flux points significance is on average compatible

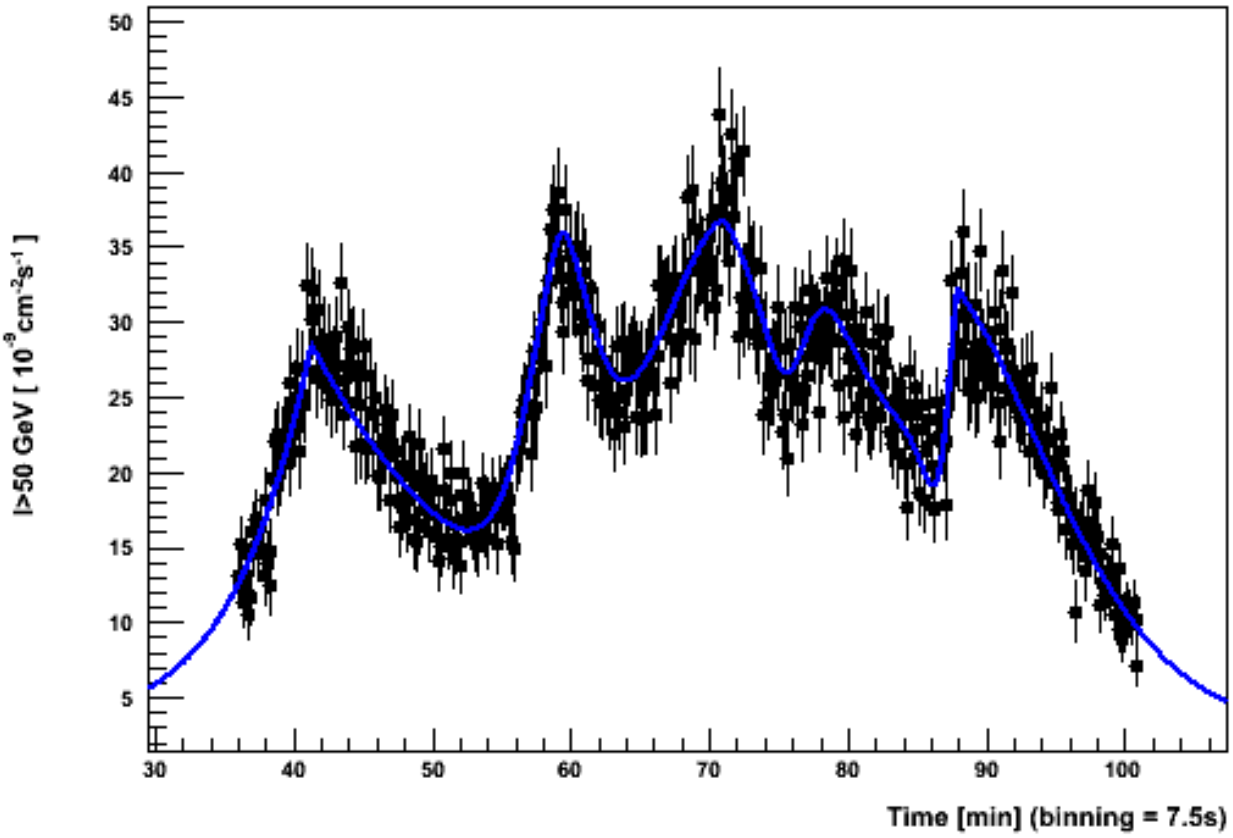

Figure 5.3: *The PKS 2155−304 flares as seen by CTA in configuration D with an energy threshold at* 50 GeV *and an input spectrum derived from the known SED. The five bursts are fit with generalized Gaussian components. While the well defined bursts from the original H.E.S.S. study have improved measured timing significances, the poorly defined ones such as bursts 4 and the rise time of burst 5 are now significant.*

t_{max} [min]	A [10^{-9} cm^{-2} s^{-1}]	τ_r [s]	τ_d [s]	κ fixed
41.3	27.3 ± 0.5	206 ± 14	570 ± 46	1.07
59.1	19.8 ± 1.2	121 ± 14	151 ± 24	1.43
71.4	31.6 ± 0.6	428 ± 52	246 ± 36	1.59
79.2	21.2 ± 1.4	160 ± 19	812 ± 143	2.01
88.3	11.8 ± 1.6	55 ± 17	563 ± 90	2.44

Table 5.1: *The results of the best* χ^2 *fit of the superposition of five bursts and a constant to the data shown in Figure 5.3. The constant term is fixed to* 2.7×10^{-9} cm^{-2} s^{-1}

with those measured by H.E.S.S. during the Big Flare, which ultimately led to $\Delta t = 7.5$ s (!). The simulated fluxes Φ were then randomly distributed with a normal distribution of width $\sigma_{\Phi_>} = \frac{\Phi_>}{\sqrt{N_\gamma}}$. This then yielded Figure 5.3 onto which the same burst fitting method was applied, giving the results in Table 5.1. Note that all the injected peaks are significantly resolved, such that now the fastest rise time τ_r is no longer the second peak but the fifth, which was already the fastest peak but also not significantly resolved. That timescale increases then by a factor ~ 3 the constraint on the Doppler factor derived in §3.2.3 such that this time, $\delta \geq (180-360) R/R_S$ if we still constrain the size of the emission region R to be smaller than the gravitational radius R_S.

Assuming that the fastest rise time from the fifth peak in the underlying structure has indeed $\tau_r = 67$ s and that with CTA, unlike H.E.S.S., this is significantly measured (which seems to be the case in Table 5.1), then Figure 5.4 shows what γ-ray opacity would need to be overcome with the Doppler factor assuming that the light curve extends up to 10 TeV and that it is well measured by CTA. It can be seen that $\delta \geq 70$ is required for 2 TeV curves, and $\delta \geq 100$ if

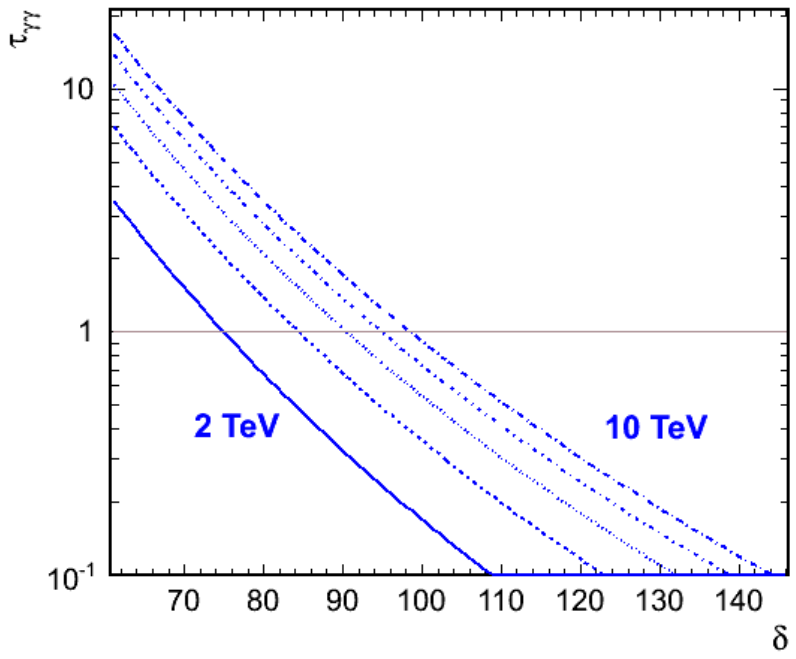

Figure 5.4: *The γ-ray opacity $\tau_{\gamma\gamma}$ derived for $t_{var} = 67$s variability for γ-ray energies of $E_\gamma = 2,4,6,8$ and 10TeV respectively. As in §2 the comoving target density field was derived from scaling by a factor 10 the synchrotron emission of the quiescent PKS 2155−304 but the energies have been increased up to 10 TeV and a 3 times faster timescale is used.*

t_{max} [min]	A [10^{-9}cm^{-2}s^{-1}]	τ_r [s]	τ_d [s]	κ
43.3	25.7 ± 1.1	202 ± 13	147 ± 13	1.42 ± 0.15
51.0	10.9 ± 1.6	32 ± 8	34 ± 6	1.85 ± 0.44
60.4	17.5 ± 2.0	210 ± 19	37 ± 8	2.19 ± 0.35
64.4	15.1 ± 2.0	124 ± 27	60 ± 11	1.32 ± 0.28
71.5	43.7 ± 1.6	74 ± 9	80 ± 6	0.80 ± 0.11
80.5	18.3 ± 1.7	108 ± 17	177 ± 17	2.99 ± 0.43
87.8	26.8 ± 1.8	25 ± 4	235 ± 12	1.27 ± 0.10

Table 5.2: *The results of the best χ^2 fit of the superposition of seven bursts and a constant to the data shown in Figure 5.5. The constant term is fixed to 2.7×10^{-9}cm^{-2}s^{-1}.*

such variability is present at 10TeV. Another interesting feature of this study case is that it implies a clear high-frequency cutoff in the PSD at $\sim 1.6\times10^{-3}$Hz. How well this cutoff can be reconstructed has yet to be established, but such a feature has never been observed in a blazar and would have interesting implications if only through the comparison with high-frequency X-ray cutoffs observed in galactic binary systems.

5.2.4 The PKS2155-304 flares with additional red noise

The above study did not incorporate any additional noise in the light curve. If the sensitivity indeed increases, there is plenty of room for higher frequency additional noise since the PSD in §3.2.3 clearly shows that the measurement noise dominates at higher frequencies, well below the Nyquist frequency.

Therefore another light curve with additional variance was derived, adding a red noise with index 2 for frequencies $> 1.6\times10^{-3}$Hz which is the frequency where the measurement errors dominate the PSD for the H.E.S.S. measurements. This yields Figure 5.5, where new features appear so the peak finding algorithm and subsequent generalized Gaussian fits were applied again.

This resulted now in 7 peaks in the light curve, where the two additional ones have faster timescales than the 5 known ones, which is not surprising (Table. 5.2). This time the fastest resolved burst has a rising time of $\tau_r = 24\pm4$s which, applying the dynamical timescale argument, would translate into $\delta > 450-900$. The opacity limit, as derived in Fig. 5.4, would constrain

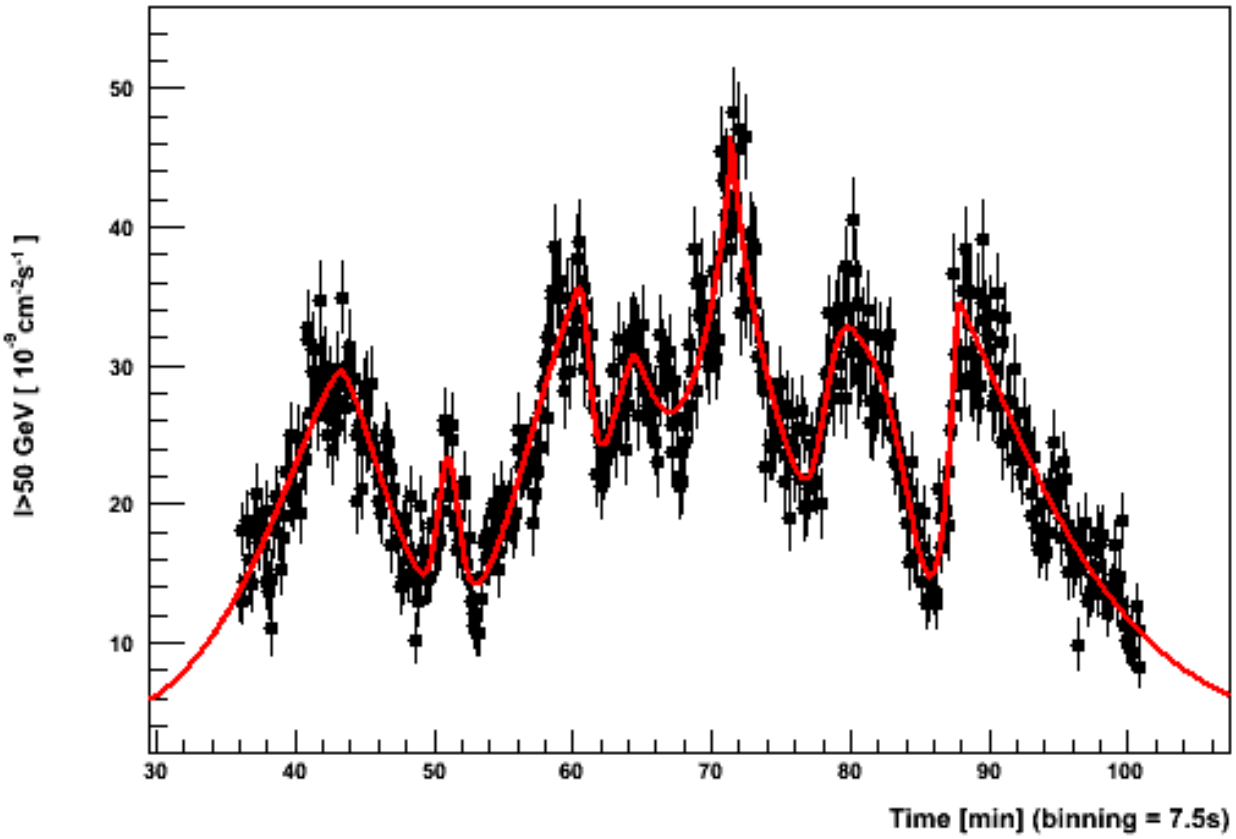

Figure 5.5: *The Big Flare as seen with CTA, with additional variance (using again the Timmer & Koenig [1995] prescription for deriving light curves from PSDs) corresponding to a $P(\nu) \propto \nu^{-2}$ red noise. The peak finding algorithm now identifies two additional peaks, with faster timescales (as expected).*

$\delta > 90$ at $1\,\mathrm{TeV}$ and $\delta > 120$ at $10\,\mathrm{TeV}$.

Future work related to AGN science with CTA and its improved capabilities over the current generation of ACTs should allow to:

- characterize energy-dependent PSDs (instead of just looking for energy-dependent estimators such as F_{var}), which has considerably improved the knowledge of X-ray binaries for instance when large area telescopes such as RXTE became available;

- Search for high-frequency cutoffs in the PSD, and estimate the sensitivity of CTA in finding those for cutoffs occuring before the PSD power law reaches the noise level at such improved sensitivities. Despite additional complexities from the nonlinear mechanism translating disk variability into jet variability, something might be learned in finding such cutoffs about the accretion time near the inner radius of the disk, exactly as expected from high frequency cutoffs in red noise PSDs found in binary systems [Lyubarskii, 1997];

- Estimate how CTA can improve the characterization of VHE emission in FSRQs after the detection of 3C 279 (MAGIC Collaboration et al. 2008; however see however Abdo et al. 2009c casting some serious doubt about at least the VHE flux normalization..) and - why not - the Seyfert class of AGN since a particular population of them are now known γ-ray emitters [Abdo et al., 2009e].

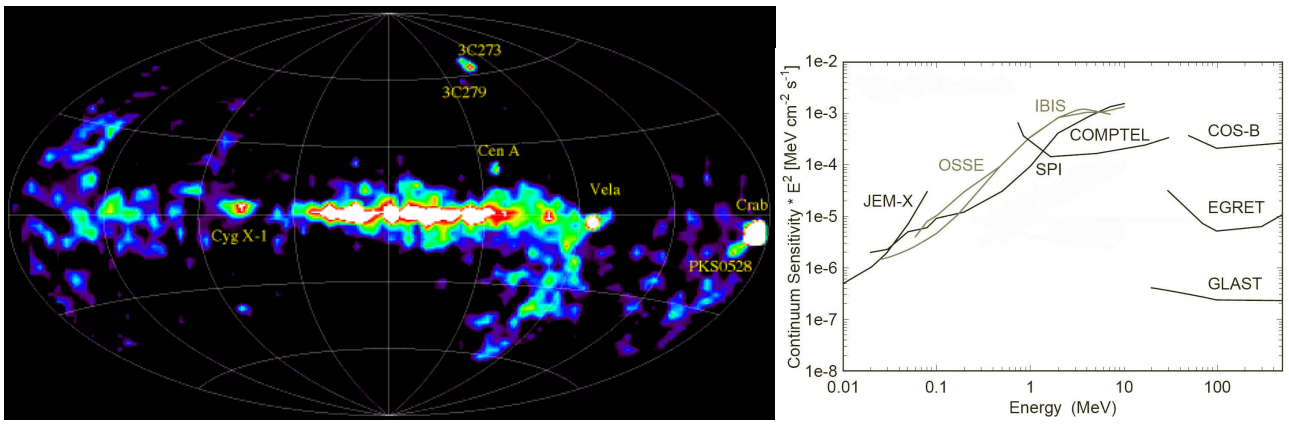

Figure 5.6: *Left: The current sky map in the* $1-30\,\mathrm{MeV}$ *energy range from the COMPTEL experiment. Right: the sensitivity in the low to medium* γ*-ray domain. (Credit: COMPTEL collaboration)*

5.3 Space-based γ-ray astronomy after *Fermi*

5.3.1 Medium energy γ-ray astronomy

The huge improvement of the sensitivity at $E > 100\,\mathrm{MeV}$ sheds a particular light at the longer wavelengths. The difficulty of astronomy in the $0.1-10\,\mathrm{MeV}$, also called the medium energy γ-rays, is well illustrated in Figure 5.3.1, arises essentially from the facts that photons interact preferentially in the Compton regime, where energy deposits and scattering angles are small, and instrumental backgrounds can be large. The recoiling electron must be well located and its energy measures, as must the scattered γ-ray and this all happening with the photon cross section at its lowest. The medium γ-ray energy range contains however a broad variety of scientific topics of great interest, such as the study of nucleosynthesis and supernova explosion processes through nuclear γ-ray spectroscopy in the MeV range, acceleration mechanisms in γ-raybinaries and FSRQ/LBL AGN where *Fermi* "overshoots" the peak IC emission, the radiative processes in GRBs since these objects have their peak luminosity in the $0.1-5\,\mathrm{MeV}$ range, or even extend the search for $\sim 70\,\mathrm{MeV}$ spectral bumps around the π_0 half-mass which would be an unambiguous signature of proton acceleration for which evidence still lacks [Gaisser et al., 1998]. Interest for this domain has been rekindled during the 2010 Astronomy and Astrophysics Decadal Survey (Astro2010), for which [Hunter et al., 2009] produced a summary paper of great interest, emphasizing the requirement of increasing the effective area and the angular resolution in order to significantly increase the sensitivity in that area. Projects in the medium γ-ray energy range, such as the Advanced Compton Telescope (ACT; Boggs 2006) using thin silicon SSD or DUAL [von Ballmoos et al., 2010], could improve by at least an order of magnitude the sensitivity limits set by COMPTEL, but have to date no visible priority by funding agencies.

5.3.2 High energy γ-ray astronomy

With *Fermi* recent start of operations, and a life time which might well extend up to 2018 or beyond, there are currently no follow-up projects in a similar energy range or in the pair-conversion regime. A few reasons exist to improve on *Fermi* in the following areas:

- **spectroscopy:** The most interesting spectra in the variety of *Fermi* sources are probably those showing new features in some GRBs where additional power law components appear on top of the expected Band functions [Ackermann et al., 2010]. An increased acceptance and a better energy resolution in the $1-100\,\mathrm{MeV}$ range is desirable. Given the very short duration of GRBs, such measurements are unlikely to require a much improved PSF as well. Finding spectral signatures around the π_0 mass would require an improved PSF as well as an improved spectroscopy, in order to efficiently deal with the overwhelming Galactic diffuse component. This is particularly obvious for remnants such as Vela X or W 28 (Figure 5.7;

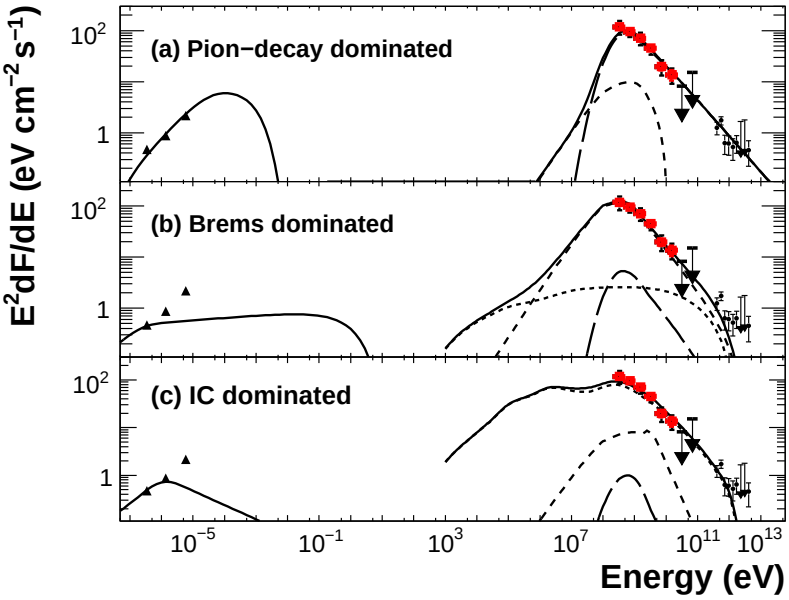

Figure 5.7: *Fermi (red) and H.E.S.S. (black) spectra on the northeast boundary of the supernova remnant W28, with three different models of dominating radiative mechanisms described in Abdo et al. 2010. The hadronic model shows a particularly marked spectrum at* $\leq 100\,\mathrm{MeV}$ *which could be entirely resolved provided an order of magnitude better resolution and also a lower energy threshold in the MeV range.*

Abdo et al. 2010) which are actually bright enough that a *Fermi*-like instrument optimised for lower energies would have the required effective area as well.

- **Effective Area:** Despite *Fermi*'s $\sim 1\,\mathrm{m}^2$ effective area, the $\geq 10-100\,\mathrm{GeV}$ sky is still poorly known in general, and the BL Lac outbursts seem still to escape us in that range due to the low fluxes. It is in this energy range that a spectral rollover is necessarily occuring due to the EBL cutoff for the most energetic BL Lac objects, as is evident from Fig. 2.2 (but also from the SED in Figure 4.6 and the associated significances $\geq 10\,\mathrm{GeV}$ in Abdo et al. 2010a), but the limited statistics (and perhaps other systematic issues) are not giving us access to them. However keeping a good spectroscopy as well means that an improvement in the HE effective area is just assembling more *Fermi*-equivalents together - and piling up their mass and consumption as well, which is probably unrealistic for the coming decades. Since the future generation of ACTs is unlikely to reach down to those energies, or to handle the systematic issues well enough if such an energy threshold is achieved, spectra will not connect significantly which is likely to impact a meaningful cross-calibration between *Fermi* and ACTs.

5.3.3 γ-ray polarimetry

The angular resolution is probably the most obvious instrumental performance with an interesting margin left which can be improved compared to *Fermi*, especially at energies $\leq 1\,\mathrm{GeV}$. All source classes would considerably benefit from an order of magnitude improvement were the resolution to reach the arcminute level, because of the improved background rejection and the reduction of source confusion especially in the Galactic plane. Improving the directional reconstruction for tracks created by the e^+/e^- pair in an instrument depends however not only on the spatial resolution of the detector, but also on the amount of Coulomb scattering the electrons are subjected to in the detector. This smears their momentum out from those at the pair creation: improving the instrumental resolution will not help if particles go through dense inert matter before they interact with the detector. According to Hunter et al. [2001], arcminute resolution is feasible at γ-ray energies $\sim$ GeV provided tracking can be done with a $\sim 10^{-5} X_0$ sampling.

It is also interesting to consider how an improved PSF would affect the sensitivity to γ-ray linear polarization, the ultimate frontier of high-energy detectors. Adding two more observational parameters to the time variability and spectral properties, namely with the linear polarization degree Π and polarization angle Φ, will be extremely useful for discriminating the different models of γ-ray emission from young pulsars, galactic and supermassive extragalactic BHs, and gamma-ray bursts (GRB) for which a controversial RHESSI measurement in the soft

γ-ray band 0.2-2 MeV exists [Coburn & Boggs, 2003] although it was probably an instrumental effect [Wigger et al., 2004]. The polarization of GRB γ-rays is considered as a very efficient way to disentangle fundamental differences in current models: electromagnetic models predict linear polarizations $\Pi \approx 30-50\%$ [Lyutikov et al., 2003; Granot, 2003], hydrodynamical models cannot exceed significantly $\Pi = 10\%$ [Ghisellini & Lazzati, 1999]. The so-called "fireball" models, with some fine tuning, may accomodate fractional polarizations as large as $\Pi \approx 100\%$ [Lazzati & Begelman, 2009], with an anti-correlation of Π with the brightness (which has possibly been observed by Götz et al. [2009]). There is also a tremendous interest in high-energy γ-ray polarimetry for pulsars, which have the good taste of not being transient sources but still very γ-ray bright, since emission model degeneracy is almost completely lifted when the phase-dependency of the polarization fraction and angles are included [Dyks et al., 2004; Takata & Chang, 2007; Takata et al., 2007].

The experimental difficulty lies in the polarization signature for the different processes, generally based on the azimuthal asymmetry $P(\Phi) \propto \Pi A \cos 2\Phi$ of the reaction product (photoelectron, comptonized electron, pair creation plane; see Maximon & Olsen [1962] and Kotov [1989] for the latter mechanism which has remarkably not been implemented in the GEANT simulation package so far) around the plane Φ of linear polarization of the incoming photons. The strength of the quadrupole asymmetry A for a given process plays an important role in the analyzing power of the polarization. In the high energy band, interaction of photons is dominated by the Compton and pair creation cross sections (for a review on Compton polarimetry in γ-ray astronomy see e.g. Lei et al. 1997). The nuclear pair cross section is proportional to Z^2 whereas the triplet production from atomic electrons is proportional to Z (hence the pair-to-triplet conversion ratio varies as Z).

Early claims of evidence for linear polarization in the e^+/e^- pair-creation plane distribution on the Vela pulsar [Caraveo et al., 1988] were actually unfounded [Mattox et al., 1990] since COS-B nor EGRET were able to find evidence for that, even for a $\Pi = 100\%$ γ-ray flux from such a bright source [Mattox, 1991]. This is also the case for *Fermi* because the multiple scattering the pairs undergo in the conversion foils of these detectors and induce an rms change $\delta\Phi \sim 14\sqrt{L}$ on the plane directions Φ, where $L = d/X_0$ is the amount of radiation lengths the electrons have gone through [Mattox, 1991]. This induced $\delta\Phi = 2.1\,\mathrm{rad}$ at each passing through EGRET's $0.022X_0$ tantalum foils and smears out even more in *Fermi*'s thinnest $0.03X_0$ tungsten foils, making them effectively insensitive to polarization, since the quadrupole asymmetry decreases roughly as $Ae^{-2\delta\Phi^2}$ [Bloser et al., 2004]. A quadrupole strength of $A \sim 0.2$ on linear polarization was achieved experimentally through the plane distribution method for GeV photons from a beam, using a $0.001X_0$ converter [Wojtsekhowski et al., 2003; de Jager et al., 2004] and measuring the conversion plane orientation after 1 m with 50 μm pitch micro-strip detectors. The 0.1% photon conversion is however unacceptable for an astronomical γ-ray polarimeter built on this principle, not to mention the required area or length to achieve a total depth of $0.5X_0$.

A way out of the conundrum would be that the conversion medium acts as an active detector as well. This is essentially what is proposed by Bloser et al. [2004] using the Time Projection Chamber technology in a large volume of Xe gas, which can achieve bubble chamber spatial resolution. Their early study however did not include ionization electrons diffusion over the drift distance d, and especially the transverse diffusion $\sigma_T \propto \sqrt{d}$ which impacts the track separation and washes out all azimuthal polarimetric information (D. Bernard, internal note). Despite a suppression of a factor Z in conversions compared to pair production, it appears that the azimuthal direction of the recoil electron in a triplet production is easier to determine than pair azimuthal planes, which is currently being investigated in the HARPO project at LLR in an Argon based TPC. Note that attempts of building a Compton telescope with a *liquid* Xenon TPC (including a balloon flight) for astronomical purposes have been attempted [Aprile et al., 2008] but does not appear to have the required sensitivity - perhaps for reasons of a poor background control.

5.4 Final Conclusions

With both the space-based and ground-based γ-ray astronomy simultaneously entering a new era, the continuously increasing amount of HE and VHE objects along with the spectacular quality of the data are improving our knowledge on an almost daily basis. The MeV-GeV sensitivity gap has been filled to a great extent, which HESS-2 should fill even more, also opening perspectives about joint space-ground analyses and a possible cross-calibration between instruments.

The new generation air shower detector HAWC (High Altitude Water Cherenkov) will be operational in a foreseeable future, operating in Mexico at an impressive altitude of 4100 m a.s.l., lowering the energy threshold to $\mathcal{O}(100\,\mathrm{GeV}$. With performance improvements of 10-15 in threshold and sensitivity over the Milagro experiment, its wide field of view and huge efficiency, this new observatory will provide another unique discovery potential for VHE astrophysics. While ACTs will keep a better sensitivity, the combination of CTA and HAWC observations at $\geq$ TeV energies forebodes interesting synergies.

Appendix A

Résumé

A.1 Les rayons γ des NAG et des blazars

L'astronomie des rayons γ de haute ($E > 100\,\mathrm{MeV}$, HE) et de très haute énergie ($E \geq 100\,\mathrm{GeV}$, VHE) ont effectué des progrès considérables en moins d'une décennie. Le nombre de sources émettrices dans ce régime d'énergie a augmenté de plus d'un ordre de grandeur, de nouvelles classes d'émetteurs ont été découvertes et des nouvelles sous-classes ont été établies basées sur l'émission γ, et les sources connues sont à présent résolues à des échelles spatiales ou temporelles sans précédent révélant de nouvelles propriétés. Les noyaux actifs de galaxie (AGN) sont l'une des classes d'émetteurs les plus énergétiques, dont le pic de puissance émis dans le spectre électromagnétique peut dans certains cas dépasser la capacité de mesure des instruments actuels, et dont l'investigation requiert la maîtrise simultanée du ciel γ HE et VHE qu'apportent les expériences Čerenkov au sol (atmospheric Čerenkov telescope, ou ACT) et le satellite *Fermi*.

Les jets de matière relativistes issus des noyaux actifs de galaxie et se déplaçant avec des facteurs de Lorentz $\Gamma \geq 10$ sont probablement l'illustration la plus spectaculaire d'un ensemble de questions non-résolus de la physique et de l'astrophysique. Pourquoi y a t-il des jets? Comment se forment-ils? Quelle source d'énergie, très certainement liée au trou noir supermassif (SMBH) au coeur de la galaxie active, les propulse? Quelle est leur composition en particules et noyaux; et ces corpuscules accélérées sont-elles à l'origine du rayonnement cosmique observé sur Terre au-delà de $10^{16}\,\mathrm{eV}$? Quels sont les mécanismes à l'oeuvre *dans* les jets qui amènent ensuite ces corpuscules à des distributions non-thermiques ayant des facteurs de Lorentz $\geq 10^6$, voire aux énergies extrêmes vus par les expériences comme l'observatoire Pierre Auger ou Fly's Eye de $10^{22}\,\mathrm{eV}$? Devant l'impossibilité de reproduire en laboratoire des conditions physiques similaires regnant auprès des trous noirs supermassifs ou des flots de plasma, l'observation des AGN avec tous les messagers possibles et les simulations de l'environnement de ces objets est le seul moyen d'arriver progressivement à des réponses. Aux hautes énergies, les moyens issus de la physique des particules - la conception et l'exploitation des instruments - est particulièrement bien adaptée à cette recherche.

Il n'y a toujours pas une réelle astronomie des rayons cosmiques notamment de par l'intéraction avec le CMBR, qui limite l'horizon observable à l'univers très proche, et les déflexions magnétiques des rayons cosmiques chargés. Les associations directes entre les directions d'arrivée des UHECR avec des sources potentielles proches, ou la recherche d'une corrélation avec les distributions spatiales trouvées dans les catalogues l'objets extragalactiques si la dépendence en $1/r^2$ du flux étale l'acceptance limitée des instruments, constituent l'approche actuelle de recherche des origines des UHECR, mais aucune certitude ne semble acquise à cette date. Les phénomènes les plus énergétiques sont essentiellement vus au travers de l'émission électromagnétique ayant lieu là où les particules accélérées interagissent avec leur milieu environnant, et où la luminosité non-thermique générée devient visible pour l'observateur. Cela concernerait environ 0.1% de toutes les galaxies, et on appelle les *blazars* ceux dont l'axe β du jet relativiste fait un angle avec la direction de l'observateur $\mathbf{n}$ inférieur à l'angle d'aberration relativiste $1/\Gamma$. Les blazars ont par ailleurs une émission électromagnétique variable dans toutes les longueurs d'onde, dans laquelle des corrélations sont souvent observés entre des flux séparés de plusieurs ordres de grandeur en fréquence indiquant une parenté dans la population radiative sous-jacente. Une complication vient de ce que l'énergie apparente est augmentée d'un facteur $\mathcal{D} = [\Gamma(1 - \beta \cdot \mathbf{n})]^{-1}$, la luminosité amplifiée d'un facteur $\sim \mathcal{D}^4$ (rendant souvent impossible de distinguer la galaxie hôte et donc la distance de l'émetteur), et les échelles de temps intrinsèques sont plus rapides pour l'observateur d'un facteur $\mathcal{D}$. L'émission électromagétique des blazars s'étend sur plus de 20

ordres de grandeur en énergie, et est composée habituellement de deux régimes d'émission assez distincts. Celui de plus basse énergie peut s'étendre des ondes décamétriques jusqu'aux rayons X, et semble inévitablement associé dans quasiment tous les cas de figure au rayonnement synchrotron d'une population d'électrons relativistes, eux mêmes issus soit d'un processus d'accélération soit des produits de réaction d'intéractions photomésoniques $p\gamma$. La composante de plus haute énergie est généralement considérée comme étant issu d'un champ de photons - en comouvement ou bien externe à la zone émettrice - comptonisé par les mêmes particules, mais, de façon plus controversée, pourrait être du rayonnement synchrotron de protons qui pour cela devraient avoir une énergie proche des 10^{22} eV fatidiques des UHECR. La puissance émise dans les rayons γ, du MeV au TeV, dominent dans la majorité des cas la luminosité globale - et quand ce n'est pas le cas, il semblerait que l'objet soit de faible luminosité mais également extrêmement *énergétique* et devienne également un émetteur détectable de rayons γ d'énergies $E_\gamma > 10^{10}$ eV.

La modélisation la plus simple de la distribution spectrale d'énergie (SED) consiste en une densité d'électrons $n(\gamma)d\gamma = \gamma^{-s}d\gamma$ bornée entre γ_{min} et γ_{max}, refroidissant (et donc rayonnant) par les mécanismes synchrotron et Compton inverse dans une région (considérée sphérique) de taille R dans un champ magnétique moyen B et se déplacant avec un facteur Doppler δ. Sur ces 6 paramètres, peut en contraindre 4 par les fréquences et les amplitudes d'émission des deux pics du SED. La variabilité du flux sur un temps caractéristique t_{var}, si elle est observée, permet de contraindre par le principe de causalité $R < ct_{var}\delta$, et l'imposition d'équipartition entre les densités cinétiques d'électrons et la densité d'énergie du champ magnétique $B^2/8\pi$ fournit habituellement la dernière contrainte. De multiples variantes de ce modèle peuvent ensuite être considérés (cf annexe de Dermer), notamment pour le rendre dépendant du temps et inclure la variabilité observée dans les contraintes du terme d'injection.

Le mécanisme d'accélération à l'oeuvre générant cette distribution de particules n'est toujours pas connu. Il puise probablement son énergie dans la puissance du jet lui-même, globalement quantifiable à $\pi R^2\Gamma^2 cU'$ où U' peut être une densité de rayonnement ou d'énergie cinétique. Parmi les scénarios classiques figurent les chocs de Fermi dont la cause peut être une instabilité dans le jet, les reconnexions magnétiques, ou encore un mécanisme continu d'accélération puisant dans la turbulence du jet.

La création, l'alimentation et la propulsion du jet lui-même sont encore un problème non résolu. Le réservoir d'énergie peut être l'accrétion de la matière, qui peut fournir théoriquement jusqu'à 40% de l'énergie de masse de la matière accrétée, ou bien la rotation du trou noir central des AGN dont l'énergie emmagasinée peut atteindre 29% de la masse du trou noir. Il faut ensuite encore un mécanisme d'extraction de l'énergie, puis un mécanisme qui forme un jet relativiste et stable sur des distances considérables. Ce sont là des questions fondamentales pour la compréhension de ces formidables machines que sont ces accélérateurs naturels. Il est peu probable que ces questions nécessitent une nouvelle physique fondamentale mais plutôt une meilleure compréhension des mécanismes à l'oeuvre impliquant des plasmas astrophysiques proches de trous noirs supermassifs en rotation dans des conditions impossibles à reproduire en laboratoire.

A.2 Observations de PKS 2155-304 avec HESS

La très faible activité des AGN de l'hémisphère sud en comparaison avec leurs contreparties de l'hémisphère nord est largement compensée par les observations par HESS du seul AGN PKS 2155−304 qui ont jusqu'ici apporté plus de conclusions originales que n'importe quel autre blazar.

L'état très actif et variable de 2006 est en passe de devenir l'icône des éruptions observées à ce jour, et les points suivants résument les faits essentiels mentionnés dans le §2:

- Les temps caractéristiques observés des différents sursauts, de l'ordre de 3 minutes, sont 2 ordres de grandeur plus court que le *light crossing time* (LCT) du rayon de Schwarzschild du trou noir supermassif central. La forme des sursauts est remarquablement proche de ceux observés dans les sursauts gamma (GRB) pour lesquels les temps caractéristiques

sont toutefois très supérieurs au LCT d'un trou noir de masse stellaire. Que ce soit en supposant que la région émettrice ne soit pas de dimension plus grande que ce rayon, ou bien en arguant que l'opacité $\tau_{\gamma\gamma}$ aux photons d'énergie $\geq 1\,\mathrm{TeV}$ ne puisse dépasser l'unité, on est contraint d'introduire un facteur Doppler inhabituellement élevé de l'ordre de $50-100$ pour la zone d'émission. Dans le premier cas, cela ramène la dimension réelle de la zone émettrice à une taille plus proche du rayon gravitationnel du système, souvent considérée comme une échelle spatiale minimale. Dans le second cas, la combinaison de la diminution de la densité de photons cibles et de l'aberration relativiste (qui ramène l'émission isotrope dans le référentiel du jet dans un cône d'ouverture $1/\Gamma$) réduit l'opacité apparente. Il s'agit donc de deux considérations bien distinctes.

- Les fluctuations r.m.s. du flux dans l'état haut sont corrélés avec l'intensité du flux lui-même, une propriété connue du flux de rayons X de certaines binaires X ou de galaxies de type Seyfert, et qui suggère que le processus sous-jacent soit stationnaire mais que le logarithme soit distribué de façon normale. La même propriété a été retrouvée dans le flux de rayons X du blazar BL Lacertae, de type LBL et donc dont les rayons X sont issus de photons comptonisés (et non pas du processus synchrotron). Il est intriguant qu'il puisse exister des similarités entre un rayonnement thermique issu très vraisemblablement de l'accrétion, et du rayonnement non-thermique dans un jet relativiste.

- La densité spectrale de puissance (DSP) $P(\nu)$, c'est à dire le lien entre l'amplitude de la variabilité et les échelles de temps, a pu être estimée grâce à l'échantillonnage dense et quasi-continu de l'état éruptif, également une première pour une étude de série temporelle obtenue par un télescope atmosphérique à effet Čerenkov. Les estimations initiales montraient que $P(\nu)\sim\nu^{-\alpha}$ avec $\alpha\lesssim 2$. Des artefacts sont toutefois induits par les conditions expérimentales dans l'espace des fréquences de toutes les transformées utilisées (DSP, fonctions de structure, ..), ce qui complique la recherche d'échelles de temps caractéristiques de l'observation. A l'instar de la reconstruction spectrale énergétique, le DSP sous-jacent peut être estimé en supposant une forme spectrale *à priori* - en l'occurence également une loi de puissance - et d'estimer ses paramètres et leurs incertitudes à partir de l'application des techniques habituelles de maximisation de vraisemblance (ou de minimum de χ^2) basés sur la connaissance de la réponse expérimentale à une grande quantité de simulations numériques de séries temporelles de type $L(t)=a_0+\sum_{n=1}^{N} A_n\cos(2\pi n\nu_0 t+\phi)$ où les A_n associés à la fréquence $2\pi n\nu_0$ sont générés depuis la distribution de "bruit rouge" $P(\nu)$ choisie.

Le meilleur échantillonnage des mesures de flux, une conséquence de l'accroissement de la sensibilité des ACT, permet ainsi de caractériser d'une façon plus complexe la dynamique des processus sous-jacents. Il est devenu tout aussi important de révéler ces propriétés que la découverte de nouveaux émetteurs de haute énergie. S'il est souvent affirmé que des mesures consécutives ne sont pas variables (au vu d'un bon ajustement avec une fonction constante dans le temps par exemple) il est plus rare de trouver une limite supérieure sur l'excès de variance - ou sur la variance normalisée. Avec la croissance de la significance d'une mesure, il devient possible de *(i)* déterminer et caractériser la variance dans plusieurs segments de la bande passante en énergie *(ii)* établir comment l'amplitude de la variabilité est reliée aux échelles de temps (DSP) *(iii)* de rechercher une échelle de temps caractéristique et de contraindre les échelles de temps les plus courts/longs respectivement limités par l'erreur statistique et la longueur des observations *(iv)* d'estimer si la variabilité a un comportement non-linéaire *(v)* de caractériser comment la variance évolue avec l'intensité du flux (si possible par segments de la bande passante en énergie). Le point *(i)* a été abordé à l'heure actuelle pour 3 blazars seulement (PKS 2155−304 Mkn 421 et Mkn 501), alors que les points *(ii)*, *(iii)* et *(v)* l'ont été seulement pour PKS 2155−304.

Si l'évolution actuelle du taux de découverte de nouveaux AGN émetteurs de rayons γ de très haute énergie se poursuit, nous devrions être capables dans un futur proche de savoir si les caractéristiques observées mentionnées ci-dessus *(vi)* peuvent changer pour un AGN donné d'une observation à une autre *(vii)* sont les mêmes pour les AGN d'une classe donnée *(viii)* sont similaires pour les différentes classes (FSRQ, BL Lacs, galaxies Radio) et sous-classes (LBL, IBL, HBL) d'émetteurs non-thermiques.

A.3 Observations multi-longueurs d'onde de PKS 2155-304

Le comportement des flux observés à différentes longueurs d'onde fournit d'importantes informations sur la dynamique de la distribution de particules radiatives. L'on cherche notamment à comparer *(i)* l'amplitude du flux et la variabilité à différentes bandes en énergie/longueurs d'onde *(ii)* comment la variabilité change avec l'intensité *(iii)* la nature de la relation qui existe entre la variabilité des différents continuums.

D'autre part, la connaissance aussi simultanée que possible du spectre synchrotron dans les énergies où ce rayonnement peut interagir avec les rayons γ en créant une paire e^+e^- est importante pour estimer le paramètre de compacité $\tau_{\gamma\gamma}$ réel, au lieu de le déterminer sur base de données d'archives. Inclure l'aberration relativiste permet l'estimation la plus "classique" du facteur Doppler requis pour permettre aux rayons γ observés de sortir de la région d'émission (dans l'hypothèse où toute l'émission observée est cospatiale et isotrope dans un repère en comouvement).

Les points suivants résument l'essentiel de ce qui est mentionné dans le §3 :

- Les observations multi-longueurs d'onde effectuées sur PKS 2155−304 en 2003 étaient déclenchées par une série consécutive de détections par HESS à des significativités $> 5\sigma$, car elles étaient considérées alors comme indicatives d'un état haut de flux. Le spectre synchrotron de rayons X mesuré simultanément par RXTE[1], représentatif de la densité des électrons les plus énergétiques avec des facteurs de Lorentz $\gamma_e > 10^5$, montra que le flux simultané était alors d'un ordre de grandeur en-dessous des flux historiques les plus élevés pris simultanément dans la bande en énergie de $2-10\,\mathrm{keV}$. La détection d'un état bas VHE d'un blazar avec une telle significativité était alors une nouveauté. De manière surprenante, les flux de rayons X et de rayons γ au VHE, pourtant significativement variables malgré un flux moyen bas, ne paraissaient pas corrélés entre eux alors que cela était pourtant considéré comme une propriété bien établie des blazars du moins dans les états haut de flux.

- Les observations multi-longueurs d'onde effectuées en 2004 lors d'un état de flux VHE plus élevé et variable a permis de montrer que ces deux bandes en énergie étaient bien corrélés également pour PKS 2155−304. C'était par ailleurs la première corrélation X/γ temporelle établie par HESS. Toutefois une corrélation entre des flux observés à des longueurs d'onde optiques (ou moins énergétique) et ceux observés en rayons X (ou plus énergétique) n'a jamais été établie, et ce pour aucun object de type BL Lac. Toutefois il apparaît une relation entre les variances normalisées de ces longueurs d'onde, et ce pour plusieurs objets. Cette relation a été retrouvée dans une simulation SSC dans lequel la densité d'électrons injectée est dépendente du temps et fluctue selon un "bruit rouge" similaire à celui décrit plus haut. Cela a permis d'en effet retrouver un effet chromatique dans la distribution des variances en fonction de l'énergie observée, indiquant que la relation elle-même est très certainement due à la dépendance en énergie des deux mécanismes radiatifs, mais la dépendance exacte de la relation aux paramètres de la simulation n'est pas encore clairement établie.

- La première campagne d'observations impliquant simultanément des observatoires de rayons γ de haute et de très haute énergie fut organisée en septembre 2008, soit à peine 3 mois après le lancement de *Fermi*. Du temps d'observation avec *RXTE* et *Swift* avait été obtenu dans les rayons X, et H.E.S.S. avait approuvé xx heures d'observation en xx nuits consécutives. La disponibilité de ces ressources nécessitait un choix de date bien défini, et donc pour un état de flux de PKS 2155−304 inconnu, mais les études préliminaires indiquaient clairement que même une limite supérieure obtenue par *Fermi* en une dizaine de jours serait très contraignante si H.E.S.S. observait un spectre correspondant à un état bas.

[1] Les observations aux longueurs d'onde plus grandes, notamment les rayons X, sont en général garanties plusieurs mois à l'avance mais il faut pour cela remporter une fraction du temps d'observation disponible dans un appel d'offres ouvert à une très large communauté par les agences spatiales. L'obtention de temps d'observation n'est donc jamais garanti.

Les observations révélèrent alors un état de flux en effet compatible avec l'état bas, avec des fluctuations d'amplitude sur des échelles de temps de l'ordre de 24 h dans toutes les bandes en énergie sauf pour *Fermi* pour lequel les grandes incertitudes sur le flux étaient toutefois compatibles avec les variances normalisées des autres mesures. Tout comme dans les mesures MWL de 2003xx, les flux de rayons X et de rayons γ étaient significativement variables mais non corrélées. Ce phénomène est explicable à présent avec un modèle SSC simple, car après ajustement du SED d'un état bas, les paramètres du modèle sont tels que les électrons les plus énergétiques, précisément ceux rayonnant dans la bande X, comptonisent essentiellement dans le régime hautement inefficace de Klein-Nishina. Leurs fluctuations sont essentiellement invisibles aux énergies $E_\gamma < 1\,\mathrm{TeV}$, c'est à dire aux énergies médianes dans des intégrations de l'ordre de quelques heures. Ces fluctuations devraient être visibles dans une courbe de lumière réalisée par un observatoire Tcherenkov ayant une plus grande surface effective à ces énergies que les observatoires actuels qui ne sont pas sensibles aux variations des électrons les plus énergétiques dans état de flux bas de PKS 2155−304. La question du spectre Compton de PKS 2155−304 dans un état de flux haut reste posée, car les observations de monitoring par H.E.S.S. n'ont plus révélé d'état haut, et *Fermi* n'a pas observé de montée dramatique de flux depuis 2 ans. Donc soit un état haut de flux similaire à celui de 2006 n'a plus eu lieu depuis le lancement de *Fermi*, soit la contrepartie dans la bande MeV-GeV n'est pas une montée d'intensité mais plutôt un "durcissement" du spectre, ce qui n'est pas exclu puisque l'indice spectral vu par *Fermi* n'est pas à la limite théorique de $\Gamma = 1.5$.

A.4 Propagation des rayons γ

A.4.1 Atténuation du flux VHE

Une recherche systématique de contreparties vues par *Fermi* aux positions d'émetteurs VHE connus a permis de déterminer le spectre Compton de la plupart de ces sources. Si toutes les sources vues au VHE ont un indice spectral $\Gamma \geq 2$, le spectre vu par *Fermi* a pour toutes ces sources $1.5 \lesssim \Gamma \leq 2$ (à l'exception des radio galaxies M 87 et Centaurus A). Cela a permis de lever le voile sur cette partie du spectre des BL Lacs, qui était la moins bien déterminée par l'expérience EGRET (le prédecesseur de *Fermi*), de confirmer la structure en "double bosse" en représentation νF_ν, et de montrer que ces objets ont le spectre le plus énergétique de toutes les sources extragalactiques vues par *Fermi*(avec dans certains cas des photons d'énergie $E_\gamma > 100\,\mathrm{GeV}$). Il est à noter que les quelques sources vues au VHE sans contrepartie *Fermi* restent compatibles avec une limite supérieure d'un spectre avec $\Gamma_{\mathrm{HE}} \simeq 1.5$. La largeur de la composante Compton du SED peut être caractérisée par le changement spectral $\Delta\Gamma = \Gamma_{\mathrm{VHE}} - \Gamma_{\mathrm{HE}}$, qui montre une très nette dépendance croissante avec le redshift z. Le fait que le spectre Compton se rétrecisse avec la distance pourraît être interprété comme une évolution de ces sources, mais une autre explication est possible.

Les intéractions γγ évoqués plus haut peuvent également se produire sur le trajet des rayons γ, mais cette fois-ci avec le fond cosmologique infrarouge (extragalactic background light, ou EBL), dont la densité exacte entre $0.1\,\mu$m et $10\,\mu$m est indéterminée à un ordre de grandeur près. Plusieurs modèles de cette densité existent, ce qui permet d'estimer comment un spectre de photons $F_{int}(E)$ émis à une distance z apparaît à un observateur au travers d'une atténuation $e^{-\tau(E,z)}$, ainsi que la variation spectrale $\Delta\Gamma(z)$ attendue dans l'hypothèse que le spectre intrinsèque observé par les ACT serait une prolongation du spectre observé dans la région MeV-GeV par *Fermi*. En utilisant un des modèles qui se rapproche le plus des limites inférieures actuelles de la densité de l'EBL on peut ainsi estimer le ΔΓ minimal attendu sur un spectre *Fermi* ininterrompu. C'est ce qui est illustré dans la Figure 1.20 du §1 et, de façon remarquable, *les valeurs de* ΔΓ *sont toutes supérieures ou compatibles avec une atténuation purement due à un EBL minimal*. Il est à noter qu'on n'attend en aucun cas une corrélation linéaire des mesures expérimentales, car une source plus distante qu'une autre peut très bien montrer un ΔΓ inférieur s'il n'y a pas d'effet intrinsèque de changement spectral. Cela est probablement le mieux illustré par la source proche PKS 0548-489 dont l'indice spectral observé est pourtant élevé $\Gamma_{VHE} \geq 4$. *La Figure 1.20*

peut ainsi être comparée à la coupure GZK observée à l'extrêmité du spectre des UHECR, issu lui de l'intéraction des rayons cosmiques avec le fond cosmologique CMB à 2.7K.

A.4.2 Signature de cascades dans le flux HE

Les électrons produits dans l'interaction avec le EBL des photons les plus énergétiques peuvent à leur tour comptoniser les photons du fond cosmologique CMB et produire ainsi des photons essentiellement au MeV-GeV. Si le champ magnétique intergalactique dans lequel la création de paire a lieu est suffisamment faible, la gyration des électrons est suffisament faible pour que la comptonisation du CMB soit dans la direction du photon initial, et que l'énergie du photon soit en grande partie ré-injecté dans le flux : si l'énergie moyenne d'un électron issu d'un photon E_γ est $\gamma_e \simeq E_\gamma/2m_ec^2$ alors le photon comptonisé aura en moyenne une énergie $E'_\gamma \simeq \gamma_e^2 h\nu_{CMB}$. Un photon de $10\,\mathrm{TeV}$ "absorbé" par le EBL réinjectera deux photon de $60\,\mathrm{GeV}$ et modifier le spectre observé. La présence d'un champ magnétique significatif dévierait en revanche les trajectoires et l'énergie du photon serait intégralement perdue. L'effet de ces cascades sur le spectre observé venant de blazars émetteurs au VHE lointains, et supposant que le spectre intrinsèque s'étende jusqu'à 100 TeV environ, est calculé numériquement dans D'Avezac, Dubus, & Giebels [2007], pour des valeurs différentes du champ magnétique intergalactique. Il y est trouvé que l'indice spectral observé au VHE est marginalement affecté, mais dans tous les cas augmente, ce qui rend robuste la contrainte posée sur la densité de l'EBL par HESS dans Aharonian et al. [2006b].

Il y est également conclu que la plus grande partie de l'énergie des cascades est injectée sous $100\,\mathrm{GeV}$, et devrait avoir une signature significative dans les spectres vus par *Fermi si* le champ magnétique est inférieur à $10^{-17}\,\mathrm{G}$, mais serait supprimée pour des valeur supérieures à $10^{-15}\,\mathrm{G}$.

A.5 Perspectives d'études de NAG

La continuité de l'exploitation GeV-TeV avec *Fermi* et les différents ACTs va continuer à dominer les activités. L'arrivée du télescope HESS-2 en 2012 devrait permettre entre autres de caractériser la nature statistique de l'état quiescent de PKS 2155−304, mais également de trouver ceux des autres blazars déjà détectés avec une significance moindre. Ce nouveau télescope devrait aussi permettre

- une meilleure résolution spectrale des sursauts lors d'un état haut de flux;
- d'établir une courbe de lumière et caractériser la variabilité d'objets encore exotiques pour les ACT tels que le FSRQ PKS 1510-089;
- d'améliorer la Figure 1.20 pour les $z \geq 0.2$ au travers d'une meilleure résolution spectrale pour ces objets plus distants.

Enfin, dans un futur plus lointain, la mise en service du Cherenkov Telescope Array (CTA) devrait amener l'astronomie gamma de très haute énergie à l'âge d'Or dans lequel se trouve à présent l'astronomie gamma de haute énergie grâce à *Fermi*. L'amélioration d'un ordre de grandeur de la sensibilité aux énergies $\sim 1\,\mathrm{TeV}$ et des seuils en énergie étendus de part et d'autre de la limite actuelle des ACT permettront le franchissement d'une autre étape dans l'étude des AGN.

Dans la droite ligne de ce qui a été évoqué ici, les simulations actuelles des performances de CTA permettent l'étude de l'extension de la DSP de PKS 2155−304 : soit elle s'étend à encore plus haute fréquence et de la variabilité à des échelles de temps de la dizaine de secondes pourrait être observée (révélant ainsi l'existence de structures énergétiques avec des tailles caractéristiques de l'ordre du millième du rayon gravitationnel), ou bien la DSP présente une coupûre spectrale, ce qui pourrait également avoir des interprétations intéressantes car une telle caractéristique spectrale n'a encore jamais été observé dans un PDS de blazar.

Bibliography

Abbasi, R. U., et al. 2008, Physical Review Letters, 100, 101101

—. 2010, "The Astrophysical Journal Letters", 713, L64

Abdo, A. A., et al. 2009a, The Astrophysical Journal, 700, 597

—. 2009b, Science, 323, 1688

—. 2009c, The Astrophysical Journal, 707, 1310

—. 2009d, The Astrophysical Journal Letters, 700, L127

—. 2009e, The Astrophysical Journal Letters, 707, L142

—. 2010a, The Astrophysical Journal Letters, 709, L152

—. 2010b, The Astrophysical Journal Supplements, 188, 405

—. 2010c, The Astrophysical Journal, 708, 1254

Abdo, A. A., et al. 2010, The Astrophysical Journal, 718, 348

Abdo, A. A., et al. 2010a, The Astrophysical Journal, 708, 1310

—. 2010b, The Astrophysical Journal, 722, 520

—. 2010c, Physical Review Letters, 104, 101101

—. 2010d, The Astrophysical Journal, 715, 429

—. 2010e, The Astrophysical Journal, 716, 30

Abraham, J., et al. 2008, Physical Review Letters, 101, 061101

Acciari, V. A., et al. 2008, The Astrophysical Journal Letters, 684, L73

—. 2009a, Science, 325, 444

—. 2009b, The Astrophysical Journal, 703, 169

Acero, F., et al. 2009, Science, 326, 1080

Achterberg, A., Gallant, Y. A., Kirk, J. G., & Guthmann, A. W. 2001, Monthly Notices of the Royal Astronomical Society, 328, 393

Ackermann, M., et al. 2010, The Astrophysical Journal, 716, 1178

Aharonian, F., Buckley, J., Kifune, T., & Sinnis, G. 2008a, Reports on Progress in Physics, 71, 096901

Aharonian, F., et al. 2001, The Astrophysical Journal, 546, 898

—. 2003a, Astronomy & Astrophysics, 406, L9

—. 2003b, Astronomy & Astrophysics, 403, 523

—. 2004, Astronomy & Astrophysics, 425, L13

—. 2005, Astronomy & Astrophysics, 442, 895

—. 2006a, Astronomy & Astrophysics, 449, 223

—. 2006b, Nature, 440, 1018

—. 2006c, Astronomy & Astrophysics, 457, 899

—. 2006d, The Astrophysical Journal, 636, 777

—. 2007, The Astrophysical Journal Letters, 664, L71

—. 2008b, Physical Review Letters, 101, 261104

—. 2009a, The Astrophysical Journal Letters, 695, L40

—. 2009b, Astronomy & Astrophysics, 502, 749

—. 2009c, The Astrophysical Journal Letters, 696, L150

Aharonian, F. A. 2000, New Astronomy, 5, 377

Aharonian, F. A., Belyanin, A. A., Derishev, E. V., Kocharovsky, V. V., & Kocharovsky, V. V. 2002, Physical Review D, 66, 023005

Aharonian, F. A., Khangulyan, D., & Costamante, L. 2008c, Monthly Notices of the Royal Astronomical Society, 387, 1206

Ahn, H. S., et al. 2009, The Astrophysical Journal, 707, 593

Aielli, G., et al. 2006, Nuclear Instruments and Methods in Physics Research Section A: Accelerators, Spectrometers, Detectors and Associated Equipment, 562, 92

Albert, J., et al. 2006, Science, 312, 1771

—. 2007, The Astrophysical Journal, 669, 862

—. 2008a, Nuclear Instruments and Methods in Physics Research A, 588, 424

—. 2008b, The Astrophysical Journal, 674, 1037

Amano, T., & Hoshino, M. 2009, The Astrophysical Journal, 690, 244

Amelino-Camelia, G., Ellis, J., Mavromatos, N. E., Nanopoulos, D. V., & Sarkar, S. 1998, Nature, 395, 525

Anderhub, H., et al. 2010, Nuclear Instruments and Methods in Physics Research Section A: Accelerators, Spectrometers, Detectors and Associated Equipment, In Press, Corrected Proof,

Antoni, T., et al. 2003, Nuclear Instruments and Methods in Physics Research A, 513, 490

Antonucci, R. 1993, Annual Review of Astronomy & Astrophysics, 31, 473

Aprile, E., Curioni, A., Giboni, K., Kobayashi, M., Oberlack, U., & Zhang, S. 2008, Nuclear Instruments and Methods in Physics Research Section A: Accelerators, Spectrometer s, Detectors and Associated Equipment, 593, 414

Arons, J. 2003, The Astrophysical Journal, 589, 871

Atkins, R., et al. 2004, The Astrophysical Journal, 608, 680

Atwood, W. B., et al. 2009, The Astrophysical Journal, 697, 1071

Ave, M., Boyle, P. J., Gahbauer, F., Höppner, C., Hörandel, J. R., Ichimura, M., Müller, D., & Romero-Wolf, A. 2008, The Astrophysical Journal, 678, 262

Baker, D. N., & Stone, E. C. 1976, Geophysical Research Letters, 3, 557

Bally, J., O'Dell, C. R., & McCaughrean, M. J. 2000, The Astrophysical Journal, 119, 2919

Band, D. L., & Grindlay, J. E. 1985, The Astrophysical Journal, 298, 128

Barbiellini, G., Fedel, G., Liello, F., Longo, F., Pontoni, C., Prest, M., Tavani, M., & Vallazza, E. 2002, Nuclear Instruments and Methods in Physics Research A, 490, 146

Baring, M. G., & Summerlin, E. J. 2009, in American Institute of Physics Conference Series, Vol. 1183, American Institute of Physics Conference Series, ed. X. Ao & G. Z. R. Burrows, 74–84

Barrau, A., et al. 1998, Nuclear Instruments and Methods in Physics Research A, 416, 278

Bednarek, W. 1993, The Astrophysical Journal Letters, 402, L29

Begelman, M. C., Blandford, R. D., & Rees, M. J. 1984, Reviews of Modern Physics, 56, 255

Begelman, M. C., Fabian, A. C., & Rees, M. J. 2008, Monthly Notices of the Royal Astronomical Society, 384, L19

Benbow, W., Costamante, L., & Giebels, B. 2006, The Astronomer's Telegram, 867, 1

Biller, S. D. 1995, Astroparticle Physics, 3, 385

Blandford, R., & Eichler, D. 1987, Physics Reports, 154, 1

Blandford, R. D. 2001, Progress of Theoretical Physics Supplement, 143, 182

—. 2002, Science, 295, 1653

Blandford, R. D., & Begelman, M. C. 1999, Monthly Notices of the Royal Astronomical Society, 303, L1

Blandford, R. D., & Konigl, A. 1979, The Astrophysical Journal, 232, 34

Blandford, R. D., & Payne, D. G. 1982, Monthly Notices of the Royal Astronomical Society, 199, 883

Blandford, R. D., & Znajek, R. L. 1977, Monthly Notices of the Royal Astronomical Society, 179, 433

Blasi, P. 2009, Physical Review Letters, 103, 051104

Bloser, P. F., Hunter, S. D., Depaola, G. O., & Longo, F. 2004, in Society of Photo-Optical Instrumentation Engineers (SPIE) Conference Series, Vol. 5165, Society of Photo-Optical Instrumentation Engineers (SPIE) Conference Series, ed. K. A. Flanagan & O. H. W. Siegmund, 322–333

Boggs, S. E. 2006, New Astronomy Reviews, 50, 604

Bongi, M., et al. 2010, Nuclear Instruments and Methods in Physics Research Section A: Accelerators, Spectrometers, Detectors and Associated Equipment, 612, 451 , proceedings of the 7th International Conference on Radiation Effects on Semiconductor materials , Detectors and Devices - RESMDD 2008

Borione, A., et al. 1994, Nuclear Instruments and Methods in Physics Research A, 346, 329

Boutelier, T., Henri, G., & Petrucci, P. 2008, Monthly Notices of the Royal Astronomical Society, 390, L73

Buckley, J., et al. 2008, ArXiv e-prints

Burbidge, G. R., Jones, T. W., & Odell, S. L. 1974, The Astrophysical Journal, 193, 43

Butt, Y. 2009, Nature, 460, 701

Caraveo, P. A., Bignami, G. F., Mitrofanov, I., & Vacanti, G. 1988, The Astrophysical Journal, 327, 203

Carilli, C. L., & Barthel, P. D. 1996, The Astronomy and Astrophysics Review, 7, 1

Catanese, M., et al. 1998, The Astrophysical Journal, 501, 616

Cavaliere, A., & D'Elia, V. 2002, The Astrophysical Journal, 571, 226

Celotti, A., Fabian, A. C., & Rees, M. J. 1998, Monthly Notices of the Royal Astronomical Society, 293, 239

Celotti, A., & Ghisellini, G. 2008, Monthly Notices of the Royal Astronomical Society, 385, 283

Chadwick, P. M., et al. 1999, The Astrophysical Journal, 513, 161

Cheng, K. S., Zhang, X., & Zhang, L. 2000, The Astrophysical Journal, 537, 80

Coburn, W., & Boggs, S. E. 2003, Nature, 423, 415

Coppi, P. S., & Aharonian, F. A. 1997, The Astrophysical Journal Letters, 487, L9+

Corbel, S. 2006, Advances in Space Research, 38, 2867

Cortina, J., Goebel, F., Schweizer, T., & for the MAGIC Collaboration. 2009, ArXiv e-prints

Costamante, L., & Ghisellini, G. 2002, Astronomy & Astrophysics, 384, 56

Couto e Silva, E. d., et al. 2001, Nuclear Instruments and Methods in Physics Research A, 474, 19

Covault, C. E., et al. 2001, in International Cosmic Ray Conference, Vol. 7, International Cosmic Ray Conference, 2810–+

CTA Consortium. 2010, Design Concepts for the Cherenkov Telescope Array, arXiv:1008.3703

Dar, A., & Laor, A. 1997, The Astrophysical Journal Letters, 478, L5+

Daum, A., et al. 1997, Astroparticle Physics, 8, 1

D'Avezac, P., Dubus, G., & Giebels, B. 2007, Astronomy & Astrophysics, 469, 857

de Angelis, A., Mansutti, O., Persic, M., & Roncadelli, M. 2009, Monthly Notices of the Royal Astronomical Society, 394, L21

de Jager, C., et al. 2004, European Physical Journal A, 19, 275

de Jager, O. C., Harding, A. K., Michelson, P. F., Nel, H. I., Nolan, P. L., Sreekumar, P., & Thompson, D. J. 1996, The Astrophysical Journal, 457, 253

de Naurois, M., & Rolland, L. 2009, Astroparticle Physics, 32, 231

de Naurois, M., et al. 2002, The Astrophysical Journal, 566, 343

Deeming, T. J. 1975, Astrophysics and Space Science, 36, 137

Deeter, J. E. 1984, The Astrophysical Journal, 281, 482

Degrange, B., Superina, G., Giebels, B., & Volpe, F. 2008, in Blazar Variability across the Electromagnetic Spectrum

Dermer, C. D., & Razzaque, S. 2010, The Astrophysical Journal, 724, 1366

Di Matteo, T., Allen, S. W., Fabian, A. C., Wilson, A. S., & Young, A. J. 2003, The Astrophysical Journal, 582, 133

Di Matteo, T., Springel, V., & Hernquist, L. 2005, Nature, 433, 604

Djannati-Atai , A., et al. 1999, Astronomy & Astrophysics, 350, 17

Dolag, K., Grasso, D., Springel, V., & Tkachev, I. 2005, "Journal of Cosmology and Astroparticle Physics", 1, 9

Dolag, K., Kachelriess, M., Ostapchenko, S., & Tomàs, R. 2011, The Astrophysical Journal Letters, 727, L4+

Done, C., & Gierliński, M. 2005, Monthly Notices of the Royal Astronomical Society, 364, 208

Drake, J. F., Swisdak, M., Che, H., & Shay, M. A. 2006, Nature, 443, 553

Drenkhahn, G., & Spruit, H. C. 2002, Astronomy & Astrophysics, 391, 1141

Dyks, J., Harding, A. K., & Rudak, B. 2004, The Astrophysical Journal, 606, 1125

Escande, L., & Tanaka, Y. T. 2009, The Astronomer's Telegram, 2328, 1

Fabian, A. C. 2009, Astronomy and Geophysics, 50, 030000

Falco, S. D. 2010, Advances in Space Research, 45, 112

Feldman, G. J., & Cousins, R. D. 1998, Phys. Rev. D, 57, 3873

Fender, R., Wu, K., Johnston, H., Tzioumis, T., Jonker, P., Spencer, R., & van der Klis, M. 2004, Nature, 427, 222

Ferreira, O., et al. 2004, Nuclear Instruments and Methods in Physics Research A, 530, 323

Fiasson, A., Dubois, F., Lamanna, G., Masbou, J., & Rosier-Lees, S. 2010, Astroparticle Physics, 34, 25

Fichtel, C. 1996, Astronomy and Astrophysics Supplement, 120, C23+

Finke, J. D., Dermer, C. D., & Böttcher, M. 2008, The Astrophysical Journal, 686, 181

Fontaine, G., et al. 1990, Nuclear Physics B Proceedings Supplements, 14, 79

Fortin, P., Horan, D., Ferrara, E., & for the Fermi-LAT Collaboration. 2009, ArXiv e-prints

Foschini, L., Ghisellini, G., Tavecchio, F., Bonnoli, G., & Stamerra, A. 2011, ArXiv e-prints

Fossati, G., Maraschi, L., Celotti, A., Comastri, A., & Ghisellini, G. 1998, Monthly Notices of the Royal Astronomical Society, 299, 433

Fossati, G., et al. 2000, The Astrophysical Journal, 541, 153

Franceschini, A., Rodighiero, G., & Vaccari, M. 2008, Astronomy & Astrophysics, 487, 837

Frank, J., King, A., & Raine, D. 1992, Accretion power in astrophysics., ed. Frank, J., King, A., & Raine, D.

Funk, S., et al. 2004, Astroparticle Physics, 22, 285

Gaidos, J. A., et al. 1996, Nature, 383, 319

Gaisser, T. K., Protheroe, R. J., & Stanev, T. 1998, The Astrophysical Journal, 492, 219

Gaskell, C. M. 2004, The Astrophysical Journal Letters, 612, L21

Gaskell, C. M., & Klimek, E. S. 2003, Astronomical and Astrophysical Transactions, 22, 661

Ghisellini, G. 1999, Astrophysical Letters Communications, 39, 17

Ghisellini, G., Ghirlanda, G., Tavecchio, F., Fraternali, F., & Pareschi, G. 2008, Monthly Notices of the Royal Astronomical Society, 390, L88

Ghisellini, G., & Lazzati, D. 1999, Monthly Notices of the Royal Astronomical Society, 309, L7

Ghisellini, G., & Madau, P. 1996, Monthly Notices of the Royal Astronomical Society, 280, 67

Ghisellini, G., Maraschi, L., & Tavecchio, F. 2009, Monthly Notices of the Royal Astronomical Society, 396, L105

Ghisellini, G., & Tavecchio, F. 2008, Monthly Notices of the Royal Astronomical Society, 386, L28

Ghisellini, G., Tavecchio, F., Foschini, L., Ghirlanda, G., Maraschi, L., & Celotti, A. 2010, Monthly Notices of the Royal Astronomical Society, 402, 497

Giannios, D., Uzdensky, D. A., & Begelman, M. C. 2009, Monthly Notices of the Royal Astronomical Society, 395, L29

Giebels, B., & Degrange, B. 2009, Astronomy & Astrophysics, 503, 797

Giebels, B., Dubus, G., & Khélifi, B. 2007, Astronomy & Astrophysics, 462, 29

Giebels, B., & the Hess collaboration. 2007, Journal of Physics Conference Series, 60, 127

Giebels, B., et al. 1998, Nuclear Instruments and Methods in Physics Research A, 412, 329

—. 2002, The Astrophysical Journal, 571, 763

Götz, D., Laurent, P., Lebrun, F., Daigne, F., & Bošnjak, Ž. 2009, The Astrophysical Journal Letters, 695, L208

Gould, R. J. 1979, Astronomy & Astrophysics, 76, 306

Gould, R. J., & Schréder, G. 1966, Physical Review Letters, 16, 252

Graff, P. B., Georganopoulos, M., Perlman, E. S., & Kazanas, D. 2008, The Astrophysical Journal, 689, 68

Granot, J. 2003, The Astrophysical Journal Letters, 596, L17

Guilbert, P. W., Fabian, A. C., & Rees, M. J. 1983, Monthly Notices of the Royal Astronomical Society, 205, 593

Halzen, F. 1992, Nature, 358, 452

Hanna, D. S., et al. 2002, Nuclear Instruments and Methods in Physics Research A, 491, 126

Hartman, R. C., et al. 1999, The Astrophysical Journal Supplements, 123, 79

Henri, G., Pelletier, G., Petrucci, P. O., & Renaud, N. 1999, Astroparticle Physics, 11, 347

HESS Collaboration et al. 2010, Astronomy & Astrophysics, 520, A83+

Hillas, A. M. 1984, "Annual Review of Astronomy and Astrophysics", 22, 425

Hinton, J. A., & Hofmann, W. 2009, Annual Review of Astronomy and Astrophysics, 47, 523

Hoffman, C. M., Sinnis, C., Fleury, P., & Punch, M. 1999, Reviews of Modern Physics, 71, 897

Hofmann, W. 2006, ArXiv Astrophysics e-prints

—. 2010, The Astronomer's Telegram, 3007, 1

Hofmann, W., & Fegan, S. 2009, The Astronomer's Telegram, 2293, 1

Huchra, J., et al. 2005, in Astronomical Society of the Pacific Conference Series, Vol. 329, Nearby Large-Scale Structures and the Zone of Avoidance, ed. A. P. Fairall & P. A. Woudt, 135–+

Hunter, S. D., Bertsch, D. L., & Deines-Jones, P. 2001, in American Institute of Physics Conference Series, Vol. 587, Gamma 2001: Gamma-Ray Astrophysics, ed. S. Ritz, N. Gehrels, & C. R. Shrader, 848–852

Hunter, S. D., et al. 2009, in submitted White Paper 137 to astro2010: The Astronomy and Astrophysics Decadal Survey

Ioka, K., & Nakamura, T. 2002, The Astrophysical Journal Letters, 570, L21

Jones, F. C. 1968, Physical Review, 167, 1159

Kachelrieß, M., Serpico, P. D., & Teshima, M. 2007, Astroparticle Physics, 26, 378

Kataoka, J., et al. 1999, The Astrophysical Journal, 514, 138

Katarzyński, K., Ghisellini, G., Tavecchio, F., Gracia, J., & Maraschi, L. 2006, Monthly Notices of the Royal Astronomical Society, 368, L52

Katarzyński, K., Ghisellini, G., Tavecchio, F., Maraschi, L., Fossati, G., & Mastichiadis, A. 2005, Astronomy & Astrophysics, 433, 479

Katarzyński, K., Lenain, J., Zech, A., Boisson, C., & Sol, H. 2008, Monthly Notices of the Royal Astronomical Society, 390, 371

Katarzyński, K., & Walczewska, K. 2010, Astronomy & Astrophysics, 510, A63+

Kirk, J. G., & Duffy, P. 1999, Journal of Physics G Nuclear Physics, 25, 163

Kneiske, T. M., Bretz, T., Mannheim, K., & Hartmann, D. H. 2004, Astronomy & Astrophysics, 413, 807

Koide, S., Shibata, K., Kudoh, T., & Meier, D. L. 2002, Science, 295, 1688

Komissarov, S. S. 2005, Monthly Notices of the Royal Astronomical Society, 359, 801

Komissarov, S. S., & Falle, S. A. E. G. 1997, Monthly Notices of the Royal Astronomical Society, 288, 833

Kotov, Y. D. 1989, Space Science Reviews, 49, 185, 10.1007/BF00173754

Kovacs, F., et al. 1990, Nuclear Physics B Proceedings Supplements, 14, 330

Krawczynski, H., et al. 2001, The Astrophysical Journal, 559, 187

—. 2004, The Astrophysical Journal, 601, 151

Krennrich, F. 2009, New Journal of Physics, 11, 115008

Krichbaum, T. P., et al. 2007, Towards the Event Horizon: High Resolution VLBI Imaging of Nuclei of Active Galaxies, ed. Lobanov, A. P., Zensus, J. A., Cesarsky, C., & Diamond, P. J. (Springer-Verlag), 189–+

Krolik, J. H. 1999, Active galactic nuclei : from the central black hole to the galactic environment, ed. Krolik, J. H.

Kusunose, M., & Takahara, F. 2008, The Astrophysical Journal, 682, 784

Lazzati, D., & Begelman, M. C. 2009, The Astrophysical Journal Letters, 700, L141

Le Bohec, S., et al. 1998, Nuclear Instruments and Methods in Physics Research A, 416, 425

Lei, F., Dean, A. J., & Hills, G. L. 1997, Space Science Reviews, 82, 309

Lemoine, M., & Waxman, E. 2009, Journal of Cosmology and Astroparticle Physics, 11, 9

Lemoine-Goumard, M., Degrange, B., & Tluczykont, M. 2006, Astroparticle Physics, 25, 195

Lenain, J., Boisson, C., Sol, H., & Katarzyński, K. 2008, Astronomy & Astrophysics, 478, 111

Lewis, D. A. 1990, Experimental Astronomy, 1, 213

Li, T., & Ma, Y. 1983, The Astrophysical Journal, 272, 317

Lin, R. P., et al. 2003, The Astrophysical Journal Letters, 595, L69

Lindsey, W. C., & Chie, C. M. 1976, IEEE Proceedings, 64, 1652

Linsley, J. 1963, Phys. Rev. Lett., 10, 146

Lister, M. L., & MOJAVE Collaboration. 2009, in Bulletin of the American Astronomical Society, Vol. 41, Bulletin of the American Astronomical Society, 294–+

Lyubarskii, Y. E. 1997, Monthly Notices of the Royal Astronomical Society, 292, 679

Lyubarsky, Y. 2010, The Astrophysical Journal Letters, 725, L234

Lyubarsky, Y., & Kirk, J. G. 2001, The Astrophysical Journal, 547, 437

Lyutikov, M., Pariev, V. I., & Blandford, R. D. 2003, The Astrophysical Journal, 597, 998

MacLeod, A. J. 2000, Nuclear Instruments and Methods in Physics Research Section A: Accelerators, Spectrometers, Detectors and Associated Equipment, 443, 540

MAGIC Collaboration et al. 2008, Science, 320, 1752

Mannheim, K. 1993, Astronomy & Astrophysics, 269, 67

Maraschi, L., & Tavecchio, F. 2003, The Astrophysical Journal, 593, 667

Maraschi, L., et al. 2002, ArXiv Astrophysics e-prints

Massaro, E., Giommi, P., Leto, C., Marchegiani, P., Maselli, A., Perri, M., Piranomonte, S., & Sclavi, S. 2009, Astronomy & Astrophysics, 495, 691

Mastichiadis, A., & Kirk, J. G. 1997, Astronomy & Astrophysics, 320, 19

Matthiae, G. 2010, New Journal of Physics, 12, 075009

Mattox, J. R. 1991, Experimental Astronomy, 2, 75

Mattox, J. R., Mayer-Hasselwander, H. A., & Strong, A. W. 1990, The Astrophysical Journal, 363, 270

Mattox, J. R., et al. 1993, The Astrophysical Journal, 410, 609

Maximon, L. C., & Olsen, H. 1962, Physical Review, 126, 310

Mayer-Hasselwander, H. A., et al. 1982, Astronomy & Astrophysics, 105, 164

McHardy, I. 2008, in Blazar Variability across the Electromagnetic Spectrum

McHardy, I., & Czerny, B. 1987, Nature, 325, 696

McKinney, J. C. 2005, The Astrophysical Journal Letters, 630, L5

Meier, D. L., Koide, S., & Uchida, Y. 2001, Science, 291, 84

Melrose, D. B. 2009, ArXiv e-prints

Mineshige, S., Ouchi, N. B., & Nishimori, H. 1994, Publications of the Astronomical Society of Japan, 46, 97

Mirabel, I. F., & Rodríguez, L. F. 1994, Nature, 371, 46

—. 1999, Annual Review of Astronomy & Astrophysics, 37, 409

Mirzoyan, R., & Andersen, M. 2009, Astroparticle Physics, 31, 1

Moiseev, A. A., Hartman, R. C., Ormes, J. F., Thompson, D. J., Amato, M. J., Johnson, T. E., Segal, K. N., & Sheppard, D. A. 2007, Astroparticle Physics, 27, 339

Morháč, M., Kliman, J., Matoušek, V., Veselský, M., & Turzo, I. 2000, Nuclear Instruments and Methods in Physics Research A, 443, 108

Mori, M. 2009, J. Phys. Soc. Jpn. Supp. A, 78

Moskalenko, I. V., Stawarz, L., Porter, T. A., & Cheung, C. C. 2009, The Astrophysical Journal, 693, 1261

Mücke, A., Protheroe, R. J., Engel, R., Rachen, J. P., & Stanev, T. 2003, Astroparticle Physics, 18, 593

Mukherjee, R., et al. 1997, The Astrophysical Journal, 490, 116

Murase, K., Ioka, K., Nagataki, S., & Nakamura, T. 2008, "Physical Review D", 78, 023005

Nandikotkur, G., Jahoda, K. M., Hartman, R. C., Mukherjee, R., Sreekumar, P., Böttcher, M., Sambruna, R. M., & Swank, J. H. 2007, The Astrophysical Journal, 657, 706

Narayan, R., Yi, I., & Mahadevan, R. 1995, Nature, 374, 623

Nemmen, R. S., Bonatto, C., & Storchi-Bergmann, T. 2010, "The Astrophysical Journal", 722, 281

Neronov, A., & Ribordy, M. 2009, Physical Review D, 80, 083008

Neronov, A., & Vovk, I. 2010, Science, 328, 73

Nishiyama, T. 1999, in International Cosmic Ray Conference, Vol. 3, International Cosmic Ray Conference, 370–+

Norris, J. P., Nemiroff, R. J., Bonnell, J. T., Scargle, J. D., Kouveliotou, C., Paciesas, W. S., Meegan, C. A., & Fishman, G. J. 1996, The Astrophysical Journal, 459, 393

O'C Drury, L. 2001, in Nuclei Far from Stability and Astrophysics, ed. D. N. Poenaru, H. Rebel, & J. Wentz, 341–+

Ohm, S., van Eldik, C., & Egberts, K. 2009, Astroparticle Physics, 31, 383

Ong, R. A. 1998, Physics Reports, 305, 93

—. 2003, ArXiv Astrophysics e-prints

—. 2009, The Astronomer's Telegram, 2309, 1

Ong, R. A., & Fortin, P. 2009, The Astronomer's Telegram, 2272, 1

Padilla, L., et al. 1998, Astronomy & Astrophysics, 337, 43

Paneque, D., Chiang, J., Giebels, B., Lonjou, V., Lott, B., & Madejski, G. 2008, in Astronomical Society of the Pacific Conference Series, Vol. 386, Extragalactic Jets: Theory and Observation from Radio to Gamma Ray, ed. T. A. Rector & D. S. De Young, 477–+

Paré, E., et al. 1990, Phys. Lett., B242, 531

Paré, E., et al. 2002, Nuclear Instruments and Methods in Physics Research A, 490, 71

Pearson, T. J., Unwin, S. C., Cohen, M. H., Linfield, R. P., Readhead, A. C. S., Seielstad, G. A., Simon, R. S., & Walker, R. C. 1981, "Nature", 290, 365

Peebles, P. J. E. 1993, Principles of physical cosmology, ed. Peebles, P. J. E.

Pelletier, G. 2001, in American Institute of Physics Conference Series, Vol. 558, American Institute of Physics Conference Series, ed. F. A. Aharonian & H. J. Völk, 289–298

Perlman, E., Addison, B., Georganopoulos, M., Wingert, B., & Graff, P. 2008, in Blazar Variability across the Electromagnetic Spectrum

Petschek, H. E. 1964, NASA Special Publication, 50, 425

Pierre AUGER Collaboration, Abraham, J., Abreu, P., Aglietta, M., Ahn, E. J., Allard, I., Zepeda, A., & Ziolkowski, M. 2010, Physics Letters B, 685, 239

Piner, B. G., & Edwards, P. G. 2004, The Astrophysical Journal, 600, 115

Piran, T. 2000, "Physics Reports", 333, 529

Pohl, M., & Schlickeiser, R. 2000, Astronomy & Astrophysics, 354, 395

Porcas, R. 1983, "Nature", 302, 753

Prandini, E., Bonnoli, G., Maraschi, L., Mariotti, M., & Tavecchio, F. 2010, Monthly Notices of the Royal Astronomical Society, 405, L76

Protheroe, R. J. 1986, Monthly Notices of the Royal Astronomical Society, 221, 769

Punch, M., et al. 1992, Nature, 358, 477

Raue, M., Kneiske, T., & Mazin, D. 2009, Astronomy & Astrophysics, 498, 25

Rawlings, S., & Saunders, R. 1991, Nature, 349, 138

Rees, M. J. 1966, "Nature", 211, 468

Rees, M. J., & Meszaros, P. 1994, The Astrophysical Journal Letters, 430, L93

Remillard, R. A., Grossan, B., Bradt, H. V., Ohashi, T., & Hayashida, K. 1991, Nature, 350, 589

Rieger, F. M., & Aharonian, F. A. 2008, Astronomy & Astrophysics, 479, L5

Rochester, L., Usher, T., Johnson, R. P., & Atwood, B. 2010, ArXiv e-prints

Rybicki, G. B., & Lightman, A. P. 1985, Radiative processes in astrophysics., ed. Rybicki, G. B. & Lightman, A. P.

Ryu, D., Das, S., & Kang, H. 2010, "The Astrophysical Journal", 710, 1422

Sanchez, D. 2010, These de l'Ecole polytechnique

Sanchez, D., & Fegan, S. 2010, The Astronomer's Telegram, 3014, 1

Sanchez, D., & Giebels, B. 2009, ArXiv e-prints

Sanchez, D., Giebels, B., & Dubus, G. 2008, in Blazar Variability across the Electromagnetic Spectrum

Saugé, L., & Henri, G. 2004, The Astrophysical Journal, 616, 136

Schliesser, A., & Mirzoyan, R. 2005, Astroparticle Physics, 24, 382

Schönfelder, V., et al. 2000, Astronomy and Astrophysics, Supplement, 143, 145

Shakura, N. I., & Sunyaev, R. A. 1973, Astronomy & Astrophysics, 24, 337

Sigl, G., Miniati, F., & Ensslin, T. A. 2003, "Physical Review D", 68, 043002

Sikora, M. 2010, ArXiv e-prints

Sikora, M., Begelman, M. C., Madejski, G. M., & Lasota, J. 2005, The Astrophysical Journal, 625, 72

Sikora, M., Begelman, M. C., & Rees, M. J. 1994, The Astrophysical Journal, 421, 153

Sikora, M., & Madejski, G. 2001, in American Institute of Physics Conference Series, Vol. 558, American Institute of Physics Conference Series, ed. F. A. Aharonian & H. J. Völk, 275–288

Sikora, M., Madejski, G., Moderski, R., & Poutanen, J. 1997, The Astrophysical Journal, 484, 108

Simonetti, J. H., Cordes, J. M., & Heeschen, D. S. 1985, The Astrophysical Journal, 296, 46

Sinnis, G. 2009, New Journal of Physics, 11, 055007

Sironi, L., & Spitkovsky, A. 2009, The Astrophysical Journal, 707, L92

Spada, M., Ghisellini, G., Lazzati, D., & Celotti, A. 2001, Monthly Notices of the Royal Astronomical Society, 325, 1559

Spandre, G., & The GLAST Lat Collaboration. 2007, Nuclear Instruments and Methods in Physics Research A, 581, 160

Spitkovsky, A. 2008, The Astrophysical Journal, 682, L5

Spruit, H. C. 2010, in Lecture Notes in Physics, Berlin Springer Verlag, Vol. 794, Lecture Notes in Physics, Berlin Springer Verlag, ed. T. Belloni, 233–+

Sreekumar, P., et al. 1998, The Astrophysical Journal, 494, 523

Stawarz, Ł., Cheung, C. C., Harris, D. E., & Ostrowski, M. 2007, The Astrophysical Journal, 662, 213

Stecker, F. W., de Jager, O. C., & Salamon, M. H. 1992, The Astrophysical Journal Letters, 390, L49

—. 1996, The Astrophysical Journal Letters, 473, L75+

Stecker, F. W., & Salamon, M. H. 1996, The Astrophysical Journal, 464, 600

Stecker, F. W., & Scully, S. T. 2010, The Astrophysical Journal Letters, 709, L124

Stern, B. E., & Poutanen, J. 2008, Monthly Notices of the Royal Astronomical Society, 383, 1695

Superina, G. 2009, These de l'Ecole polytechnique

Suzuki-Vidal, F., et al. 2010, Astrophysics and Space Science, 340

Swordy, S. 2007, Journal of Physics Conference Series, 60, 139

Takahashi, T., Madejski, G., & Kubo, H. 1999, Astroparticle Physics, 11, 177 , teV Astrophysics of Extragalactic Sources

Takahashi, Y., & the JEM-EUSO Collaboration. 2009, New Journal of Physics, 11, 065009

Takata, J., & Chang, H. 2007, The Astrophysical Journal, 670, 677

Takata, J., Chang, H., & Cheng, K. S. 2007, The Astrophysical Journal, 656, 1044

Tavani, M., et al. 2008, Nuclear Instruments and Methods in Physics Research A, 588, 52

—. 2009, Astronomy & Astrophysics, 502, 995

Tavecchio, F., & Ghisellini, G. 2008, Monthly Notices of the Royal Astronomical Society, 385, L98

Tavecchio, F., Ghisellini, G., Bonnoli, G., & Foschini, L. 2010, ArXiv e-prints

Tavecchio, F., et al. 2001, The Astrophysical Journal, 554, 725

The Pierre Auger Collaboration et al. 2007, Science, 318, 938

—. 2010, Astroparticle Physics, 34, 314

Thompson, D. J., et al. 1993, The Astrophysical Journal Supplements, 86, 629

Thorne, K. S. 1974, The Astrophysical Journal, 191, 507

Timmer, J., & Koenig, M. 1995, Astronomy & Astrophysics, 300, 707

Tingay, S. J., et al. 1998, The Astrophysical Journal, 115, 960

Tluczykont, M., Bernardini, E., Satalecka, K., Clavero, R., Shayduk, M., & Kalekin, O. 2010, Astronomy & Astrophysics, 524, A48+

Tonachini, A. S. 2011, Nuclear Instruments and Methods in Physics Research Section A: Accelerators, Spectrometer s, Detectors and Associated Equipment, 630, 87 , proceedings of the 2nd Roma International Conference on Astroparticle Physics (RICAP 2009)

Urry, C. M., & Padovani, P. 1995, Publications of the Astronomical Society of the Pacific, 107, 803

Uttley, P., & McHardy, I. M. 2001, Monthly Notices of the Royal Astronomical Society, 323, L26

Uttley, P., McHardy, I. M., & Papadakis, I. E. 2002, Monthly Notices of the Royal Astronomical Society, 332, 231

Uttley, P., McHardy, I. M., & Vaughan, S. 2005, Monthly Notices of the Royal Astronomical Society, 359, 345

Uzdensky, D. A. 2006, ArXiv Astrophysics e-prints

van der Klis, M. 1989, in Timing Neutron Stars, ed. H. Ögelman & E. P. J. van den Heuvel, 27–+

Vassiliev, V., Fegan, S., & Brousseau, P. 2007, Astroparticle Physics, 28, 10

VERITAS Collaboration et al. 2009, Nature, 462, 770

Véron-Cetty, M., & Véron, P. 2006, Astronomy & Astrophysics, 455, 773

—. 2010, Astronomy & Astrophysics, 518, A10+

Vestrand, W. T., Stacy, J. G., & Sreekumar, P. 1995, The Astrophysical Journal Letters, 454, L93+

von Ballmoos, P., Takahashi, T., & Boggs, S. E. 2010, Nuclear Instruments and Methods in Physics Research A, 623, 431

Vukcevic, M., & Schlickeiser, R. 2007, Astronomy & Astrophysics, 467, 15

Wagner, R. 2009, in American Institute of Physics Conference Series, Vol. 1112, American Institute of Physics Conference Series, ed. D. Bastieri & R. Rando, 187–197

Waxman, E. 1995a, Physical Review Letters, 75, 386

—. 1995b, The Astrophysical Journal Letters, 452, L1+

—. 2004, New Journal of Physics, 6, 140

Weekes, T. 2007, Nature, 448, 760

Weekes, T. C., et al. 1989, The Astrophysical Journal, 342, 379

—. 2002, Astroparticle Physics, 17, 221

Wigger, C., Hajdas, W., Arzner, K., Güdel, M., & Zehnder, A. 2004, The Astrophysical Journal, 613, 1088

Wojtsekhowski, B., Tedeschi, D., & Vlahovic, B. 2003, Nuclear Instruments and Methods in Physics Research A, 515, 605

Yang, J., & Wang, J. 2010, Astronomy & Astrophysics, 522, A12+

Yüksel, H., Kistler, M. D., & Stanev, T. 2009, Physical Review Letters, 103, 051101

Zenitani, S., & Hoshino, M. 2001, The Astrophysical Journal Letters, 562, L63

Zhang, Y. H., et al. 1999, The Astrophysical Journal, 527, 719